From local degrees of freedom to correlated states in anisotropic $3d$ transition metal compounds

Harry Lane

Doctor of Philosophy
The University of Edinburgh
May 2022

Abstract

Anisotropy plays a crucial role in a wide variety of magnetic systems. In low-dimensional materials it can stabilise magnetic structures, overcoming the tendency for thermal fluctuations to disorder the magnetic correlations. It can also give rise to exotic dynamics such as nonlinear excitations and amplitude fluctuations that are not present in purely isotropic magnets. The origin of magnetic anisotropy lies in the physics of the individual magnetic ion and the crystallographic environment in which it finds itself. The nature of the magnetocrystalline anisotropy is therefore highly dependent on both the crystal structure and the species of magnetic ion. This dependence on the particulars of the system gives rise to starkly different phenomena in different compounds.

In this Thesis, the physics of a number of anisotropic $3d$ transition metal compounds will be investigated, with a particular focus on the interplay between the single-ion physics and correlated phenomena. The Thesis begins with a discussion of the nature of magnetic interactions in the solid state, focusing on the quantum mechanical nature of the spin and orbital degrees of freedom that give rise to magnetism. Chapter 2 then provides an overview of neutron scattering – the principle experimental technique employed in this Thesis. This chapter concentrates on the instrumentation and neutron scattering theory required to interpret the results detailed in the later chapters and includes sections on both time-of-flight and triple-axis spectroscopy.

Following the two introductory chapters, Chapter 3 explores the low energy dynamics of quasi-one-dimensional, large-S quantum antiferromagnets with easy-axis anisotropy. Such a situation is present in some $3d$ transition metal compounds based on ions such as Fe^{3+} or Mn^{2+}. A description of these systems is developed using a semiclassical nonlinear σ model. The saddle point approximation leads to a sine-Gordon equation which supports soliton solutions. These correspond to the movement of spatially extended domain walls. Long-

range magnetic order in spin chain compounds is typically a consequence of a weak inter-chain coupling. Below the ordering temperature, the coupling to nearby chains leads to an energy cost associated with the separation of two domain walls. From the kink-antikink two-soliton solution, an effective confinement potential is computed. At distances that are large compared to the size of the solitons the potential is linear, as expected for point-like domain walls. At small distances the gradual annihilation of the solitons weakens the effective attraction and renders the potential quadratic. By numerically solving the effective one-dimensional Schrödinger equation with this nonlinear confinement potential, the soliton bound state spectrum is computed. The theory is then applied to $CaFe_2O_4$, an anisotropic magnet based upon an antiferromagnetic zig-zag network of $3d^5$ Fe^{3+} ions with $S = 5/2$ and $L = 0$. Neutron scattering measurements are able to resolve seven discrete energy levels for spectra recorded slightly below the Néel temperature $T_N \approx 200$ K. These modes are well described by the nonlinear confinement model in the regime of large spatially extended solitons.

Chapter 4 concerns a $j_{eff} = \frac{1}{2}$ magnet α-CoV_2O_6, where spin-orbit coupling is much larger than the inter-ion coupling and hence the $j_{eff} = \frac{1}{2}$ manifold is well separated from spin-orbital levels. Here, the anisotropy originates from a small crystallographic distortion which can be treated as a small perturbation motivating an effective $S = 1/2$ Hamiltonian with an Ising/uniaxial symmetry. Low temperature magnetisation data show the existence of magnetisation plateaux, yet these are not accompanied by Bragg peaks in neutron diffraction data and hence are not indicative of transitions to new phases of long-range magnetic order. By application of the Lieb-Schultz-Mattis theorem, the existence of these magnetisation plateaux is reconciled with the absence of corresponding Bragg peaks in α-CoV_2O_6. This analysis relates the underlying symmetries of the ground state to the magnetisation. The presence of uniaxial anisotropy is shown to stabilise metastable short-range magnetic order at different field strengths and temperatures, constructed from antiphase boundaries.

Remaining on the theme of metastable antiphase boundary order, Chapter 5 returns to the $S = 5/2$ antiferromagnet $CaFe_2O_4$ which exhibits two magnetic orders that show regions of coexistence at some temperatures. By applying neutron scattering and a Green's function formalism, the spin wave excitations in this material are characterised, elucidating the relevant terms in the spin Hamiltonian. In doing so, it is suggested that the low temperature A phase order ($\uparrow\uparrow\downarrow\downarrow$) finds its origins in the freezing of antiphase boundaries created by thermal fluctuations in a parent B phase order ($\uparrow\downarrow\uparrow\downarrow$). The low temperature magnetic order observed in $CaFe_2O_4$ is thus the result of a competition between the exchange coupling along c, which favors the B phase, and the single-ion anisotropy, which stabilises thermally-generated antiphase boundaries, leading to static metastable A phase order at low temperatures.

In Chapter 6, an iron-rich sample of the two-dimensional van der Waals itinerant ferromagnet Fe_3GeTe_2 is investigated using neutron scattering. The excitations are shown to be predominantly two-dimensional in nature and broadened, as expected for an itinerant magnet. The anisotropy strength is shown to be greater in magnitude than has been reported in a recent study of iron-deficient samples, hinting at a crucial role of the iron concentration in the single-ion properties of Fe_3GeTe_2. A model of domain walls is developed and the extracted exchange parameters from the neutron scattering results are used to calculate the expected domain wall width, based on bulk exchange parameters. This is then compared with scanning tunnelling microscopy (STM) data which are reflective of the surface physics. Strong agreement is found with the STM data suggesting that the surface properties are similar to that of the bulk.

Chapter 7 concerns another two-dimensional van der Waals ferromagnet, VI_3. Unlike the $3d^5$ transition metal compound discussed in the preceding chapter, VI_3 is formed from a honeycomb of $3d^2$ V^{3+} ions which carry an orbital degree of freedom. Here the Green's function formalism is extended to treat systems with an orbital degree of freedom, treating the spin-orbit coupling and crystal distortions explicitly. Neutron scattering is used to understand the nature of the low energy spin dynamics in VI_3, demonstrating the existence of two qualitatively different low energy modes. The neutron data are then modelled using the Green's function formalism, allowing a connection to be made between the spectrum and the crystallographic structure and indicating the presence of two differently distorted domains. It is shown that the anisotropy arising due to the cooperative effect of spin-orbit coupling and crystal distortions allows for the stable two-dimensional magnetism at finite temperature.

Finally, in Chapter 8 the Green's function formalism is extended to treat noncollinear structures. This formalism is then applied to the noncollinear charge-ordered antiferromagnet $RbFe^{2+}Fe^{3+}F_6$ – a system of mixed valance formed by two coupled networks of Fe^{2+} ($3d^6$) and Fe^{3+} ($3d^5$) chains. The spin-orbit coupling and effect of crystal distortions on the Fe^{2+} ion are considered explicitly and the neutron scattering response is calculated using the noncollinear Green's function

formalism. In addition to spin-orbit excitons, it is shown that the low symmetry of the Fe^{2+} coordination may give rise to low energy amplitude fluctuations that are not captured by linear spin wave theory. It is suggested that noncollinear magnets with low local symmetry may provide candidate systems for stable low energy amplitude modes in condensed matter systems.

Declaration

This Thesis describes projects that are the result of collaborative efforts.

(i) In Chapter 2, a method of single crystal alignment is discussed based on the software package written by Z. Liu.

(ii) In Chapter 3, the neutron scattering experiment on OSIRIS was carried out by C. Stock and F. Demmel.

(iii) In Chapter 4, the neutron diffraction measurements were performed by L. Edwards, C. Stock and S. Giblin. Magnetisation measurements were made by C. Paulsen, E. LHotel and M. Songvilay.

(iv) In Chapter 5, neutron diffraction was carried out by E. E. Rodriguez. Neutron scattering experiments on LET were carried out by C. Stock, R. I. Bewley and D. J. Voneshen. Phonon measurements using EIGER were carried out by C. Stock and U. Stuhr. Neutron scattering measurements on RITA II were carried out by C. Stock and Ch. Niedermeyer.

(v) In Chapter 6, STM measurements were carried out by C. Trainer, O. Armitage, I. Benedičič and Peter Wahl.

I declare that this Thesis was composed by myself under the supervision of C. Stock, R. A. Ewings and J. P. Attfield, that the work contained herein is my own except where explicitly stated otherwise in the text, and that this work has not been submitted for any other degree or professional qualification except as specified.

Chapters 3, 4, 5, 7 and parts of Chapter 2 have been published in [1–5]. Chapters 6 and 8 have been submitted for publication.

(*Harry Lane, May 2022*)

Acknowledgements

The group of people who have contributed to the completion of this Thesis is innumerable. Firstly I would like to express my unbounded gratitude to my team of supervisors Chris Stock, Russell Ewings and Paul Attfield, I count myself very fortunate to have benefited from their combined knowledge and experience. I thank Chris for sharing his wealth of knowledge about neutron scattering and for the countless hours he has sacrificed to help me develop as a scientist. I would also like to thank Russell for his guidance on technical matters and his supreme clarity of thought – our weekly meetings never failed to help me overcome some hurdle or other. I am grateful to Paul for his insight on materials and for encouraging me to think more about single-ion physics. I would also like to thank Frank Krüger for his theoretical insights and for introducing me to the joys of condensed matter physics.

Over the course of my PhD I have had the good fortune of meeting many gifted and inspiring scientists. I would like to thank the current and former members of the Stock group at Edinburgh and the Excitations group at ISIS Neutron and Muon Source. In particular I would like to explicitly thank Paul Sarte, Nathan Giles-Donovan, Edmond Chan, Zihao Liu and Manila Songvilay of Edinburgh, and Manh Duc Le, Gøran Nilsen, Helen Walker and David Voneshen of ISIS. I also thank Peter Gehring and Jose Rodriguez-Rivera of NIST for their assistance with experiments, Sean Giblin and Lewis Edwards for their diffraction measurements, and Joseph Vovrosh for the enjoyable weeks discussing trimers.

Finally I would like to extend my heartfelt thanks to my friends and family for keeping me going these past years. To my friends, Rory, Arnav, Zhangqi, Josie, JV, Becky, Ash, Emmie and Zoë, to name a few. Thank you for your friendship and being a welcome distraction from work. To the Mansfield family, thank you for your hospitality and companionship during the uncertain early days of the pandemic – I will look back fondly on the evenings watching National Theatre at home. To my parents, grandparents, and to my sister Natasha, your unwavering support and belief in me made this possible. Your encouragement of my love of learning from early childhood was instrumental in my development as a person. Most of all, thank you Ally for your continued support, your patience, your calming influence and for suffering the countless hours of discussion about spin waves.

Contents

List of Figures

List of Tables

Chapter 1

Introduction

This Thesis aims to address the nature of magnetic order and excitations in crystalline materials comprising ions belonging to the $3d$ group of elements. Though magnetism has been observed and exploited for millennia [25], its origin is deeply rooted in the quantum mechanical nature of matter. In crystals, there exists an interplay between the physics governing the behaviour of individual ions in the material and the correlation between these ions in a macroscopic sample, often leading to novel phenomena that differs from that of the constituent elements. A full quantum mechanical treatment of the many-body problem scales exponentially with the system size – this remains one of the fundamental difficulties in condensed matter physics. Nonetheless, methods have been developed that reduce the scale of the problem and shed light on the behaviour of many-body quantum systems. These approaches rely on approximations that reduce the number of degrees of freedom, treating only those deemed most important in describing the problem.

Neutron scattering remains the principle probe of magnetic excitations in crystals. By fully characterising the magnetic excitation spectrum, one can write down a Hamiltonian describing the system and gain an insight into the dominant interactions present in the material. This can offer insight into novel physical processes and further the collective understanding of magnetic materials. Though neutron scattering interrogates the correlation between spins in the system, there are identifiable signatures of single-ion physics present in the neutron scattering data. Through neutron scattering experiments and complementary theoretical analysis, this Thesis will outline how the neutron data can be interrogated for these single-ion effects, offering insights into order, the interplay of spin and orbital degrees of freedom and opportunities for control of magnetic properties by materials engineering. It will be shown that single-ion effects play a central role in the correlated states of matter emerging in magnetic systems.

This chapter will begin with an outline of the types of interactions present in magnetic crystals, beginning with the single-ion physics. There will then be a discussion of the magnetic interactions between ions that occur in solids and the order and excitations resulting therefrom. A full exposition of the influence of single-ion physics on the correlated behaviour in magnetic systems will be deferred to the later chapters, with reference to specific transition metal compounds. These discussions will be accompanied by neutron spectroscopic measurements and complementary theoretical analysis, demonstrating the manifestation of single-ion physics in the spectra.

1.1 Single-ion physics

Magnetism in solids is primarily a result of the magnetic moment associated with electrons in the unfilled outer shells of ions. The contribution from the nuclear magnetic moment is typically much smaller, since the magnetic moment is proportional to $\frac{1}{m}$ and the mass of a nucleus is orders of magnitude greater than that of an electron [26]. The consequences of the electron magnetic moment for ions in solids will now be discussed. This discussion will follow a number of seminal texts on the subject [21, 26–28] and will predominantly concern the $3d$ (Iron group) ions, although much of this analysis can be readily adapted to the $4f$ (Lanthanide) or $5f$ (Actinide) groups, with an appropriate reordering of the hierarchy of single-ion energy scales.

1.1.1 Angular momentum

The discussion of electron magnetism is begun by taking the simple case of a single electron of charge $-e$ orbiting a nucleus of charge Ze. This system can be described by the Schrödinger equation

$$\left(-\frac{\hbar^2}{2\mu}\nabla^2 - \frac{Ze^2}{r}\right)\psi(\mathbf{r}) = E\psi(\mathbf{r}) \tag{1.1}$$

where μ is the reduced mass of the composite system and r is the distance between the electron and the nucleus. The Laplace operator can be written in spherical coordinates [29]

$$\nabla^2 = \frac{1}{r^2}\frac{\partial}{\partial r}\left(r^2\frac{\partial}{\partial r}\right) + \frac{1}{r^2\mathrm{sin}\theta}\frac{\partial}{\partial\theta}\left(\mathrm{sin}\theta\frac{\partial}{\partial\theta}\right) + \frac{1}{r^2\mathrm{sin}^2\theta}\frac{\partial^2}{\partial\phi^2}. \tag{1.2}$$

By performing a separation of variables $\psi(\mathbf{r}) = R(r)\Theta(\theta)\Phi(\phi)$,

$$\begin{aligned} \frac{1}{r^2}\frac{\mathrm{d}}{\mathrm{d}r}\left(r^2\frac{\mathrm{d}R(r)}{\mathrm{d}r}\right) - \frac{\beta}{r^2}R(r) + \frac{2\mu}{\hbar^2}\left[E + \frac{Ze^2}{r}\right] &= 0 && \text{(1.3a)} \\ \frac{\mathrm{d}^2\Phi}{\mathrm{d}\phi^2} &= -m^2\Phi && \text{(1.3b)} \\ \frac{1}{\mathrm{sin}\theta}\frac{\mathrm{d}}{\mathrm{d}\theta}\left(\mathrm{sin}\theta\frac{\mathrm{d}\Theta(\theta)}{\mathrm{d}\theta}\right) - \frac{m^2}{\mathrm{sin}^2\theta}\Theta(\theta) + \beta\Theta(\theta) &= 0 && \text{(1.3c)} \end{aligned}$$

the Schrödinger equation can be solved [28] and admits quantised energy levels

$$E_n = -\frac{\mu Z^2 e^4}{2\hbar^2 n^2}. \tag{1.4}$$

The solutions to Eqns. 1.3a, 1.3b and 1.3c are given by [28]

$$\begin{aligned} R(r) &= -\sqrt{\left(\frac{2Z}{na_0}\right)^3 \frac{(n-l-1)!}{2n[(n+1)!]^3}}\, e^{-\frac{\rho}{2}}\rho^l L_{n+l}^{2l+1}(\rho) && \text{(1.5a)} \\ \Phi(\phi) &= \frac{1}{\sqrt{2\pi}}e^{im\phi} && \text{(1.5b)} \\ \Theta_{lm}(\theta) &= \sqrt{\frac{(2l+1)(l-|m|)!}{2(l+|m|)!}}\, P_l^{|m|}\left(\cos(\theta)\right) && \text{(1.5c)} \end{aligned}$$

with $\rho = \frac{2Zr}{na_0}$ and $a_0 = \frac{\hbar^2}{\mu e^2}$ and where $P_l^{|m|}(\mathrm{cos}\theta)$ and $L_{n+l}^{2l+1}(\rho)$ are the associated Legendre and associated Laguerre polynomials. The product of the angular parts of the wavefunction (Eqns. 1.5b and 1.5c) are proportional to the spherical harmonic function $Y_m^l = e^{im\phi}P_l^m(\mathrm{cos}\theta)$. By examining Eqn. 1.5b, it is clear that $m \in \mathbb{Z}$ in order that $\Phi(0) = \Phi(\pm 2\pi)$. Finally, from Eqns. 1.5a and 1.5c the following allowed values can be found

$$n = 1, 2, 3, ... \tag{1.6a}$$

$$l = 0, 1, 2, ..., n - 1 \tag{1.6b}$$

$$m = -l, -l + 1, ..., l - 1, l. \tag{1.6c}$$

The wavefunction can thus be fully defined by three quantum numbers, $|n, l, m\rangle$. The orbital angular momentum operator, $\mathbf{L} = -i\hbar\mathbf{r} \times \nabla$ satisfies the following eigenvalue equations [30]

$$\hat{L}^2 Y_l^m = \hbar^2 l(l+1) Y_l^m \tag{1.7a}$$

$$\hat{L}_z Y_l^m = m\hbar Y_l^m. \tag{1.7b}$$

The operators, $\hat{L}^2$ and $\hat{L}_z$ commute with the Hamiltonian and thus $\mathcal{H}$, $\hat{L}_z$ and $\hat{L}^2$ form a complete set of commuting observables.

The discussion outlined above does not capture the full number of degrees of freedom that are present for an atom of a hydrogen-like system. This is apparent when a magnetic field is applied, which linearly splits the atomic levels, an effect known as the Zeeman effect. The magnetic field couples to the spin degree of freedom of the electron, which has the quantum mechanical operator

$$\hat{S}^2 |s, m_s\rangle = \hbar^2 s(s+1) |s, m_s\rangle \tag{1.8a}$$

$$\hat{S}^z |s, m_s\rangle = \hbar m_s |s, m_s\rangle \tag{1.8b}$$

with $m_s = \pm\frac{1}{2}$. The presence of a spin degree of freedom was first conclusively demonstrated by Stern and Gerlach by passing silver atoms through a magnetic field and observing the trajectory under the resultant Zeeman field [31]. The atoms were observed to bifurcate, striking the detector in two places above and below the path of the initial beam, depending on the sign of m_s.

1.1.2 Spin-orbit coupling

Having introduced the spin and orbital angular momentum degrees of freedom, there will now be a discussion about the interaction between the spin and orbital moments. This interaction, known as spin-orbit coupling can be rigorously derived using the Dirac equation [32], however an illustrative and reasonably accurate derivation can be performed using the Bohr model [27]. For the ease of comprehension, this simple derivation will be presented, since in practice the factors dictating the strength of the spin-orbit interaction will be treated as parameters to be found experimentally. Let us consider a single electron orbiting a nucleus with charge Ze. If the electron moves with velocity v it will experience a magnetic field [27]

$$\mathbf{H} = \frac{Ze}{c}\frac{\mathbf{r}\times\mathbf{v}}{r^3}. \tag{1.9}$$

This field couples to the spin moment of the electron giving rise to a Zeeman term in the Hamiltonian

$$\mathcal{H} = g\mu_B \frac{Ze\hbar}{mc}\frac{\mathbf{s}\cdot\mathbf{l}}{r^3} \tag{1.10}$$

where it has been used that $\mathbf{r}\times\mathbf{v} = \hbar\mathbf{l}$, that is to say, that $\hbar\mathbf{l}$ is simply the angular momentum of the orbiting electron. Since the electric field of the nucleus causes the electron to accelerate, the electron is in a non-inertial reference frame and should ideally be treated relativistically. Doing so results in the "Thomas correction" [32], the full details of which will not change the subsequent discussion, therefore the equality can be replaced with a proportionality. Summing over all electrons one has

$$\mathcal{H}_{SO} \propto Z\sum_i \frac{\mathbf{s}_i\cdot\mathbf{l}_i}{r_i^3}. \tag{1.11}$$

The total spin and total angular momentum are then

$$\mathbf{S}_i = \sum_i \mathbf{s}_i \tag{1.12a}$$

$$\mathbf{L}_i = \sum_i \mathbf{l}_i. \tag{1.12b}$$

Electron spins tend to align[1] and so in a system containing fewer electrons than orbital levels ($n < 2l+1$) this allows the replacement $\mathbf{s}_i = \frac{1}{n}\mathbf{S} = \frac{1}{2S}\mathbf{S}$. If $n > 2l+1$, all orbital states (from $+l$ to $-l$) will be occupied with $\mathbf{s}_i$ parallel to $\mathbf{S}$ and hence the sum over $\mathbf{l}_i$ for the spins parallel to $\mathbf{S}$ will go to zero. The only nonzero terms in the sum will originate from spins anti-aligned with $\mathbf{S}$, thus $\mathbf{s}_i = -\frac{1}{2S}\mathbf{S}$. Overall this leads to a spin-orbit interaction of the form

$$\mathcal{H}_{SO} = \lambda\mathbf{L}\cdot\mathbf{S} \tag{1.13}$$

---

[1] The origin of this alignment will be discussed further in the section regarding Hund's rules.

where the sign of λ depends on whether the shell is more or less than half-filled [27]. The eigenstates of the spin-orbit Hamiltonian can be readily calculated by rewriting Eqn. 1.13 as

$$\mathcal{H}_{SO} = \lambda \mathbf{L} \cdot \mathbf{S} = \frac{\lambda}{2} \left((\mathbf{L} + \mathbf{S})^2 - \mathbf{L}^2 - \mathbf{S}^2 \right). \tag{1.14}$$

The eigenvalues of $\mathbf{S}^2$ and $\mathbf{L}^2$ are $S(S+1)$ and $L(L+1)$ respectively, so that

$$\mathcal{H}_{SO} = \frac{\lambda}{2} \left(J(J+1) - L(L+1) - S(S+1) \right) \tag{1.15}$$

where a new angular momentum operator, $\mathbf{J} = \mathbf{L} + \mathbf{S}$, has been defined – the *total* angular momentum. The total angular momentum quantum number can take integer values between $J = L + S$ and $|L - S|$. In some systems where the spin-orbit coupling is large, $\mathbf{J}$ is a good quantum number and the single-ion eigenstates are well described by the total angular momentum quantum numbers. Such a situation is typical of the iridates [33] but not the $3d$ ions, although one particular example where this is the case is discussed in Chapter 4.

1.1.3 Hund's rules and the Aufbau principle

Having discussed the spin and orbital quantum numbers, the discussion now turns to how the ground state of a many-electron atom is determined. There exists a list of rules known as Hund's rules that form a set of principles for the determination of the ground state of an atom, which should be applied in order. But first one must consider how electrons arrange themselves within atoms. As discussed in the last section, the state of an electron can be described by four quantum numbers $|n, l, m, m_s\rangle$. Electron shells labeled with s, p, d, f, g, h,... have $l = 0, 1, 2, 3, 4, 5$,... and can hold $2(2l + 1)$ electrons. There are two principles that dictate how these shells are filled.

1. *The Aufbau principle:* Shells are to be filled from the lowest available energy state, filling each shell entirely before populating the next.
2. *Madelung's rule:* The lowest energy shell has the smallest value of $n + l$. If two shells have the same value of $n + l$, the smallest n shell is filled first. This rule is visually depicted in Fig. 1.1.

Using these principles, the electronic configuration of many electron atoms can

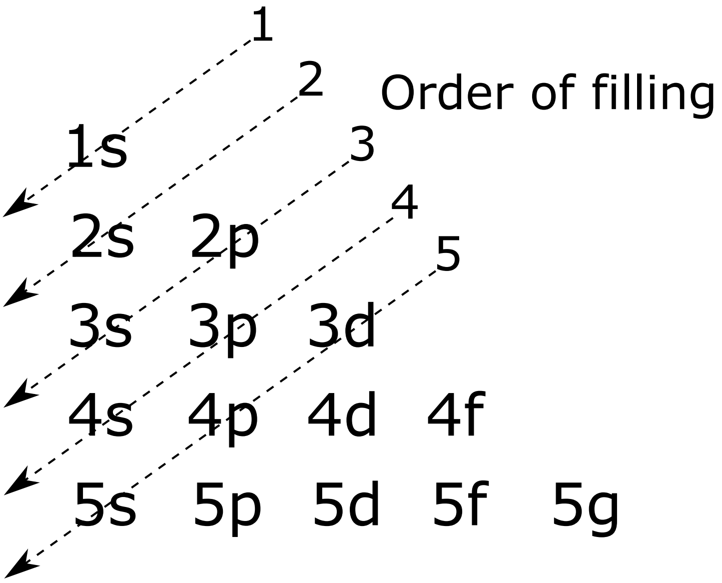

Figure 1.1 *The order of electron orbital shell filling according to Madelung's rule.*

be written down. The Madelung rule applies to the filling of atomic electron shells, however when atoms form ions, this rule can be violated. Typically the $3d$ elements lose the $4s^2$ electrons before those in the $3d$ shell, as seen in Co^{2+} [21]. As an example, below are listed the electron configurations for ions of relevance to this Thesis.

$$\mathrm{Fe}^{2+}\text{: } 1s^2 2s^2 2p^6 3s^2 3p^6 3d^6$$
$$\mathrm{Fe}^{3+}\text{: } 1s^2 2s^2 2p^6 3s^2 3p^6 3d^5$$
$$\mathrm{V}^{3+}\text{: } 1s^2 2s^2 2p^6 3s^2 3p^6 3d^2$$
$$\mathrm{Co}^{2+}\text{: } 1s^2 2s^2 2p^6 3s^2 3p^6 3d^7$$

Given the electronic configuration of an atom, Hund's rules can be used to determine the quantum numbers that describe the ground state. The rules will first be summarised before explaining their origin in more detail.

1. The ground state is that which maximises the value of S. In other words, electrons seeks to align themselves.
2. Within the states of maximal S, the state with largest the L value is lowest in energy.

3. Pursuant to Hund's first two rules, the total angular momentum is given by $J = |L \pm S|$, with the sign being positive (negative) if the outer shell is more than (less than) half full.

Hund's first rule is a consequence of the Pauli exclusion principle. Aligned spins are unable to come close to one another and hence provide little screening of the attractive Coulomb potential from the nucleus. Anti-aligned spins are not precluded from coming close to one another and therefore can give rise to a screening of the Coulomb potential. Thus the configuration where electron spins are aligned is the minimum energy state. The second of Hund's rules can be understood by considering the picture of orbiting electrons in the Bohr model. Electrons orbiting in the same direction encounter each other less and therefore provide less screening of each other than if they were to travel in opposite directions. This means that the state with where electron orbital angular momenta have the same sign leads to a lower energy configuration. This argument is analogous to that of Hund's first rule, demonstrating the similar behaviour of the spin and orbital moments [26]. Finally, the last of Hund's rules finds its origin in spin-orbit coupling. The spin-orbit coupling term $\mathcal{H} = \lambda \mathbf{L} \cdot \mathbf{S}$, splits the spectrum into levels based on the total angular momentum, $\mathbf{J}$. The order of the energy hierarchy of these levels depends on the spin-orbit coupling parameter λ, which is positive for less than half-filled shells and negative if the shell is greater than half-filled. Having assigned the quantum numbers in accordance with Hund's rules, the ground state can be described by its term symbol $^{2\mathrm{S}+1}\mathrm{L}_\mathrm{J}$, where the indices are given in terms of their numerical value and L is S, P, D,... for a ground state that has an orbital quantum number of 0,1,2,... following the standard orbital labelling convention. It is important to note that the energy scale of the spin-orbit coupling is typically much lower than that of the Coulomb interaction between electrons [21]. In fact, for the $3d$ ions considered in this Thesis, there is a another term in the single-ion Hamiltonian which is larger in magnitude.

1.1.4 Crystal field

Typically in the $3d$ ions the strength of the spin-orbit coupling is exceeded by that of the crystalline electric field. This contribution is a result of the Coulomb potential created by the local environment of surrounding ions, (ligands) and hence is often termed the ligand field. The effect of this crystal field is to lower the degeneracy of the fivefold degenerate d orbitals, and often permits the projection onto a lower dimensional manifold, described by an effective orbital angular momentum smaller than that of the free ion. This splitting is dependent on the local symmetry of the crystal field and hence the coordination of the central ion. All of the systems discussed in this Thesis are octahedrally coordinated and comprise a central metal ion X surrounded by six ligands, L, such that the local coordination is XL_6. It is typical to discuss the crystal field in terms of the real space basis functions of the atomic orbitals. For d electron system, this gives rise to five orbital levels, which are split by an octahedral crystal field into a ground state triplet of three $|t_{2g}\rangle$ levels and an excited doublet of two $|e_g\rangle$ levels. The discussion that follows will use the language of the "intermediate crystal field picture" as appropriate for the $3d$ ions and will consider octahedrally coordinated $3d$ ions. A more complete exposition of crystal fields can be found in Ref. [34].

The crystal field Hamiltonian can be written as

$$\mathcal{H}_{CEF} = -e\sum_{i=1}^{N} V(\mathbf{r}_i) \tag{1.16a}$$

$$V(\mathbf{r}) = \frac{1}{4\pi\epsilon_0}\int \frac{\rho(\mathbf{R})}{|\mathbf{r}-\mathbf{R}|}\mathrm{d}^3R \tag{1.16b}$$

where the sum is over the electrons in the outer shell of the central ion and $\rho(\mathbf{R})$ is the charge at position $\mathbf{R}$. The potential can be expanded in terms of the tesseral harmonics. These functions are related to the spherical harmonics and form a more convenient basis in which to expand the crystal field potential. The correspondence between the tesseral and spherical harmonics can be found in Appendix A

$$V(\mathbf{r}) = \sum_{k=0}^{\infty}\sum_{q=-k}^{k} r^k Z_k^q(\mathbf{r})\frac{1}{2k+1}\int \mathrm{d}^3R\frac{\rho(\mathbf{R})Z_k^q(\mathbf{R})}{\epsilon_0 R^{k+1}}. \tag{1.17}$$

Following Ref. [34], Eqn 1.16a can be conveniently written as

$$\mathcal{H}_{CEF} = \sum_{kq}\gamma_k^q H_k^q \tag{1.18a}$$

$$\gamma_k^q = \frac{1}{2k+1}\int \mathrm{d}^3R\frac{\rho(\mathbf{R})Z_k^q(\mathbf{R})}{\epsilon_0 R^{k+1}} \tag{1.18b}$$

$$H_k^q = \sum_{i}^{N} r_i^k Z_k^q(\mathbf{r}_i) \tag{1.18c}$$

Table 1.1 *Sign of B_4 for different filling factors [21].*

d^1, d^3, d^6, d^8	B_4 positive
d^2, d^4, d^7, d^9	B_4 negative

where the operator H_k^q is a polynomial. Such polynomial operators are inconvenient to work with, however there exists a mapping between these polynomials and equivalent quantum mechanical operators. This mapping can be verified by checking that the equivalent quantum mechanical operators transform according to the same irreducible representation of the rotation group as the polynomial. The equivalent operators for a number of polynomial functions relevant to crystal field theory were first calculated by Stevens [35]. The crystal field, in terms of quantum mechanical operators takes the form

$$\mathcal{H}_{CEF} = \sum_{kq} B_k^q \mathcal{O}_k^q \tag{1.19a}$$

$$\mathcal{O}_k^q = \left(p_k^q \Theta_k \langle r^k \rangle\right)^{-1} H_k^q \tag{1.19b}$$

$$B_k^q = -e p_k^q \langle r^k \rangle \gamma_k^q \Theta_k. \tag{1.19c}$$

The quantum mechanical operator equivalent “Stevens operators”, $\mathcal{O}_k^q$, are listed in Appendix B. The coefficients p_k^q are numerical factors associated with the tesseral functions and the factors Θ_k depend on the $3d$ electron wavefunctions and for $k = 2, 4, 6$ are the well-known Stevens coefficients $\alpha_J, \beta_J, \gamma_J$ [36]. In general, one should sum over all even k and all $q < k$, however in highly symmetric environments many of the Stevens parameters, B_k^q, vanish [34]. All compounds in this Thesis feature $3d$ ions in an octahedral coordination, which is naturally favoured for its stability. For a perfectly octahedral environment only the $\mathcal{O}_4^0$ and $\mathcal{O}_4^4$ components survive such that the crystal field takes the form [21]

$$\mathcal{H}_{CEF} = B_4 \left(\mathcal{O}_4^0 + 5\mathcal{O}_4^4\right). \tag{1.20}$$

The crystal field spectrum then depends on the orbital ground state (determined using Hund’s rules) and the sign of B_4 which depends on the filling of the outer shell. The sign for $3d$ ions is listed in Table 1.1 for octahedral coordination. The case of half-filling, d^5, is not listed since the ground state is already an orbital singlet and hence does not experience any crystal field splitting, to first order.

The spectrum for both the D and F ground states is shown in Fig. 1.2. The ground state degeneracy is ultimately determined by the sign of B_4. For example

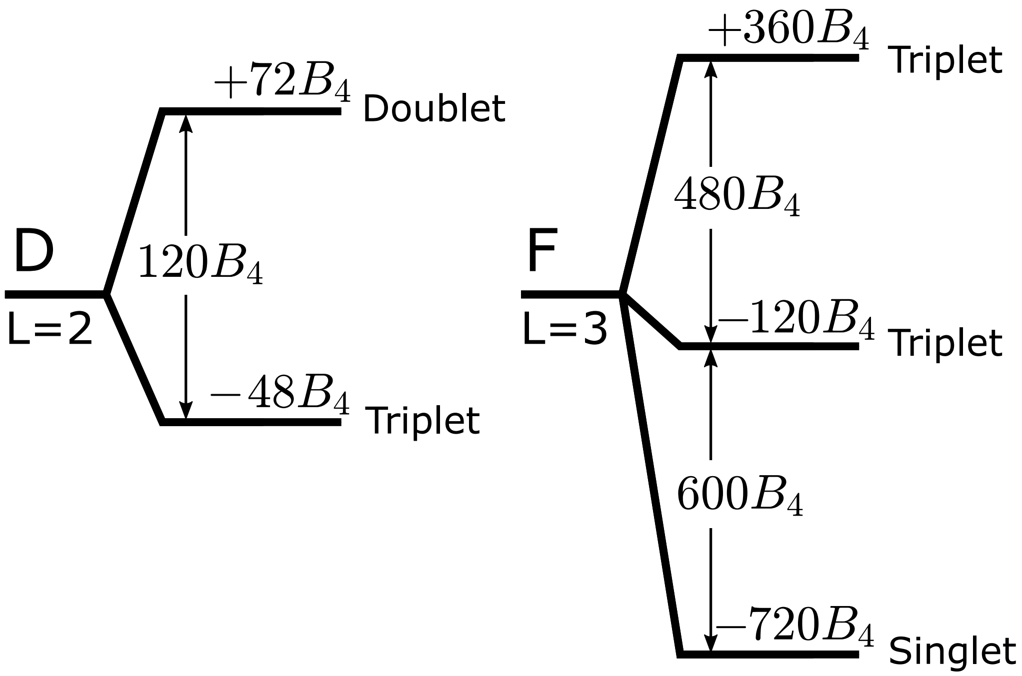

Figure 1.2 *Crystal field splitting for the D and F states.*

in a $3d^6$ ion with $B_4 > 0$ the crystal field gives rise to an orbital triplet ground state, as is the case for a $3d^2$ ion with $B_4 < 0$ [21]. Typically if the splitting between this ground state orbital triplet and the excited multiplets is large, a projection onto an effective orbital angular momentum of $\mathbf{l}$ can be performed since the inter-multiplet matrix elements are negligible. The projection onto an effective orbital angular momentum will be discussed at greater length in later chapters.

1.1.5 Crystallographic distortions

In the previous section, the nature of the crystalline electric field for an octahedrally coordinated $3d$ ion was discussed. In many $3d$ transition metal compounds, the local environment is distorted away from that of a perfect octahedron. Such a distortion can typically lower the configurational energy by lowering the local symmetry and reducing the orbital degeneracy – a phenomenon often referred to as the Jahn-Teller effect [37]. As a result of this, systems with a ground state degeneracy are typically unstable to distortions, leading to the the breaking of this degeneracy and the quenching of the orbital angular momentum $\langle \mathbf{L} \rangle$. The orbital quenching follows from the fact that the crystal field Hamiltonian has real eigenfunctions, yet the operator $\mathbf{L}$ is pure imaginary. Therefore it follows that $\langle \mathbf{L} \rangle$ is imaginary. Since the operator is Hermitian its diagonal elements must be real and thus $\langle \mathrm{GS} | \mathbf{L} | \mathrm{GS} \rangle = 0$ if the ground state $|\mathrm{GS}\rangle$ is non-degenerate [27].

In principle, one need not make the distinction between the octahedral crystalline electric field and the distortion term, since the origin is the same for both. However, if the distortion is sufficiently small, it can be treated as a perturbation and one can take advantage of a projection onto the effective orbital angular momentum operator $\mathbf{l}$ as described in the previous section. The precise form of the distortion Hamiltonian depends on the local symmetry. In $3d$ transition metal compounds, tetragonal or trigonal distortions are typical. Both distortion Hamiltonians are proportional to $\mathcal{O}_2^0$ and can be written as

$$\mathcal{H}_{dis} = \Gamma \left(3\hat{L}_z^2 - L(L+1) \right) \tag{1.21}$$

which can readily projected onto the manifold of $\mathbf{l}$. In the case of a ground state orbital triplet, a tetragonal or trigonal distortion breaks the degeneracy giving rise to a singlet and doublet. Further terms may be considered if the symmetry is lowered [38], for example a rhombic distortion gives rise to terms proportional to $\mathcal{O}_2^2$ [21]. These low symmetry terms break the doublet degeneracy and give rise to three energetically separated singlets.

To this point the physics governing the ions surrounded by a local ligand field has been discussed. As was seen in the previous section, the interaction between electrons in the unfilled outer shell, both among themselves and with their neigbouring cations gives rise to a hierarchy of energy scales. In the following section the physics that governs the interaction of magnetic ions with one another will be discussed. Some reference will be made to the influence of the local degrees of freedom on this cooperative magnetic behaviour from a perturbative perspective.

1.2 Cooperative magnetism

Attention is now turned to the interaction between neighbouring magnetic ions. The focus will be on orbitally non-degenerate magnetic ions. As discussed in the previous section, the Jahn-Teller effect generally works to remove the ground state orbital degeneracy in the $3d$ ions thus such a simplification is sufficient to describe most systems discussed in this Thesis. These cooperative interactions ultimately determine the magnetic order and excitations present in $3d$ transition metal compounds.

1.2.1 Exchange interactions

There are two predominant means by which magnetic ions couple, both of which lead to an inter-ion Hamiltonian of the form first introduced by Heisenberg [39]. The first of which, known as *direct exchange*, finds its origin in the Heitler-London theory of molecular bonding [40] and gives rise to a spin-spin coupling between neighbouring ions with overlapping electron wavefunctions.

To illustrate the origin of direct exchange, a toy model comprising two hydrogen atoms is now considered. The electronic wavefunction can be written as a linear combination of the wavefunctions of the electrons from atom 1 and atom 2,

$$\psi_{s,a}(\mathbf{r}_1, \mathbf{r}_2) = \frac{1}{\sqrt{2(1 \pm |\langle \mathrm{I}|\mathrm{II}\rangle|^2}} \left(\phi_{\mathrm{I}}(\mathbf{r}_1)\phi_{\mathrm{II}}(\mathbf{r}_2) \pm \phi_{\mathrm{I}}(\mathbf{r}_2)\phi_{\mathrm{II}}(\mathbf{r}_1)\right), \tag{1.22}$$

with the normalisation $\langle \mathrm{I}|\mathrm{II}\rangle = \int \phi_{\mathrm{I}}(\mathbf{r})\phi^*_{\mathrm{II}}(\mathbf{r})\mathrm{d}\mathbf{r}$. The spin state for the two electron system is either a singlet or triplet state [41, 42],

$$|s\rangle = \frac{1}{\sqrt{2}}\left(|\uparrow\downarrow\rangle - |\downarrow\uparrow\rangle\right) \tag{1.23a}$$

$$|t_1\rangle = |\uparrow\uparrow\rangle \tag{1.23b}$$

$$|t_2\rangle = \frac{1}{\sqrt{2}}\left(|\uparrow\downarrow\rangle + |\downarrow\uparrow\rangle\right) \tag{1.23c}$$

$$|t_3\rangle = |\downarrow\downarrow\rangle\,. \tag{1.23d}$$

The Pauli exclusion principle dictates that the total wavefunction must be antisymmetric with respect to electron exchange. Therefore, the antisymmetric electron wavefunction implies the symmetric triplet state and the symmetric electron wavefunction the antisymmetric spin singlet. The Hamiltonian has contributions from the Coulomb interaction between each electron and the two nuclei, as well as an electron-electron repulsion term. The energy of the states with a symmetric and antisymmetric electron wavefunction are then [41, 42]

$$E = \frac{\langle\psi_{s,a}|\,\mathcal{H}\,|\psi_{s,a}\rangle}{\langle\psi_{s,a}|\,|\,|\psi_{s,a}\rangle} = 2E_0 + \frac{C \pm A}{1 \pm S} \tag{1.24a}$$

$$\begin{aligned} C =& \frac{e^2}{4\pi\epsilon_0}\int\Big(\frac{1}{|\mathbf{R}_\mathrm{I}-\mathbf{R}_\mathrm{II}|}+\frac{1}{|\mathbf{r}_1-\mathbf{r}_2|}-\frac{1}{|\mathbf{r}_1-\mathbf{R}_\mathrm{I}|}-\frac{1}{|\mathbf{r}_2-\mathbf{R}_\mathrm{II}|}\Big) \\ &\times|\phi_\mathrm{I}(r_1)|^2|\phi_\mathrm{II}(r_2)|^2\mathrm{d}\mathbf{r}_1\mathrm{d}\mathbf{r}_2 \end{aligned} \tag{1.24b}$$

$$\begin{aligned} A =& \frac{e^2}{4\pi\epsilon_0}\int\Big(\frac{1}{|\mathbf{R}_\mathrm{I}-\mathbf{R}_\mathrm{II}|}+\frac{1}{|\mathbf{r}_1-\mathbf{r}_2|}-\frac{1}{|\mathbf{r}_2-\mathbf{R}_\mathrm{I}|}-\frac{1}{|\mathbf{r}_1-\mathbf{R}_\mathrm{II}|}\Big) \\ &\times\phi^*_\mathrm{I}(\mathbf{r}_1)\phi_\mathrm{I}(\mathbf{r}_2)\phi_\mathrm{II}(\mathbf{r}_1)\phi^*_\mathrm{II}(\mathbf{r}_2)\mathrm{d}\mathbf{r}_1\mathrm{d}\mathbf{r}_2 \end{aligned} \tag{1.24c}$$

$$S = \int\phi^*_\mathrm{I}(\mathbf{r}_1)\phi_\mathrm{I}(\mathbf{r}_2)\phi_\mathrm{II}(\mathbf{r}_1)\phi^*_\mathrm{II}(\mathbf{r}_2)\mathrm{d}\mathbf{r}_1\mathrm{d}\mathbf{r}_2. \tag{1.24d}$$

The first term in Eqn. 1.24a is the ionisation energy of the two hydrogen atoms, whilst A and C are known as the exchange and Coulomb integrals respectively. The difference in energy between the singlet and triplet states is thus

$$E_t - E_s = \frac{1}{2}J = 2\frac{CS-A}{1-S^2} \tag{1.25}$$

where the "exchange constant", J, has been introduced[2]. The exchange constant quantifies the energy difference between the parallel spin arrangement and the anti-parallel spin configuration. A Hamiltonian which gives rise to this spectrum is now sought. As discovered by Heisenberg [39], the spin-spin interaction

$$\mathcal{H} = J\mathbf{s}_1\cdot\mathbf{s}_2 \tag{1.26}$$

gives rise to the required splitting, up to a constant term. The above argument can be extended to multi-electron atoms where the electron wavefunction is given by the Slater determinant. If one assumes that the overlap of the single electron wavefunctions is negligible, then $S = 0$ and J is always negative and hence ferromagnetic [43].

It has long been known that the theory of direct exchange is insufficient to describe the magnetic interactions in the $3d$ ions [44]. As far back as 1949, whilst neutron spectroscopy was still in its infancy, Shull and Smart reported that the neutron diffraction pattern of MnO was consistent with a doubling of

---

[2] Note that in the literature the sign on the definition of J is frequently swapped from that defined here and the factor of $\frac{1}{2}$ omitted. Here the definition is chosen to be consistent with the models used in the rest of the Thesis and in keeping with modern convention.

the crystallographic unit cell – a direct measurement of a hitherto illusive ordered phase of matter, the *antiferromagnet* [45]. A more complete account of the origin of this behaviour was given in 1959 by P.W. Anderson [46] in his description of the superexchange interaction. To sketch out the arguments of Anderson, an orbitally non-degenerate ground state is now considered, with each atomic site contributing a single electron. Such a situation can be readily described by a Hubbard model [47]

$$\mathcal{H} = -t \sum_{\langle i,j \rangle \sigma} \hat{c}^{\dagger}_{i\sigma} \hat{c}_{j\sigma} + U \sum_{i} \hat{n}_{i\uparrow} \hat{n}_{i\downarrow}. \tag{1.27}$$

The operators $\hat{c}^{(\dagger)}_{i\sigma}$ are the creation (annihilation) operators for an electron of spin σ on site i, and obey the fermionic anticommutation relation $\{\hat{c}_{i\sigma}, \hat{c}^{\dagger}_{j\sigma'}\} = \delta_{\sigma\sigma'}\delta_{ij}$. The first term describes electron hopping between neighbouring sites and the second the Coulomb repulsion which must be overcome to doubly occupy one site. The large magnitude of the Coulomb repulsion in $3d$ ions ($U \gg t$) dictates that the lowest energy state is that in which each site is occupied by a single electron. Treating the hopping term perturbatively, at second order one has the contribution to the ground state energy [48]

$$\Delta E_2 = \sum_{n} \frac{| \langle 0 | \mathcal{H}' | n \rangle |^2}{E_0 - E_n} \tag{1.28}$$

where the sum is over all excited states and $\mathcal{H}'$ is the first term in Eqn. 1.27, treated as the perturbation. If one concentrates on two neighbouring sites (Fig. 1.3), the excited state comprises one empty site and one doubly occupied by anti-aligned electrons. In this case, the perturbative correction (Eqn. 1.28) describes the virtual hopping of one electron to a neighbouring site and back again. The energy associated with this process is $-2\frac{t^2}{U}$ with the multiplicity factor coming from the fact that there are two excited states possible (i.e. where the left/right site is doubly occupied). It is important to note that this process is forbidden by the Pauli Exclusion Principle if the electron spins are coaligned (Fig. 1.3 (a)), thus the superexchange interaction favours antiferromagnetic alignment (Fig. 1.3 (b)). A transformation to spin operators [49] is now introduced

$$\hat{s}_{\alpha} = \frac{1}{2} \begin{pmatrix} \hat{c}^{\dagger}_{\uparrow} & \hat{c}^{\dagger}_{\downarrow} \end{pmatrix} \sigma^{\alpha} \begin{pmatrix} \hat{c}_{\uparrow} \\ \hat{c}_{\downarrow} \end{pmatrix}. \tag{1.29a}$$

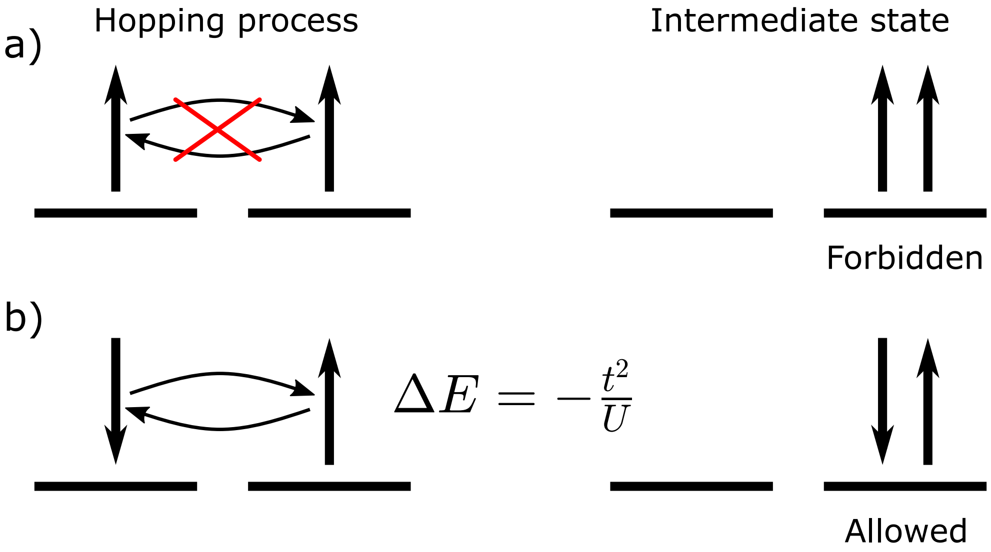

Figure 1.3 *Virtual electron hopping process giving rise to the superexchange interaction. For coaligned spins (a) the hopping process is forbidden by the Pauli Exclusion Principle. If the electrons are anti-aligned (b), the ground state energy is lowered by* $\Delta E = -\frac{t^2}{U}$*, promoting the formation of antiferromagnetic order.*

The matrices σ^α are the Pauli matrices which means the spin operators obey the usual spin commutation relations, $\mathbf{s} \times \mathbf{s} = i\mathbf{s}$. Using these spin operators in the limit that $U \gg t$ the Hamiltonian takes the form of the familiar Heisenberg model

$$\mathcal{H} = J \sum_{\langle i,j \rangle} \mathbf{s}_i \cdot \mathbf{s}_j \tag{1.30}$$

with the exchange constant $J = \frac{4t^2}{U}$ [49]. In contrast to the case of direct exchange discussed above, $J > 0$ hence the superexchange interaction promotes the anti-alignment of neighbouring spins and an antiferromagnetic order. In the $3d$ ions the superexchange interaction is typically the dominant form of magnetic exchange [48].

Further to the direct and superexchange discussed above, there are a number of other indirect exchange process that occur in magnetic compounds which depend specifically on the energetics of the single-ion physics and orbital overlap, giving rise to both ferromagnetic and antiferromagnetic couplings. A full discussion of these is beyond the scope of this Thesis, however further details can be found in the literature [48]. Accurate quantitative calculations of the exchange interaction strength are difficult to perform. In practice, spectroscopic and structural studies are used to determine the magnetic order and nature of interactions in systems of interest, with the exchange parameter, J, being treated as a parameter to be determined experimentally. However, the consideration of a general Heisenberg model

$$\mathcal{H} = \sum_{ij} \mathcal{J}_{ij} \mathbf{S}_i \cdot \mathbf{S}_j \tag{1.31}$$

is still insufficient to describe all but the simplest magnetic systems. The effects of single-ion physics can be observed in the dynamics of the spin moments and give rise to additional features in the spectrum. In the following sections, additional terms will be added to the spin Hamiltonian (Eqn. 1.31) by considering the perturbative effects of the local single-ion terms, noting the approximations made. In subsequent chapters, examples will be given where these approximations are not valid and alternative approaches will be discussed that allow for the treatment of single-ion terms in a non-perturbative manner.

1.2.2 Spin anisotropy

The presence of non-trivial single-ion physics most commonly manifests itself in the breaking of spin-rotational symmetry via anisotropic terms in the spin Hamiltonian. The derivation of the spin anisotropy begins by considering an ion with a quenched orbital angular momentum and hence a non-degenerate orbital ground state. Such a situation can be achieved in the presence of strong symmetry-lowering crystallographic distortions. The spin-orbit coupling, which partially restores the orbital angular momentum [27], is then

$$\mathcal{H}' = \lambda \mathbf{L} \cdot \mathbf{S}. \tag{1.32}$$

Treating the spin-orbit coupling to second order in perturbation theory, the energy correction to the ground state is [27]

$$\Delta E_2 = -\lambda^2 \sum_{\mu\nu} \Lambda_{\mu\nu} \hat{S}_\mu \hat{S}_\nu \tag{1.33a}$$

$$\Lambda = \sum_n \frac{\langle 0| \hat{L}_\mu |n\rangle \langle n| \hat{L}_\nu |0\rangle}{E_n - E_0} \tag{1.33b}$$

The decision is made to leave the spin as an operator and transitions due to the orbital angular momentum operator are calculated. This is because the inter-ion Hamiltonian depends only on the spin operators. In this way a term dependent only on spin operators can be found that captures the spin-orbit interaction perturbatively. By writing Eqn. 1.33a in terms of its Cartesian components, one can isolate the single-ion anisotropy term [27]

$$\begin{aligned}\mathcal{H} = -\lambda^2 \Bigg[&\frac{1}{3}(\Lambda_x + \Lambda_y + \Lambda_z)S(S+1) \\ &+ \frac{1}{3}[\Lambda_z - \frac{1}{2}(\Lambda_x + \Lambda_y)][3\hat{S}_z^2 - S(S+1)] \\ &+ \frac{1}{2}(\Lambda_x - \Lambda_y)(\hat{S}_x^2 - \hat{S}_y^2)\Bigg]\end{aligned} \tag{1.34}$$

which, neglecting constant terms, gives rise to the spin anisotropy terms

$$\mathcal{H}_{anis} = D\hat{S}_z^2 + E(\hat{S}_x^2 - \hat{S}_y^2). \tag{1.35}$$

These terms, referred to as the single-ion anisotropy terms, break spin-rotational symmetry, promoting the alignment of the spins along a particular direction or within a particular plane. Such terms are key in low-dimensional systems which lack spontaneous symmetry breaking [50] as the explicit breaking of continuous spin-rotational symmetry allows for the development of long-range magnetic order. The existence of single-ion anisotropy is often marked by a spectral gap in the neutron scattering spectrum proportional to the magnitude of the anisotropy parameter.

Whilst single-ion anisotropy is frequently observed in many transition metal compounds, Eqn. 1.35 vanishes for $S = 1/2$. Nonetheless, anisotropic spin terms exist in these systems, occurring at higher order. Consider two neighbouring ions with spin-orbit coupling and an inter-ion exchange term,

$$\mathcal{H} = \lambda \mathbf{L}_1 \cdot \mathbf{S}_1 + \lambda \mathbf{L}_2 \cdot \mathbf{S}_2 + \mathbf{S}_1 \cdot \mathbf{S}_2 \tag{1.36}$$

At third order in perturbation theory, for $S = 1/2$ ions one has the term [27]

$$\Delta E_3 = -\sum_{\mu\nu} \left(\hat{S}_{1\mu}\Gamma^{(1)}_{\nu\mu}\mathbf{S}_1 \cdot \mathbf{S}_2 \hat{S}_{1\nu} + \hat{S}_{2\mu}\Gamma^{(2)}_{\nu\mu}\mathbf{S}_1 \cdot \mathbf{S}_2 \hat{S}_{2\nu} \right) \tag{1.37a}$$

$$\Gamma^{(1)}_{\mu\nu} = 2\lambda^2 \sum_{n_1 n_1'} \frac{\langle g_1 | \hat{L}_\mu | n_1 \rangle \, J(n_1 g_2, n_1' g_2) \, \langle n_1' | \hat{L}_\nu | g_1 \rangle}{(E_{n_1} - E_{g_1})(E_{n_1'} - E_{g_1})}. \tag{1.37b}$$

The sum is performed over intermediate states $|n\rangle$ and $|n'\rangle$ with the initial and final states on sites 1 and 2 being $|g_1\rangle$ and $|g_2\rangle$ respectively. J is the exchange integral and generally gives rise to a nonzero Γ even in a perfectly octahedral environment [27]. The correction to the isotropic Heisenberg model is then [27]

$$\mathcal{H}_{anis} = -\frac{1}{4}\sum_{\mu\nu}^{i=1,2}\left[(\Gamma^{(i)}_{\mu\nu} + \Gamma^{(i)}_{\nu\mu}) - \delta_{\mu\nu}(\Gamma^{(i)}_{xx} + \Gamma^{(i)}_{yy} + \Gamma^{(i)}_{zz})\right]\hat{S}_{1\mu}\hat{S}_{2\nu}. \tag{1.38}$$

This correction refers to a process where one ion is excited by the spin-orbit coupling, interacts with a neighbouring unexcited ion via the exchange interaction and is returned to the ground state by the spin-orbit interaction.

1.2.3 Dzyaloshinskii-Moriya interaction

The final spin Hamiltonian term that will be considered is the Dzyaloshinskii-Moriya (DM) interaction [51, 52], often referred to as antisymmetric exchange. This has a similar origin to the anisotropic exchange interaction, however in the case of the DM interaction, both ions are simultaneous excited by spin-orbit coupling before interacting via the exchange Hamiltonian and being returned to their ground states by the spin-orbit coupling. Following Ref. [27] this term is equal to

$$\begin{aligned}\mathcal{H}_{DM} =& 2\lambda\sum_{\mu}\Bigg(\sum_{n_1}\frac{J(n_1g_2, g_1g_2)\langle g_1|\hat{L}_{1\mu}|n_1\rangle[\hat{S}_{1\mu}, \mathbf{S}_1\cdot\mathbf{S}_2]}{E_{n_1} - E_{g_1}} \\ &+ \sum_{n_2}\frac{J(n_2g_2, g_1g_2)\langle g_2|\hat{L}_{1\mu}|n_2\rangle[\hat{S}_{2\mu}, \mathbf{S}_1\cdot\mathbf{S}_2]}{E_{n_2} - E_{g_2}}\Bigg).\end{aligned} \tag{1.39}$$

Since $[\mathbf{S}_1, \mathbf{S}_1\cdot\mathbf{S}_2] = -i\mathbf{S}_1\times\mathbf{S}_2$ this correction can be written as

$$\mathcal{H} = \mathbf{D}\cdot\mathbf{S}_1\times\mathbf{S}_2 \tag{1.40a}$$

$$\begin{aligned}\mathbf{D} =& -2i\lambda\Bigg(\sum_{n_1}\frac{\langle g_1|\mathbf{L}_1|n_1\rangle}{E_{n_1} - E_{g_1}}J(n_1g_2, g_1g_2) \\ &- \sum_{n_2}\frac{\langle g_2|\mathbf{L}_2|n_2\rangle}{E_{n_2} - E_{g_2}}J(g_1n_2, g_1g_2)\Bigg).\end{aligned} \tag{1.40b}$$

The non-zero components of **D** can be determined by the local symmetry and examination of Eqn. 1.40b shows that all components of **D** vanish if a centre of inversion exists between the two ions. This can be seen by equating Eqn. 1.40b with the same expression with the ion labelling reversed. Defining the line between ions 1 and 2 as the line AB with bisection point C, the general rules governing the the existence of these terms can be written as follows [52]

1. When C is a centre of inversion, $\mathbf{D} = 0$.
2. When a mirror plane perpendicular to AB passes through C, $\mathbf{D} \perp$ AB.
3. When A and B lie in a mirror plane, $\mathbf{D} \perp$ mirror plane.
4. When a two-fold axis $\perp$ AB passes through C, $\mathbf{D} \perp$ two-fold axis.
5. When an $(n \geq 2)$-fold axis lies along AB, $\mathbf{D} \parallel$ AB.

1.3 Final remarks

In Section 1.2, a number of key results in the construction of spin interaction Hamiltonians was presented. The approach was to treat the single-ion physics, either implicitly through assumptions about the nature of the crystal field ground state, or perturbatively in the case of the spin-orbit coupling. However, as presented in Section 1.1, these single-ion terms depend greatly on both the species of the magnetic ion and the local crystallographic environment. In fact, it is not evident *a priori* that these on-site degrees of freedom can be treated perturbatively for all the $3d$ ions. In later chapters, a number of cases will be discussed for which the single-ion and exchange energy scales are not well separated and the validity of the perturbative approach fails.

Whilst Section 1.2 discusses, at length, the considerations that must be made to write down a spin Hamiltonian describing the interaction of local spin moments, strategies for solving these spin Hamiltonians have yet to be presented. On the face of it, this is a formidable task. The Hilbert space of the spin Hamiltonian is $(2S+1)^N$ where N is the system size. For typical crystalline samples comprising $\sim 10^{23}$ atoms, the Hilbert space becomes prohibitively large, hence exact quantum mechanical treatments are limited to systems sizes $N \leq 100$ or most typically molecular magnets and oligomers comprising few ions. Luckily there exist a variety of toolkits to approach these problems, ranging from discrete fermionic and bosonic transformations [53] to continuum field theories [54]. Each of these methods carries its own sets of assumptions and limits of validity. A full presentation of the many-body theoretical techniques relevant to this work is deferred to the later chapters where each will be discussed in the context of the physical problems against which they are brought to bear.

Chapter 2

Neutron scattering

In this Thesis, neutron scattering is used to elucidate the nature of magnetic interactions in $3d$ transition metal compounds. The aim of the following chapter is to present a general overview of the technique, covering both spallation and continuous sources. This chapter follows the classic texts of Squires [55], Shirane [56], Boothroyd [57], Carpenter & Loong [58] and Lovesey [59], with additional references noted explicitly in the text. Further details of data analysis and modelling specific to the experiments performed for this Thesis are deferred to later chapters where they are discussed in the context of concrete examples.

2.1 Neutron sources

There are two commonly used methods of neutron production for the purpose of neutron scattering. The first of these is achieved by employing nuclear fission. Typically at reactor neutron sources, ^{235}U is used as the fissionable material. The absorption of a neutron by this heavy nucleus creates an instability leading to decay into smaller nuclei (Fig. 2.1), with the release of energy ($\sim$ 2 MeV) and an excess of neutrons to sustain a chain reaction [57]. This neutron production occurs continuously, hence reactor sources are often referred to as *continuous* sources. The energy scale of the neutrons produced is far too high to be used to probe the fundamental excitations in solids, which are $<$ 1 eV. The emitted neutrons are therefore passed through a moderator where the neutrons thermalise to a Maxwellian distribution of energies determined by the moderator temperature.

The moderator material is chosen depending on the energy scale of interest and hence whether cold (0.1-10 meV) or thermal (5-100 meV) neutrons are required. Cold sources typically use liquid hydrogen or liquid deuterium as a moderator with thermal neutrons produced using graphite or heavy water as a moderator. Modern reactor-based neutron facilities typically have both thermal and cold sources allowing for a wide variety of spectroscopy instruments utilizing both thermal and cold neutrons. Fig. 2.2 shows a schematic of the Institut Laue-Langevin (ILL) reactor core identifying the different beam ports for cold, thermal and hot neutrons. Whilst this Thesis concerns the use of neutron spectroscopy, it is important to note that attached to beam ports, viewing both hot and cold sources, are a variety of diffractometers for the investigation of structure and order in condensed matter. In particular, cold neutron diffraction is well suited to the study of long d-spacings which is particularly useful in the study of magnetism due to the fall-off of the magnetic form factor at large Q.

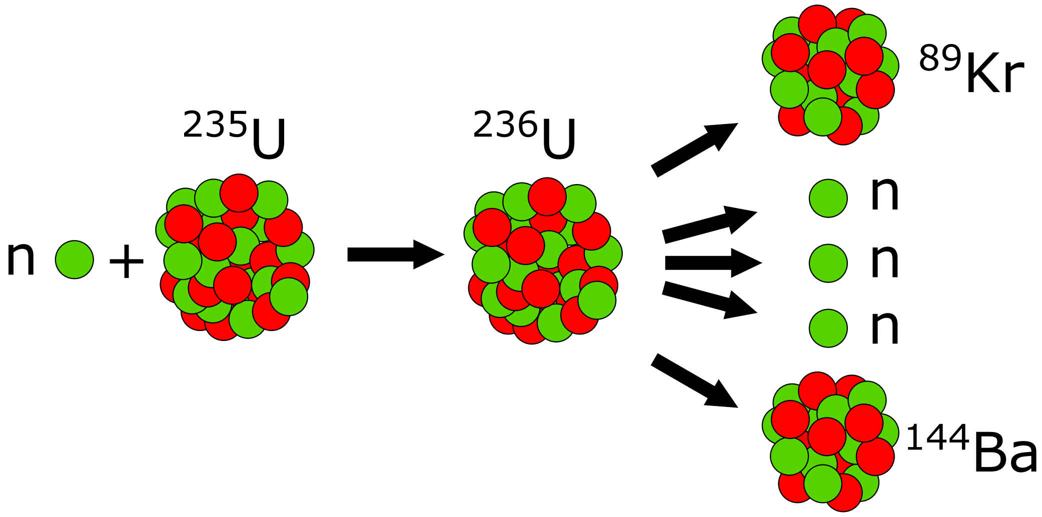

Figure 2.1 *Nuclear fission of a ^{235}U nucleus, as takes place in reactor sources.*

Though continuous sources historically held a monopoly on neutron science, significant investment led to the development of a number of pulsed neutron sources around the world in the latter part of the 20th century. The operating principle of these facilities is to produce pulses of neutrons through the process of *spallation*. A synchrotron is employed to accelerate protons produced by a linear accelerator to extremely high velocities (in the case of ISIS Neutron and Muon Source, the protons are accelerated to 0.84c [60]). The high energy protons

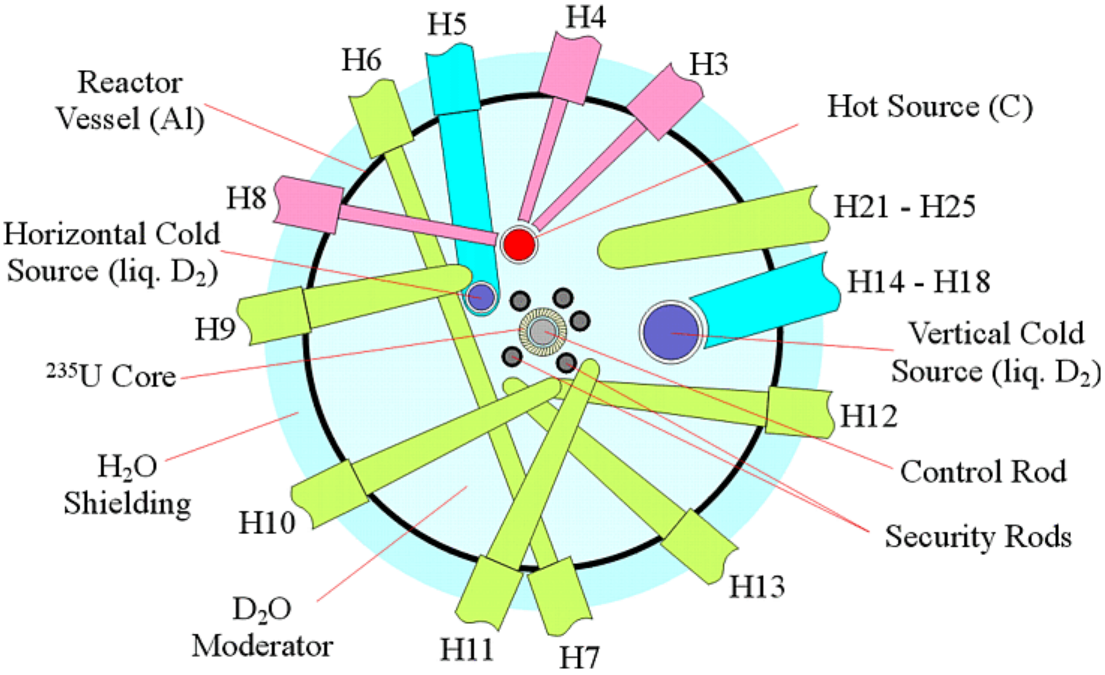

Figure 2.2 *Schematic of the ILL reactor with the beam ports connected to the hot, thermal and cold sources rendered in red, green and blue respectively. Figure reproduced from Ref. [6].*

collide with a heavy metal target, often tungsten. The heavy metal ion undergoes a process known as spallation: the proton is absorbed, exciting the metal nucleus, which then decays releasing neutrons. The number of neutrons released in this process is variable but is typically around thirty, each having an energy of about 2 MeV [57]. The produced neutrons pass from the target through a moderator, such as solid methane, water, or liquid hydrogen [7] and then down beam tubes to the beam ports at which the instruments are situated.

The protons produced by the linear accelerator are produced in pulses resulting in a discontinuous neutron flux from the source[1]. The neutron pulse shape is highly irregular, with a strong peak from the fast neutrons and a secondary, broader peak from thermal neutrons arriving at the instrument at a later time. There exists a finite frame overlap between those late arriving thermal neutrons and the fast neutrons of the next pulse which typically arrive $\sim 100\mu s$ later [57], leading to spurious signals in the neutron scattering data as the energy transfer cannot be determined unambiguously. Frame overlap can be limited by employing frame overlap choppers which reduce the frame overlap at the expense of lowering

---

[1] Whilst spallation sources produce pulsed neutron beams, the Swiss Spallation Source (SINQ) [61] and the IBR-2 reactor (Dubna, Russia) [62] have a pulse rate high enough to render the beam continuous.

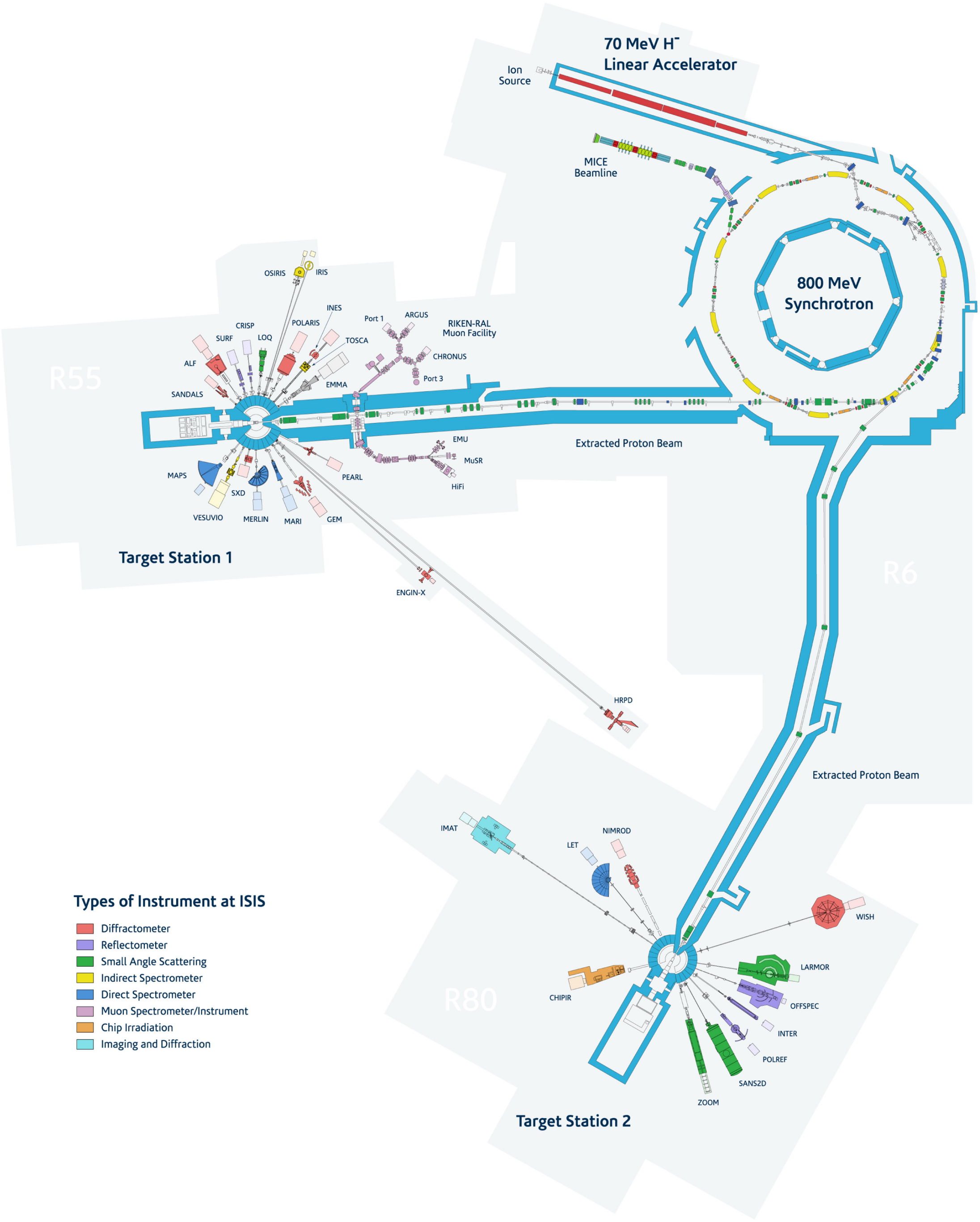

Figure 2.3 *Schematic of the spallation source at ISIS Pulsed Neutron and Muon Source in Didcot, Oxfordshire. Protons pass from the synchrotron to two target stations. The instruments are rendered according to instrument type. Figure reproduced from Ref. [7].*

the effective repetition rate of the pulsed source, or by employing frame overlap mirrors which reflect long wavelength neutrons out of the beam.

2.2 Scattering theory

2.2.1 The scattering triangle

At neutron facilities, the interrogation of the sample is performed by the scattering of neutrons from matter. This scattering occurs in instruments connected to beam ports, where the scattered neutrons are detected and offer insights into the structure and dynamics of the sample. These instruments are highly optimised to probe phenomena of a specific nature and energy scale, but the underlying operating principle is similar. In this section, the physics of neutron scattering will be presented.

The results below will be presented without rigorous proof. Readers are referred to texts such as Refs. [55–57, 59] for full mathematical details. The arguments presented below were developed first in the context of x-ray scattering by father and son William Henry and Lawrence Bragg [63]. There exist important differences between the scattering of neutrons and x-rays from matter – in fact the fundamental physics of the interaction is very different. Nonetheless, the qualitative picture is substantially similar and it is the intensity of the scattering that differs for the different probes. This Thesis will focus only on the case of neutron scattering with only passing reference to x-ray scattering for the purpose of pointing out the key differences.

A neutron scattering experiment is performed when a neutron incident on the sample, with wavevector $\mathbf{k}_i$ is scattered through a scattering angle 2θ, resulting in a final neutron wavevector $\mathbf{k}_f$. The difference between the initial and final wavevector is given by the scattering vector

$$\mathbf{Q} = \mathbf{k}_i - \mathbf{k}_f. \tag{2.1}$$

The difference between the neutron's incident and final energy is

$$\Delta E = \frac{\hbar^2}{2m}\left(k_i^2 - k_f^2\right) \tag{2.2}$$

which can be zero (elastic scattering) or nonzero (inelastic scattering). If the scattering is elastic, the magnitude of the initial and outgoing wavevector must be equal, $|\mathbf{k}_i| = |\mathbf{k}_f|$. In order for scattering from a sample to occur, the Laue condition must be satisfied, that is $\mathbf{G} = \mathbf{k}_i - \mathbf{k}_f$, or in other words, the scattering vector must be a reciprocal lattice vector (Fig. 2.4 (*a*)). This fact follows directly from Bragg's law

$$n\lambda = 2d\sin\theta \tag{2.3}$$

upon the insertion of the lattice spacing $d = \frac{2\pi}{|\mathbf{G}|}$ and wavelength $\lambda = \frac{2\pi}{|\mathbf{k}|}$. Here n is an integer, allowing for higher order scattering. If the scattering is elastic, the scattering triangle is isosceles (Fig. 2.4 (*a*)).

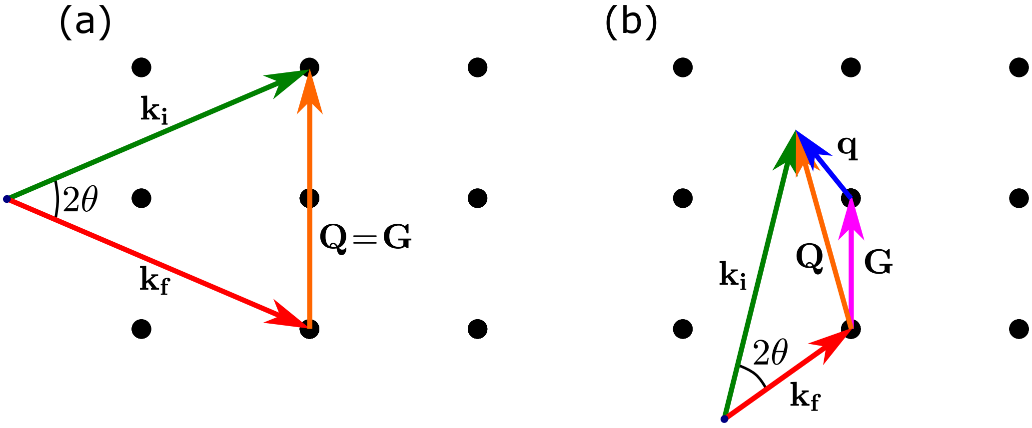

Figure 2.4 *Scattering triangles for the case of* (*a*) *elastic and* (*b*) *inelastic scattering. The reciprocal lattice points are shown in black.*

So far, no mention of dynamics has been made. In the case of inelastic scattering, an incoming neutron may gain or lose energy from its interaction with the sample. In this case $|\mathbf{k}_i| \neq |\mathbf{k}_f|$. The term "inelastic scattering" is, in some sense, a slight misnomer. Both energy and momentum are in fact conserved, as one would expect. The inelasticity of the interaction is only from the perspective of the neutron, rather than the system as a whole. It is conventional to refer to elastic scattering as "diffraction" and inelastic scattering as simply "scattering". This Thesis will mainly be concerned with the latter, which will be referred to throughout as neutron scattering or neutron spectroscopy. In a neutron scattering experiment, the change in energy of the neutron is equal to the energy of the excitation, $\Delta E = \hbar\omega$. The scattering triangle in this case is shown in Fig. 2.4 (*b*). The fact that the scattering triangle shown in Fig. 2.4 (*b*) must close places constraints on the wavevector and energy transfers accessible on a given spectrometer. By geometry, the magnitude of the scattering vector is given by

$$Q = \sqrt{k_i^2 + k_f^2 - 2k_i k_f \cos 2\theta}. \tag{2.4}$$

Given the energy transfer

$$\Delta E = \frac{\hbar^2}{2m}\left(k_i^2 - k_f^2\right) \tag{2.5}$$

the scattering wavevector can be related to the energy transfer

$$\frac{\hbar^2 Q^2}{2m} = 2E_i - \Delta E - 2\cos 2\theta\sqrt{E_i\left(E_i - \Delta E\right)} \tag{2.6a}$$
$$\frac{\hbar^2 Q^2}{2m} = 2E_f + \Delta E - 2\cos 2\theta\sqrt{E_f\left(E_f + \Delta E\right)} \tag{2.6b}$$

both in terms of the incident neutron energy and the final neutron energy. The first of which is relevant for direct geometry spectrometers and the latter for indirect geometry spectrometers. The specifics of spectrometer design will be discussed at length in Section 2.3 .

2.2.2 Neutron interaction with matter

Neutrons interact with matter predominantly through the strong nuclear force with nuclei or electromagnetically with the magnetic flux in the sample owing to the magnetic dipole moment of the neutron. Let it be supposed that the incident neutron sees a potential, $V(\mathbf{r})$, and one has an initial state of the composite system of neutron and sample $|i\rangle$ and final state $|f\rangle$. If the potential is weak, the first Born approximation is valid and Fermi's golden rule can be used to evaluate the transition rate

$$\Gamma_{i\to f} = \frac{2\pi}{\hbar}|\langle f|\,\hat{V}\,|i\rangle|^2 g(E_f)\frac{\mathrm{d}\Omega}{4\pi} \tag{2.7}$$

where $E_f + E_{\lambda_f} = E_i + E_{\lambda_i}$ with E_{λ_i} the initial energy of the sample and E_i the initial energy of the neutron [57]. The density of states of the scattered neutron is given by $g(E_f)$ and $\mathrm{d}\Omega$ is the solid angle element.

The quantity of interest in neutron scattering is the partial differential cross section. This is defined as the number of neutrons scattered into the solid angle element within the energy interval $E_f + \mathrm{d}E_f$. The partial differential cross section is given by

$$\left(\frac{\mathrm{d}^2\sigma}{\mathrm{d}\Omega\mathrm{d}E_f}\right)_{(k_i,\sigma_i)\rightarrow(k_f,\sigma_f)} = \lim_{\mathrm{d}\Omega,\mathrm{d}E_f\rightarrow 0} \frac{\sum_{\lambda_i} p_{\lambda_i} \sum_{\lambda_f} \Gamma_{i\rightarrow f}}{\Phi_0 \mathrm{d}\Omega\mathrm{d}E_f} \tag{2.8}$$

where σ is the polarisation state of the neutron and Φ_0 is the incident neutron flux. The flux is defined as the number of neutrons per second entering a unit area and for neutrons with speed $v = \frac{\hbar k_i}{m_n}$ is given by $\Phi_0 = \frac{\hbar k_i}{V_0 m_n}$. The probability of the state with energy λ_i is p_{λ_i}. Inserting the transition amplitude (Eqn. 2.7) and the neutron density of states, $g(E) = \frac{V_0 m_n k}{2\pi^2\hbar^2}$, one finds the master equation

$$\begin{aligned}\left(\frac{\mathrm{d}^2\sigma}{\mathrm{d}\Omega\mathrm{d}E_f}\right)_{(k_i,\sigma_i)\rightarrow(k_f,\sigma_f)} &= \lim_{\mathrm{d}\Omega,\mathrm{d}E_f\rightarrow 0} V_0^2 \frac{k_f}{k_i} \left(\frac{m_n}{2\pi\hbar^2}\right)^2 \sum_{\lambda_i} p_{\lambda_i} \\ &\quad \times \sum_{\lambda_f} |\langle f|\hat{V}|i\rangle|^2 \delta(E_{\lambda_f} - E_{\lambda_i} - \hbar\omega)\end{aligned} \tag{2.9}$$

which forms the basis of all of the scattering formulae that will be used in this Thesis. The central challenge now is to calculate the matrix element $\langle k|V|i\rangle$. The states $|i\rangle$ are indexed by the neutron wavevector $\mathbf{k}_i$, the target wavefunction λ_i and the neutron polarisation state σ_i. An integration is first performed over $\mathbf{r}$

$$\langle \mathbf{k}_f|\hat{V}|\mathbf{k}_i\rangle = \int \mathrm{d}\mathbf{r}^3 e^{-i\mathbf{k}_f\cdot\mathbf{r}} V(\mathbf{r}) e^{i\mathbf{k}_i\cdot\mathbf{r}} = V(\mathbf{k}_i - \mathbf{k}_f) = V(\mathbf{Q}) \tag{2.10}$$

to yield the Fourier transform of the interaction potential. One can thus replace $|\langle k|\hat{V}|i\rangle|^2$ with $|\langle\sigma_f\lambda_f|\hat{V}(\mathbf{Q})|\sigma_i\lambda_i\rangle|^2$. One might wish that the partial differential cross section were written in terms of system observables. Though it might not be clear from the form of Eqn. 2.9, the partial differential cross section can be written as a correlation function, dependent on observables of the system. In order to make this clear, the definition of the delta function is introduced in terms of exponential functions

$$\delta(E_{\lambda_f} - E_{\lambda_i} - \hbar\omega) = \frac{1}{2\pi\hbar} \int_{\infty}^{\infty} \mathrm{d}t \left\{ \exp\left(\frac{iE_{\lambda_f}t}{\hbar}\right) \exp\left(\frac{-iE_{\lambda_i}t}{\hbar}\right) e^{-i\omega t} \right\} \tag{2.11}$$

and the Heisenberg operator, $\hat{A}(t)$, is defined as

$$\hat{A}(t) = e^{\frac{i\mathcal{H}t}{\hbar}} \hat{A} e^{-\frac{i\mathcal{H}t}{\hbar}} = \left(\frac{m_n}{2\pi\hbar^2}\right) \langle\sigma_f|\hat{V}(\mathbf{Q},t)|\sigma_i\rangle \tag{2.12}$$

where the static operator $\hat{A}$ is simply the interaction potential $\hat{V}$. Substituting Eqns. 2.11 and 2.12 into Eqn. 2.9. one finds that the cross section can be conveniently cast in terms of a temporal Fourier transform of a correlation function

$$\left(\frac{\mathrm{d}^2\sigma}{\mathrm{d}\Omega\mathrm{d}E_f}\right) = \frac{k_f}{k_i} S(\mathbf{Q},\omega) \tag{2.13a}$$

$$S(\mathbf{Q},\omega) = \frac{1}{2\pi\hbar}\int_{-\infty}^{\infty} \langle \hat{A}^\dagger(0)\hat{A}(t)\rangle e^{-i\omega t}\mathrm{d}t \tag{2.13b}$$

$$\left\langle \hat{A}^\dagger(0)\hat{A}(t)\right\rangle = \left(\frac{m_n}{2\pi\hbar^2}\right)^2 \left\langle \langle\sigma_i|\,\hat{V}^\dagger(\mathbf{Q})\,|\sigma_f\rangle\,\langle\sigma_f|\,\hat{V}(\mathbf{Q},t)\,|\sigma_i\rangle\right\rangle \tag{2.13c}$$

where the *dynamical structure factor*, $S(\mathbf{Q},\omega)$, has been introduced. The dynamical structure factor depends only on the physics of the system under investigation and not on the neutron probe. The calculation of the dynamical structure factor is the central problem of much of the work in this Thesis. The following section will detail the properties of the dynamical structure factor.

2.2.3 The dynamical structure factor

As described above, neutrons interact with matter both through the strong nuclear interaction with the nuclei of the sample and through the electromagnetic interaction with the magnetic fields present in the sample [57]. Since this Thesis is predominantly concerned with magnetic dynamics, the contribution from nuclear scattering is quoted without derivation; a full discussion is presented in Ref. [57].

The interaction potential governing the *nuclear* interaction is commonly represented by a delta function: the Fermi pseudopotential. Although the true form of the interaction potential is likely more complicated, at large separations, the weak interaction between the neutron and sample nucleus is well captured [57]. The nuclear scattering has a coherent and an incoherent contribution

$$S^{\mathrm{coh}}(\mathbf{Q},\omega) = \frac{1}{2\pi\hbar}\int_{-\infty}^{\infty} e^{-i\omega t}\sum_{jk}\overline{\beta^\dagger}_j\overline{\beta}_k\langle e^{-i\mathbf{Q}\cdot\hat{\mathbf{r}}_j}e^{i\mathbf{Q}\cdot\hat{\mathbf{r}}_k(t)}\rangle\mathrm{d}t \tag{2.14a}$$

$$S^{\mathrm{inc}}(\mathbf{Q},\omega) = \frac{1}{2\pi\hbar}\int_{-\infty}^{\infty} e^{-i\omega t}\sum_{j}\left(\overline{|\beta_j|^2} - |\overline{\beta}_j|^2\right)\langle e^{-i\mathbf{Q}\cdot\hat{\mathbf{r}}_j}e^{i\mathbf{Q}\cdot\hat{\mathbf{r}}_j(t)}\rangle\mathrm{d}t. \tag{2.14b}$$

Above, the operator $\hat{\beta}_j(t) = \langle\sigma_f|\,\hat{b}_j(t)\,|\sigma_i\rangle$ has been defined using the operator $\hat{b}$ which, when applied to the up $|+\rangle$ and down $|-\rangle$ spin states, yields the neutron scattering length, $\hat{b}_\pm\,|\pm\rangle = \hat{b}_\pm\,|\pm\rangle$. The neutron scattering length varies non-monotonically with the atomic number in contrast to the x-ray scattering length. This consideration often helps inform the choice of probe for a given material, particularly in diffraction experiments where one is not concerned with the kinematics associated with probing low energy excitations.

The primary cause of *magnetic* neutron scattering from matter is the interaction between the neutron's dipole moment and the magnetic flux density in the sample

$$V_M(\mathbf{r}) = -\boldsymbol{\mu}_n \cdot \mathbf{B}(\mathbf{r}) \tag{2.15}$$

where the neutron dipole moment is given by $\boldsymbol{\mu}_n = -2\gamma\mu_N\mathbf{s}$. The magnetic field from a single electron has a spin and orbital contribution [57, 59]

$$V_M(\mathbf{r}) = -\boldsymbol{\mu}_n \cdot [\mathbf{B}_S(\mathbf{r}) + \mathbf{B}_L(\mathbf{r})] \tag{2.16a}$$

$$\mathbf{B}_S(\mathbf{r}) = -2\mu_B\frac{\mu_0}{4\pi}\nabla \times \left(\frac{\mathbf{s}\times\mathbf{r}}{r^3}\right) \tag{2.16b}$$

$$\mathbf{B}_L(\mathbf{r}) = -2\mu_B\frac{\mu_0}{4\pi\hbar}\frac{\mathbf{p}\times\mathbf{r}}{r^3} \tag{2.16c}$$

where $\mathbf{p}$ is the electron momentum, $\mathbf{s}$ is the electron spin and $\mathbf{r}$ is the position vector. For a system comprising many electrons, in Fourier space, the magnetic interaction potential is then [57, 59]

$$V_M(\mathbf{Q}) = -4\gamma\mu_0\mu_B\mu_N\mathbf{s}_n \cdot \sum_j \left(\hat{\mathbf{Q}} \times (\mathbf{s}_j \times \hat{\mathbf{Q}}) + \frac{i}{\hbar Q}(\mathbf{p}_j \times \hat{\mathbf{Q}})\right) e^{i\mathbf{Q}\cdot\mathbf{r}_j} \tag{2.17}$$

where for the purpose of clarity, the neutron spin is labeled as $\mathbf{s}_n$. $\hat{\mathbf{Q}}$ is the unit vector along the direction of $\mathbf{Q}$. It can be shown that the magnetic field that the neutron interacts with the perpendicular component of the Fourier transformed sample magnetisation [64]

$$V_M(\mathbf{Q}) = 2\gamma\mu_N\mu_0\mathbf{s}_n \cdot \mathbf{M}_\perp(\mathbf{Q}). \tag{2.18}$$

In general the total magnetisation has contributions from both the orbital and spin moments, $\mathbf{M}(\mathbf{r}) = \mathbf{M}_L(\mathbf{r}) + \mathbf{M}_S(\mathbf{r})$. The matrix elements of $\langle\lambda_f|\,\mathbf{M}(\mathbf{Q})\,|\lambda_i\rangle$ are complicated to calculate in general [55, 57], but under the assumption that $|\mathbf{Q}|$ is small [65],

$$\mathbf{M}(\mathbf{Q}) \approx -2\mu_B\left[\langle j_0(Q)\rangle\mathbf{S} + \langle j_2(Q)\rangle\mathbf{L}\right] \tag{2.19}$$

where $\langle j_n(Q)\rangle$ is the radial integral of the n^{th} order spherical Bessel function [29]. If the spin-orbit coupling is large compared to a weak crystal field, the total angular momentum is a good quantum number and the magnetisation is proportional to $\mathbf{J}$. This is often the case in the $4f$ and $5f$ compounds [66–68]. In such systems the magnetisation is [57]

$$\mathbf{M}(\mathbf{Q}) \approx -\mu_B g_J f(\mathbf{Q})\mathbf{J} \tag{2.20}$$

where g_J is the Landé g-factor and $f(\mathbf{Q})$ is a magnetic form factor, depending on the radial average of the spherical Bessel function. In this Thesis, all systems considered are composed of $3d$ ions, for which the crystal field is typically of intermediate strength. In these systems, the orbital moment is typically quenched to some degree. The magnetisation in the $3d$ ions can therefore be written as

$$\mathbf{M}(\mathbf{Q}) \approx -g\mu_B f(\mathbf{Q})\mathbf{S} \tag{2.21}$$

where $g = 2$ if the orbital moment is entirely quenched by the crystal field. Armed with this relationship between the magnetisation and the spin operator, $\mathbf{S}$, (as appropriate for $3d$ ions), the dynamical structure factor can be written in terms of the local degrees of freedom of the sample. This is most straightforwardly done by inserting the expression for the magnetic interaction potential (Eqn. 2.18) into the correlator (Eqn. 2.13c) using Eqn. 2.21. The matrix elements in Eqn. 2.13c, $\langle\sigma_f|\,\hat{V}(\mathbf{Q})\,|\sigma_i\rangle$, depend on the initial and final polarisation states of the scattered neutron. This allows for polarisation analysis, where an incident beam is polarised along a particular axis and the final polarisation state of the scattered neutron is measured in order to extract further information about the source of the scattering.

In the case where the incident beam is unpolarised, the incident neutron is equally likely to be in each polarisation state $|\pm\rangle$. Calculating the matrix elements of the neutron spin operator, $\langle\sigma_f|\,\mathbf{s}_n\,|\sigma_i\rangle$, one finds that the correlator in the case of unpolarised neutrons is proportional to $\langle\mathbf{M}_\perp^\dagger\mathbf{M}_\perp(t)\rangle$ [59]. All that remains is to put all of these components together. For the $3d$ systems discussed in this Thesis, the structure factor is given by

$$S(\mathbf{Q},\omega) = g^2\mu_B^2 f^2(\mathbf{Q})\sum_{\alpha\beta}(\delta_{\alpha\beta} - \hat{Q}_\alpha\hat{Q}_\beta)S^{\alpha\beta}(\mathbf{Q},\omega) \tag{2.22a}$$

$$S^{\alpha\beta}(\mathbf{Q},\omega) = \frac{1}{2\pi\hbar}\int \mathrm{d}t e^{-i\omega t}\langle\hat{S}^\alpha(\mathbf{Q},0)\hat{S}^\beta(-\mathbf{Q},t)\rangle. \tag{2.22b}$$

The structure factor has been broken into the *partial* dynamical structure factor (Eqn 2.22b) which has nine components representing the combinations of the Cartesian basis vectors, x, y and z. The factor in front of the partial dynamical structure factor (Eqn. 2.22a) is known as the polarisation (or orientation) factor, that selects the component of the magnetisation perpendicular to the scattering wavevector $\mathbf{Q}$. Assuming the excitations are isotropic, the dynamical structure factor can be approximated by one of the diagonal components, $\mathbf{S}(\mathbf{Q},\omega) \sim \mathbf{S}^{xx}(\mathbf{Q},\omega)$ [69].

2.2.4 The principle of detailed balance

In the derivation of the structure factor $S(\mathbf{Q},\omega)$, transitions between an initial and final neutron state were considered. In a neutron scattering event, the initial neutron state σ_i can be higher or lower in energy than the final state. Let the initial energy of the neutron to be higher than the final neutron energy, i.e. the energy loss channel, with the dynamical structure factor, $S(\mathbf{Q},\omega)_{\sigma_i\rightarrow\sigma_f}$. The corresponding reverse process has a structure factor $S(-\mathbf{Q},-\omega)_{\sigma_f\rightarrow\sigma_i}$. There exists a relationship between the response functions for these two processes [55]

$$S(-\mathbf{Q},-\omega)_{\sigma_f\rightarrow\sigma_i} = e^{-\frac{\hbar\omega}{k_B T}} S(\mathbf{Q},\omega)_{\sigma_i\rightarrow\sigma_f} \tag{2.23}$$

where the prefactor on the right is the Boltzmann distribution. This relation, known as the principle of detailed balance, reflects the fact that neutron energy gain processes (where energy is transformed from the system to the neutron) require that excited states be thermally populated. At $\mathrm{T} = 0\,\mathrm{K}$ a peak is measured on the energy loss side only and as temperature increases, the intensity on the energy gain side grows.

2.3 Neutron instruments

The previous sections lay out the basic theory of inelastic neutron scattering. Attention will now be paid to the design of instruments that exploit the phenomenon of neutron scattering in order to probe the magnetic dynamics of crystalline materials. There are typically a wide variety of experiments that can be performed on a given instrument, but each spectrometer is designed to strike a balance between a number of competing desirable properties. Some spectrometers are designed to be high resolution, such as IRIS [70], whereas some, like MERLIN [71], are designed to optimise neutron count, or reduce background as with MARI [9]. The decision of the optimal instrument for a particular experiment is often a complicated trade-off between the required $(\mathbf{Q}, E)$ resolution, neutron flux and the dynamic range. The choice may also depend on the physics under investigation and sample details, for example one may need to make use of out-of-plane detectors if the excitations perpendicular to the scattering plane are of interest. Moreover, the necessary $\mathbf{Q}$ coverage required depends both on the nature of the sample and whether one is probing phonons or magnons. In the following sections there will therefore be a focus on the application of these instruments to the study of low energy magnetic excitations in single crystal samples, as is relevant to the physical problems discussed in this Thesis. The instruments of interest are typically referred to as spectrometers, distinguishing them from diffractometers (used to probe structure) and neutron spin echo (NSE) spectrometers (employed to measure very long timescale dynamics such as domain wall dynamics).

2.3.1 Triple-axis spectrometers

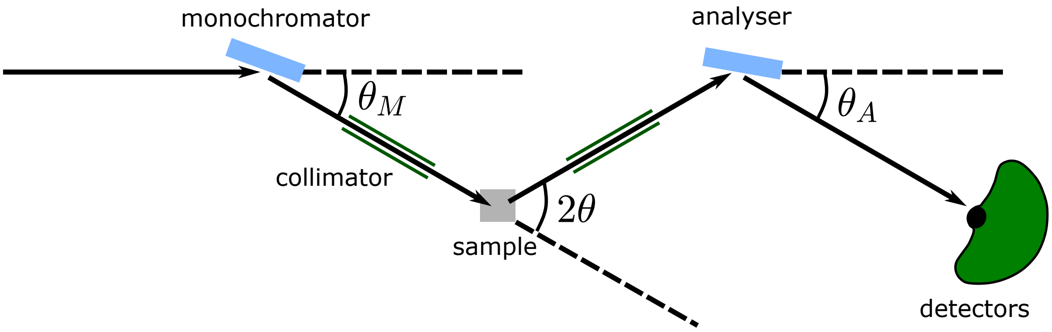

Figure 2.5 *Schematic of a triple-axis spectrometer. The name is derived from the three axes that define the angles θ_M, θ_A and 2θ. The monochromator selects the incident wavevector, $\mathbf{k}_i$ and the analyser crystal selects the scattered wavevector $\mathbf{k}_f$. The scattered neutrons are then incident on a detector. Collimators reduce the beam divergence, improving the instrument resolution. Depicted is a bank of neutron detectors as employed on MACS [8]. Many such instruments employ a single-wire detector.*

The first category of spectrometer is also the most physically intuitive. The triple-axis spectrometer (TAS), first developed at Chalk River by Brockhouse [72] has been employed at continuous sources since the genesis of neutron science and remains in use at modern continuous sources [8, 73]. The operating principle of the TAS is simple; a monochromator crystal selects the incoming neutron wavevector, k_i and an analyser crystal selects the final scattered wavevector, k_f (Fig. 2.5). In defining the incident and final wavevectors, the scattering wavevector $\mathbf{Q}$, is fixed allowing the full neutron flux to be directed to a particular wavevector and energy of interest. This makes triple-axis spectrometry a powerful tool in studying high symmetry directions.

The monochromator is usually a "mosaic crystal" made from many small crystals with slight misorientations [56] such that the scattering angle has some angular distribution. This is because the neutron beam divergences at scattering facilities is typically larger than the angular width of the diffracted beam from a perfect crystal. The crystals themselves are chosen to have a large reflectivity, low neutron absorption and a small incoherent cross section to limit background. Whilst there are a number of materials that fulfill these criteria, pyrolytic graphite (PG) [74, 75] is most commonly used [56] as it does not suffer from the problems associated with other candidate materials, such as double Bragg scattering or small mosaicity [56]. PG is effectively randomly oriented in all planes other than the $(00l)$ plane, but the (002) peak can have a mosaicity of $\lesssim 0.5°$ which is well suited for a monochromator, along with high neutron reflectivity [56]. Many of the considerations for the selection of a monochromating crystals apply to the selection of the analyser crystal which plays a similar role in selecting a given wavevector and energy. Further optimisation can be performed by introducing a curvature to the monochromator and analyser, boosting the intensity by focusing the neutron beam [56]. For a monochromator using the reflection (h, k, l) with a lattice plane spacing d_{hkl}, there is the possibility of contamination from higher order reflections from lattice planes with spacing d_{hkl}/n which reflect neutrons of wavelength λ/n. This higher order contamination can give rise to spurious peaks and must be eliminated by filters which are chosen to absorb scattered neutrons within a certain energy window. For example, Be and BeO filters are employed on the MACS spectrometer at NIST [8] and cut out neutrons below $\lambda \approx 3.5$ Å and $\lambda \approx 4.5$ Å respectively [56]. Fast neutron filters such as sapphire can also be employed to reduce the background resulting from high energy neutrons [76].

Once the scattered neutrons Bragg reflect from the analyser, they are then incident on a detector allowing the measurement of the neutron differential cross section (Eqn. 2.13a). Detector design can vary between instruments, with the early spectrometers implementing a single-wire detector acting as a single detector pixel. Other spectrometers, like MACS at NIST [8], employ a large bank of detectors so that multiple final energies can be recorded at the same time (Fig. 2.5). Neutron detector tubes are filled with a gas which, upon absorption of a neutron, emits charged particles. Typically ^{3}He is used

$$^{3}\mathrm{He} + \mathrm{n} \rightarrow {}^{3}\mathrm{H} + {}^{1}\mathrm{H} + \mathrm{energy} \tag{2.24}$$

which releases tritium, a proton and energy [77]. The charged particles ionise the surrounding atoms and the displaced electrons move towards a metal wire, causing current to flow. The electrical signal is then amplified and registered as a neutron scattering event.

The design of a TAS offers the ability to control both the incoming and outgoing neutron wavevector and energy. Thus one can operate the instrument in a number of "modes" by controlling the orientation of the monochromator and analyser crystals. The most common mode of operation is the constant-k_f mode, where E_f is fixed by the analyser crystal and the monochromator is rotated to vary E_i. It is also possible to fix E_i and vary E_f, operating a constant-k_i scheme, however normalisation of the neutron intensity is more difficult in this mode compared with the constant-k_f which can be straightforwardly normalised by monitor count.

2.3.2 Time-of-flight spectrometers

At pulsed neutron sources, a different type of instrument is typically employed. These instruments rely on the relationship between a neutron's energy and the time taken for the neutron to traverse a known distance. The pulsed nature of spallation neutron production makes these facilities optimal for the implementation of time-of-flight (ToF) spectrometry where the separation of incident neutron into pulses is necessary such that neutron energies can be distinguished according to their arrival time. That being said, ToF spectrometers can be employed at continuous sources, where choppers are used to create a pulsed structure for the incident neutrons. Examples of this include IN5 [78] at the Institut Laue-Langevin and DCS [79] at the NIST Center for Neutron Research.

ToF instruments fall into two broad categories based on the geometry of their construction. Broadly speaking these two geometries correspond to the two modes of operation in triple-axis spectrometers. Direct geometry spectrometers fix k_i in a manner similar to the constant-k_i TAS mode, with k_f determined by a time-of-flight analysis. Indirect spectrometers do precisely the opposite, with the k_f fixed and the initial wavevector determined by time-of-flight methods.

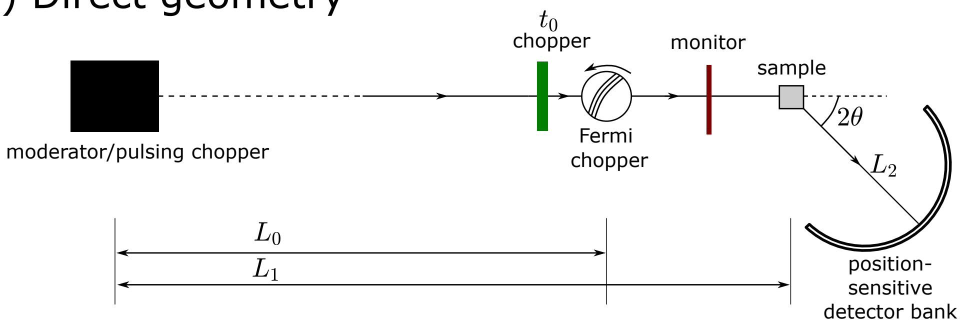
(a) Direct geometry

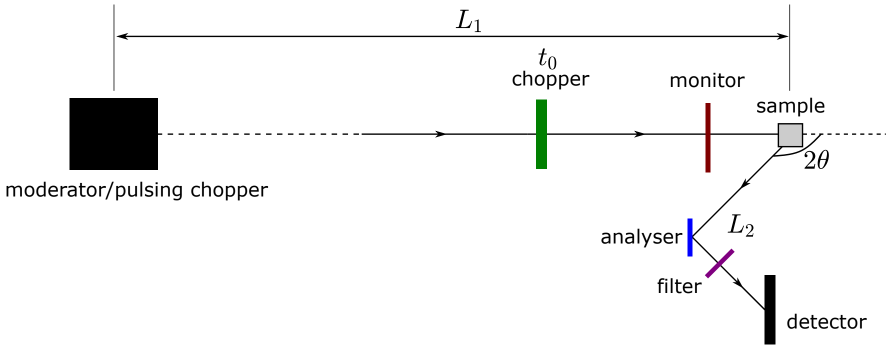
(b) Indirect geometry

Figure 2.6 *(a) Schematic of a direct geometry time-of-flight spectrometer. The distance between the moderator and Fermi chopper, which selects* k_i*, is* L_0*. (b) Schematic of an indirect geometry time-of-flight spectrometer. The distance between the moderator and sample in both geometries is* L_1*. The flight distance between the sample and the detectors is* L_2*. Note that in the case of indirect geometry,* L_2 *includes the path from the sample to the analyser and from the analyser to the detector.*

Direct geometry

As discussed in Section 2.1, at a pulsed source, the neutrons produced via spallation enter a moderator, thermalising with a Maxwellian distribution , before passing down the beam tube to the instrument, and ultimately the sample. The distance between the moderator and the sample is typically on the order of tens of meters, with $L_1 = 12$ m on MAPS [20], MARI [9] and MERLIN [71]. Direct geometry ToF spectrometers employ a series of neutron choppers that shape the beam (Fig. 2.6 (a)). The first of which, the t_0 chopper, is synchronised with the proton hitting the target, meaning that very high energy neutrons, that contribute significantly to the background, are blocked from proceeding towards the instrument. The t_0 chopper is a useful tool in reducing the background at spallation sources, but is omitted at continuous source ToF instruments such as IN5 [78] and DCS [79], which employ pulsing choppers to shape the beam originating at a reactor cold source. For instruments with a long flight-path, such as LET at ISIS [80], the t_0 chopper can be omitted since the fast neutrons have slowed significantly by the time they reach the instrument. After the t_0 chopper some instruments incorporate a disk chopper to reduce frame overlap leading to a reduced background. This is the case on the MAPS [20], MARI [9] and MERLIN [71] spectrometers. The disk chopper can engineered to serve a dual-purpose, not only reducing background, but allowing multiple neutron energies to pass through the subsequent Fermi chopper. This process, known as repetition rate multiplication, allowing for multiple incident neutron energies to be used simultaneously [20, 80–82].

After the t_0 chopper (and disk chopper, if present), there is a Fermi chopper which plays the role of the monochromator in a TAS and selects the k_i of the incident beam. The Fermi chopper is usually a cylinder with “slats” made of strongly neutron absorbing material such as borated aluminium [83] and slits that allow the transmission of neutrons. The chopper rotates at an integer multiple of the source frequency with the phase determining the the incident energy. For cold spectrometers like IN5 [78] and LET [80], the Fermi chopper is often replaced by a fast disk chopper which has a better transmission profile. Removing the E_i-defining chopper renders the incident beam polychromatic (known as running in “white beam mode”), allowing a direct geometry spectrometer to function as a diffractometer. This process is typically conducted prior to a neutron scattering experiment to help align the crystal by rotating it about the vertical axis.

Having passed the choppers, the neutrons pass through a monitor which is used to normalise the neutron count and determine the true E_i before scattering off the sample and being detected by an array of position sensitive detectors, pixelated such that the detector tubes offer sensitivity to the out-of-plane angle[2]. The

---

[2] The MARI spectrometer at ISIS Neutron and Muon Source does not have a pixelated

L_2 for each pixel then allows the determination of E_f from the neutron arrival position by time-of-flight analysis. The detectors are typically gas tube detectors (e.g. ^{3}He) such as on MAPS [20] or scintillation detectors (such as ZnS scintillator strips) [85], with the decision of detector type depending on a number of factors including spatial resolution, stability, efficiency and cost.

Indirect geometry

The geometry described above can be inverted such that polychromatic neutrons are incident on the sample and the time-of-flight analysis is carried out only on the scattered side in the so-called indirect (or inverted) geometry (Fig. 2.6 (*b*)). These spectrometers select the wavevector and energy on the scattered side akin to a TAS instrument operating in constant-k_f mode. The Fermi chopper is therefore not required in this geometry, however indirect spectrometers may employ a bandwidth chopper to reduce the number of low energy neutrons from prior pulses contaminating the signal and contributing to the background.

There are several ways that the final energy is selected in these instruments including analyser crystals and filter-difference systems. The crystal analyser spectrometer, (depicted in Fig. 2.6 (*b*)) operates by selecting a known E_f from Bragg scattering from a crystal analyser, usually PG(002) as employed on many TAS instruments. The analyser crystal is typically cooled to low temperatures to reduce thermal diffuse scattering resulting from population of phonon modes, which adds to the background. To reduce the background, Be filters can be used (as implemented on TOSCA [86]) to cut out high energy neutrons and suppress the contamination from higher order scattering. Time-of-flight analysis can then be used to calculate the energy and wavevector transfer. Examples of this type of design can be found on TOSCA [86] and IRIS [70] at the ISIS Neutron and Muon Source. Alternatively, filter-detector spectrometers employ a filter, usually Be (at 77 K), on the scattered side to create an cutoff for E_f, usually ≈ 5 meV [58] defining a larger neutron energy acceptance window than crystal analyser instruments. This window can be narrowed by comparing the spectra with that recorded using a BeO filter (at 300K), defining a smaller effective energy acceptance window [58]. These instruments can be designed

---

detector bank, but a low and high angle detector bank [84]. Each of the detector tubes cover a different scattering angle which is directly related to the magnitude of the scattering wavevector, $|\mathbf{Q}|$, making MARI well-suited to the studying of powder samples where only the magnitude of the scattering wavevector is of any relevance.

to be compact, offering a large angular detector coverage, and the large energy acceptance window can result in a large gain in intensity at comparable resolution towards the high energy transfer regime[3]. It is on this basis that a Be-filter indirect spectrometer has been proposed at the Spallation Neutron Source at Oak Ridge National Laboratory, to support the crystal analyser spectrometer, VISION [87].

For indirect geometry instruments, neutrons within a wide energy band are incident on the sample and are reflected by the analyser crystal onto the detector. This has the consequence that indirect geometry instruments are typically high intensity [88] if equipped with a large-area crystal-analyser. The trade-off is that indirect instruments experience background from both the structures behind the analyser and the thermal diffuse scattering from the analyser itself.

Time-of-flight analysis

The following section will detail how time-of-flight analysis can be used to determine the energy and wavevector transfer in a ToF spectrometry experiment. In terms of the distances labeled in Fig. 2.6, the incident and final neutron energies can be written as

$$E_i = \frac{L_1^2 m_n}{2t_1^2} \tag{2.25a}$$

$$E_f = \frac{L_2^2 m_n}{2t_2^2} \tag{2.25b}$$

where t_μ is the time taken for the neutron to traverse the distance L_μ and m_n is the neutron mass. The energy of the excitation is therefore (in the energy loss channel)

$$\hbar\omega = \frac{m_n}{2}\left(\frac{L_1^2}{t_1^2} - \frac{L_2^2}{t_2^2}\right). \tag{2.26}$$

In ToF spectrometers the conversion of neutron counts to the partial differential cross section is performed in a different manner from the approach in TAS instruments. For a TAS, the instrument defines the two wavevectors, $\mathbf{k}_i$ and $\mathbf{k}_f$ from which the scattering vector $\mathbf{Q}$ and energy $E = \hbar\omega$ can be calculated. The detector therefore directly measures the differential cross section, $\frac{\mathrm{d}^2\sigma}{\mathrm{d}\Omega\mathrm{d}\hbar\omega}$ [57, 58]. In a ToF spectrometer, the instrument measures the number of neutron counts

---

[3] At large energy transfers the energy resolution is determined predominantly by the time resolution of the detector and the time-of-flight, rather than the energy acceptance window [87].

per solid angle in discretised time intervals. The detector thus measures the differential cross section, $\frac{\mathrm{d}^2\sigma}{\mathrm{d}\Omega \mathrm{d}t}$. This can be straightforwardly related to the differential cross section previously defined (Eqn. 2.8), and hence the dynamical structure factor

$$S(\mathbf{Q},\omega) = \frac{t_2^4}{t_1 m_n L_2^2} \frac{\mathrm{d}^2\sigma}{\mathrm{d}\Omega \mathrm{d}t}. \tag{2.27}$$

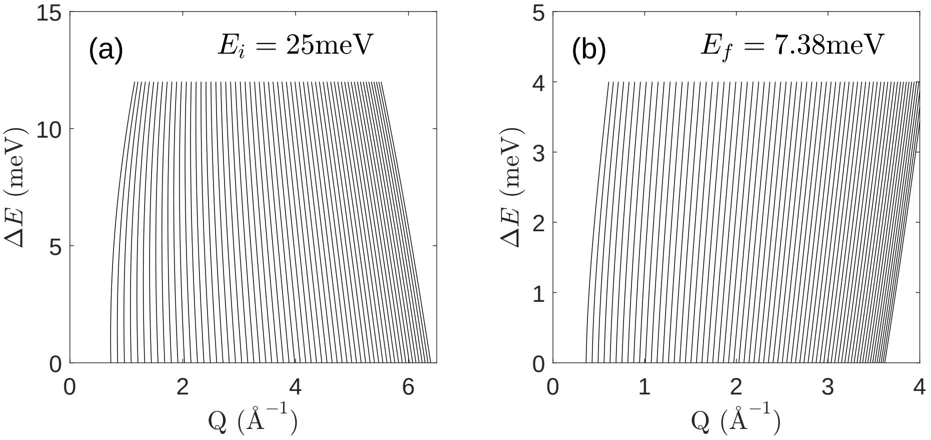

Figure 2.7 (*a*) *The dynamical range calculated for a direct geometry ToF spectrometer calculated in 2° steps of 2θ from 12° to 135° (the 2θ coverage of the MARI spectrometer at ISIS [9]).* (*b*) *Inverse geometry dynamical range, with 2θ in 2° steps from 11° to 148° (the 2θ coverage of the OSIRIS spectrometer at ISIS [10]).* E_f *was chosen to be 7.38 meV consistent with the PG(004) analyser in operation on OSIRIS [10].*

Choosing a spectrometer

The specificities of the design of individual ToF and TAS instruments makes each individual instrument well-suited to answering particular physical questions. In the course of this chapter, the basic operating principles of direct and indirect ToF spectrometers and TAS instruments have been covered, however there are a plethora of design details that optimise different aspects of the instrumental operation. For TAS instruments these include specialised analysers and filters to cut down background and multiple scattering [75, 76] and multiplexing analyers to increase energy coverage [89, 90]. For ToF spectrometers, much innovation has centered around optimising the neutron guide to increase neutron flux [20, 91] and the implementation of repetition rate multiplication which offers access to multiple incident energies [80–82]. The dynamic range required must also be considered when choosing a spectrometer. This differs from spectrometer to spectrometer and depends on the geometry, the incident and final energies accessible and the detector coverage. Pictured in Fig. 2.7 is the dynamical range accessible on two ToF instruments of different geometries.

One consideration when choosing a spectrometer is whether polarisation analysis can be of use. Polarisation analysis can be implemented on TAS instruments such as IN20 [92] and SPINS [93], as well as ToF instruments, HYSPEC [94] and LET [80]. Polarisation analysis allows for the separation of the longitudinal and transverse components of the dynamical structure factor and so can be used to identify exotic excitations in quantum magnets [95] and shed light on chiral spin dynamics [96]. Polarisation analysis also allows one to unambiguously determine whether scattering has a magnetic or structural origin, offering insight into the interplay of competing degrees of freedom [97]. Polarisation analysis was not used in any of the experiments presented in this Thesis. Extensive discussions of the use of this technique can be found in classic neutron scattering texts [55–57].

Whilst each instrument differs slightly in design and purpose, a number of general comments can be made. TAS instruments at continuous sources typically have a higher neutron flux than ToF spectrometers at pulsed sources. This has been particularly useful in the study of the van der Waals two-dimensional magnets VI_3 and Fe_3GeTe_2 where single crystal samples are small and many need to be coaligned to produce a sample of sufficient mass to study. Where large single crystals exist, ToF spectrometers are extremely useful in generating a broad survey in $(\mathbf{Q}, E)$. This is of particular use in three-dimensional systems and those in which the nature of the excitations is completely unknown. Typically, the advantages of using ToF instruments come at the cost of relatively low neutron flux compared to continuous sources. This is set to change when the high flux European Spallation Source (ESS) [98], currently under construction in Lund, comes online in late 2027 [99].

2.3.3 Single crystal alignment

The first challenge when beginning a neutron scattering experiment is orientating the crystal such that a direction of interest lies within the scattering plane. In principle this can be achieved by placing the sample in the beam with the chopper removed meaning that all incident wavevectors are permitted (known as a white beam) and finding and identifying a Bragg peak based on the d-spacing extracted from time-of-flight analysis. The sample can then be aligned such that $\mathbf{k}_i$ is parallel to a given direction by rotating the sample. However, the sample environment often places restrictions on how the sample can be manipulated. Most sample sticks only allow for the rotation of the sample about one axis. It is for this reason that samples need to be aligned prior to arrival on the instrument. Some user facilities also provide access to dedicated beam lines prior to the start of the experiment. These instruments, such as ALF at ISIS [100] and OrientExpress at the ILL [101], were commissioned in the hope that they would allow users to make best use of their beam time with less time spent aligning their sample at the beginning of the experiment.

In the following section a protocol for aligning single crystal samples at the alignment facility, ALF [100], at ISIS Neutron and Muon Source will be discussed. A software package, principally designed and built by Z. Liu at the University of Edinburgh [3], will now be presented.

ALF instrument design

ALF has been constructed on beam port N2 at Target Station 1 at ISIS Neutron and Muon Source (Fig. 2.3) and views a liquid methane moderator. The total flight path is 13.86 m with no monochromating chopper on the incident side, hence the neutrons that reach the sample are polychromatic and the instrument functions solely in white beam mode. Scattered neutrons are detected by a bank of 37 position sensitive detector tubes, each 1m long, with the centre point 1.32 m from the sample. The angular coverage of the detectors is $20.2^\circ < 2\theta < 60.3^\circ$ in the horizontal scattering plane. A three-axis goniometer rests in the sample position. This goniometer allows the position and height of the sample to be adjusted, both parallel and perpendicular to the incident beam. The goniometer design is depicted in Fig. 2.8. The lower rail is aligned along the x-axis and the upper rail along the y-axis. Both rails are mounted on a rotation axis which allows the assembly to rotate about the z-axis.

Since a white beam is incident on the sample, if Bragg's law is satisfied for any wavevector, $\mathbf{k}_i$, a reflection will occur, and a Bragg spot observed if the reflected beam is incident on the detector. This principle is employed in Laue diffractometers, where the characteristic (Laue) diffraction pattern, measured on large area, high-performance detectors [101], is used to fully characterise the crystal structure. On ALF, since there are no analysers on the scattered side,

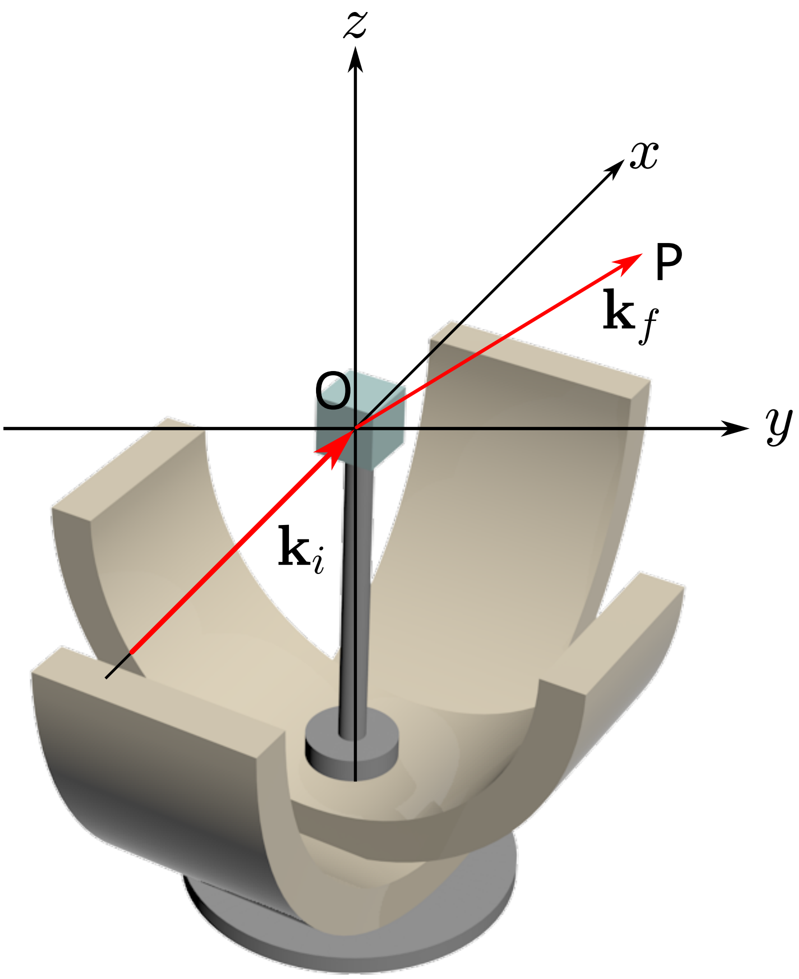

Figure 2.8 *The layout of the goniometer and definition of the laboratory frame. The sample is depicted by a blue square at the origin, O. The flight path of the scattered neutron is shown in red. The incident wavevector* $\mathbf{k}_i$ *is along the* x*-axis and the final wavevector* $\mathbf{k}_f$ *is directed towards the activated detector pixel, P. Figure adapted from Ref. [3].*

it is assumed that all measured neutrons are scattered elastically. The energy of the scattered neutrons is determined using a time-of-flight analysis. Since the scattering is assumed to be elastic, $|\mathbf{k}_i| = |\mathbf{k}_f|$, with the scattering vector, $\mathbf{Q} = \mathbf{k}_i - \mathbf{k}_f$. The energy of the scattered and incident neutron is

$$E = \hbar^2 k^2/2m = \frac{1}{2}mv^2 = \frac{1}{2}m(\frac{l}{t})^2 \tag{2.28}$$

where t is the time-of-flight and l is the length of the flight path. From Bragg's law one has that

$$|\mathbf{Q}| = 2|\mathbf{k}_i|\sin\theta \tag{2.29}$$

where θ is half the angle between $\mathbf{k}_i$ and $\mathbf{k}_f$. Using Bragg's law, the time-of-flight of a neutron detected at each pixel of the position sensitive detector determines the momentum transfer.

Visualisation

For a given goniometer setting, a diffraction pattern will be recorded on the position sensitive detector bank. It will now be detailed how these can be mapped onto a common coordinate system so that multiple detector images can be analysed at the same time. First consider the Ewald sphere centered on the crystal (Fig. 2.9). The Ewald sphere is a sphere of radius $|\mathbf{k}_i| = |\mathbf{k}_f|$ constructed

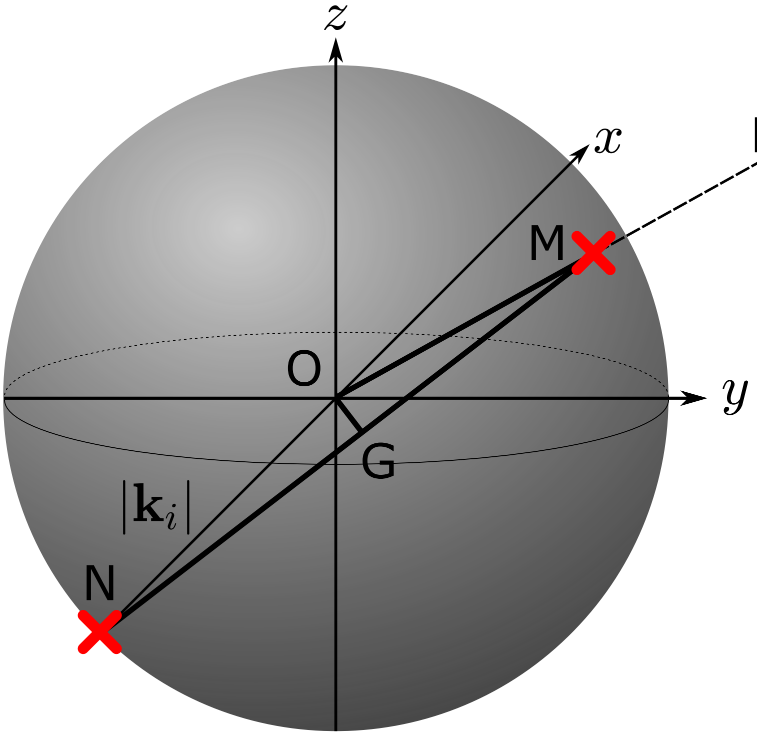

Figure 2.9 *The Ewald sphere with radius $|\mathbf{k}_i|$ centered on the crystal at the origin, O. OP intersects the sphere at M and the x-axis intersects the sphere at N. G is a point on the sphere such that the vector $\overrightarrow{OG}$ bisects $\overrightarrow{ON}$ and $\overrightarrow{OM}$. Figure adapted from Ref. [3].*

such that the Bragg condition is satisfied only for reciprocal lattice points lying on the surface of the sphere separated by a distance $|\mathbf{Q}|$. The vector $\overrightarrow{OG}$ lies in the scattering plane and bisects the vectors $\overrightarrow{OM}$ and $\overrightarrow{ON}$ such that it makes an angle θ with both $\mathbf{k}_i$ and $\mathbf{k}_f$. The vector $\overrightarrow{OG}$ is always perpendicular to the plane of atoms from which the diffraction occurs meaning this vector can be used to determine the orientation of the crystal. The rotations of the crystal achievable by the three-axis goniometer can be described by three rotation matrices which represent the crystal rotations about its base and along the lower and upper goniometer rails respectively

$$\underline{G}_{rotated} = \underline{\underline{R}}_{rot} \underline{\underline{R}}_{lower} \underline{\underline{R}}_{upper} \underline{G}_{lab} \tag{2.30}$$

where the rotation matrices are defined as

$$\underline{\underline{R}}_{rot} = \begin{pmatrix} \cos\lambda & -\sin\lambda & 0 \\ \sin\lambda & \cos\lambda & 0 \\ 0 & 0 & 1 \end{pmatrix} \tag{2.31a}$$

$$\underline{\underline{R}}_{upper} = \begin{pmatrix} 1 & 0 & 0 \\ 0 & \cos\mu & -\sin\mu \\ 0 & \sin\mu & \cos\mu \end{pmatrix} \tag{2.31b}$$

$$\underline{\underline{R}}_{lower} = \begin{pmatrix} \cos\tau & 0 & -\sin\tau \\ 0 & 1 & 0 \\ \sin\tau & 0 & \cos\mu \end{pmatrix} \tag{2.31c}$$

with the rotation angles, λ, μ and τ are the rotation angles about the z, x and y axis respectively (Fig. 2.10). The column vectors, $\underline{G}_{lab}$ and $\underline{G}_{rotated}$ describe the vector $\overrightarrow{OG}$ in the laboratory and rotated frames. The rotation matrices, $\underline{\underline{R}}_{rot}$, $\underline{\underline{R}}_{upper}$ and $\underline{\underline{R}}_{lower}$ do not, in general, commute, although since the goniometer arcs are constructed on top of one another, it does not matter in which order the user drives the angles as the final configuration will be the same, regardless of order of operation.

The pixel location, P, can be described with the three variables, (l, α, β) where l is the distance from the crystal to the pixel and α and β are two rotation angles around the x and z axes respectively. In terms of these variables, the pixel

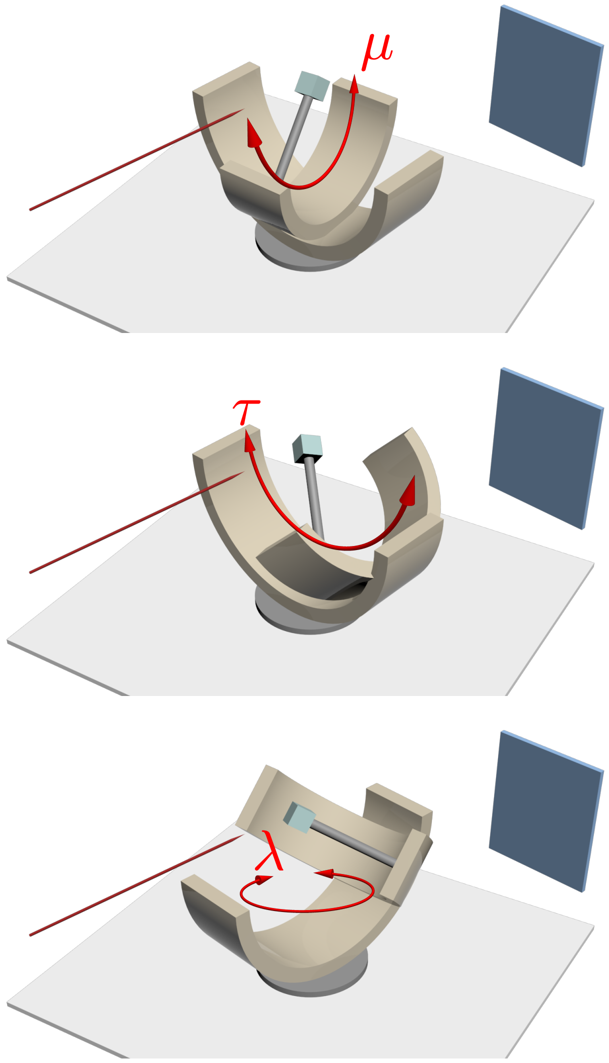

Figure 2.10 *Rotation angles as defined in the rotation matrices,* $\underline{\underline{R}}_{rot}$, $\underline{\underline{R}}_{upper}$ *and* $\underline{\underline{R}}_{lower}$. *The path of the incident neutron is indicated in red, with the detector bank indicated by the blue square. Figure reproduced from Ref. [3].*

location is defined as

$$\underline{P} = \underline{\underline{A}}\,\underline{\underline{B}} \begin{pmatrix} l \\ 0 \\ 0 \end{pmatrix} \tag{2.32}$$

with the rotation matrices defined as

$$\underline{\underline{A}} = \begin{pmatrix} 1 & 0 & 0 \\ 0 & \cos\alpha & -\sin\alpha \\ 0 & \sin\alpha & \cos\alpha \end{pmatrix} \tag{2.33a}$$

$$\underline{\underline{B}} = \begin{pmatrix} \cos\beta & -\sin\beta & 0 \\ \sin\beta & \cos\beta & 0 \\ 0 & 0 & 1 \end{pmatrix} \tag{2.33b}$$

The coordinates of $\underline{G}_{rotated}$ can be calculated by geometry. Since $\overrightarrow{OG}$ and $\overrightarrow{OP}$ lie in the same plane, the coordinate G can be rotated onto the x-y plane by rotating by the angle α, clockwise about the x-axis. The vector $\overrightarrow{OG}$ bisects $\overrightarrow{OM}$ and $\overrightarrow{ON}$, so by further rotating by angle $\frac{\beta}{2}$ about the z-axis, $\overrightarrow{OG}$ is aligned with the y-axis,

$$\underline{\underline{G}}_{rotated} = \underline{\underline{A}}\,\underline{\underline{\Omega}} \begin{pmatrix} 0 \\ 1 \\ 0 \end{pmatrix} \tag{2.34}$$

with the rotation matrix defined as

$$\underline{\underline{\Omega}} = \begin{pmatrix} \cos\frac{\beta}{2} & -\sin\frac{\beta}{2} & 0 \\ \sin\frac{\beta}{2} & \cos\frac{\beta}{2} & 0 \\ 0 & 0 & 1 \end{pmatrix}. \tag{2.35}$$

Eqn. 2.30 and Eqn. 2.34 can then be combined to find $\underline{G}_{lab}$ in terms of the pixel location and goniometer settings

$$\underline{G}_{lab} = \underline{\underline{R}}^{-1}_{upper}\,\underline{\underline{R}}^{-1}_{lower}\,\underline{\underline{R}}^{-1}_{rot}\,\underline{\underline{A}}\,\underline{\underline{\Omega}} \begin{pmatrix} 0 \\ 1 \\ 0 \end{pmatrix}. \tag{2.36}$$

The rotation matrices in Eqn. 2.36 depend on the three goniometer angles and the two pixel angles. However, the vector $\underline{G}_{lab}$ is uniquely defined by two spherical coordinates, (ϑ, ϕ). Therefore, by scanning the five angles $(\alpha, \beta, \mu, \tau, \lambda)$ which are defined for each detector image, a two-dimensional colour map can be built up from a multiple detector images. This method of data visualisation is known as a pole figure and can be particularly useful if there are few strong Bragg spots that are visible in a given detector image. A software package that automates this process has been developed at the University of Edinburgh and can be found at [102]. A full demonstration of the use of this software package to co-align a single crystal of $Pb(Mg_{1/3}Nb_{2/3})O_3$ is given in Ref. [3].

Chapter 3

Nonlinear soliton confinement in weakly coupled antiferromagnetic spin chains

3.1 Introduction

Confinement and deconfinement of particles, topological defects or fractionalised excitations are recurring motifs in many areas of physics. A famous example is the quark-gluon plasma, which is predicted to form at extremely high temperatures. In this new state of matter the quarks and gluons, which under normal conditions are strongly confined in atomic nuclei, behave as asymptotically free particles [103]. Another example of a confinement-deconfinement transition is the Berezinskii-Kosterlitz-Thouless transition [104, 105] in two-dimensional XY magnets that is driven by an unbinding of thermally excited vortex-antivortex pairs.

Spin-charge separation in one dimension [106–108] can be viewed as a fractionalisation of the electrons into holons and spinons, carrying the charge and spin degrees of freedom, respectively. If local repulsions lead to charge localisation, the insulating system is well described by the antiferromagnetic $S = 1/2$ Heisenberg model. In the presence of Ising exchange anisotropy, spinons can be viewed as domain walls in the antiferromagnetic order and are created in pairs by a single spin flip (Fig. 3.1(a)). They are therefore fractionalised excitations that carry half of the spin-1 quantum of a magnon excitation [109]. If spinons are free to propagate, these pairs are expected to form a triplet excitation continuum. Such continua are predicted theoretically [110–112], building on the analytical Bethe Ansatz solution [113], and observed experimentally in a number of quasi one-dimensional $S = 1/2$ antiferromagnets [114–117].

Staggered g-tensors and Dzyaloshinskii-Moriya interactions can lead to an unusual field dependence, such as an induced gap [118, 119], $\Delta \sim H^{2/3}$, and field dependent soft modes at incommensurate wave vectors [120, 121], as predicted by spinon and Bethe Ansatz descriptions [122–124]. Through a procedure of bosonisation [125], the dynamics of such systems can be shown to be governed by the quantum sine-Gordon model which admits soliton and breather solutions, corresponding to propagating and oscillating domain walls, respectively [119, 126]. This suggests that spinons can be viewed as quantum solitons [127] and therefore exhibit chirality, which was indeed confirmed by polarised neutron scattering [128]. Soliton and breather modes have been identified in neutron scattering [129, 130] and electron spin resonance [131, 132] experiments.

The effect of a weak inter-chain interaction is twofold. Firstly, it sets the temperature scale T_{N} at which two or three-dimensional long-range order develops. Secondly, it generates an effective attraction between spinons below T_{N} since the separation of domain walls will frustrate inter-chain interactions with an associated energy cost that grows linearly with their distance. Such a linear confinement potential gives rise to spinon bound states, leading to a quantisation of the excitation continuum into discrete energy levels, as observed in $\mathrm{BaCo_2V_2O_8}$ [133], $\mathrm{SrCo_2V_2O_8}$ [115, 134], and $\mathrm{Yb_2Pt_2Pb}$ [116]. These systems all consist of weakly coupled Ising-Heisenberg antiferromagnetic (XXZ) chains of $S = 1/2$ moments and the measured spinon bound state energies are almost perfectly described by the eigenvalues of a one-dimensional Schrödinger equation with an attractive linear potential.

Linear confinement due to weak inter-chain coupling is not specific to spinons in $S = 1/2$ quantum antiferromagnets but occurs generically for any type of kink-like domain wall excitations. In $\mathrm{CoNb_2O_6}$, a quasi-one-dimensional Ising ferromagnet, the two-kink continuum breaks up into discrete bound state excitations below the magnetic ordering temperature, with the same characteristic level spacing as in the spinon case [135].

In this chapter, the domain wall confinement in large-S spin chain antiferromagnets with easy axis, single-ion anisotropy will be analysed. This work is motivated by the observation of discrete energy levels in the anisotropic antiferromagnet $\mathrm{CaFe_2O_4}$ [11], an $S = 5/2$ system consisting of weakly coupled zig-zag networks of Fe^{3+} ($3d^5$) ions. As expected for confinement due to frustrated inter-chain coupling, the bound states form below the the Néel temperature $T_{\mathrm{N}} \approx 200$ K. However, the energy levels do not follow the negative zeros of the Airy function, as predicted for a linear confinement potential.

In the large-S limit, the low energy effective field theory of the quantum antiferromagnet is the nonlinear σ model. Starting from this semiclassical description, Haldane demonstrated that the spin dynamics of the one-dimensional quantum antiferromagnet with easy-axis anisotropy is governed by a sine-Gordon equation which supports soliton solutions [136], hence the domain walls in the antiferromagnetic chain are chiral solitons. In these spin textures the staggered magnetisation rotates between the two favoured orientations in a clockwise or anti-clockwise direction over a typical distance ξ (Fig. 3.1 (*b*)). Since the overall chirality in the system is conserved, the domain walls are created in pairs of soliton (kink, K) and anti-soliton (anti-kink, $\overline{\mathrm{K}}$).

In this chapter, the confinement potential $V(y)$ will be computed from the $\mathrm{K}\overline{\mathrm{K}}$ two-soliton solution of the sine-Gordon equation showing that the extended nature of semiclassical solitons gives rise to a crossover as a function of the domain wall separation $|y|$. At large separations, $|y| \gg \xi$, the solitons can be considered as point-like objects, giving rise to a linear confinement potential, $V(y) \sim |y|$. For $|y| < \xi$ the soliton and anti-soliton overlap, leading to a gradual annihilation of the defects and preventing the staggered magnetisation between domain walls from fully rotating to the other easy direction. This reduces the inter-chain frustration energy, corresponding to a weakening of the effective confinement potential. It will be shown that at small distances, $|y| \ll \xi$, the confinement potential is rendered quadratic, $V(y) \sim y^2$.

The bound state spectrum will be obtained from the numerical solutions of a one-dimensional Schrödinger equation with the computed potential $V(y)$. Because of the crossover in $V(y)$, the energies of tightly-bound states are almost equidistant, as expected for a harmonic oscillator, while for the weakly bound states at higher energies they approach Airy function behaviour as predicted for linear confinement.

In order to test this theory of nonlinear soliton confinement, the computed spectra is compared to those obtained in neutron scattering experiments on high-quality single crystals of $CaFe_2O_4$. Slightly below the Néel ordering temperature, it is possible to resolve seven bound states which are well described by the theory of nonlinear confinement of spatially-extended solitons.

The outline of this chapter is as follows. Beginning with insights gained in the author's MSci project, in Section 3.2 a generic spin Hamiltonian and resulting low energy, nonlinear σ model description of a system of weakly coupled antiferromagnetic chains with single-ion Ising anisotropy is introduced. It is shown that the saddle-point approximation results in a sine-Gordon equation and briefly review the one and two-soliton solutions. In Section 3.3 the energy of a single spin chain with a pair of domain walls from the kink-antikink solution is computed, treating the inter-chain coupling at mean-field level. Extending previous work, the bound state energies are obtained from numerical solutions of the effective Schrödinger equation with the effective nonlinear confinement potential. Experimental details and results of inelastic neutron scattering experiments performed on $CaFe_2O_4$ by C. Stock are presented in Section 3.4. It is demonstrated that the measured bound state energies are well described by this theoretical model. Finally, in Section 3.5 the results are summarised and discussed.

3.2 Theoretical model

The starting point is a generic spin model of weakly coupled chains with antiferromagnetic Heisenberg coupling J between nearest neighbours along the chains and $J_\perp \ll J$ between the chains. Each spin is subject to a single-ion, easy-axis anisotropy $\alpha > 0$. The Hamiltonian of the system is given by

$$\begin{aligned} \hat{\mathcal{H}} &= J\sum_{i,m}\mathbf{S}_{i,m}\cdot\mathbf{S}_{i+1,m} - \alpha\sum_{i,m}\left(\hat{S}^z_{i,m}\right)^2 \\ &\quad + J_\perp\sum_{i,\langle m,n\rangle}\mathbf{S}_{i,m}\cdot\mathbf{S}_{i,n}, \end{aligned} \tag{3.1}$$

where i labels the positions in the chains, m, n the different chains, and $\langle m, n\rangle$ denotes nearest-neighbour bonds between adjacent chains. In this minimal model, longer-range exchanges are neglected and the inter-chain couplings are assumed to be the same in all directions. For simplicity, exchange anisotropy

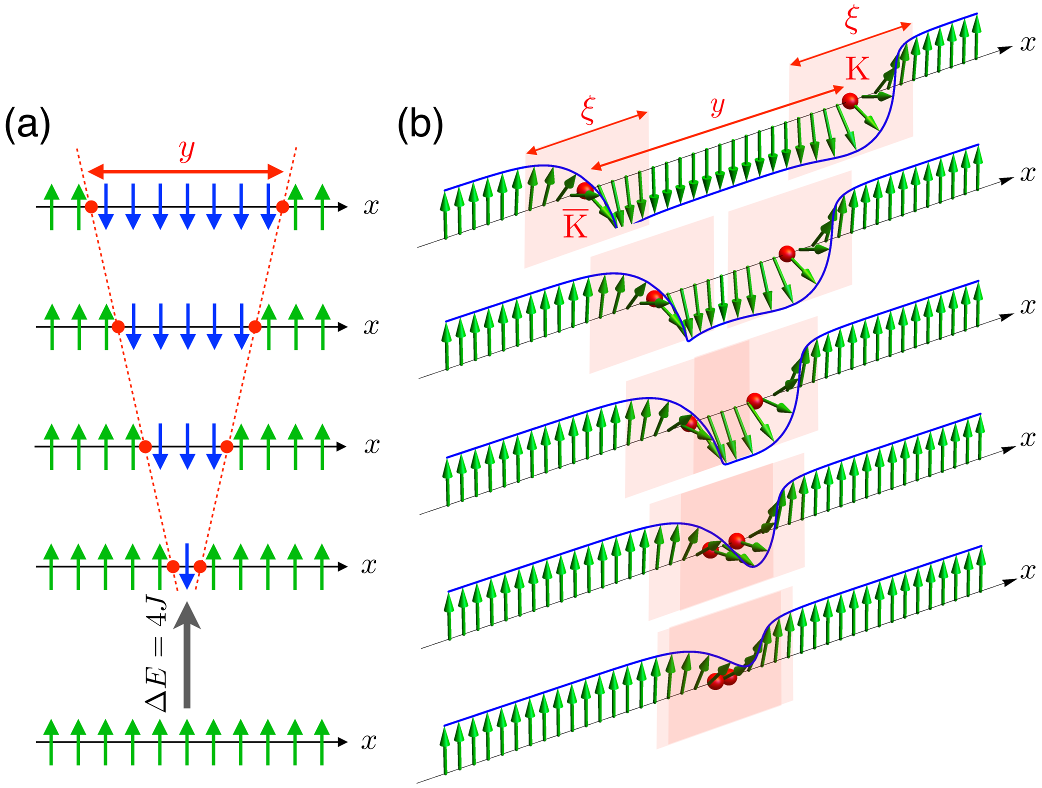

Figure 3.1 *Staggered magnetisations of antiferromagnetic spin chains with Ising anisotropy in the presence of two domain walls (red). (a) For the $S = 1/2$ chain, a spin-flip excitation fractionalises into a pair of spinons. The energy cost due to the coupling to nearby chains scales with the number of spins between the domain walls, giving rise to a linear confinement potential, $V(y) \sim |y|$. (b) For large-S spin chains the domain walls are semiclassical chiral solitons of size ξ. Shown are different time instances of the collision of a soliton (K) and anti-soliton ($\overline{K}$) obtained from the $K\overline{K}$ two-soliton solution of the sine-Gordon equation. The spatial extent of the domain walls causes them to annihilate gradually, rendering the effective confinement potential quadratic at small distances, $V(y) \sim y^2$.*

between different spin components and Dzyaloshinskii-Moriya interactions have been neglected. Such terms are not relevant in the case of calcium ferrite ($S = 5/2$, $L = 0$) because of the lack of any orbital degrees of freedom. A discussion of single-ion anisotropy in systems with quenched orbital moment can be found in Ref. [27].

3.2.1 Nonlinear σ model

Firstly attention is focused on an isolated antiferromagnetic chain ($J_\perp \to 0$) and the chain index is dropped for brevity. The effective long-wavelength, nonlinear σ model is obtained using a path integral in imaginary time $\tau \in [0, \beta]$, $\beta = 1/(k_\mathrm{B}T)$, and resolving the identities between adjacent time slices in terms of over-complete spin-coherent states, $|\mathbf{N}_i(\tau)\rangle$. These states are parametrised by unit vectors $\mathbf{N}_i(\tau)$ and have the property $\langle \mathbf{N}_i(\tau)|\mathbf{S}_i|\mathbf{N}_i(\tau)\rangle = S\mathbf{N}_i(\tau)$.

In order to perform a spatial continuum limit, the staggered Néel order-parameter field $\mathbf{n}_i(\tau)$ is introduced through the relation $\mathbf{N}_i(\tau) = (-1)^i\mathbf{n}_i(\tau) + a\mathbf{L}_i(\tau)$, where a denotes the lattice constant and $\mathbf{L}_i(\tau)$ describes the spin fluctuations perpendicular to $\mathbf{n}_i(\tau)$. The latter fluctuations are massive and can therefore be integrated out. After taking the continuum limit, this procedure leads to the nonlinear σ model [54, 136, 137],

$$S = \frac{\rho_S}{2}\int_0^\beta \mathrm{d}\tau \int_{-\infty}^{\infty} \mathrm{d}x \left\{ (\partial_x \mathbf{n})^2 + \frac{1}{c^2}(\partial_\tau \mathbf{n})^2 - \kappa n_z^2 \right\}, \tag{3.2}$$

with spin stiffness ρ_S, spin wave velocity c and easy-axis anisotropy κ. A derivation of Eqn. 3.2 is given in Appendix C. These parameters are related to the microscopic parameters in the spin Hamiltonian (Eqn. 3.1),

$$\rho_S = JS^2a, \quad c = \sqrt{2}JSa, \quad \text{and} \quad \kappa = \frac{2\alpha}{a^2 J}. \tag{3.3}$$

In the absence of anisotropy, $\kappa = 0$, the relativistic field theory gives rise to a linear dispersion $\omega = ck$, corresponding to spin wave excitations of the antiferromagnet. This is also reflected by the saddle-point approximation $\delta S/\delta\mathbf{n}(x,t) = 0$ in real time $t = -i\tau$, which gives rise to the classical wave equation $\partial_x^2\mathbf{n} - \frac{1}{c^2}\partial_t^2\mathbf{n} = 0$.

3.2.2 Sine-Gordon equation and soliton solutions

In the presence of anisotropy, it is useful to express the unit vector field $\mathbf{n}(x,\tau)$ in terms of spherical coordinates, $\mathbf{n} = (\sin\theta\cos\phi, \sin\theta\sin\phi, \cos\theta)$ since the anisotropy only depends on the polar-angle field $\theta(x,\tau)$,

$$\begin{aligned} S &= \frac{\rho_S}{2}\int_0^\beta \mathrm{d}\tau \int_{-\infty}^{\infty} \mathrm{d}x \Bigg\{ \left(\partial_x\theta\right)^2 + \frac{1}{c^2}\left(\partial_\tau\theta\right)^2 \\ &\qquad + \sin^2\theta\Big[\left(\partial_x\phi\right)^2 + \frac{1}{c^2}\left(\partial_\tau\phi\right)^2\Big] - \kappa\cos^2\theta\Bigg\}. \end{aligned} \tag{3.4}$$

The equations of motion are obtained from the saddle-point equations $\delta S/\delta\phi(x,t) = 0$ and $\delta S/\delta\theta(x,t) = 0$. For the azimuthal angle, a classical wave equation is obtained, $\partial_x^2\phi - \frac{1}{c^2}\partial_t^2\phi = 0$. Since this work concerns soliton excitations and not spin waves, it is assumed that $\phi(x,t) = \text{const}$. In a system with z-axis Ising anisotropy the free energy is independent of the choice of this constant. This removes all dependence of the action (Eqn. 3.4) on ϕ and the dynamics for the polar angle is governed by the sine-Gordon equation,

$$\partial_x^2\theta - \frac{1}{c^2}\partial_t^2\theta = \frac{1}{2}\kappa\sin(2\theta), \tag{3.5}$$

which is known to admit soliton solutions [138, 139]. In terms of dimensionless length and time,

$$\tilde{x} := \sqrt{\kappa}x, \quad \text{and } \tilde{t} := \sqrt{\kappa}ct, \tag{3.6}$$

the 1-soliton solutions are given by

$$\theta_{1,\mathrm{K}/\overline{\mathrm{K}}}(\tilde{x},\tilde{t}) = 2\arctan\left[e^{\pm\gamma(\tilde{x}-\tilde{v}\tilde{t})+\delta_0}\right], \tag{3.7}$$

where $\gamma = 1/\sqrt{1-\tilde{v}^2}$ denotes the Lorentz factor and $\tilde{v} = v/c$ the velocity of the relativistic soliton excitation in units of the spin wave velocity c, which plays the role of the speed of light. The different signs in the exponent correspond to kink (K) and antikink ($\overline{\mathrm{K}}$), respectively. δ_0 is a constant that is determined by the initial conditions. A derivation of the soliton solutions is given in Appendix D.

New soliton solutions can be generated from known solutions via transformations from one pseudospherical surface to another [140]. By application of such a transformation, known as a Bäcklund transformation, one can generate multiple-soliton solutions from the single soliton [141]. Important for this analysis is the "kink-antikink" (K$\overline{\mathrm{K}}$), 2-soliton solution [142]

$$\theta_{2,\mathrm{K}\overline{\mathrm{K}}}(\tilde{x},\tilde{t}) = 2\arctan\left[\frac{\sinh\left(\frac{\tilde{v}\tilde{t}}{\sqrt{1-\tilde{v}^2}}\right)}{\tilde{v}\cosh\left(\frac{\tilde{x}}{\sqrt{1-\tilde{v}^2}}\right)}\right], \tag{3.8}$$

where the initial conditions have been chosen such that $\theta_{2,\mathrm{K}\overline{\mathrm{K}}}(\tilde{x}, \tilde{t} = 0) = 0$, corresponding to a perfectly ordered chain $\mathbf{n}(x) \equiv \hat{\mathbf{e}}_z$ with no defects. The K$\overline{\mathrm{K}}$ solution (3.8) therefore describes the creation of a soliton and anti-soliton at $x = 0$ at $t = 0$ that propagate outwards in opposite directions for $t > 0$. This situation is therefore similar to the creation of two spinons by a single spin flip in the $S = 1/2$ antiferromagnetic chain. The staggered magnetisations for outwards propagating solitons are shown in Fig. 3.1 and compared with point-like domain walls. A derivation of the 2-soliton solution is found in Appendix D.

Another class of 2-soliton solutions that satisfy the sine-Gordon equation (Eqn. 3.5) are the breathers [139, 142]. These can be obtained directly from the $\overline{\mathrm{K}}$K solution by analytic continuation to imaginary values of the velocity $\tilde{v}$. By doing so, one arrives at the breather solution

$$\theta_{2,\mathrm{B}}(\tilde{x}, \tilde{t}) = 2 \arctan \left[\frac{\sqrt{1 - \tilde{\omega}^2}}{\tilde{\omega}} \frac{\sin\left(\tilde{\omega}\tilde{t}\right)}{\cosh\left(\tilde{x}\sqrt{1 - \tilde{\omega}^2}\right)} \right]. \tag{3.9}$$

Such semiclassical breathers correspond to two domain walls which oscillate anharmonically within a maximum distance. Crucially, both the breather and K$\overline{\mathrm{K}}$ solutions have spatially-extended domain walls and so the annihilation of a soliton and an anti-soliton happens gradually (Fig. 3.1 (*b*)).

3.3 Soliton confinement

The theory of linear confinement of spinons in weakly coupled $S = 1/2$ antiferromagnetic chains with XXZ-Ising exchange anisotropy [115, 116, 133, 134] or of domain walls in quasi one-dimensional Ising ferromagnets [135] is based on the assumption that domain walls are point-like. In this case, the inter-chain frustration energy cost associated with the separation of two domain walls is simply proportional to the number of spins $N_y = |y|/a$ between two domain walls with distance $|y|$. This gives rise to a linear confinement potential $V(y) \simeq J_\perp S^2 n_\perp |y|/a$, where $n_\perp$ denotes the number of neighbouring chains and $J_\perp$ is the nearest-neighbour inter-chain coupling. The bound state spectrum obtained from a one-dimensional Schrödinger equation with an attractive linear potential indeed gives a convincing description of the experimental data [115, 116, 133–135].

Here this approach is generalised to describe the nonlinear confinement of spatially-extended soliton domain walls. This semiclassical path integral approach allows us to treat the finite width of domain walls and to drop the assumption of Ising alignment. As will be shown, in the limit of strong Ising anisotropy, the theory of linear confinement is recovered.

3.3.1 Effective confinement potential

For a given spin profile along the chain, described by a field $\theta(\tilde{x})$ and constant $\phi(\tilde{x}) = \phi_0$, the energy of the chain is given by

$$E_{\parallel} = \frac{\rho_S\sqrt{\kappa}}{2}\int_{-\infty}^{\infty} \mathrm{d}\tilde{x}\Big\{ \left(\partial_{\tilde{x}}\theta\right)^2 - \left(\cos^2\theta - 1\right) \Big\}, \tag{3.10}$$

where the energy of a fully polarised chain ($\theta(\tilde{x}) \equiv 0$), which diverges in the thermodynamic limit, is subtracted. The inter-chain coupling is treated at mean-field level, introducing the staggered magnetisation $M = \left|\langle \hat{S}^z_{i,m}\rangle\right|$. The resulting energy contribution per chain is given by

$$E_{\perp} = \frac{\rho_S}{2\sqrt{\kappa}} g_{\perp}\int_{-\infty}^{\infty} \mathrm{d}\tilde{x}\Big\{1 - \cos\theta\Big\}, \tag{3.11}$$

where the contribution for a fully polarised chain has again been subtracted and defined the coupling

$$g_{\perp} = \frac{2n_{\perp}MJ_{\perp}}{a^2SJ}, \tag{3.12}$$

with $n_{\perp}$ the number of neighbouring chains and $J_{\perp}$ the inter-chain coupling. Because of the dependence on the magnetic order parameter M, the coupling $g_{\perp}$ vanishes above T_{N}.

The effective confinement potential $V(y)$ between a soliton and an anti-soliton can be obtained by evaluating the total energy $E_{\parallel} + E_{\perp}$ for the $\mathrm{K\overline{K}}$ solution (Eqn. 3.8) at given times t_0 corresponding to a distance $y = 2vt_0$ between the domain walls.

Note that $\theta_{2,\mathrm{K\overline{K}}}$ is obtained for $g_{\perp} = 0$, neglecting the feedback of the inter-chain coupling on the soliton dynamics of the spin chain. This approximation is justified in the limit $J_{\perp} \ll J$ or slightly below the ordering temperature where $M \ll 1$. For larger $g_{\perp}$ one would have to self-consistently determine the soliton solutions in the presence of the mean field from ordered neighbouring chains. In this case the equation of motion is a double sine-Gordon equation which is not, in general,

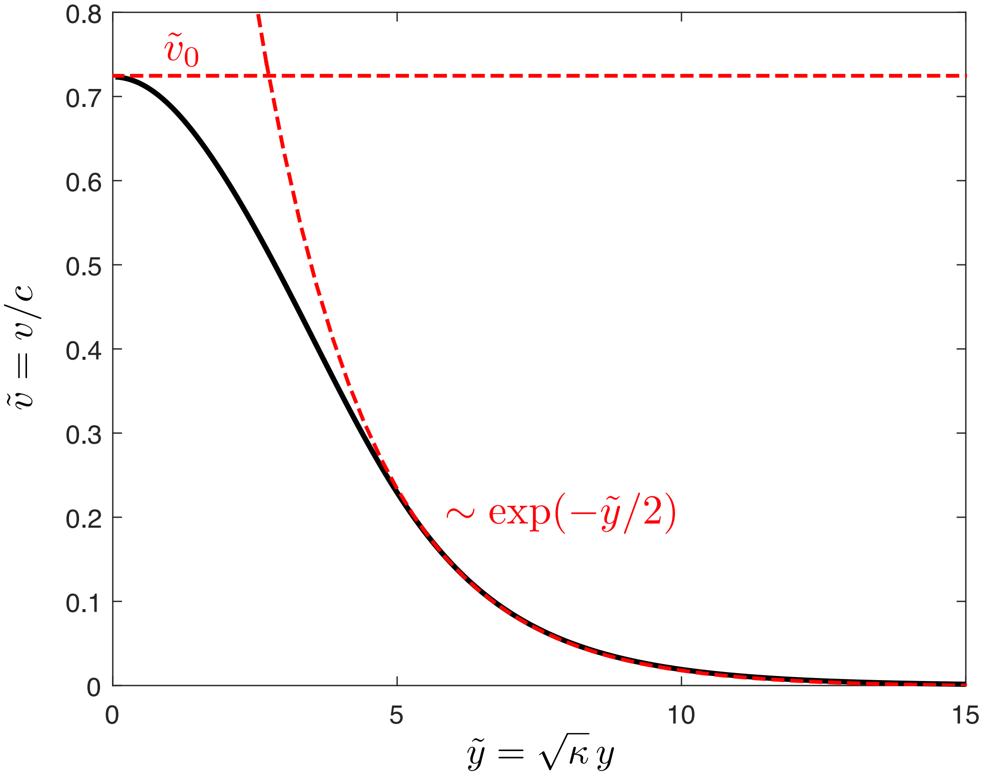

Figure 3.2 *Optimum dimensionless soliton velocity, $\tilde{v} = v/c$, as a function of dimensionless domain wall separation $\tilde{y}$, obtained by minimising $V_\parallel(\tilde{y})$ with respect to $\tilde{v}$.*

integrable but nonetheless can be solved numerically [143, 144].

Using the solution $\theta_{2,\mathrm{K}\overline{\mathrm{K}}}$ of the isolated chain, the confinement potential $V(y) = V_\parallel(y) + V_\perp(y)$ can be computed analytically. As a function of the dimensionless separation $\tilde{y} = \sqrt{\kappa}y$

$$\begin{aligned} \frac{V_\parallel(\tilde{y})}{E_0} &= \sqrt{1-\tilde{v}^2}\frac{A(\tilde{y})^2}{1+A(\tilde{y})^2}\left(1+\frac{\mathrm{arcsinh}A(\tilde{y})}{A(\tilde{y})\sqrt{1+A(\tilde{y})^2}}\right) \\ &\quad + \frac{1}{\sqrt{1-\tilde{v}^2}}\left(1-\frac{\mathrm{arcsinh}A(\tilde{y})}{A(\tilde{y})\sqrt{1+A(\tilde{y})^2}}\right) \qquad (3.13) \\ \frac{V_\perp(\tilde{y})}{E_0} &= \frac{g_\perp}{\kappa}\sqrt{1-\tilde{v}^2}\frac{A(\tilde{y})\mathrm{arcsinh}A(\tilde{y})}{\sqrt{1+A(\tilde{y})^2}}, \qquad (3.14) \end{aligned}$$

where the potential has been normalised by the rest energy

$$E_0 = mc^2 = 2\rho_S\sqrt{\kappa} \tag{3.15}$$

of a single soliton and the function $A(\tilde{y}) = \tilde{v}^{-1}\sinh(\tilde{y}/2\sqrt{1-\tilde{v}^2})$ has been defined.

The effective potential still depends on the dimensionless velocity $\tilde{v}$. This parameter can be expressed as a function of the domain wall separation $\tilde{y}$ if the energy of the isolated chain, $E_\parallel = V_\parallel(\tilde{y})$, is minimised with respect to $\tilde{v}$. The resulting function $\tilde{v}(\tilde{y})$ is determined numerically and plotted in Fig. 3.2. While for $\tilde{y} \to 0$ the velocity approaches a constant $\tilde{v}_0 \approx 0.725$, for large domain wall separations the velocity decays exponentially, $\tilde{v} \simeq 2.85 \exp(-|\tilde{y}|/2)$.

The asymptotic behaviour of the contributions $V_\parallel$ (Eqn. 3.13) and $V_\perp$ (Eqn. 3.14) to the potential is first investigated. At large distances ($|\tilde{y}| \to \infty$), the intra-chain contribution $V_\parallel(\tilde{y})$ approaches the energy $2E_0$ of two free solitons at rest, while the inter-chain contribution grows linearly,

$$\frac{V_\perp(\tilde{y})}{E_0} \approx \frac{g_\perp}{\kappa}|\tilde{y}|. \tag{3.16}$$

This is the same behaviour as for point-like domain walls. This is expected since at large distances the spatial extent ξ of the solitons becomes irrelevant. Expressed in terms of the microscopic parameters, using Eqns. 3.3, 3.12 and the definition of E_0 (Eqn. 3.15),the asymptotic result can be expressed in terms of the microscopic parameters to recover $V \sim n_\perp J_\perp |y|/a$.

At small separations ($\tilde{y} \ll 1$), both contributions are quadratic,

$$\begin{aligned} \frac{V_\parallel(\tilde{y})}{E_0} &\approx \frac{4 - 3\tilde{v}_0^2}{6\tilde{v}_0^2\sqrt{1-\tilde{v}_0^2}^3}\tilde{y}^2 \approx 2.35\,\tilde{y}^2, & (3.17) \\ \frac{V_\perp(\tilde{y})}{E_0} &\approx \frac{1}{4\tilde{v}_0^2\sqrt{1-\tilde{v}_0^2}}\frac{g_\perp}{\kappa}\tilde{y}^2 \approx 0.69\frac{g_\perp}{\kappa}\tilde{y}^2, & (3.18) \end{aligned}$$

which is the result of the gradual annihilation of the extended soliton and anti-soliton.

The intra-chain contribution $V_\parallel(\tilde{y})$ and the full confinement potential $V(\tilde{y}) = V_\parallel(\tilde{y}) + V_\perp(\tilde{y})$ are shown in Fig. 3.3 as a function of the dimensionless domain wall separation $\tilde{y} = \sqrt{\kappa}y$. They display the asymptotic behaviour discussed above. The crossover from linear to quadratic behaviour of $V(\tilde{y})$ occurs at $\tilde{y} = 1$. Since the crossover is expected to occur when the solitons start to overlap (Fig. 3.1 (*b*)), the size of the solitons can be identified as

$$\xi \simeq \frac{1}{\sqrt{\kappa}} = a\sqrt{\frac{J}{2\alpha}}. \tag{3.19}$$

This equation shows that the size of the solitons is controlled by the relative strength of the Ising anisotropy, α/J. In the case of strong Ising anisotropy, the size of the solitons is of the order of the lattice spacing a. On the other hand, in systems with very weak anisotropy, the spatial extent of soliton domain walls can be of the order of hundreds of lattice spacings.

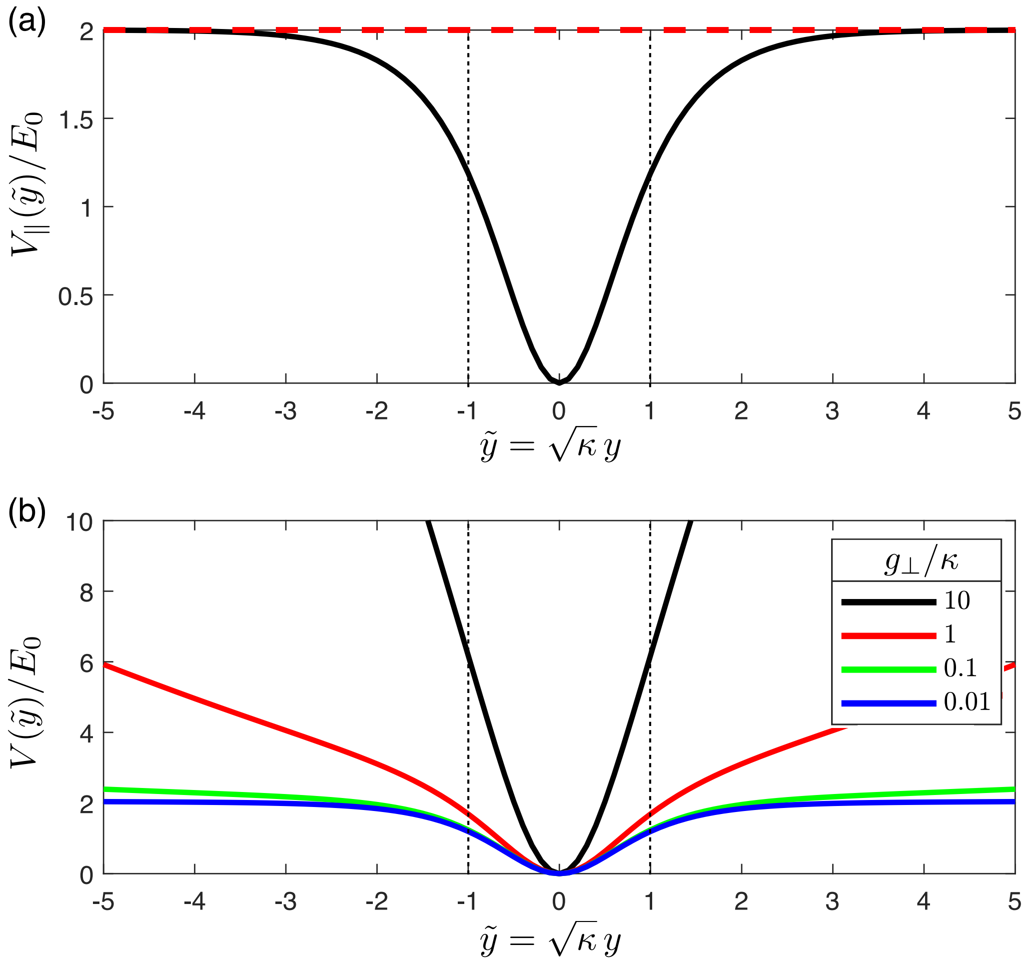

Figure 3.3 *(a) In-chain* $\mathrm{K}\overline{\mathrm{K}}$ *potential* $V_{\parallel}(\tilde{y})$ *as a function of dimensionless separation* $\tilde{y} = \sqrt{\kappa}y$*. At large separations,* $V_{\parallel}$ *approaches the energy* $2E_0$ *of two free solitons. Due to the gradual destructive interference of the solitons,* $V_{\parallel}$ *is rendered quadratic at small distances. The crossover occurs at* $\tilde{y} = 1$*, corresponding to a soliton size* $\xi = 1/\sqrt{\kappa}$*. (b) The same crossover is found in the effective confinement potential* $V(\tilde{y}) = V_{\parallel}(\tilde{y}) + V_{\perp}(\tilde{y})$*. At large separations the potential is linear,* $V(\tilde{y})/E_0 \approx (g_{\perp}/\kappa)|\tilde{y}|$*, while at small separations the potential is quadratic due to the gradual annihilation of the extended solitons.*

3.3.2 Bound state spectrum

The gradual destructive interference of extended solitons at separations $y < \xi$ weakens the confinement potential and renders it quadratic. In the following the solitons will be considered as point-like particles interacting with the effective nonlinear potential $V(y)$ and determine the discrete bound state spectrum from the solution of the one-dimensional Schrödinger equation

$$-\frac{\hbar^2}{2\mu}\frac{\mathrm{d}^2\psi}{\mathrm{d}y^2} + V(y)\psi = \epsilon\psi \tag{3.20}$$

for the effective one-body problem for the relative coordinate y of the soliton pair. Here $\mu = m/2$ denotes the reduced mass in terms of the single-soliton mass m.

As a point of reference, the limit of very strong Ising anisotropy is first considered. In this case the potential is linear down to lattice scale, $V(y) = \lambda|y|$, and the theory of linear confinement [115, 116, 133–135] applies. The resulting bound state energies are given by [134]

$$\epsilon_j^{>} = 2E_0 + \xi_j \lambda^{2/3}\left(\frac{\hbar^2}{\mu}\right)^{1/3}, \tag{3.21}$$

where ξ_j are the negative zeros of the Airy function, $\mathrm{Ai}(-\xi_j) = 0$, $\xi_1 \approx 2.338$, $\xi_2 \approx 4.088$, $\xi_3 \approx 5.520$, ...

In the limit of very weak anisotropy on the other hand, the confinement potential is quadratic over a significant range, $V(y) \simeq \frac{1}{2}\mu\omega^2 y^2$, giving rise to equidistant energy levels

$$\epsilon_j^{<} = \hbar\omega\left(j + \frac{1}{2}\right). \tag{3.22}$$

Due to the crossover of $V(y)$ from quadratic behaviour at short distances to linear behaviour at large distances, a related crossover in the energy level spacing of the bound states is expected. The strongly bound states at low energies will be almost equidistant, as described by $\epsilon_j^{<}$ (Eqn. 3.22), while the weakly bound states at higher energies will approach the sequence $\epsilon_j^{>}$ (Eqn. 3.21). This crossover is controlled by the strength of the Ising anisotropy α/J.

In order to obtain the bound state spectrum for the full confinement potential

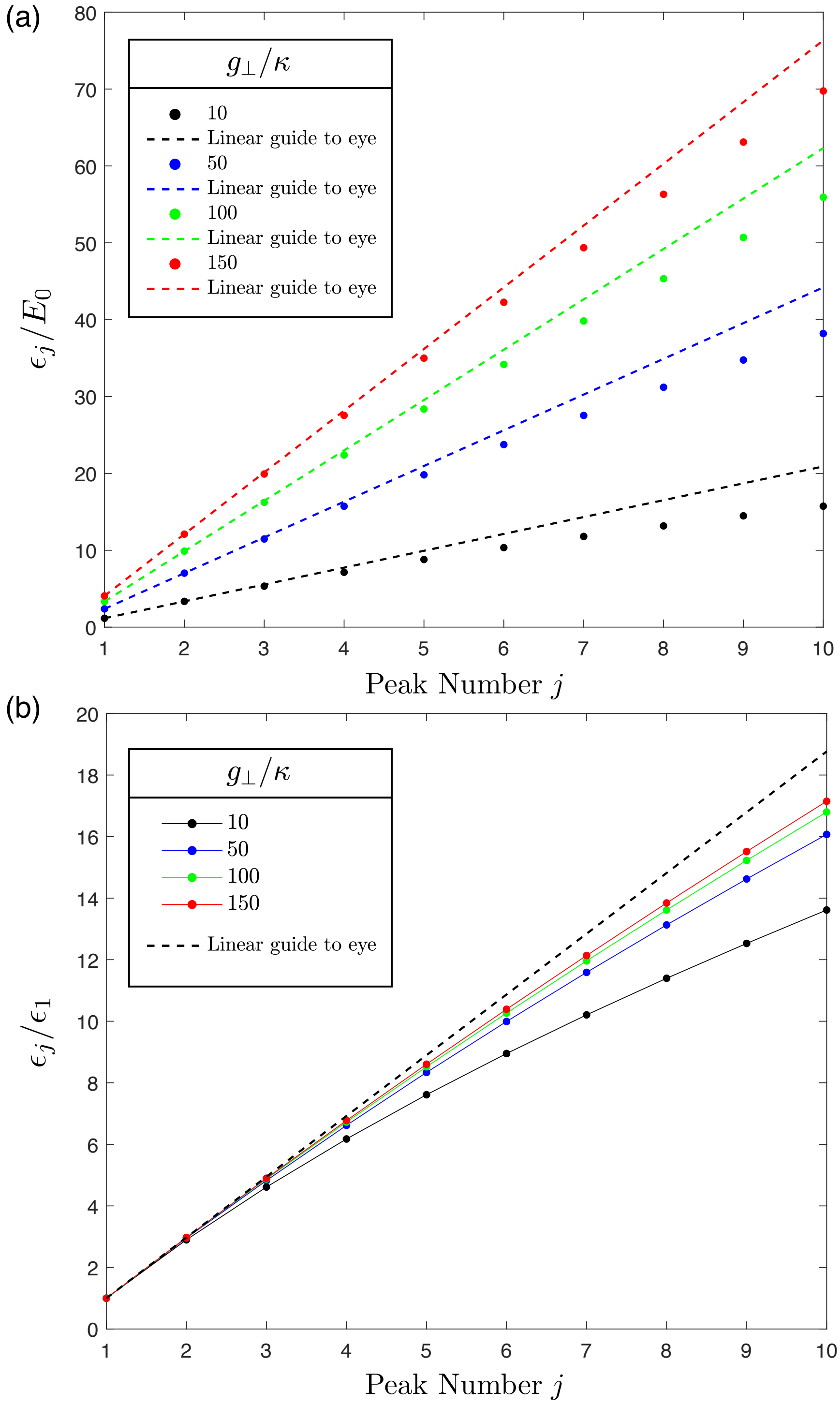

Figure 3.4 *(a) Soliton-antisoliton bound state energies* ϵ_j *in units of the single soliton energy* E_0 *for different ratios* $g_\perp/\kappa$ *and* $S = 5/2$*. The corresponding confinement potentials are shown in the inset. (b) The same spectra but normalised by the energy* ϵ_1 *of the first bound state. For larger values of* $g_\perp/\kappa$ *the level spacing becomes more harmonic oscillator like (dashed line).*

the Schrödinger equation (Eqn. 3.20) is transformed to dimensionless units,

$$-\frac{1}{2S^2}\frac{\mathrm{d}^2\psi}{\mathrm{d}\tilde{y}^2} + \tilde{V}(\tilde{y})\psi = \tilde{\epsilon}\psi, \tag{3.23}$$

with $\tilde{y} = \sqrt{\kappa}y$, $\tilde{\epsilon} = \epsilon/E_0$ and $\tilde{V}(\tilde{y}) = V_{\parallel}(\tilde{y})/E_0 + V_{\perp}(\tilde{y})/E_0$. The potential functions are defined by Eqn. 3.13 and Eqn. 3.14. The Schrödinger equation is then numerically solved using the finite-element method implemented in Mathematica [145].

In Fig. 3.4 (*a*) the resulting bound state energies ϵ_j/E_0 for $S = 5/2$ (value for $CaFe_2O_4$) and different values of $g_{\perp}/\kappa$ are shown. In the regime of large $g_{\perp}/\kappa$, the dominant contribution to the confinement potential comes from the frustrated inter-chain coupling. The tightly bound states have almost equidistant energy levels with spacing $\Delta\epsilon/E_0 \approx (1.17/S)\sqrt{g_{\perp}/\kappa}$, as expected for the asymptotic quadratic form of the potential at small distances, $\tilde{V}(\tilde{y}) \approx \tilde{V}_{\perp}(\tilde{y}) \approx 0.69(g_{\perp}/\kappa)\tilde{y}^2$. At higher energies, the level spacing is reduced because of the crossover of the potential to a linear form at large distances. Normalising the energies by the energy ϵ_1 of the first bound state (Fig. 3.4 (*b*)), it is apparent that the spectrum becomes more like that of a harmonic oscillator if the value of $g_{\perp}/\kappa$ is increased.

3.4 Application to calcium ferrite

In this section the theory of nonlinear soliton confinement will be applied to the $S = 5/2$ antiferromagnet $CaFe_2O_4$. Recent neutron scattering experiments [11] found signatures of solitary magnons in this material with a sequence of nine quantised excitations below the magnetic ordering transition at $T_N \approx 200$ K.

$CaFe_2O_4$ has a complex magnetic phase diagram due a competition between two different spin arrangements, termed the A and B phases [146]. The magnetic structure of the B phase, which dominates at high temperatures, consists of antiferromagnetic zig-zag chains along the *b* axis (Fig. 3.5). The moments are oriented along *b* due to a small easy-axis anisotropy. In Fig. 3.5 only the two shortest bonds are plotted to illustrate the antiferromagnetic zig-zag chain pattern formed by the magnetic ions in the B phase. A full analysis of the nature of the magnetic interactions in $CaFe_2O_4$ is given in Chapter 5.

The A phase might coexist with the B phase over the full temperature range but becomes clearly visible only below 170 K, which has been identified as its onset temperature in early studies [146]. The two phases are distinguished by their c-axis stacking of ferromagnetic b-axis stripes: the B phase consists of stripes with antiferromagnetic alignment within the zig-zag chain, (↑↓)(↑↓), while in the A phase the zig-zag chains are ferromagnetic with stacking (↑↑)(↓↓) along c [146]. It has been suggested [11] that the gradual increase of the A phase component is linked to antiphase domain boundaries along c, combined with a continuous change of the Fe-O-Fe bond angle which controls the strength and sign of the superexchange [147, 148] between the two legs forming the zig-zag chain. This scenario is supported by the presence of diffuse scattering rods along the L direction and spin wave excitations that show magnetic order in the ab-plane with short-ranged correlations along c [11]. The magnetic order in $CaFe_2O_4$ will be investigated further in Chapter 5 using neutron scattering and complementary theoretical analysis.

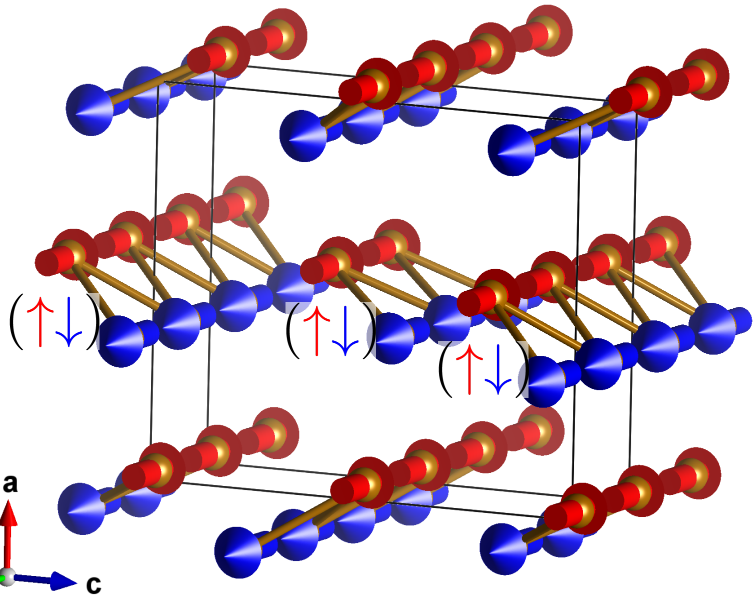

Figure 3.5 *Magnetic structure in the high temperature B phase of* $CaFe_2O_4$ *[11], showing antiferromagnetic zig-zag chains along the* b *axis. The system exhibits a weak easy-axis anisotropy along* b*. Calcium ferrite is based upon an orthorhombic unit cell (space group 62 Pnma) with dimensions* $a = 9.230$ *Å,* $b = 3.017$ *Å, and* $c = 10.689$ *Å[12, 13].*

From now on, focus is concentrated on the B phase that completely dominates at high temperatures where the discrete excitations are observed. As pointed out in Ref. [11], the level spacing of the excitations cannot be explained based on the linear confinement picture. This led the authors to speculate that the discrete nature of the excitations is not due to interaction-driven bound state formation but instead a result of spatial confinement along the *c*-axis. Here it is shown that an effective nonlinear interaction potential arising from the extended nature of solitons in $CaFe_2O_4$ would lead to a bound state spectrum that is consistent with the data.

The discrete energy-level spectrum presented in Ref. [11] is first inspected more closely. The excitations can only be observed above the spin wave anisotropy gap, which shows a strong temperature dependence. The gap opens below $T_\mathrm{N} \approx 200$ K and saturates to a value of $\Delta \approx 3$ meV below 100 K. For this reason, the lowest energy excitation can only be resolved slightly below T_N where strong fluctuations almost completely fill in the gap. The data at 200 K show six discrete energy levels below 2 meV. At 150 K the spin wave gap almost completely masks this energy range. Instead three energy levels become visible above around 1.8 meV. In Ref. [11] it was assumed that the discrete excitations energies have a negligible temperature dependence and that the three levels observed at 150 K are the continuation of the energy sequence at 200 K.

If the discrete excitations were due to soliton bound state formation one would expect the excitation spectrum to depend on temperature. Based on this theory, it is expected that the main temperature dependence enters through the effective mean-field coupling $g_\perp$ to neighbouring chains. Since $g_\perp$ is proportional to the magnetisation of the system, it increases as temperature is lowered and the magnetisation saturates. This would explain why the bound states at 150 K have a larger level spacing than those at 200 K.

Moreover, magnetoelastic effects and small changes to the Fe-O-Fe bond angle close to the threshold at which the superexchange would change sign could give rise to a non-negligible temperature dependence of magnetic exchange couplings [24]. Finally, the gradual onset of the A phase could give rise to additional effects which might obscure the soliton signal in the neutron scattering experiment.

3.4.1 Experimental results

Here are presented previously unpublished data that were collected alongside those published in Ref. [11] by C. Stock and collaborators. Instead of combining measurements at different temperatures, focus is concentrated on $T = 200$ K, allowing the consideration of excitations down to very low energies. This also mitigates against any potential temperature dependence of the bound state spectrum.

The experiments were performed on single crystals of $CaFe_2O_4$ grown using a mirror furnace. High momentum and energy resolution data was obtained using the OSIRIS backscattering spectrometer located at the ISIS Neutron and Muon Source [10]. A white beam of neutrons was incident on the sample and the final energy of the scattered neutrons was fixed at $E_f = 1.84$ meV using cooled graphite analysers. A cooled beryllium filter was used on the scattered side to reduce background. The default configuration is set for a symmetric dynamic range of ± 0.5 meV, however by shifting the incoming energy band width using a chopper the dynamic range was extended into the inelastic region. For this experimental setup, the elastic energy resolution (full-width) was $2\delta E = 0.025$ meV. Due to kinematic constraints, the measurements are focused around $\mathbf{Q} = (2, 0, 0)$ (r.l.u) so that the quantised excitations could be tracked up to energy transfers of $\sim$ 3 meV.

As shown in Fig. 3.6 (a), at 200 K, there are seven discrete excitations in low energy scattering data below 2 meV, located at $\mathbf{Q} = (2, 0, 0)$ and with a weak quadratic dispersion along L. The intensities are integrated over a small window of 2 ± 0.05 r.l.u. in the H direction. The excitations have an almost linear level spacing $\Delta\epsilon \approx 0.3$ meV, in very good agreement with previous results [11].

In comparison, at 125 K the spin wave gap masks the excitations below 2 meV but three discrete excitations at $\tilde{\epsilon}_1$, $\tilde{\epsilon}_2$ and $\tilde{\epsilon}_3$ are visible above this energy (Fig. 3.6 (b)). The modes are at slightly higher energies than those identified at 150 K in Ref. [11], suggesting that there might exists a non-negligible temperature dependence. In the following, the excitations above 2 meV are discarded since they cannot be resolved at 200 K.

In Fig. 3.6 (c), the scattering intensity at 200 K as a function of energy at $\mathbf{Q} = (2, 0, 0)$ is shown. Peaks at the energy levels $\epsilon_2, \ldots \epsilon_7$ are very clearly visible. The first excitation ϵ_1 is beneath the incoherent background in the OSIRIS data and cannot be resolved in the energy cut. However, the energy ϵ_1 can be estimated thanks to the weak quadratic dispersion along L (see dashed yellow lines in Fig. 3.6 (a)).

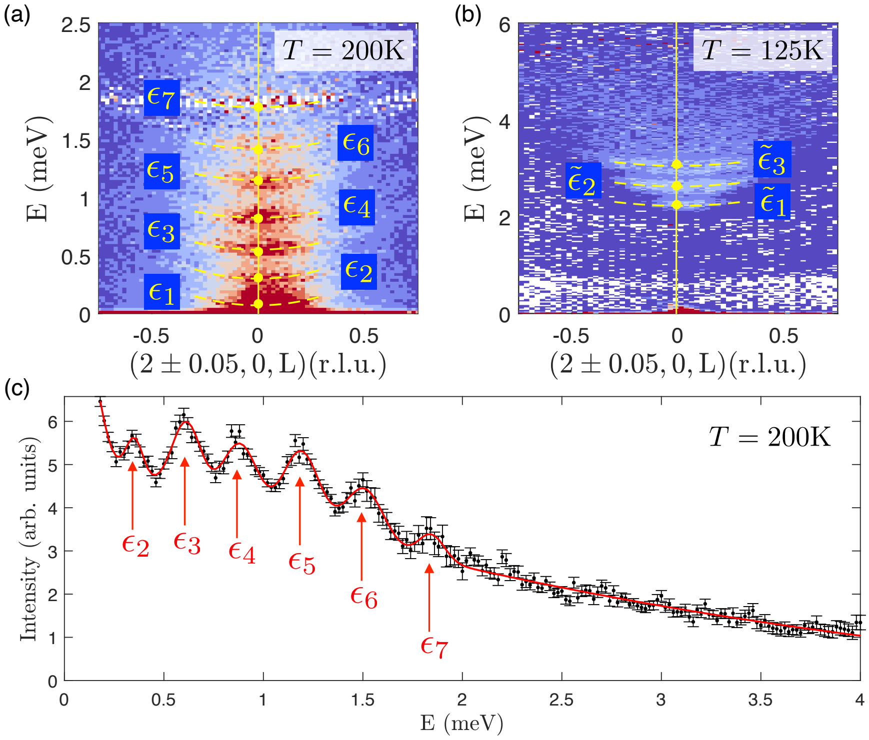

Figure 3.6 *(a) High resolution low energy data recorded on OSIRIS at* $T = 200$ *K, showing seven clearly discernible excitations* ϵ_j *at* $\mathbf{Q} = (2,0,0)$ *(r.l.u.). The modes show a weak quadratic dispersion along L, highlighted by dashed yellow lines. (b) At* $T = 125$ *K the spin wave gap masks excitations below 2 meV. Above this energy, three additional excitations* $\tilde{\epsilon}_j$ *are visible. (c) Scattering intensity at* $\mathbf{Q} = (2,0,0)$ *as a function of energy. Peaks at* $\epsilon_2, \ldots, \epsilon_7$ *are clearly resolved. The energy* ϵ_1 *is below the elastic line.*

3.4.2 Fitting to nonlinear confinement model

It is now investigated whether the seven discrete excitations measured at 200 K can be explained in terms of soliton bound state formation. In this section, the one-dimensional soliton confinement model is applied to the case of $\mathrm{CaFe_2O_4}$. Despite the convenience of such a description, it should be noted that the magnetic interactions in $\mathrm{CaFe_2O_4}$ are more consistent with two-dimensional zig-zag networks which are weakly coupled along the *c*-axis (as described in Chapter 5). Nonetheless, the nonlinear σ model can be trivially extended to higher spatial dimensions [137], yielding a sine-Gordon equation in $d + 1$ dimensions. Neglecting the effect of damping, the solutions of the equation of motion in 2+1 dimensions are solitons with a number of different two-dimensional geometries such as lines and circular or elliptical rings [149–152]. Crucially, the domain wall profile takes the shape of a soliton and the solutions can be considered to behave as extended one-dimensional solitons [150]. In the construction of the nonlinear confinement potential, one takes the difference between the maximally polarised state and the soliton-populated state and hence one is sensitive to the domain wall profile which takes the same shape as in the one-dimensional case. Therefore it should be expected that the physics in higher dimensions is qualitatively similar to the one-dimensional case. Owing to its qualitative similarity and conceptual simplicity, in this chapter the one-dimensional model will be applied to the case of $CaFe_2O_4$.

The quantised excitations ϵ_j extracted from the neutron scattering experiment are shown as open circles in Fig. 3.7. For the levels $j = 2, \dots, 7$ the experimental error $\delta\epsilon_j$ is estimated from the full peak width at half maximum. For the lowest energy state, which is masked by the incoherent background of the elastic line, a larger uncertainty of $\delta\epsilon_1 \approx 0.15$ meV is assumed, given that the bottom of this mode is estimated from the dispersion away from the zone centre.

As point of reference, a linear confinement potential is first assumed. In this case the soliton bound state energies would be given by $\epsilon_j = A + B\xi_j$, where ξ_j are the negative zeros of the Airy function and the energies A and B are related to the soliton rest mass and the slope of the linear potential, as defined in Eqn. 3.21. Here A and B are used as free fitting parameters, not imposing any additional constraints. The resulting best case scenario for the linear-confinement model (dashed magenta line in Fig. 3.7) strongly deviates from the data, showing that the discrete excitations in $CaFe_2O_4$ cannot be understood in terms of a linear confinement of solitons.

The bound state spectra obtained from the effective nonlinear confinement potential depend on two parameters, the soliton rest energy $E_0 = 2\rho_S\sqrt{\kappa}$ and the dimensionless ratio $g_\perp/\kappa$. For a given value of $g_\perp/\kappa$ the best fit to the data $\{\epsilon_j \pm \delta\epsilon_j\}$ is obtained by minimising

$$\chi^2 = \sum_j \left(\frac{\epsilon_j^{\text{th}}(E_0) - \epsilon_j}{\delta\epsilon_j} \right)^2 \tag{3.24}$$

with respect to E_0, where $\{\epsilon_j^{\text{th}}\}$ refers to the spectrum obtained from this theoretical model.

As shown in Fig. 3.7, the fits improve with increasing values of $g_\perp/\kappa$, corresponding to decreasing optimum values of E_0. A good description of the data is

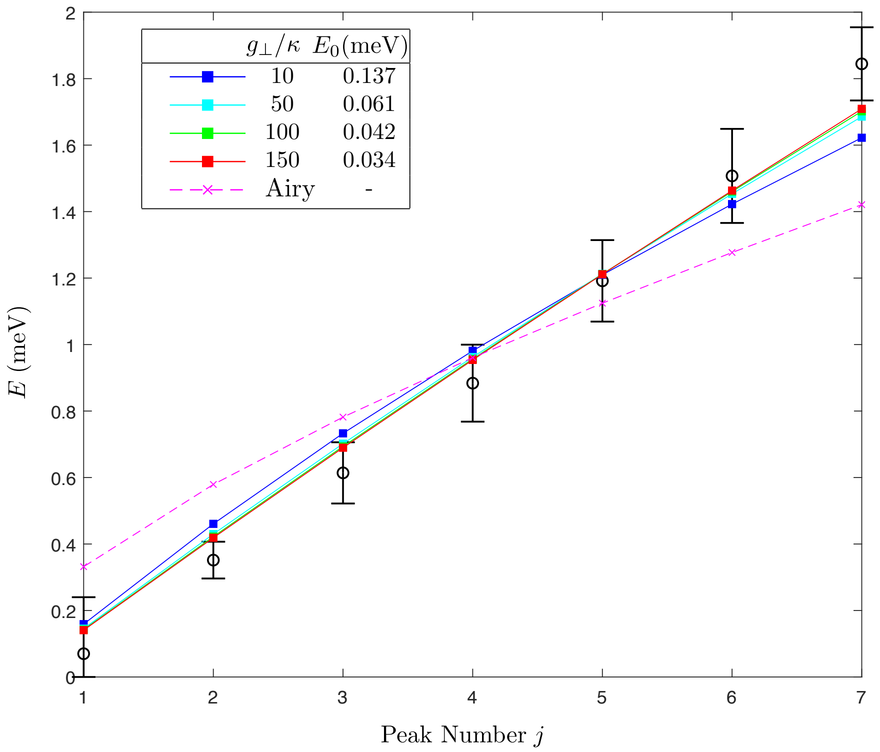

Figure 3.7 *Comparison between the measured excitation energies (open circles) and the soliton bound state energies calculated from the nonlinear confinement model. The figure shows best fits to the data for different values of $g_\perp/\kappa$. The quality of the fits improves with increasing values of $g_\perp/\kappa$ and decreasing soliton energy E_0. Good agreement is achieved for $g_\perp/\kappa \geq 50$. For comparison, the best fit of the linear confinement model is shown in magenta.*

obtained for $g_\perp/\kappa = 50$ and $E_0 = 0.061$ meV. Although for larger values of $g_\perp/\kappa$ the fits continue to improve slightly, the soliton size $\xi = 1/\sqrt{\kappa} = 2\rho_S/E_0$ would eventually become too large for this theoretical description to be valid.

For $g_\perp/\kappa = 50$ the levels are almost equidistant, showing that the first seven levels fall in the harmonic potential regime. To check consistency, the average mean-square displacement of the soliton bound states, $d_j = \sqrt{\langle \hat{y}^2 \rangle_j}$, is calculated using the approximate quadratic potential (Eqn. 3.17) at small distances, $y < \xi$. For the highest level resolved experimentally $d_7/\xi \approx 0.55 < 1$ is obtained, indicating a significant overlap of the bound solitons.

The parameters ρ_S, $g_\perp$ and κ describe the long-wavelength, low energy behaviour of the system. This effective continuum description is completely generic and applies to any system of weakly coupled antiferromagnetic spin chains in the the large-S limit.

For illustrative purposes, a minimal spin model (Eqn. 3.1) has been considered and established how the effective parameters in the continuum field theory depend on the exchange couplings and single-ion anisotropy of the lattice Hamiltonian (see Eqn. 3.3 and Eqn. 3.12). However, this model is too simplistic for $CaFe_2O_4$, e.g. it neglects the ferromagnetic exchange along the legs of the zig-zag chains, which is likely to be non-negligible. Unfortunately, spin wave excitations at T = 200 K, which would allow for an unambiguous determination of the spin wave stiffness in the regime considered in this chapter, have not been measured. Neutron scattering measurements performed at T = 175 K and T = 5 K are presented in Chapter 5, demonstrating the true nature of the magnetic order in $CaFe_2O_4$ and indicating that the nature of the magnetic interactions is more complicated than the simple chain model applied here.

However despite the simplifications used, close to the Néel transition collective fluctuations are very strong, leading to universal behaviour detached from microscopic details. The spin stiffness is expected to vanish continuously at T_{N}, satisfying Josephson scaling $\rho_S \sim (T_{\mathrm{N}} - T)^{(d-2)\nu}$ [153, 154], where ν is the correlation-length exponent and d the spatial dimension. The bound states are observed slightly below T_{N} where the stiffness is strongly reduced. If $\rho_S/a \approx 3$ meV is assumed, which is of the order of the gap and about a tenth of the spin wave bandwidth at low temperature, a soliton size of about 100 lattice constants, $\xi/a = 2(\rho_S/a)/E_0 \approx 100$ would be obtained.

As suggested in Ref. [11], quantised excitations in $CaFe_2O_4$ could also arise from antiphase boundaries along the c-axis that separate the two competing magnetic phases and lead to spatial confinement. This mechanism is unlikely to be relevant close to T_{N} where the phase boundaries are dynamic and the A phase is almost completely absent. At low temperatures, however, the antiphase domain boundaries become static and carry an uncompensated moment that can be tuned by a magnetic field [15]. The presence of uncompensated spins at phase or domain boundaries is also confirmed by thin-film experiments [155]. Isolated clusters of such orphan spins would provide a natural explanation of the discrete magnetic excitations observed at very low temperatures below the spin wave gap [15].

3.5 Conclusion

To summarise, a theory for the confinement of solitons in weakly coupled, large-spin antiferromagnetic chains with easy-axis anisotropy has been developed. Below the Néel transition the frustrated inter-chain coupling generates an attractive potential that leads to the formation of soliton-antisoliton bound states. This mechanism is analogous to the confinement of spinons in $S = 1/2$ antiferromagnetic XXZ chains [115, 116, 133, 134] or of domain wall kinks in ferromagnetic Ising chains [135]. But while for these systems the domain wall defects can be considered as point-like, leading to a linear confinement potential, semiclassical solitons have a significant spatial extent. This renders the effective confinement potential quadratic on length scales smaller than the size of the solitons, giving rise to a crossover in the energy level spacing of the bound states.

The $S = 5/2$ antiferromagnet $\mathrm{CaFe_2O_4}$ is a good candidate system to test this theory since this material shows a sequence of discrete low-energy excitations [11] below T_N and exhibits a magnetic structure that consists of antiferromagnetic zig-zag networks, subject to a weak Ising anisotropy [146]. The inelastic neutron scattering experiments, performed slightly below T_N, confirmed the existence of seven discrete excitations below 2 meV with an almost linear level spacing. This analysis shows that the quantised excitations can be explained well by the nonlinear confinement of large, spatially-extended solitons. It is argued that strong collective fluctuations close to T_N play a crucial role, collapsing the anisotropy gap and strongly reducing the spin stiffness.

There are many possible ways in which this theory can be extended to describe a rich variety of physical systems. To model materials with strong inter-chain coupling one can include the feedback of the effective field from neighbouring chains on the soliton dynamics. Such a staggered field changes the equation of motion to a double sine-Gordon equation which is no longer integrable but nonetheless can be solved numerically [143, 144]. Staggered fields could also be generated by applying external fields in systems with staggered g tensors [118, 119]. Since solitons and antisolitons have opposite chirality it would be interesting to study the effects of a weak Dzyaloshinskii-Moriya interaction which would introduce chirality in the antiferromagnetic background. Finally, one might include finite-lifetime effects due to collisions of bound soliton pairs and the interactions with spin wave excitations.

Thanks to recent advances in crystal growth and neutron scattering technology it is now possible to resolve soliton bound states at very low energies. The relevant theoretical parameters in the effective long-wavelength description, such as the spin stiffness, spin wave velocity and staggered magnetisation, vanish at the continuous Néel transition, showing characteristic power-law behaviour. The measurement of soliton bound states close to the transition could therefore provide a novel route to study universal critical behaviour in inelastic neutron scattering experiments.

Chapter 4

Metastable and localised Ising magnetism in α-CoV$_2$O$_6$ magnetisation plateaux

4.1 Introduction

In a classical Néel magnet, the magnetisation is expected to vary continuously with an applied field, rotating to align with the field direction in order to minimise the Zeeman energy. The situation is more complicated in quantum antiferromagnets [156, 157] and those exhibiting magnetic frustration [158] where the magnetisation-field curve can exhibit steps or plateaux, where $\hat{S}^z_{\text{total}} = \sum_i \hat{S}^z_i$ remains unchanged despite a varying applied magnetic field [159]. These plateaux often accompany phase transitions between long-range ordered plases [160–163]. In this chapter, the magnetisation of the $j_{eff} = \frac{1}{2}$ α-CoV$_2$O$_6$ in an applied field is analysed based on neutron diffraction measured by L. Edwards, C. Stock and S. Giblin and magnetisation data taken by C. Paulsen, E. LHotel and M. Songvilay. It will be shown that α-CoV$_2$O$_6$ exhibits a cascading series of spatially short-ranged periodicities which are characterised by a plateaux in the magnetisation data.

In insulating magnets, the presence of a plateau in the magnetisation indicates an energy gap in the spin wave spectrum. This is the case in $S = 1$ compounds which exhibit a Haldane gap [164–166]. Such a gap is not expected in $S = 1/2$

compounds like $KCuF_3$ which exhibit gapless spectra [167–169] in accordance with the Haldane conjecture [136]. Nonetheless, dimerised $S = 1/2$ magnets do display a spectral gap and hence can display magnetisation plateaux [170–172]. This is perhaps not so surprising if one views each strongly coupled dimer as an effective $S = 1$ subsystem whose spectrum comprises a singlet and three triplet states. On general grounds, based on the Lieb-Schultz-Mattis theorem [173], it has been proposed that analogous Haldane gapped phases are possible, even for half-integer spin systems [174]. These arguments can indicate the criteria for the observation of magnetisation plateaux and hence shed light on the nature of underlying magnetic interactions. This explanation has been advanced to predict spatially short-ranged dilute dimer phases in half-integer spins [175]. Other explanations for the observation of these magnetisation plateaux have been suggested, including order-by-disorder [176–178] – a mechanism whereby a ground state is selected through quantum fluctuations.

There have been a number of insulating compounds where magnetisation plateaux have been reported [179–193] as well as in materials with continuous symmetry [194–197] where field-induced magnetic transitions are observed. In many of these examples, the magnetisation steps define phase transitions between states with long-range magnetic correlations, which are accompanied by new Bragg peaks. These systems can generally be understood in terms of a magnetic Hamiltonian with competing exchange interactions, where the influence of the Zeeman field lowers the energy of a particular magnetically ordered state below that of the previous ground state. In this chapter another situation will be discussed – where the magnetisation plateaux are defined by short-range and metastable order, rather than long-range magnetic correlations. The experimental results will first be briefly discussed before the Lieb-Schultz-Mattis theorem is applied to α-CoV_2O_6 in order to understand the nature of magnetic order in this system.

α-CoV_2O_6 crystallises in the centrosymmetric monoclinic space group $C2/m$, with lattice parameters $a = 9.2283(1)$ Å, $b = 3.50167(5)$ Å, $c = 6.5983(1)$ Å, $\beta = 112.0461(7)^\circ$ differing from the triclinic γ-CoV_2O_6 polymorph [198], which exhibits two inequivalent Co sites. The structure is based on Co^{2+} $(S = 3/2, L = 2)$ ions sited on an anisotropic triangular motif [199–203]. The small exchange coupling between the spins relative to the anisotropy energy [14], is suggestive of an underlying Ising/uniaxial symmetry.

The Co^{2+} ions exist within a local environment of octahedrally coordinated oxygen ions. An intermediate crystal field, as is typical in the $3d$ ions, leaves an orbital triplet ground state [21]. The orbital triplet ground state is split by spin-orbit coupling, $\mathcal{H} = \alpha\lambda\mathbf{l}\cdot\mathbf{S}$, into $j_{eff} = \frac{1}{2}, \frac{3}{2}, \frac{5}{2}$ levels. The energy spacings of these j_{eff} levels, follow the Landé interval rule, with a $j_{eff} = \frac{1}{2}$ ground state separated from the $j_{eff} = \frac{3}{2}$ by $\Delta = \frac{3}{2}\alpha\lambda$ (Fig. 4.1). In α-CoV$_2$O$_6$ the spin-orbit coupling is observed to be much greater in magnitude than the exchange coupling strength $|\lambda| \gg |J|$ justifying the projection onto the $j_{eff} = \frac{1}{2}$ multiplet [204, 205], in contrast to the rocksalt CoO, where a large exchange constant induces strong mixing between the j_{eff} spin-orbit levels [206–208]. A local crystalline distortion further supports an Ising anisotropy in the spin orientation [209, 210], evidenced by a gap in the neutron scattering spectrum [14] and and a critical scaling exponent consistent with Ising symmetry.

4.2 Experiment

4.2.1 Experimental setup

In this section, the experimental results of L. Edwards, C. Stock and S. Giblin will be briefly summarised in order to set the scene for a discussion of the magnetic order present in α-CoV$_2$O$_6$. Further experimental details can be found in Ref. [2]. Flux-grown single crystals [211] and powder samples [212] were characterised using the WISH (ISIS, UK) [213] diffractometer. Kinematic constraints on WISH combined with the magnetic field and detector layout required that the field have a significant b-axis component in order that the reciprocal space around the $(10\frac{1}{2})$ magnetic Bragg peak could be accessed. A refinement of the UB matrix from nuclear and magnetic Bragg peaks indicated that the the vertical magnetic field was orientated with components of 2.1°, 15.2° and 85.3° along the a, b and c axes respectively. Further measurements were carried out on the cold triple-axis spectrometer RITA II (PSI, Switzerland) [214] using a horizontal magnet such that the field could be aligned along the c-axis. $E_i = E_f = 5.0$ meV was chosen for the diffraction experiment, with the sample in a dilution fridge so that temperatures of less than 1 K could be achieved. Further diffraction measurements were also performed on the TASP spectrometer (PSI, Switzerland) on a pressed pellet powder sample with $E_i = E_f = 3.0$ meV. The magnetisation experiments were performed by colleagues at the Insitut Néel using a low temperature superconducting quantum interference device (SQUID) and a

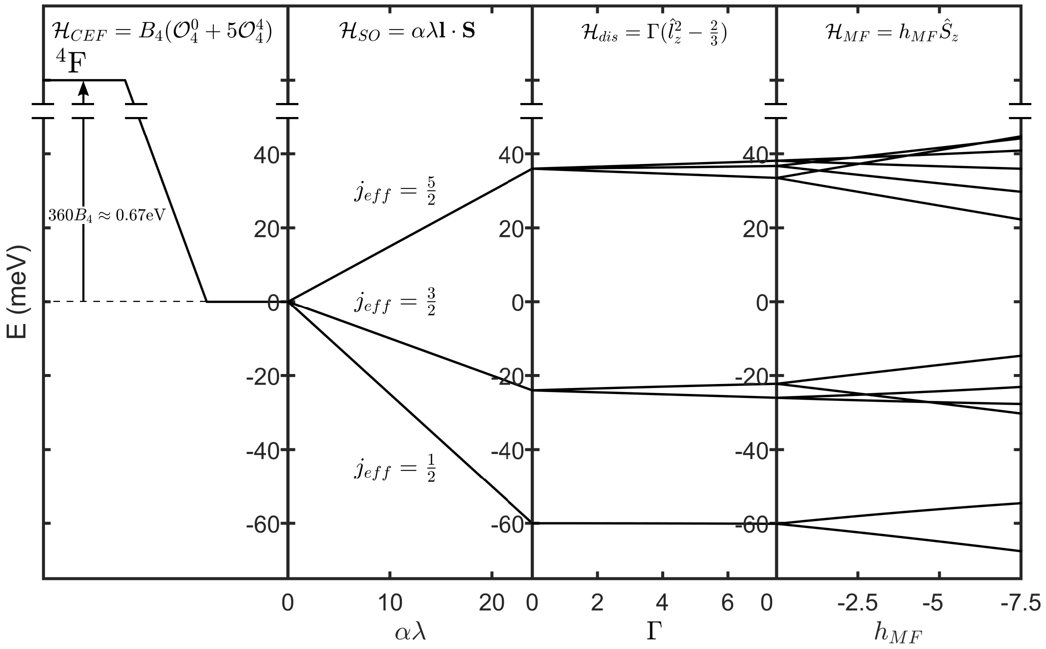

Figure 4.1 *Single-ion energy levels in Co^{2+}. In an intermediate octahedral field the ^4F ground state is split, with an orbital triplet ground state. The effect of spin-orbit coupling splits this triplet into three j_{eff} levels, with a $j_{eff} = \frac{1}{2}$ ground state. A tetragonal distortion, related to an elongation of the octahedron has no effect on the ground state manifold. Finally, the application of a molecular mean field, arising due to inter-ion coupling, splits the two-fold degeneracy of the ground state. Maximal values of Γ and $\alpha\lambda$ have been taken from Ref. [14]. Spin wave excitations were observed to be resolution limited and it was estimated that $J/\lambda \approx 0.05$ which would likely lead to a mean field on the lower end of the plotted range. The $j_{eff} = \frac{1}{2}$ is well separated from the excited levels, justifying the projection onto the $j_{eff} = \frac{1}{2}$ manifold.*

Physical Properties Measurement System (PPMS).

4.2.2 Results

The WISH results on the single crystal samples in the $(h0l)$ scattering plane are shown in Figs. 4.2$(a-c)$[1]. Fig. 4.2(a) shows data measured at T = 0.1 K and μ_0H = 0.015 T after zero-field cooling. A peak is observed at $\mathbf{k} = (10\frac{1}{2})$ consistent with a doubling of the unit cell along the c-axis. Here the notation

---

[1] The WISH data have been background-subtracted using a high magnetic field measurement (μ_0H=6 T). In such a scan, the magnetic moment is saturated hence it can be used as a measure of background due to the instrument and sample environment.

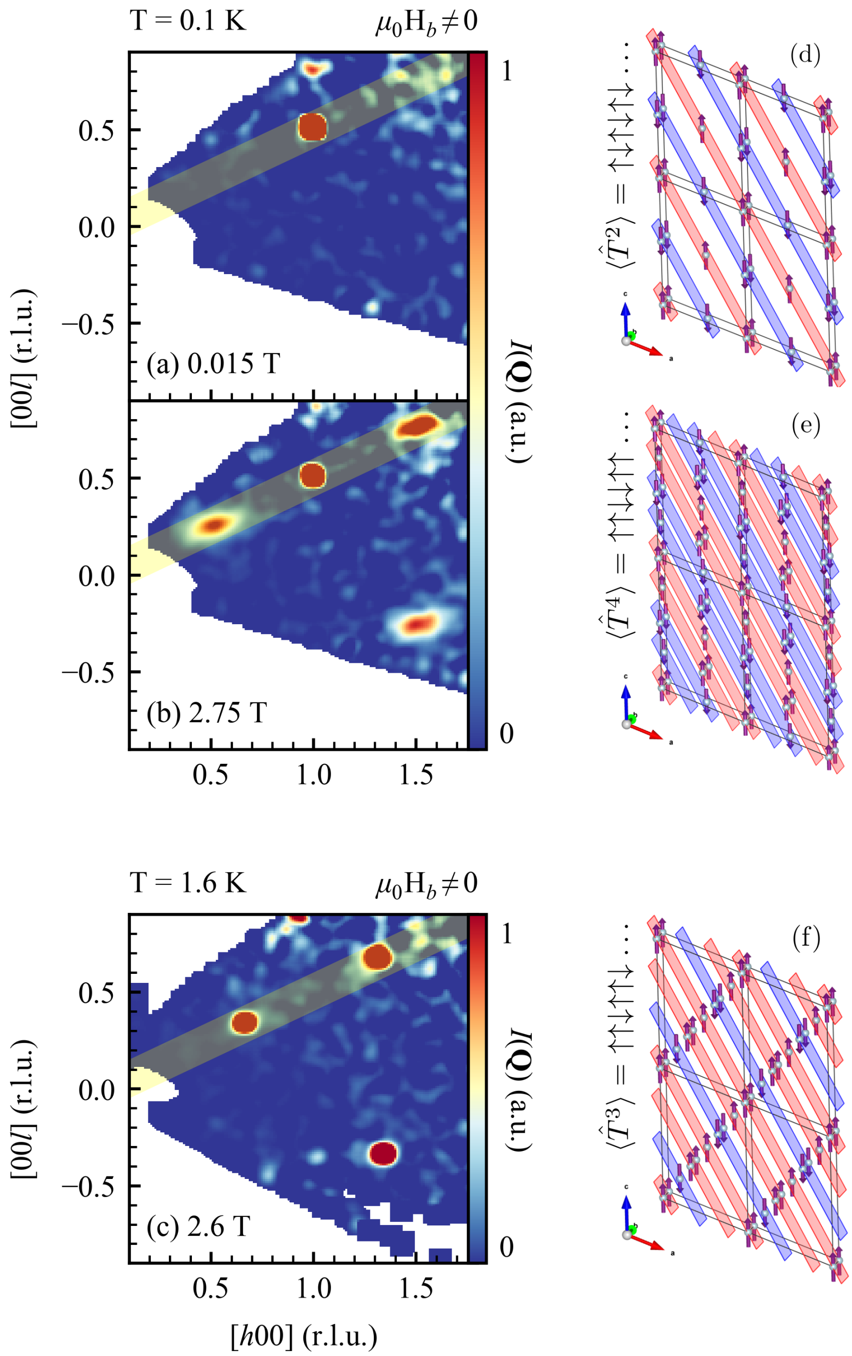

Figure 4.2 *Low temperature (T = 0.1 K) diffraction maps on single crystal* CoV_2O_6 *at (a)* $\mu_0\mathrm{H} = 0.015$ T *and (b)* $\mu_0\mathrm{H} = 2.75$ T *starting from a zero field cooled state. (c) Scan at* T = 1.6 K *at* $\mu_0\mathrm{H} = 2.6$ T*. Yellow regions indicate the cut directions. The corresponding magnetic periodicity is shown for each scan in panels* $(d - f)$*, with moment directions fixed to that of the refined zero field structure. Figure reproduced from Ref. [2].*

$\langle \hat{T}^q \rangle$ is introduced to represent the translational symmetry of a given periodicity in real space, with $\langle \hat{T}^2 \rangle = \uparrow\downarrow$ representing a doubling of the real space periodicity, associated with the $(10\frac{1}{2})$ peak [215, 216] (Fig. 4.2(d)). Upon increasing the field to μ_0H = 2.75 T, additional momentum broadened peaks at $\mathbf{k} = (\frac{1}{2}0\frac{1}{4})$ are observed, characteristic of spatially short-range correlations of $\langle\hat{T}^4\rangle = \uparrow\uparrow\downarrow\downarrow$ or $\langle\hat{T}^4\rangle = \uparrow\uparrow\uparrow\downarrow$ translational periodicity. From the momentum dependence it is ambiguous which of these two spin arrangements is present. In contrast, in the high field case, at T = 1.6 K, only peaks at $\mathbf{k} = (\frac{2}{3}0\frac{1}{3})$ are observed indicating the presence of $\langle\hat{T}^3\rangle = \uparrow\uparrow\downarrow$ periodicity, consistent with previous magnetic field powder diffraction in the literature [215, 216]. These peaks are momentum resolution limited, consistent with long-range spatial correlations. The WISH data (Fig. 4.2($a-c$)) indicate a uniaxial arrangement of Co^{2+} spins along the $[h0\frac{h}{2}]$ direction (highlighted in yellow) with $\langle\hat{T}^2\rangle$, $\langle\hat{T}^3\rangle$ and $\langle\hat{T}^4\rangle$ translational symmetry, depending on both magnetic field and temperature. The cuts along the $[h0\frac{1}{2}h]$ direction (denoted by the yellow shading in Fig. 4.2) are plotted in Fig. 4.3, showing the momentum broadened peaks that appear on cycling the field up and then down. The situation is somewhat different in the powder diffraction data (Fig. 4.4($a-d$)) where a more complex pattern of diffraction peaks is observed due to the spherical averaging of the magnetic field direction relative to the moment orientation. Nonetheless, the peaks indicate the presence of all three periodicities $\langle\hat{T}^2\rangle$, $\langle\hat{T}^3\rangle$ and $\langle\hat{T}^4\rangle$ in agreement with the single crystal data.

Single crystal diffraction was carried out on the triple-axis spectrometer, RITA II, this time with the field parallel to the c-axis (Fig. 4.4($e-h$)). Here only spatially long-range $\langle\hat{T}^3\rangle$ order was observed. This contrasts with the WISH data where it was shown that if the magnetic field is tilted away from the c-axis a $\langle\hat{T}^4\rangle$ periodicity can be established. It should be noted that both $\langle\hat{T}^4\rangle$ orders, $\uparrow\uparrow\downarrow\downarrow$ and $\uparrow\uparrow\uparrow\downarrow$, can be constructed from an underlying $\langle\hat{T}^3\rangle$ order with antiphase boundaries [11]. In fact, coexisting $\langle\hat{T}^{2,3,4}\rangle$ order can be created from an underlying $\langle\hat{T}^3\rangle$ order with antiphase boundaries as can be seen by considering the following example of an antiphase boundary between $\langle\hat{T}^{3+}\rangle = \uparrow\uparrow\downarrow$ and $\langle\hat{T}^{3-}\rangle = \uparrow\downarrow\downarrow$ order

$$\langle\hat{T}^{3+}\hat{T}^{3+}\hat{T}^{3-}\hat{T}^{3-}\rangle = \uparrow\uparrow\downarrow\uparrow\uparrow\downarrow\downarrow\downarrow\uparrow\downarrow\downarrow\uparrow = \langle\hat{T}^{3+}\hat{T}^{4}\hat{T}^{2}\hat{T}^{3-}\rangle. \quad (4.1)$$

The antiphase boundaries here differ from those in large-spin antiferromagnets such as $CaFe_2O_4$ [1, 15] in that they are not spatially-extended but instead are expected to be sharp owing to the $j_{eff} = \frac{1}{2}$ Ising nature of the magnetism in α-CoV_2O_6.

To summarise the results of the single crystal neutron diffraction experiments,

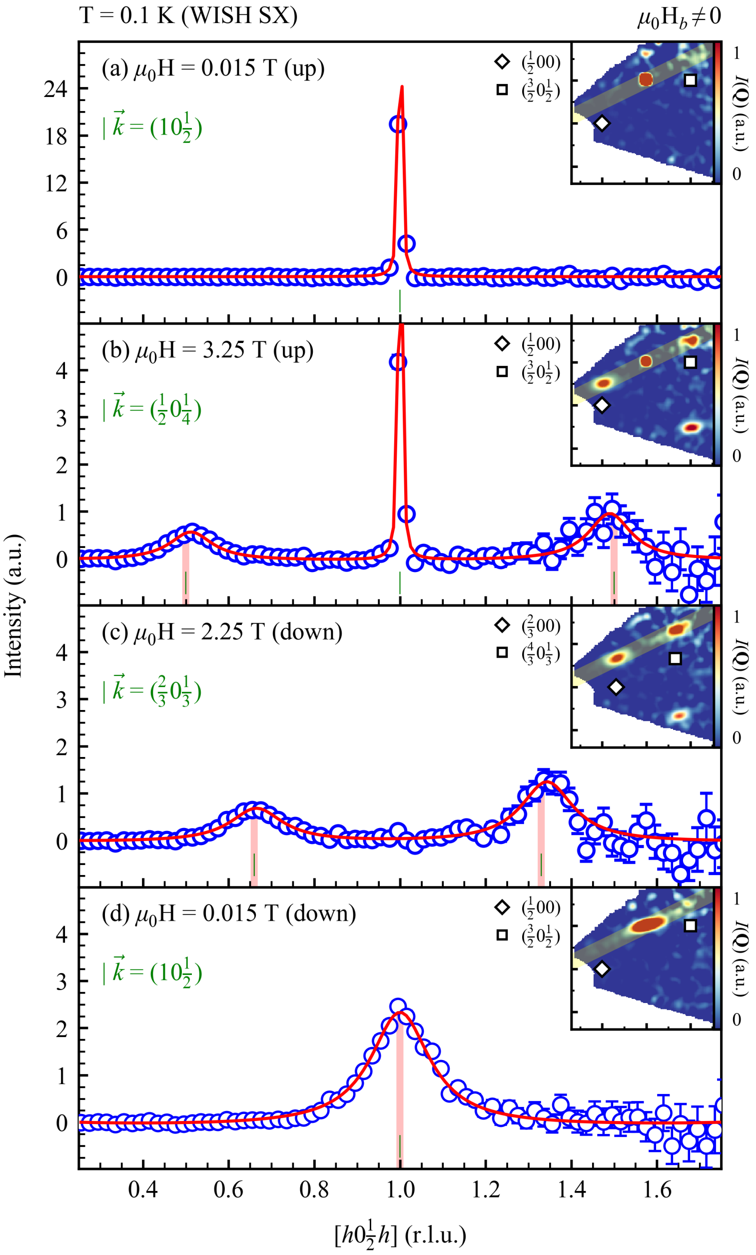

Figure 4.3 (T = 0.1 K) *scans along* $[h0\frac{h}{2}]$ *from WISH. On increasing the field, momentum broadened* $\vec{k} = (\frac{1}{2}0\frac{1}{4})$ *(panel b) peaks draw intensity from* $\vec{Q} = (10\frac{1}{2})$*. On decreasing the field from saturation, these are replaced by momentum broadened peaks at* $\vec{k} = (\frac{2}{3}0\frac{1}{3})$*. At low fields (panel (d)), the zero-field structure characterised by* $\vec{k} = (10\frac{1}{2})$*. Red bars indicate the momentum resolution. Figure reproduced from Ref. [2].*

with the magnetic field $\mathbf{H} \not\parallel c$ the magnetic ground state upon zero-field cooling is marked by spatially long-ranged $\langle \hat{T}^2 \rangle$ order, indicated by resolution-limited Bragg peaks. Upon ramping the magnetic field, momentum broadened peaks

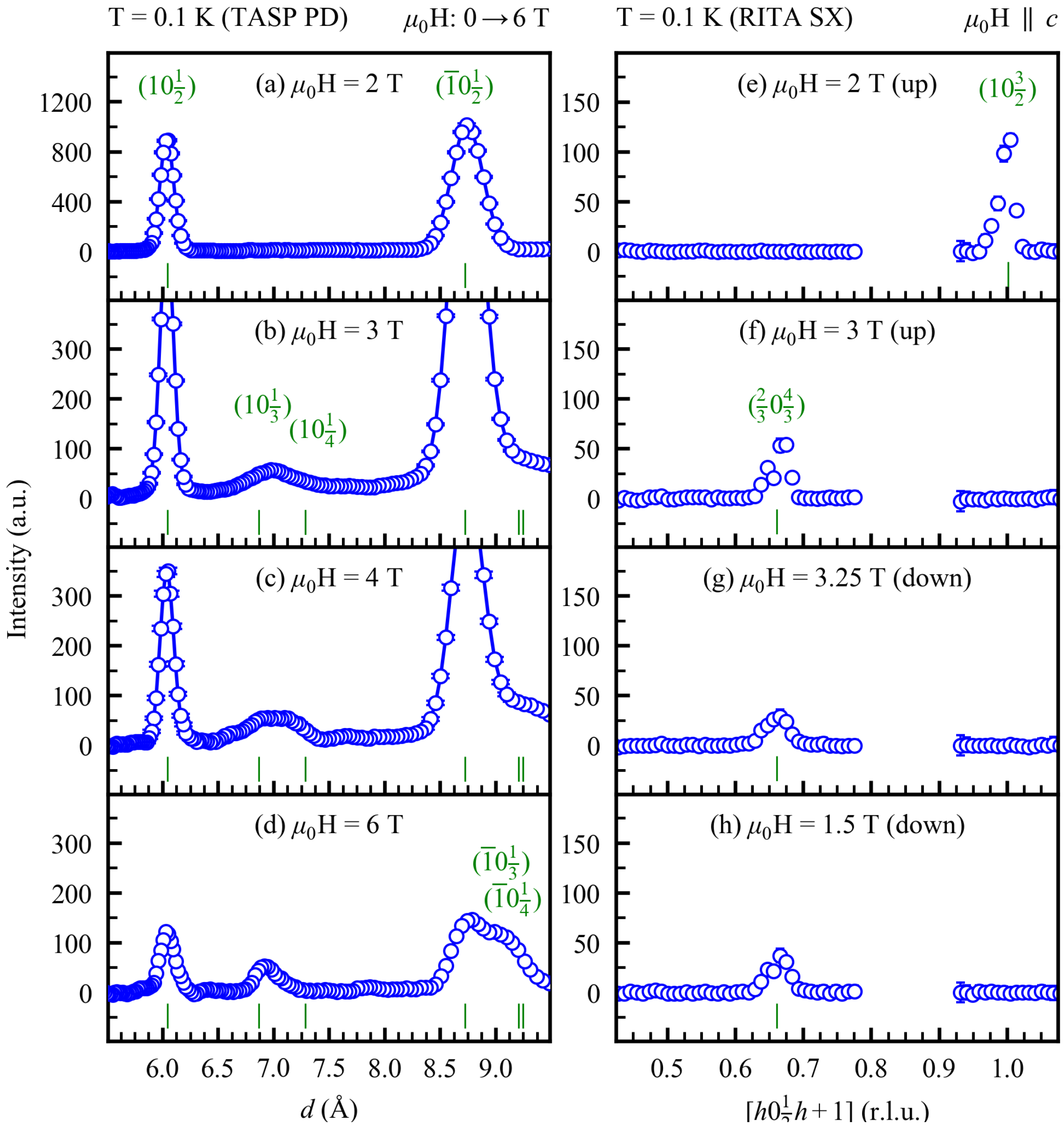

Figure 4.4 *(a–d) powder data from TASP at* T = 0.1 K *with a vertical magnetic field showing the presence of both* $\langle\hat{T}^3\rangle$ *and* $\langle\hat{T}^4\rangle$. *(e–h) single crystal data taken on RITA II in the* $(h0l)$ *plane with the field aligned along the c-axis at* T = 0.1 K *showing* $\langle\hat{T}^3\rangle$ *and no observable* $\langle\hat{T}^4\rangle$ *order in this field geometry. Figure reproduced from Ref. [2].*

at $\mathbf{k} = (\frac{1}{2}0\frac{1}{4})$ appear, drawing their intensity from the $(10\frac{1}{2})$ Bragg peak. This indicates the development of short-range correlations with the periodicity $\langle\hat{T}^4\rangle$. When the magnetic field is then cycled down, the Bragg peak loses all intensity and momentum broadened peaks are measured at $\mathbf{k} = (\frac{2}{3}0\frac{1}{3})$ and $\mathbf{k} = (\frac{4}{3}0\frac{1}{3})$, consistent with entirely short-range magnetic order with a periodicity $\langle\hat{T}^3\rangle$. Finally, as the magnetic field is reduced to zero, a momentum broadened peak is observed at $(10\frac{1}{2})$ indicating that the magnetic order reverts back to a $\langle\hat{T}^2\rangle$ periodicity but the correlations are spatially short-ranged. In contrast, if $\mathbf{H} \parallel c$

as achieved on RITA II, only long-range $\langle \hat{T}^3 \rangle$ order is observed.

Finally, it should be noted that the critical scaling exponent, $\beta = 0.16(2)$, was extracted [2] according to $|M|^2 \propto |T - T_N|^{2\beta}$, confirming the Ising nature of the magnetic order [217, 218].

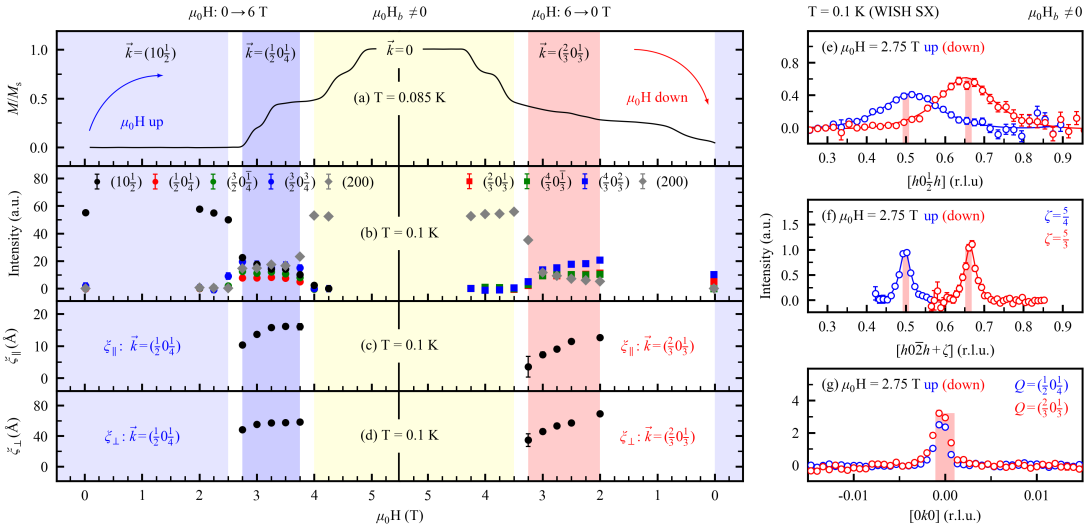

Figure 4.5 *(a) Low temperature magnetisation data in the same field arrangement as the WISH experiments. The thermodynamic data is compared against the (b) intensity and (c, d) correlation lengths extracted from WISH single crystal diffraction. Data is presented for field increasing and decreasing experiments where $\langle \hat{T}^4 \rangle$ and $\langle \hat{T}^3 \rangle$ periodicities are observed. (e) Line cut along $[h0\frac{h}{2}]$. (f, g) Cuts perpendicular to $[h0\frac{h}{2}]$. Figure reproduced from Ref. [2].*

Attention is now paid to the low temperature magnetisation measurements of α-CoV$_2$O$_6$, which were performed in the same field configuration as the WISH experiments. Fig. 4.5 presents the magnetisation data alongside the WISH data, identifying the diffraction peaks measured at each field strength. The field is ramped from zero to saturation and back down again, with the correlation length indicated both parallel ($\xi_{\|}$) and perpendicular ($\perp$) to the scan direction[2] Figs. 4.4 $(e - g)$ show cuts along the stacking direction (e) and perpendicular direction $(f - g)$ demonstrating that order is short-range (with correlation length of just a few unit cells) along the stacking direction but long range along $[0k0]$, further indicating the role of short-range correlations along the stacking direction.

A series of plateaux are observed in the magnetisation data as the field is cycled. A

---

[2] The correlation length was calculated by L. Edwards from a fit to lattice Lorentzians, characteristic of exponentially decaying spatial correlations. Further details of this can be found in Ref. [2] and Refs. [219, 220].

large plateau at zero magnetisation is observed before the magnetisation begins to increase at $\mu_0 H \approx 2.75$ T. A small plateau is seen at around 3.0 T ($M/M_S = 0.25$) before a large plateau at 3.25 T ($M/M_S = 0.5$). One final kink is seen around 4.5 T ($M/M_S = 0.75$) before the magnetisation saturates. On cycling the field back down, a plateau is seen around 4.0 T ($M/M_S = 0.75$) but no further plateaux are observed below this field, save for a slight kink around 0.75 T ($M/M_S = 0.25$).

4.3 Origin of magnetisation plateaux

Theoretical work performed on the Ising model [221] reports the existence of an infinite number of commensurate and collinear magnetic phases at low temperatures, based on the presence of antiphase boundaries. This was found to be supported when the anisotropic next-nearest neighbour interaction (ANNNI) satisfies $\frac{-J_2}{J_1} > \frac{1}{2}$. With decreasing temperature, it is observed that both $\langle \hat{T}^3 \rangle$ ($\uparrow\uparrow\downarrow$) and spatially short-range $\langle \hat{T}^4 \rangle$ ($\uparrow\uparrow\downarrow\downarrow$) can be stabilised. In future studies, it will be interesting for lower temperatures to be pursued to determine if further periodicities can be be stabilised. Judging from the spatially short-range nature of the $\langle \hat{T}^4 \rangle$ periodicity with neutron diffraction, such phases may be too weakly correlated or short-lived to observe [222]. These results suggest that strongly Ising-like α-CoV$_2$O$_6$ may have the correct balance of exchange couplings to support an infinite series of commensurate phases with decreasing temperature.

However, α-CoV$_2$O$_6$ displays low temperature magnetisation plateaux built upon metastable, spatially short-range, and commensurate magnetic correlations that do not break long-range translational symmetry owing to the finite spatial correlation lengths. These are not phase transitions with a well defined Bragg peak and these plateaux cannot be understood in terms of the competing exchange interactions as reported in some localised magnets (for example in Ref. [196, 223]). The presence of a plateau is indicative of an energetic gap, yet translational symmetry is not broken in α-Co$_2$V$_2$O$_6$. This apparent dichotomy is now discussed.

Following Ref. [174], on general grounds, without specifying the particular form of the microscopic magnetic Hamiltonian, the origin of discrete steps in the magnetisation will now be discussed in terms of the underlying translational symmetry of the Hamiltonian. This underlying symmetry places restrictions on the values of the complex geometric phase acquired when rotating the spins around an axis of symmetry. Given the Ising nature of α-CoV$_2$O$_6$ and observed anisotropy gap [14], the Hamiltonian can be assumed to be invariant under rotation about the magnetisation axis $\hat{z}$. A unitary rotation about the $\hat{z}$-axis can be written as

$$\hat{U} = \exp\left(-i\sum_{j=1}^{L}\left(\frac{2\pi j}{L}\right)\hat{S}_j^z\right) \tag{4.2}$$

for a system size, L. By acting on a state $|\psi\rangle$ which has the energy ϵ, with the operator $\hat{U}$, one can rotate onto a new state with energy ϵ'

$$\mathcal{H}\left(\hat{U}|\psi\rangle\right) = \epsilon'\left(\hat{U}|\psi\rangle\right). \tag{4.3}$$

With some algebraic manipulation,

$$\langle\psi|\left(\hat{U}^\dagger\mathcal{H}\hat{U} - \mathcal{H}\right)|\psi\rangle = \epsilon' - \epsilon = \delta\epsilon \tag{4.4}$$

where the difference in energy between the initial state and rotated state is defined as $\delta\epsilon = \epsilon' - \epsilon$. By expanding the unitary rotation operator

$$\langle\psi|\left[(1+\mathcal{O}(1/L))\,\mathcal{H}\,(1+\mathcal{O}(1/L)) - \mathcal{H}\right]|\psi\rangle = \delta\epsilon \implies \delta\epsilon \sim \mathcal{O}(1/L) \tag{4.5}$$

it can be seen that there is an excited state with energy $\sim \mathcal{O}(1/L)$. This is the case unless $\hat{U}|\psi\rangle$ is not orthogonal to $|\psi\rangle$ – in this case $\epsilon = \epsilon'$. This can be seen by considering the two eigenstates of the Hamiltonian, $|\psi_1\rangle$ and $|\psi_2\rangle$, with energies ϵ_1 and ϵ_2 respectively

$$\langle\psi_2|\mathcal{H}|\psi_1\rangle = \epsilon_1\langle\psi_2|\psi_1\rangle \tag{4.6a}$$

$$\langle\psi_1|\mathcal{H}|\psi_2\rangle = \epsilon_2\langle\psi_1|\psi_2\rangle. \tag{4.6b}$$

Eqn. 4.6a can be equated with the Hermitian conjugate of Eqn. 4.6b

$$\epsilon_2\langle\psi_1|\psi_2\rangle = \epsilon_1\langle\psi_2|\psi_1\rangle. \tag{4.7}$$

It can be seen that Eqn. 4.7 can only be satisfied if $\epsilon_1 = \epsilon_2$ or $\langle\psi_2|\psi_1\rangle$. In other words, for two energy eigenvalues to be different, the eigenstates must be orthogonal. Therefore, after the rotation, in order for there to be a low-lying state with a different energy to the ground state, $|\psi\rangle$ and $\hat{U}|\psi\rangle$ must be orthogonal.

For a Hamiltonian invariant under a site translation $\mathcal{H} \mapsto \hat{T}\mathcal{H}\hat{T}^{-1}$, a norm preserving unitary rotation of the spins using the operator $\hat{U}$ (Eqn. 4.3) generates a geometric phase under the gauge transformation

$$\hat{T}\hat{U}\hat{T}^{-1} = \hat{U}e^{2\pi i(S-m)}, \tag{4.8}$$

where $m = \frac{1}{L}\sum_{i=1}^{L} \hat{S}_i^z$. This is akin to that gained by a Foucault pendulum as it undergoes a unitary transformation about the Earth's axis. For $(S-m) \notin \mathbb{Z}$, the rotated state must be orthogonal to the ground state and represent an excited state with an infinitesimally larger energy in the thermodynamic limit [174]. These states lead to a gapless continuum as Haldane suggested [164]. In the case of integer values, states are gapped and cannot be smoothly transformed through with the application of field, leading to the emergence of magnetisation plateaux and a Bloch state analogue of the quantum Hall effect [174, 224, 225]. This is the Lieb-Mattis-Shultz theorem [173] which states that a spin chain can have an energy gap without breaking translational symmetry when the magnetisation per spin satisfies $(S-m) \in \mathbb{Z}$. In the case that $(S-m) = p/q$, where p and q are coprime, $\hat{T}^q$ preserves gauge invariance and the ground state is endowed with $\hat{T}^q$ symmetry. This new magnetisation-induced symmetry can give rise to modulated ground states, though the stability of such states is ultimately determined by the interaction terms present in the microscopic Hamiltonian.

The presence of a strong spin-orbit splitting between the $j_{\text{eff}} = \frac{1}{2}$ ground state doublet and the excited $j_{\text{eff}} = \frac{3}{2}$ and $j_{\text{eff}} = \frac{5}{2}$ multiplets allows the inter-site interaction Hamiltonian to be written in terms of effective spin-half operators, $\tilde{\mathbf{S}}_i = \gamma\tilde{\mathbf{j}}_i$, where γ is a projection factor [21]. Using the general arguments discussed previously, one can assign a value of p/q to each of the magnetisation plateaux and hence extract the translational symmetry of the ground state.

Considering first the plateau associated with the saturation of the magnetic moment. After projection onto the $j_{eff} = \frac{1}{2}$ manifold, the spin value is $S = 1/2$. At saturation the magnetisation is $m = 1/2$ and hence $(S-m) = 0$. The Hamiltonian therefore satisfies $\hat{T}^1$ symmetry, as expected in a fully saturated state. In contrast, at zero magnetisation, $m = 0$ and hence $(S-m) = \frac{1}{2}$. In this case $(S-m) = p/q$, where p and q are coprime. The denominator $q = 2$ reveals that the plateau at zero magnetisation is consistent with a twofold periodicity, $\langle\hat{T}^2\rangle$. The plateau at $M/M_S = \frac{1}{3}$ arises when the magnetisation is one third of the magnitude of the spin value, $S = 1/2$. It therefore occurs at a magnetisation value $m = \frac{1}{6}$ leading to $p/q = \frac{1}{3}$. From the arguments of the Lieb-Schultz-Mattis theorem, this plateau is therefore consistent with $\langle \hat{T}^3 \rangle$. Finally, the plateau at $M/M_S = \frac{1}{2}$ can thus be understood as corresponding to $m = \frac{1}{4}$ and hence $p/q = \frac{1}{4}$. This plateau is thus consistent with $\langle \hat{T}^4 \rangle$ order. The corresponding values of p/q, M/M_S and the implied magnetic order $\langle \hat{T}^q \rangle$ are reproduced in Table 4.1.

Table 4.1 *Values of $(S - m) = p/q$ for each of the magnetisation plateaux observed in Fig. 4.5 (a).*

$S - m = p/q$	M/M_S	$\langle \hat{T}^q \rangle$
$\frac{1}{2} - \frac{1}{2} = 0$	1	$\langle \hat{T}^1 \rangle = \uparrow\uparrow$
$\frac{1}{2} - 0 = \frac{1}{2}$	0	$\langle \hat{T}^2 \rangle = \uparrow\downarrow$
$\frac{1}{2} - \frac{1}{6} = \frac{1}{3}$	$\frac{1}{3}$	$\langle \hat{T}^3 \rangle = \uparrow\uparrow\downarrow$
$\frac{1}{2} - \frac{1}{4} = \frac{1}{4}$	$\frac{1}{2}$	$\langle \hat{T}^4 \rangle = \uparrow\uparrow\downarrow\downarrow, \uparrow\uparrow\uparrow\downarrow$

Regarding the hysteresis found in Fig. 4.5, given the insulating nature [226] and the requirement of gauge invariance, this change in the ground state, despite completing a closed loop of unitary transformations, maybe indicative of a non-trivial underlying topological structure. A violation of the adiabatic theorem is not expected given the large excitation gap ($\sim$ 1 meV) in comparison to the applied fields (1 T $\sim$ 0.1 meV), however a highly degenerate ground state is expected for Ising spins on a triangular motif [227]. In further analogy to the Hall effect, It should be noted that hysteresis effects have been reported in the fractional quantum Hall effect [228, 229]. The hysteresis here is distinct from the very slow critical behaviour observed in $Ca_3Co_2O_6$ [178] where a phase transition occurs, yet occurs on the timescale of hours.

4.4 Conclusion

In this chapter, neutron diffraction and magnetisation results on the $j_{eff} = \frac{1}{2}$ Ising magnet α-CoV_2O_6 have been presented. The magnetisation data show the emergence of a number of discrete plateaux at fractions of M/M_S which do not correspond to distinct long-range ordered magnetic phases which would be accompanied by resolution limited Bragg peaks. Instead these plateaux are are marked by the emergence of momentum broadened peaks which indicate a short correlation length.

In search of an explanation for the cascade of plateaux observed, the Lieb-Schultz-Mattis theorem was applied, linking the magnetisation plateau and the underlying translational symmetry of the ground state. This analysis demonstrates the presence of multiple commensurate periodicities that are absent from powder samples [216]. The transitions are observed to be hysteretic in nature, with $\langle \hat{T}^4 \rangle$ observed on an upward field sweep but not seen on the downward sweep. Using the insight gained from the Lieb-Schultz-Mattis theorem in concert with the observation of momentum broadened peaks, the multiple commensurate periodicities are understood in terms of metastable antiphase boundaries. The underlying field-induced order is thus understood to be $\langle \hat{T}^3 \rangle = \uparrow\uparrow\downarrow$, consistent with the field-induced phase observed in powder samples [215, 216]. Antiphase boundary creation in this $\langle \hat{T}^3 \rangle$ order was shown to give rise to $\langle \hat{T}^4 \rangle$ and $\langle \hat{T}^2 \rangle$ locally, thus explaining the coexistence of these peaks in the finite field neutron data (Fig. 4.5). The absence of the emerging $\langle \hat{T}^4 \rangle$ order in powder samples can thus understood to be due to the spherical averaging of the magnetic field. Given the short-range nature of correlations in α-CoV$_2$O$_6$, the stabilisation of metastable antiphase boundaries in field offers a more compelling explanation for the magnetisation plateaux than order-by-disorder which has been used to explain the 1/3 plateau in other triangular systems [161, 230–232] where the plateaux typically accompany long-range magnetic phase transitions.

Further neutron scattering experiments would likely further elucidate the nature of the magnetic interactions in α-CoV$_2$O$_6$. Given the small bandwidth of the spin wave excitations in α-CoV$_2$O$_6$, an instrument such as the indirect geometry crystal-analyser spectrometer OSIRIS [10] would be required. This experiment would likely present considerable challenges owing to the small crystal size and rod-like geometry [14], necessitating the coalignment of many single crystals.

Chapter 5

Metastable antiphase boundary ordering in $CaFe_2O_4$

5.1 Introduction

The manipulation of the domain wall motion of ferromagnets via a coupling to external fields has been suggested as a promising mechanism for the design of logic gates [233] and racetrack memory devices [234, 235] for the next generation of quantum devices. Additional attention has been paid to the control of antiferromagnetic domain walls, which overcome the practical difficulties of the large stray fields associated with their ferromagnetic counterparts, yet cannot be controlled with a simple external field [236]. Nonetheless, mechanisms have been suggested for the control of antiferromagnetic domain walls ranging from thermal activation [237] to spin-orbital torques [238] and magnon-driving [239].

One antiferromagnetic system which may prove instructive in the study of magnon-soliton interactions and antiphase boundary effects is the $S = 5/2$ antiferromagnet $CaFe_2O_4$. Polarised neutron diffraction data show the existence of spatially-extended Bloch walls separating antiphase regions of antiferromagnetic order [15]. The antiphase boundaries have been found to carry an uncompensated local moment and are hence tunable in field [15]. Furthermore, the low energy magnetic excitation spectrum was found to exhibit discrete modes [11], perhaps indicative of confinement of solitons within a nonlinear potential which arises due to frustration between domains on weakly coupled chains [1], as discussed in

Chapter 3. Knowledge of the microscopic spin Hamiltonian is a necessity before a full understanding of the antiphase boundaries can be gained, yet a consistent picture of the magnetic interactions in $CaFe_2O_4$ has proved elusive.

$CaFe_2O_4$ exhibits two magnetically ordered phases. The high temperature B phase, consists of two-dimensional networks of coupled zig-zag chains which are stacked along c in the $(\uparrow\downarrow\uparrow\downarrow)$ pattern (see Fig. 5.1 (a)). As temperature is decreased, the A phase develops, which differs only in its $(\uparrow\uparrow\downarrow\downarrow)$ c-axis stacking [11, 146]. These two phases are observed to coexist, yet the temperature range of this coexistence and the ultimate low temperature structure differ between single crystal and powder samples [24, 240]. In single crystals the ordered moment does not saturate at $5\mu_B$, with spectral weight redistributed to momentum-broadened rods of scattering along c^*, confirmed by polarisation analysis to be magnetic in origin [11], indicative of antiphase boundaries along c. From polarised diffraction data of the momentum-broadened component, at $\mathrm{T} = 5$ K the correlation length along c was determined to be $\sim 1 - 2$ unit cells [11] indicating highly localised correlations. The ability to measure magnetic diffuse scattering in powders without polarisation analysis or a large amount of diffuse spectral weight is limited, making the presence of antiphase boundaries in powder samples difficult to detect. However, the ordered moment is observed to be suppressed in polycrystalline samples [24]. A full characterisation of the magnetic excitations at both high and low temperature has not yet been presented.

In this chapter, the nature of the magnetic order in $CaFe_2O_4$ is addressed and an explanation is offered for the differing behaviour observed in powders and single crystals. The low temperature A phase is shown to be metastable, with short-range correlations, analogous to the field-induced metastable states recently reported in CoV_2O_6 [2] and discussed in Chapter 4, in which antiphase boundaries order to form a new phase with a different translational symmetry [221]. These arguments are supported by neutron scattering data at both high and low temperatures, demonstrating the nature of the magnetic fluctuations in single crystal $CaFe_2O_4$. Finally, using a random phase approximation (RPA) Green's function formalism, the magnetic excitations in $CaFe_2O_4$ are modelled and the spin Hamiltonian determined.

5.2 Antiphase boundaries

5.2.1 Structure

$CaFe_2O_4$ crystallises in the orthorhombic *Pnma* space group (a=9.230Å, b=3.017Å, c=10.689Å), with coupled zig-zag chains of Fe^{3+} (S=5/2, L=0) ions in the $a-b$ plane [12, 13, 146, 241]. Previous studies have reported the stabilisation of two competing magnetic orders below $T_N \approx 200$ K [11, 24, 146, 240, 242]. In the low temperature A phase (Fig. 5.1 (*a*)) the stacking along c is (↑↑↓↓) with the couplings J_{2a} and J_{2b} connecting parallel spins. In the high temperature B phase (Fig. 5.1 (*b*)), the c-axis stacking is (↑↓↑↓) with J_{2a} and J_{2b} coupling antiparallel spins.

The behaviour observed is qualitatively different between powder and single crystal samples and is summarised in Table 5.1. To examine the magnetic structure of the powder samples, the BT-1 diffractometer at the NIST Center for Neutron Research (NCNR) [243] was used, with wavelength λ=2.0782 Å (Ge 311 monochromator). The low and high temperature diffraction patterns are shown in Fig. 5.2 (*a*) and (*b*) respectively. In the powder samples, B phase order, as indicated by the presence of the $Q=(1,0,1)$ peak, is observed on cooling below T $\approx$ 200 K and is maximal at T $\approx$ 175 K. Below this temperature, the $Q=(1,0,2)$ peak begins to accumulate spectral weight, overtaking the B phase in intensity at T $\approx$ 150 K (Fig. 5.2 (*c*)). The B phase peaks are observed to disappear at around T = 125 K after a brief temperature window of coexistence between T $\approx$ 125 K and T $\approx$ 175 K. The powder diffraction data would thus indicate a preferential A phase ordering at low temperature, with (↑↑↓↓) stacking along c, rather than the B phase order with its (↑↓↑↓) arrangement. This result is in agreement with the findings of Songvilay *et al* [24] who have further shown that chemical doping with Cr prevents the stabilisation of A phase order, observing only the B phase in $CaCr_{0.5}Fe_{1.5}O_4$. Pure $CaCr_2O_4$ shows an altogether different magnetic structure, with an incommensurate cycloidal propagation vector [244–246].

The story is somewhat different in single crystal samples. Between T $\approx$ 200 K and T $\approx$ 100 K, B phase magnetic order is dominant as seen in Fig. 5.1 (*d*). This is confirmed by magnetic susceptibility measurements [240] showing a feature at the onset of B phase order. Below T $\approx$ 100K the A phase becomes the more prevalent magnetic order (Fig. 5.1 (*d*)). The existence of a transition to the A phase is

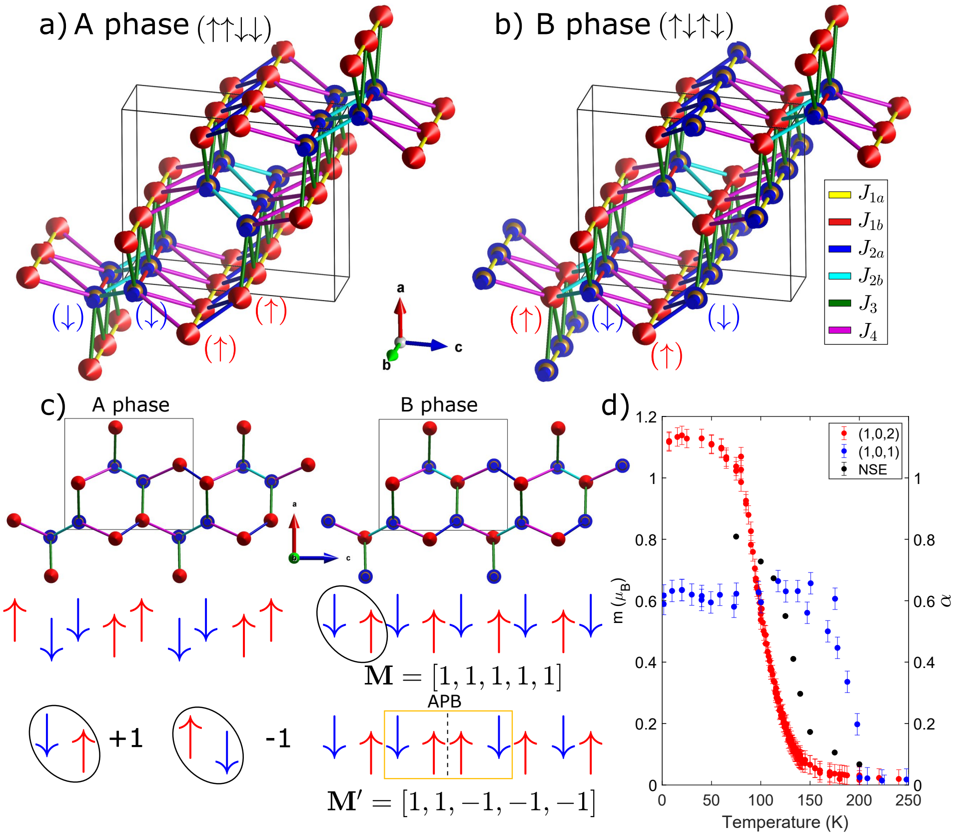

Figure 5.1 *Structure of $CaFe_2O_4$ in the A (a) and B (b) phases, which differ in their c-axis stacking. Red arrows identify Fe^{3+} spins pointing along $+b$ and blue arrows identify spins pointing along $-b$. The couplings J_{1a} and J_{1b} link parallel spins along b, with the J_{2a} and J_{2b} linking parallel and antiparallel spins in the A and B phases respectively. The exchanges J_3 and J_4 define antiferromagnetically aligned chains in both phases. (c) Magnetic structure along the c-axis showing the (↑↑↓↓) and (↑↓↑↓) configuration of the A and B phases respectively. The effect of an antiphase boundary (APB) in the B phase order is illustrated, giving rise to local A phase order (golden rectangle). The mapping onto the matrix $\mathbf{M}$ is demonstrated, with each spin pair mapped onto ±1. (d) Temperature dependence of the order parameters of the A and B phases, Q=(1,0,2) and Q=(1,0,1) respectively. Black points show the temperature dependence of the static component, α, of neutron spin echo (NSE) at Q=(1,0,1.5), data reproduced from Ref. [11].*

argued on the grounds of the appearance of the peak at $Q = (1, 0, 2)$, however it is important to note that no thermodynamic measurements have been reported showing the existence of a second phase transition, and only a single order parameter was detected in the Mössbauer spectroscopy measurements, showing a power law temperature dependence [155]. Observing the relative intensities of the $(1, 0, 2)$ and $(1, 0, 1)$ peaks, the two phases can be seen to saturate in a 2:1

Table 5.1 *Magnetic structures observed in $CaFe_2O_4$. Data from Cr doped sample reproduced from Ref. [24].*

Sample	B phase	A phase	Coexistence?
$CaFe_2O_4$ single crystal	200-5 K	175-5 K	175-5 K
$CaFe_2O_4$ powder	200-150 K	175-5 K	175-150 K
$CaCr_{0.5}Fe_{1.5}O_4$ powder	200-5 K	×	×

ratio at low temperature (Fig. 5.1 (*d*)).

It has previously been suggested that the phase coexistence could originate from a fine balancing of the exchange parameter $J_{2a/b}$ on the ferromagnetic/antiferromagnetic threshold which is sensitive to subtle changes in the bond angle as a function of temperature [24]. However, these arguments rely on an element of exchange disorder to account for the persistence of B phase order down to low temperatures in the single crystal samples, and the region of phase coexistence in the high temperature phase of the powder. Moreover, the discrepancy between the powder and single crystal data remains unexplained. An alternative explanation for the temperature dependence of the phase coexistence based on antiphase domain formation is now presented.

Firstly, single crystal samples are discussed, before turning attention to the powder samples. The single crystals described in this chapter are the same as those used in Refs. [1, 11, 15] and were grown using a mirror furnace, as described in the Supplemental Material of Ref. [11]. Previous studies of these single crystals [11, 15] have demonstrated the presence of rods of diffuse magnetic scattering along [0,0,L] indicating that correlations along c are short-range. Furthermore, at T = 200 K neutron spin echo (NSE) measurements reveal the dynamical nature of this diffuse scattering [11, 15], with the static component increasing rapidly as the sample was cooled below T = 100 K (Fig. 5.1 (*d*)). By examining the magnetic structure in the two phases, it can be seen that the creation of an antiphase domain boundary in global B phase order gives rise to a local A phase stacking (and vice versa) as demonstrated in Fig. 5.1 (*c*) [15]. Consequently, it is argued that the phase coexistence at low temperature can be understood as arising due to the freezing-in of antiphase boundaries in a parent B phase order. In order to demonstrate this, the following toy model of domain formation is introduced.

The chain along c is split into pairs of spins, with each pair assigned the value of +1 or -1 depending on the orientation of the spin pair (Fig. 5.1 (*c*)). In a pure

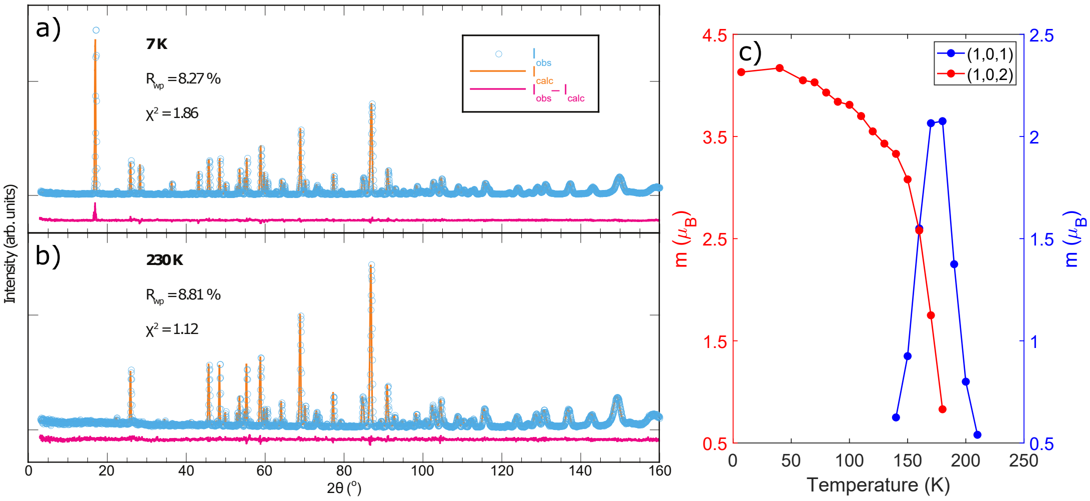

Figure 5.2 *(a) Neutron diffraction data of a powder sample of* $CaFe_2O_4$ *measured on BT-1 at (a)* $T = 7$ *K and (b)* $T = 230$ *K. (c) Magnetic moment of the* $Q = (1, 0, 1)$ *and* $Q = (1, 0, 2)$ *Bragg peaks in the powder sample. The small window of coexistence and loss of the B phase at low temperature shows a qualitatively different behaviour to the single crystal sample [11]. Diffraction measurements performed by E. E. Rodriguez.*

B phase arrangement the magnetic structure can be represented by the infinite array, $\mathbf{M} = \pm[1, 1, 1, 1, ...]$. Where $\pm$ labels the two degenerate spin configurations (of which the positive state is selected from now on, to be explicit). To introduce a domain wall at position i, the signs from position $i + 1$ onwards are flipped, $\mathbf{M} = [1, 1, -1, -1, ...]$, for example. Let $\mathcal{F}(i, p)$ be the operator that has a $p(\%)$ chance of flipping the signs on all sites after site i, hence creating an antiphase boundary at site i. After operating on each element of the array with the nonlocal operator

$$\mathbf{M}' = \prod_{i}^{N} \mathcal{F}(i, p)\mathbf{M}, \tag{5.1}$$

the local order is then analysed by examining the relative signs on each site. Each occurrence of the pattern $\mathbf{M}' = [..., \pm1, \pm1, ...]$ can be assigned to the B phase, with $\mathbf{M}' = [..., \pm1, \mp1, ...]$ belonging to the A phase, leading to an array of length $N - 1$, $\mathbf{P} = [A, B, B, A, ...]$, for example, describing the local order.

For $p = 67\%$, the ratios of A to B phase are found to be 2:1 in agreement with the low temperature neutron diffraction data [11]. The B phase magnetic unit cell consists of along two spins along c (or one element of $\mathbf{M}$) and hence a flipping ratio of $p = 67\%$ gives rise to domains with an average size of 1.5 elements, corresponding to 1.5 unit cells, in agreement with the measured correlation length of 1-2 unit cells, from neutron diffraction [11]. The same analysis can be applied to a parent A phase order, with $p = 33\%$, leading to an average domain size of four elements of $\mathbf{M}$ which, again corresponds to a correlation length of 1.5 unit cells (owing to the doubled magnetic unit cell of the A phase). However, the appearance of the $Q = (1, 0, 1)$ peak at T_N along with a significant component of magnetic dynamical diffuse scattering, which becomes static on the onset of A phase order is suggestive of the former scenario. It is thus concluded that the single crystal data are consistent with a parent B phase order with antiphase domain boundaries that freeze-in at low temperature leading to local A phase order. This is still suggestive of a small $J_{2a/b}$ so that the energy cost of creating an antiphase boundary is of the order of the temperature, but it is concluded that this bond must be strictly antiferromagnetic, in order that the parent magnetic order is B phase.

The persistence of the B phase $(1, 0, 1)$ peak down to low temperature in the single crystal sample is indicative of domain pinning effects arising due the presence of oxygen vacancies, known to be present in $CaFe_2O_4$ single crystals[1] [240]. If the flipping ratio were to tend towards $p = 100\%$, pure A phase order would be expected at low temperature and a disappearance of the B phase Bragg peaks, precisely as observed in the $CaFe_2O_4$ powder samples [24]. This is to be expected if the powder samples were to have fewer oxygen vacancies and hence facilitate the full conversion of B phase to A phase order. The magnetisation measurements of Das *et al* [240] demonstrate that vacancy-driven disorder alone cannot account for the discrepancy between the powder and single crystal samples, indeed another ingredient is needed.

Crucial to the survival of the low temperature A phase is the presence of an anisotropy gap that stabilises the A phase structure at low temperature despite the frustration of $J_{2a/b}$. It is notable that the neutron scattering measurements of Songvilay *et al* suggest a significant reduction in the anisotropy gap in the Cr doped samples [24], which may explain the failure to stabilise A phase order at low temperatures. In the $3d^5$ high spin complexes, owing to the absence of an orbital moment, the spin Hamiltonian is expected to be isotropic. The observed anisotropy gap is thus evidence of the mixing of higher energy multiplets into the ground state orbital singlet, ^6S. This mixing occurs due to higher order processes such as a second order process involving the spin-spin interaction and an axial crystal field via the ^6D state [247] or to fourth order via squares of the spin-orbit

---

[1] To the author's knowledge, no samples with excess oxygen have been reported.

and distortion terms [248]. Ultimately, the anisotropy terms that appear in the effective spin Hamiltonian must respect the crystal symmetry [249] and hence should be proportional to the Steven's parameter, $\mu \sim B_2^0$ [21, 27]. The vital role of the axial distortion term in mixing higher order multiplets into the ^6S ground state indicates that the anisotropy should couple strongly to strain in $\mathrm{CaFe_2O_4}$, which exhibits a significant distortion of the local octahedral environment [13]. It is therefore unsurprising that doping suppresses the magnitude of the anisotropy [24] and that the magnetic behaviour shows a strong dependence on the density of oxygen vacancies [240], since both processes affect the local axial crystal field. The role that anisotropy plays in the stabilisation of the A phase in turn suggests an explanation for the differing behaviour in powder and single crystal samples. In powder samples, the grinding process introduces strain which would indicate an enhancement of the single ion anisotropy parameter, μ, promoting the stabilisation of A phase order. The temperature dependence of the anisotropy gap in single crystal samples is now further explored using neutron scattering measurements made by C. Stock and Ch. Niedermayer.

5.2.2 Anisotropy

Temperature dependent constant Q scans at the $Q = (-1, 0, 2)$ position were conducted on the RITA II triple-axis spectrometer at the Paul Scherrer Institute (Villigen, Switzerland) [250] (Fig. 5.3 (a)). The asymmetric lineshape arises from the finite resolution and the curvature of the dispersion curve. The peaks are resolution limited and for convenience the asymmetric lineshape is approximated with an antisymmetric Lorentzian function,

$$I(E) \propto [n(\omega)+1]\left(\frac{1}{1+\left(\frac{E-\Omega_0}{\Gamma}\right)^2} - \frac{1}{1+\left(\frac{E+\Omega_0}{\Gamma}\right)^2}\right) \tag{5.2}$$

whose peak width is allowed to vary sigmoidally

$$\Gamma(E) = \frac{2\Gamma_0}{1+\exp\left[a(E-\Omega_0)\right]} \tag{5.3}$$

such that the degree of asymmetry is controlled by a single parameter, a and for $a = 0$, the width becomes symmetric, $\Gamma = \Gamma_0$ [251]. The value of the asymmetry parameter, along with Γ_0, Ω_0 and an overall scaling factor were fitted using the

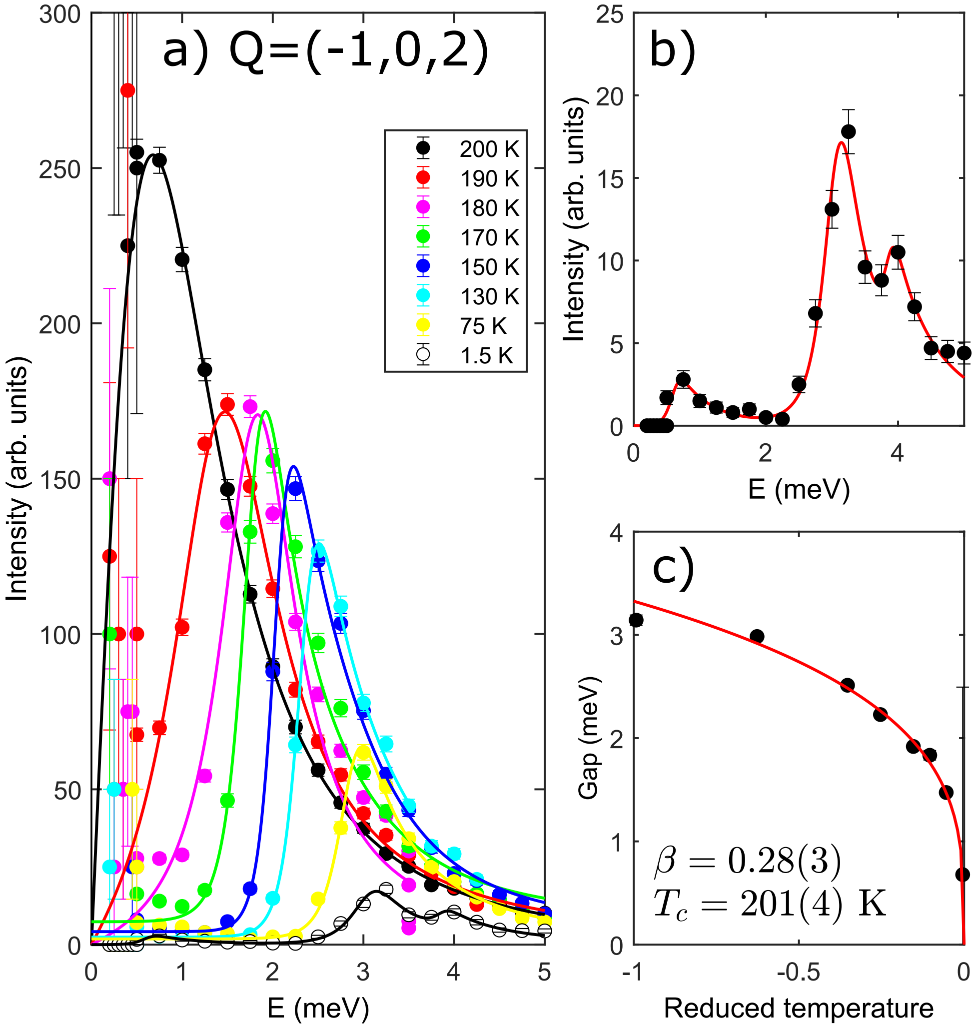

Figure 5.3 *(a) Temperature dependence of the gap at $Q = (-1, 0, 2)$ measured on the RITA II spectrometer. Solid lines are fits to asymmetric Lorentzians. (b) Anisotropy gap at T=1.5 K with $\Delta = 3.14(5)$meV. A low intensity peak at 1 meV is seen originating from in-gap mode, discussed in Ref. [15] in addition to a discrete mode at 3.9 meV originating from non-classical excitations [1, 11, 11]. (c) Extracted magnitudes of the gap as a function of reduced temperature, t. The data have been corrected for the Bose-Einstein population factor at each temperature.*

`Horace` package [252]. The value of the gap follows a power law behaviour, vanishing above T ≈ 200 K, concomitant with the loss of order along c. This is in good agreement with the temperature at which the $Q = (1, 0, 1)$ peak vanishes (Fig. 5.1 (d)). At T = 1.5 K a second peak is seen above the gap ~ 4 meV, in Fig. 5.3 (b), which can be understood in terms of the discrete non-classical excitations reported previously in this system [1, 11, 15] and discussed at length in Chapter 3. By plotting the gap as a function of reduced temperature $t = (T - T_c)/T_c$, a dimensionless scaling exponent and critical temperature can be fitted according to $\Delta \sim |t|^{\beta}$. The fitted value of $\beta = 0.28(3)$ is below the expected scaling exponent for the 3d Ising model ($\beta = 0.3265(15)$) [253]. The departure of the gap's scaling exponent from the expected critical exponent of the order parameter indicates the presence of some temperature dependence of the anisotropy parameter, beyond a simple renormalisation due to a thermal fluctuation-driven reduction of the magnetisation, and hence a decoupling of the magnetic order parameter and the anisotropy parameter. Such a temperature dependence has been observed in other ferrites and materials exhibiting strong magnetostrictive effects [254–256]. The ramifications of this temperature dependence of the anisotropy parameter will be discussed further later in the chapter. The phonon excitations are now analysed, which would be sensitive to any structural domains.

5.2.3 Acoustic phonons

The spin wave analysis presented here shows that the magnetic excitations in $CaFe_2O_4$ can be consistently understood in terms of the same exchange constants in the high (B phase) and low (A phase) temperature phases, up to a small temperature renormalisation. To confirm the lack of temperature dependent structural effects, the transverse acoustic phonons are discussed.

The lifetime and energy positions of acoustic phonons are sensitive to the formation of structural defects or localised structural domains. This has been shown in scattering studies of, for example, localised polar domains [257] in relaxor ferroelectrics such as $Pb(Zn,Mg)_{1/3}Nb_{2/3}O_3$ [258–261] and the disordered perovskite $K_{1-x}Li_xTaO_3$ [262]. To confirm the lack of any structural domains forming that may drive either the antiphase boundaries discussed above or the transition from the B phase to the A phase, on cooling, the temperature dependence of transverse acoustic phonons propagating both along c and a axes in $CaFe_2O_4$ was investigated. Acoustic phonon measurements were performed on the EIGER triple-axis spectrometer (PSI, Switzerland) [73] by C. Stock and U. Stuhr. The incident neutron beam was monochromated with a vertically focused PG(002) monochromator defining E_i and the final energy was fixed to $E_f = 14.6$ meV with a PG(002) analyser, with the energy transfer defined by $E = E_i - E_f$. Collimation was set to 80 minutes before and after the sample position and a pyrolytic graphite filter was used after the sample to remove higher order contamination of the neturon beam. The sample was aligned such that

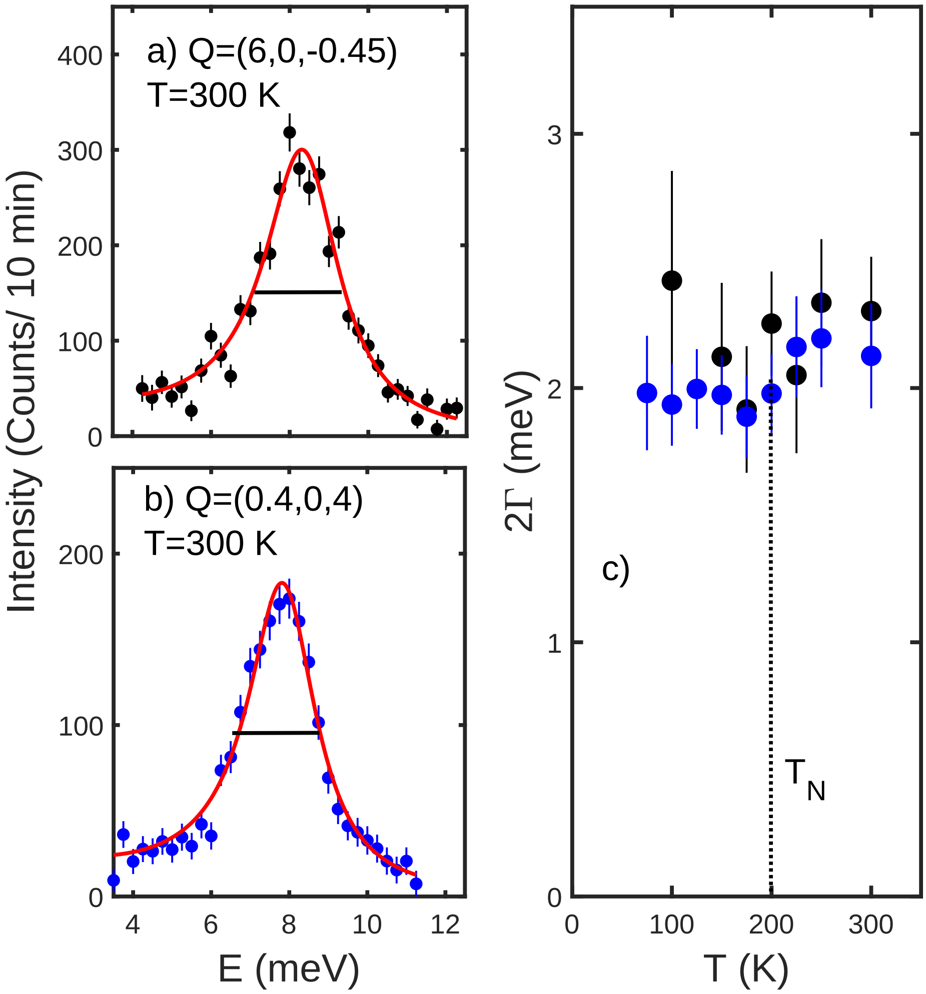

Figure 5.4 *The transverse acoustic phonons propagating along (a) the c and (b) the a axes. The resolution is depicted by the solid horizontal lines. (c) illustrates the temperature dependence of both phonon modes. No measurable anisotropy or temperature dependence is observed.*

Bragg reflections of the form $(H, K, 0)$ lay within the horizontal plane.

Constant momentum cuts through the transverse acoustic phonons propagating along the c and a axes are illustrated in Fig. 5.4 (a) and (b). The solid line is a fit to a damped simple harmonic oscillator characterised by the antisymmetric Lorentzian lineshape (Eqn. 5.2), with Ω_0 defining the energy position of the phonon and Γ the half-width in energy, inversely proportional to the lifetime τ. The full width 2Γ is shown in Fig. 5.4 (c) for phonons propagating along both directions. The function defined in Eqn. 5.2 consists of the Bose factor multiplying an odd function which ensures that the scattering cross section satisfies the principle of detailed balance [56].

In analogy to the relaxor ferroelectrics mentioned above where nanoregions of polar order are present, one would expect that phonons travelling along the *c*axis, where antiphase domain boundaries exist, to possibly be damped and this damping to be temperature dependent. Fig. 5.4 shows three key results; first, the acoustic phonons are not measurably broader than the resolution defined by the spectrometer; second, there is no observable temperature dependence to the linewidth; third, there is no observable anisotropy to the linewidth with phonons travelling along both the *a* and *c* axes showing similar responses. While constraints are placed by the energy resolution of the spectrometer and also the possibility that any effect from the domains affects lower energy phonons, this result does support the idea presented in this chapter that there is no observable structural changes with temperatures that drive the magnetism.

5.3 Fluctuations and neutron scattering

The arguments presented in Sect 5.2 rely on knowledge of the exchange parameters in the spin Hamiltonian. In order to validate the model of A phase formation through antiphase boundary freezing attention is now paid to the low energy dynamics.

Neutron scattering data are now presented for $CaFe_2O_4$ showing the magnetic fluctuations in both the high and low temperature phases. Following Refs. [207, 263–265], a Green's function formalism is applied to model the low energy excitations in both phases, demonstrating the utility of this method in systems without an orbital degree of freedom. A complete derivation of the Green's function for a general collinear system can be found in Appendix G. In applying the Green's function formalism to $CaFe_2O_4$, it is shown that, in the case of a single-ion Hamiltonian that consists solely of a mean field term, the Green's function collapses to a simple expression allowing the calculation of the dispersion relation and dynamical structure factor. Finally, the neutron scattering data are fitted, extracting exchange constants and determining the microscopic spin Hamiltonian.

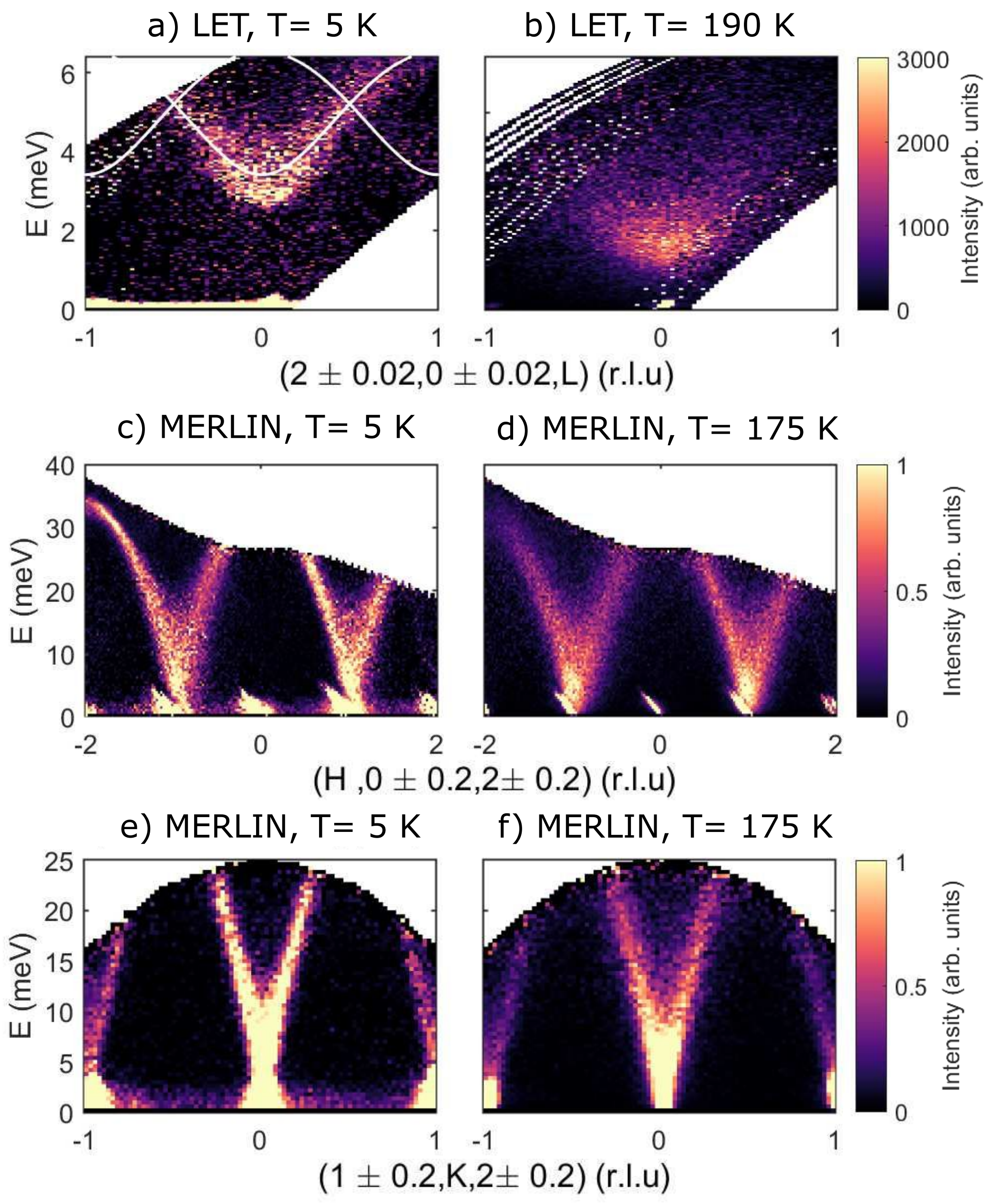

Figure 5.5 *Dispersion along c^* at (a) $T = 5$ K and (b) $T = 190$ K. Overlaid is the calculated low temperature dispersion, with the fitted exchange constants from Section 5.3.2. Spectral weight is concentrated in the mode whose minimum is at $Q = (2, 0, 0)$. As temperature is increased, the signal broadens and becomes incoherent as correlations along c are lost. (c) Dispersion along H at $T = 5$ K and (d) 175 K, measured on MERLIN. (e) Dispersion along K at $T = 5$ K and (f) 175 K. The intensities for both datasets on each instrument have been corrected for the Bose-Einstein population factor.*

5.3.1 Magnon excitations

The dynamics of $CaFe_2O_4$ are now discussed. Previous studies have shown the presence of rods of diffuse scattering, indicating the presence of antiphase boundaries and revealing the short range nature of correlations along c [11, 15]. Despite this, at low temperature, a measurable dispersion along L is observed [11]. Data are now presented from the cold chopper spectrometer LET [80] at ISIS Pulsed Neutron and Muon Source (Didcot, UK), measured by C. Stock, R. I. Bewley and D. J. Voneshen, concerning the low energy dynamics along L. The incident energy was selected to be $E_i = 8$ meV, with the high flux chopper in the 280/140 configuration, giving an elastic resolution of $\Delta E = 0.2$ meV.

At T = 5 K, a broad gapped low energy mode is observed, extending up to ~ 7 meV as seen in Fig. 5.5 (a). The gap is ~ 3 meV, in agreement with the data from RITA II (Fig. 5.3 (b)). Upon heating to T = 190 K, the gap closes in agreement with the RITA II data (Fig. 5.3 (c)), and the scattering broadens becoming incoherent, consistent with the loss of correlations along c. It is important to note that these calculations for the dispersion (in both the pure A phase and pure B phase structures) suggest that two modes are present, crossing at $L = 0.5$ (Fig. 5.5 (a)). Only one of these modes is observed to carry any spectral weight.

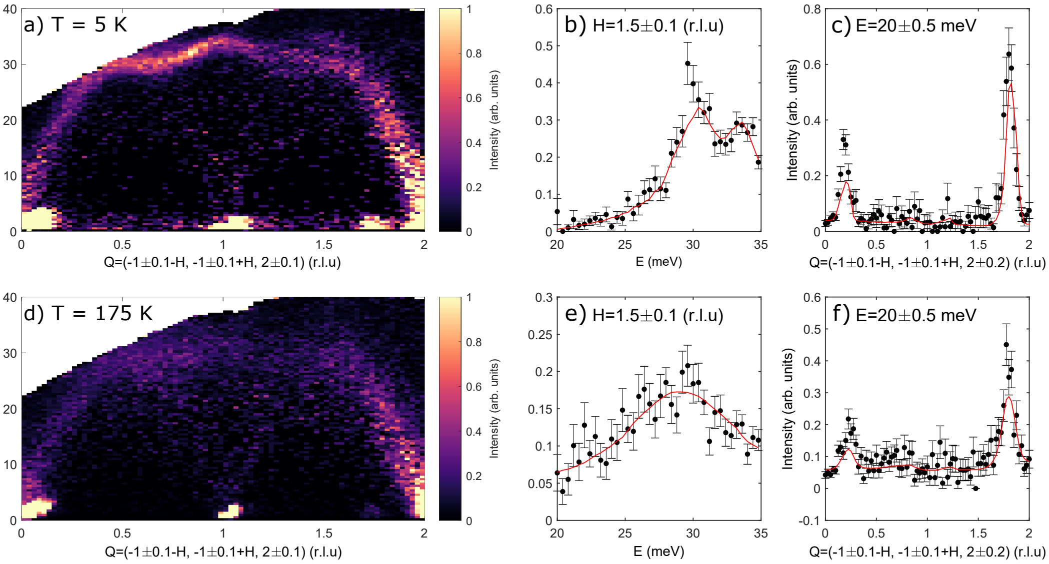

Figure 5.6 (a) *Cut along [H,-H] at* $T = 5$ *K, showing the presence of two modes, with non-trivial structure factor variation.* (b) *Constant Q cut at the zone boundary. Red line is the fit to the Green's function model.* (c) *Constant energy cut at* $E = 27.5$ *meV with fitted Green's function model.* $(d)-(f)$ $T = 175$ *K data showing a broadening of excitations and a small bandwidth renormalisation. The intensities for both datasets have been corrected for the Bose-Einstein population factor.*

In order to map out the excitations to higher energies in the (H, K) plane, neutron scattering was carried out on the time-of-flight spectrometer MERLIN at ISIS Neutron and Muon Source (Didcot, UK) [71]. The sample was cooled to T = 5 K and an incident energy of 70 meV was selected, with a gadolinium chopper spinning at $\nu = 300$ Hz, allowing for an elastic resolution of $\Delta E = 3.6$ meV. Strongly dispersive modes were observed along H (Fig. 5.5 (c)), extending up to ~ 35 meV, in agreement with Ref. [11]. Steeply dispersing spin waves were also measured along K (Fig. 5.5 (e)) confirming the three-dimensional nature of the spin waves in this system.

The sample was then warmed to T = 175 K and the measurement repeated (Fig 5.5 (b, d, f)). The excitations broaden at this temperature, along with a small renormalisation of the bandwidth. The dispersion remains qualitatively similar at this temperature, with similar structure factor modulation. Fig. 5.6 shows the dispersion along $[-H, H]$. At low temperature, two modes are seen with two peaks observed at the zone boundary (Fig. 5.6 (b)). At high temperature, once again the dispersion looks qualitatively similar, but the broadening obscures many of the features seen at low temperature, and the two peaks at the zone boundary are no longer resolved. A microscopic spin Hamiltonian is now constructed to model the spin wave excitations measured at high and low temperatures.

5.3.2 Theory

The Fe^{3+} ($S = 5/2, L = 0$) ions in $CaFe_2O_4$ are surrounded by an octahedron of oxygen ions [13]. The distorted nature of these octahedra allows for the presence of an easy-axis anisotropy term $\mu \sim B_2^0$ [21, 27], breaking spin-rotational symmetry and aligning the spins along b. The dependence of the anisotropy parameter on the Steven's parameter, B_2^0, suggests an origin for the anomalous temperature dependence of the anisotropy gap presented in Section 5.2.2, as the anisotropy parameter is coupled to the local crystalline environment of the Fe^{3+} spins due to the mixing of higher energy multiplets into the ground state orbital singlet [247–249]. As such, very subtle changes in lattice parameters originating from magnetoelastic coupling, as reported for $CaFe_2O_4$ in Ref. [24], can be expected to have a marked effect on the strength of the anisotropy, despite having only a small effect on the Fe-O-Fe bond angle.

The absence of an orbital degree of freedom motivates a spin-only Hamiltonian,

$$\mathcal{H} = \sum_{ij} \mathcal{J}_{ij} \mathbf{S}_i \cdot \mathbf{S}_j + \mu \sum_i \left(\hat{S}_i^z \right)^2 \tag{5.4}$$

where $\mu < 0$ represents an easy-axis single-ion anisotropy. The existence of two crystallographically inequivalent Fe^{3+} sites, in conjunction with the magnetic order, necessitates the use of an enlarged magnetic supercell of four sites in the B phase. The breaking of inversion symmetry in the low temperature A phase further enlarges the unit cell to eight sites and necessitates the averaging of the spin-inverted structure factors since $S^{+-}(\mathbf{q}, \omega) \neq S^{-+}(\mathbf{q}, \omega)$. The spin Hamiltonian can be separated into single and inter-ion terms, $\mathcal{H} = \mathcal{H}_1 + \mathcal{H}_2$, by performing a mean field decoupling, $\mathbf{S}_{i,\gamma} \to \langle \mathbf{S}_{i\gamma} \rangle + \delta \mathbf{S}_{i\gamma}$ and discarding terms $\sim \mathcal{O}(\delta \mathbf{S}_{i\gamma})^2$

$$\mathcal{H}_1 = \sum_{i\gamma} \hat{S}_{i\gamma}^z \left(2 \sum_{j\gamma'} J_{ij}^{\gamma\gamma'} \langle \hat{S}_{j\gamma'}^z \rangle + 2\mu \langle \hat{S}_{i\gamma}^z \rangle \right) \tag{5.5a}$$

$$\begin{aligned} \mathcal{H}_2 = & \sum_{ij}^{\gamma\gamma'} \mathcal{J}_{ij}^{\gamma\gamma'} \hat{S}_{i\gamma}^z \left(\hat{S}_{j\gamma'}^z - 2 \langle \hat{S}_{j\gamma'}^z \rangle \right) \\ & + \frac{1}{2} \sum_{ij}^{\gamma\gamma'} \mathcal{J}_{ij}^{\gamma\gamma'} \left(\hat{S}_{i\gamma}^+ \hat{S}_{j\gamma'}^- + \hat{S}_{i\gamma}^- \hat{S}_{j\gamma'}^+ \right). \end{aligned} \tag{5.5b}$$

The first term is a Zeeman term describing the molecular mean field felt by each site $\mathcal{H}_1 = \sum_{i\gamma} h_{i\gamma}^{MF} \hat{S}_{i\gamma}^z$. This splits the $2S + 1$ degenerate energy levels (Fig. 5.7). The commutators $[\hat{S}_{i'\tilde{\gamma}}^{\alpha}, \mathcal{H}]$ can be calculated to mean field level; only the transverse elements survive

$$[\hat{S}_{i'\tilde{\gamma}}^+, \mathcal{H}] = \sum_{j\gamma'} A_{i'j}^{\tilde{\gamma}\gamma'} \hat{S}_{j\gamma'}^+ \tag{5.6a}$$

$$A_{i'j}^{\tilde{\gamma}\gamma'} = -h_{i'\tilde{\gamma}}^{MF} \delta_{i'j} \delta_{\tilde{\gamma}\gamma'} + 2\mathcal{J}_{i'j}^{\tilde{\gamma}\gamma'} \langle \hat{S}_{i'\tilde{\gamma}}^z \rangle. \tag{5.6b}$$

This commutator can be inserted into the Green's function equation of motion (Appendix G) to yield the Green's functions,

$$\begin{aligned} \omega G_{\tilde{\gamma}\tilde{\gamma}'}^{+-}(i'j', \omega) = & \langle [\hat{S}_{i'\tilde{\gamma}}^+, \hat{S}_{j'\tilde{\gamma}'}^-] \rangle \\ & + \sum_{j\gamma'} A_{i'j}^{\tilde{\gamma}\gamma'} G_{\gamma'\tilde{\gamma}'}^{+-}(jj', \omega). \end{aligned} \tag{5.7}$$

This can be written as

$$\begin{aligned}\sum_{j\gamma'} G^{+-}_{\gamma'\tilde{\gamma}'}(jj',\omega)\left[\omega\delta_{i'j}\delta_{\tilde{\gamma}\gamma'} - A^{\tilde{\gamma}\gamma'}_{i'j}\right] \\ = \langle[\hat{S}^{+}_{i'\tilde{\gamma}}, \hat{S}^{-}_{j'\tilde{\gamma}'}]\rangle.\end{aligned} \tag{5.8}$$

Taking the Fourier transform and performing the summation, Eqn. 5.8 can be written as a matrix equation. On doing so, the Green's functions take the convenient form

$$\underline{\underline{G}}^{+-}(\mathbf{q},\omega) = \underline{\underline{B}}\left[\mathbb{I}\omega - \underline{\underline{A}}(\mathbf{q})\right]^{-1}. \tag{5.9}$$

where $B^{\tilde{\gamma}\tilde{\gamma}'} = \delta_{\tilde{\gamma}\tilde{\gamma}'}\langle\hat{S}_{\tilde{\gamma}}\rangle$. This expression for the transverse Green's function is similar to the expression found by dynamical mean field theory [266], where the correlation function is found from the Landau-Lifshitz equation. The dispersion relation can be found analytically by diagonalising the matrix $A^{\tilde{\gamma}\tilde{\gamma}'}(\mathbf{q})$ and the Green's function found by calculating the matrix product on the right-hand side of Eqn. 5.9 on a grid in energy-momentum space. The dynamical structure factor can then be calculated via the fluctuation-dissipation theorem [57]

$$S(\mathbf{q},\omega) = -\frac{1}{\pi}\left(1+n(\omega)\right)\mathfrak{Im}\left[G(\mathbf{q},\omega)\right]. \tag{5.10}$$

The calculation of the transverse Green's function (Eqn. 5.9) requires knowledge of the matrix elements, $A^{\tilde{\gamma}\tilde{\gamma}'}$ and $B^{\tilde{\gamma}\tilde{\gamma}'}$. The low temperature A phase structure necessitates an eight site model, owing to the broken inversion symmetry. The matrix $\underline{\underline{B}}$ encodes the magnetic structure of the ground state in each phase (Fig.

5.1 (a, b)), and can be written as

$$\underline{\underline{B}}_A = \begin{pmatrix} -S & 0 & 0 & 0 & 0 & 0 & 0 & 0 \\ 0 & -S & 0 & 0 & 0 & 0 & 0 & 0 \\ 0 & 0 & S & 0 & 0 & 0 & 0 & 0 \\ 0 & 0 & 0 & S & 0 & 0 & 0 & 0 \\ 0 & 0 & 0 & 0 & S & 0 & 0 & 0 \\ 0 & 0 & 0 & 0 & 0 & S & 0 & 0 \\ 0 & 0 & 0 & 0 & 0 & 0 & -S & 0 \\ 0 & 0 & 0 & 0 & 0 & 0 & 0 & -S \end{pmatrix} \tag{5.11a}$$

$$\underline{\underline{B}}_B = \begin{pmatrix} S & 0 & 0 & 0 & 0 & 0 & 0 & 0 \\ 0 & -S & 0 & 0 & 0 & 0 & 0 & 0 \\ 0 & 0 & S & 0 & 0 & 0 & 0 & 0 \\ 0 & 0 & 0 & -S & 0 & 0 & 0 & 0 \\ 0 & 0 & 0 & 0 & S & 0 & 0 & 0 \\ 0 & 0 & 0 & 0 & 0 & -S & 0 & 0 \\ 0 & 0 & 0 & 0 & 0 & 0 & S & 0 \\ 0 & 0 & 0 & 0 & 0 & 0 & 0 & -S \end{pmatrix} \tag{5.11b}$$

in the A and B phase respectively, where $S = 5/2$. The matrix for the B phase can be written as a scalar matrix whose elements are 4×4 matrices, reflecting the inversion symmetry of the B phase magnetic structure. The mean molecular field can be calculated by expanding the spin operators around their expectation values (Eqn. 5.5). The presence of the bond inequivalence, $J_{1a} \neq J_{1b}$, and $J_{2a} \neq J_{2b}$, gives rise to two molecular mean field terms,

$$h_a^{MF} = -2J_{1a}S + 2J_{2a}S + 2J_3S + 2J_4S - 2\mu S \tag{5.12a}$$

$$h_b^{MF} = -2J_{1b}S + 2J_{2b}S + 2J_3S + 2J_4S - 2\mu S \tag{5.12b}$$

where the minus sign in front of the first term reflects the fact that J_{1a} and J_{1b} couple parallel spins, whilst the other exchanges couple spins that are anti-parallel. The matrix $A^{\tilde{\gamma}\gamma'}(\mathbf{q})$ consists of a contribution from the molecular mean field and from the Fourier transform of the exchange interaction, $\underline{\underline{A}} = \underline{\underline{A}}^{MF} +$

$\underline{\underline{A}}^{exch}$. Its matrix elements can be calculated using Eqn. 5.6b

$$\underline{\underline{A}}^{MF}_{A} = \begin{pmatrix} -h_a^{MF} & 0 & 0 & 0 & 0 & 0 & 0 & 0 \\ 0 & -h_a^{MF} & 0 & 0 & 0 & 0 & 0 & 0 \\ 0 & 0 & h_b^{MF} & 0 & 0 & 0 & 0 & 0 \\ 0 & 0 & 0 & h_b^{MF} & 0 & 0 & 0 & 0 \\ 0 & 0 & 0 & 0 & h_b^{MF} & 0 & 0 & 0 \\ 0 & 0 & 0 & 0 & 0 & h_b^{MF} & 0 & 0 \\ 0 & 0 & 0 & 0 & 0 & 0 & -h_a^{MF} & 0 \\ 0 & 0 & 0 & 0 & 0 & 0 & 0 & -h_a^{MF} \end{pmatrix} \tag{5.13a}$$

$$\underline{\underline{A}}^{MF}_{B} = \begin{pmatrix} h_a^{MF} & 0 & 0 & 0 & 0 & 0 & 0 & 0 \\ 0 & -h_a^{MF} & 0 & 0 & 0 & 0 & 0 & 0 \\ 0 & 0 & h_b^{MF} & 0 & 0 & 0 & 0 & 0 \\ 0 & 0 & 0 & -h_b^{MF} & 0 & 0 & 0 & 0 \\ 0 & 0 & 0 & 0 & h_b^{MF} & 0 & 0 & 0 \\ 0 & 0 & 0 & 0 & 0 & -h_b^{MF} & 0 & 0 \\ 0 & 0 & 0 & 0 & 0 & 0 & h_a^{MF} & 0 \\ 0 & 0 & 0 & 0 & 0 & 0 & 0 & -h_a^{MF} \end{pmatrix}. \tag{5.13b}$$

Finally, the contribution from the exchange term can be calculated by taking the product of $2\underline{\underline{B}}$ and the Fourier transform of the exchange interaction, which is the same for both phases,

$$\underline{\underline{A}}^{exch}_{A/B} = 2\underline{\underline{B}}_{A/B} \cdot \underline{\underline{\mathcal{J}}}(\mathbf{q}). \tag{5.14}$$

By diagonalising the matrix $\underline{\underline{A}}$ one can obtain an expression for the spin wave dispersion and the Green's function can be calculated using Eqn. 5.9.

A small imaginary offset is added to the energy, $\omega \rightarrow \omega + i\epsilon$ to give the intensity peak a finite width. The resultant lineshape takes the form of a Lorentzian of width $2\Gamma = 2\epsilon$, which in the low temperature analysis will be set to a value smaller than the instrument resolution.

The six shortest bonds have bond lengths of between 3.01-3.66 Å, therefore it is not clear by distance alone which should be the strongest. The shortest two bonds J_{1a} and J_{1b} are of the same length, both linking parallel spins along b, but are crystallographically inequivalent, with J_{1a} and J_{1b} forming the legs of

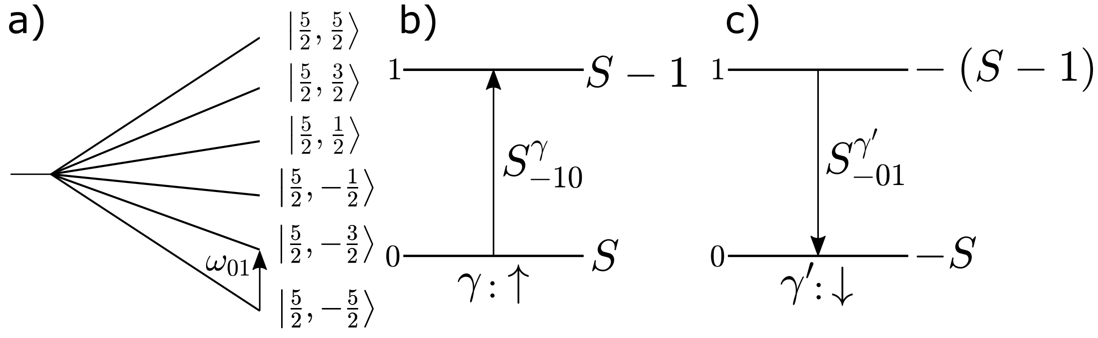

Figure 5.7 *(a) Visualisation of the splitting of the* $2S+1$ *single-ion energy levels for an* $S=5/2, L=0$ *ion, due to a molecular mean field. The separation between energy levels is given by* $\omega_{01}=\omega_1-\omega_0$*. (b), (c) The effect of the operation of* $\hat{S}^-$ *on sites in the* ↑ *(b) and* ↓ *(c) state [16].*

the blue and cyan zig-zag chains respectively. The presence of antiphase domain boundaries, and the near 90° Fe-O-Fe exchange path along a shared octahedral edge, indicates that the next two shortest bonds J_{2a} and J_{2b} are likely to be small [48]. The measurable dispersion along H and L (Fig. 5.5) is suggestive of a non-negligible J_3 and J_4. Thus in order to write down the minimal physically-motivated model, the six shortest bonds can be included (Fig. 5.1 (*a*)),

$$\underline{\underline{\mathcal{J}}} = \begin{pmatrix} J_{1a} & J_{2a} & 0 & J_3 & 0 & J_4 & 0 & 0 \\ J_{2a} & J_{1a} & J_3 & 0 & J_4 & 0 & 0 & 0 \\ 0 & J_3 & J_{1b} & J_{2b} & 0 & 0 & 0 & J_4 \\ J_3 & 0 & J_{2b} & J_{1b} & 0 & 0 & J_4 & 0 \\ 0 & J_4 & 0 & 0 & J_{1b} & J_{2b} & 0 & J_3 \\ J_4 & 0 & 0 & 0 & J_{2b} & J_{1b} & J_3 & 0 \\ 0 & 0 & 0 & J_4 & 0 & J_3 & J_{1a} & J_{2a} \\ 0 & 0 & J_4 & 0 & J_3 & 0 & J_{2a} & J_{1a} \end{pmatrix}. \tag{5.15}$$

The MERLIN data at T = 5 K were fitted using `Horace` [252] with values of μ, J_{2a} and J_{2b} fixed. The `Tobyfit` package was used to account for the resolution function on MERLIN and contributions from the guide, chopper and moderator were considered. In accordance with the conclusion that the underlying magnetic order is B phase, a B phase only model was used. These parameters were then refined by fitting the LET data using the values obtained from the MERLIN fit. This process was iterated until good agreement was achieved. The effect of taking $J_{2a} \neq J_{2b}$ is to open a gap at the crossing point along L (Fig. 5.8). Such a gap is not seen in the data so the assignment is made $J_{2a} = J_{2b} = J_2$. The refined values of the exchange constants are listed in Table 5.2. The dominant exchange

Table 5.2 *Fitted exchange constants, J_i, and anisotropy parameter, μ, for the bonds labelled in Fig. 5.1 (a).*

J_i	Distance (Å)	Value (meV)
J_{1a}	3.018	0.03(1)
J_{1b}	3.018	0.38(1)
J_{2a}	3.077	0.047(2)
J_{2b}	3.096	0.047(2)
J_3	3.570	3.4(3)
J_4	3.659	3.2(3)
μ	-	-0.035(1)

couplings were determined to be J_3 and J_4, with J_2 confirmed to be small. The frustrated nature of the bonds J_{1a} and J_{1b} gives rise to the arch-like dispersion at (-2,0,L) (Fig. 5.6), which is well reproduced in this model (Fig. 5.9) . Crucially, J_2 was determined to be small, $J_2 < 0.05$ meV, meaning that the creation of an antiphase boundary carries a small energy cost and thermal fluctuations at high temperature can overcome this barrier, thus explaining the significant fraction of dynamical diffuse scattering [15].

The effect of nonzero J_2 warrants some consideration. In one of the two magnetic structures, this bond is expected to be frustrated and hence two copies of the dispersion curve along c^* would be expected (with a different gap and bandwidth) if both phases were to contribute to the signal along c^*. No such duplication of modes is observed (Fig. 5.8 (a)). Furthermore, it can be ruled out that $J_2 < 0$ since the mode whose minimum lies at $Q = (2, 0, 0)$ carries the most spectral weight contrary to the calculation (Fig. 5.8 (c)). This is in agreement with the conclusion based on the neutron diffraction data. Finally, the dispersion along all other directions, along with the measured anisotropy gap put strong constraints on the values of the exchange parameters. With positive J_2, the magnitude of anisotropy required to stabilise spin waves in the A phase is inconsistent with the observed gap from RITA II (Fig. 5.3), LET (Fig. 5.5 (a, b)) and MERLIN (Fig. 5.5 $(c - f)$). It is thus concluded that the low temperature A phase is metastable in this single crystal sample. This phase obtains a long lifetime due to the anisotropy, which prevents the relaxation of the antiphase domain boundary disordered high temperature state into the B phase ground state structure. The extracted exchange constants do not give rise to stable A phase spin waves, as shown in Fig. 5.8 (d). Note that in the powder samples, the story need not be identical, with an expected increased value of μ due to the inevitable finite

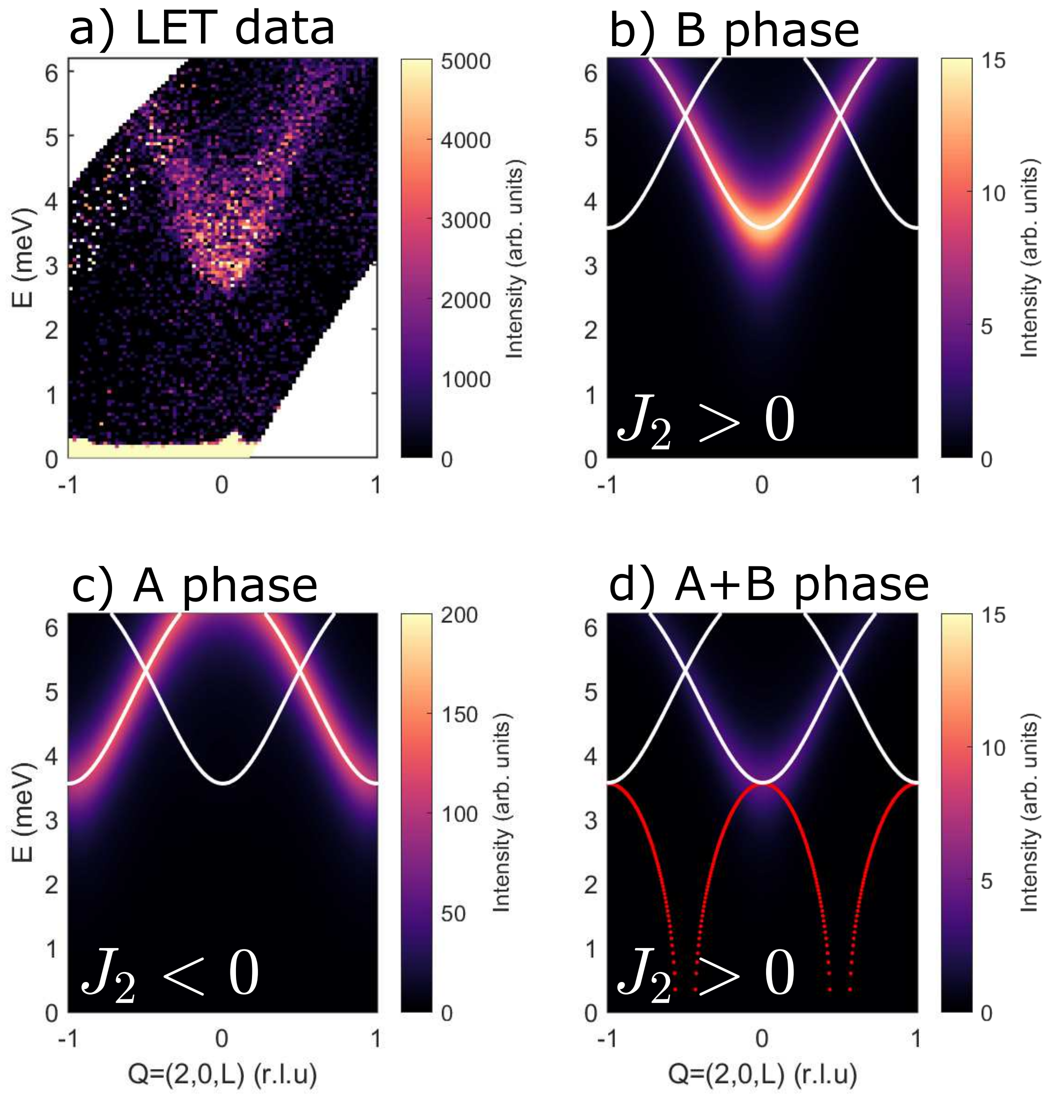

Figure 5.8 *Comparison of calculated dispersion along c^* against (a) the data from LET at $T = 5$ K for a model consisting of (b) B phase order with antiferromagnetic J_2, (c) A phase order and (d) A and B phase order in a 2:1 ratio. It is clear that for $J_2 < 0$ the mode that is maximal at $Q = (2,0,0)$ lights up, in contrast to the data. Furthermore, for $J_2 > 0$ the A phase leads to imaginary eigenvalues (red dispersion) using the fitted values unless μ is large.*

strain induced by the grinding of the powders, it may in fact be possible to stabilise spin waves in the A phase, despite the lower energy of the B phase configuration. Indeed, the smaller magnitude of the anisotropy gap measured in the low temperature phase [24] as compared to single crystals (Fig. 5.3) could be due to the suppression of the gap originating from the frustrated J_2 bond. Attention is now turned to the T = 175 K data.

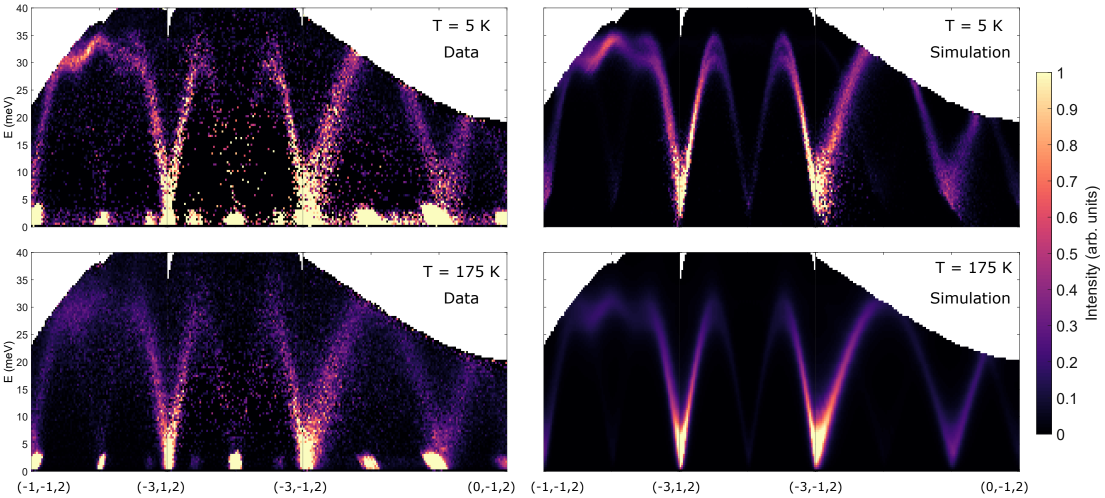

Figure 5.9 *(a) Constant Q plot of a path through reciprocal space at $T = 5$ K, showing strongly dispersing excitations in the (H,K) plane. (b) Simulation of the data using the resolution convoluted Green's function model and the fitted parameters. (c) $T = 175$ K data. (d) Simulation at $T = 175$ K. The intensities for both datasets have been corrected for the Bose factor.*

It was explained earlier in Section 5.2.1 how the magnetic A phase arises, not as a distinct phase in the bulk but locally in antiphase boundaries between different B phase domains. This explanation, of the low temperature A phase not existing in bulk, means that its formation is not driven by, for example, a change in sign of J_2 arising from a change in crystal structure. It should be noted that, although the c lattice constant does show some temperature dependence [24], this is on the order of 10^{-2}Å and hence is unlikely to affect either the sign or magnitude of J_2. In the absence of temperature dependence of the exchange parameters, the primary effects of the increased temperature should be the damping and renormalisation of the spectrum due to higher order terms in the Dyson series. The damping can be accounted for phenomenologically by increasing the value of ϵ, thereby increasing the Lorentzian linewidth [267]. The renormalisation takes the form of a reduced spin moment and can be treated straightforwardly by renormalising the exchange parameters and the anisotropy parameter, $\{\mathcal{J}_{ij}, \mu\} \to \{\gamma\mathcal{J}_{ij}, \gamma\mu\}$, where γ is some constant between zero and unity. This follows from the fact that S is a dimensionless parameter and so only appears in the dispersion as a multiple of an exchange or anisotropy parameter, allowing the renormalisation factor to be absorbed into the exchange parameters. As discussed in Section 5.2.2, the anisotropy gap shows an anomalous temperature dependence and so a further suppression of μ beyond that expected by spin moment renormalisation alone is expected. Fixing the fitted low temperature exchange parameters and setting $\epsilon = 2.5$ meV, an overall renormalisation factor, $\gamma = 0.930(4)$, was fitted showing excellent agreement with the data (Fig. 5.9). At high temperature, the $Q = (1, 0, 1)$ neutron diffraction peak is not resolution limited and the width is expected to vary in both energy and momentum due to magnon-magnon and magnon-soliton interactions [268]. The value of ϵ was selected according to the approximate width of the peak at the zone boundary. Using the value of the anisotropy gap at T = 175 K, the Hamiltonian was diagonalised with the fitted renormalised exchange parameters and solved for the high temperature anisotropy parameter $\mu_{175\mathrm{K}} = -0.0098(2)$ meV.

From the fitted exchange parameters the Curie-Weiss temperature can be estimated

$$k_B \Theta_{CW} = \frac{1}{3} S(S+1) \sum_n J_n, \tag{5.16}$$

where the sum is over nearest neighbours. Due to the inequivalence of J_{1a} and J_{1b}, the average of their fitted values is taken. The expression above stems from a mean field treatment of the single-ion, and hence a minus sign is attached to the frustrated J_{1a} and J_{1b} bonds. Evaluating Eqn. 5.16, it is found that $\Theta_{CW} \approx 435$ K. It should be noted that this is significantly larger than that found by Das *et al* [240], and much larger than the magnetic ordering temperature of T $\approx$ 200 K. However, one should note that the loss of correlations along c, owing to the small value of J_2 renders $\mathrm{CaFe_2O_4}$ quasi-two-dimensional at high temperatures. The absence of spontaneous symmetry breaking for $d \leq 2$ [50] thus makes long-range order marginal. Long-range order is stabilised by the presence of single-ion anisotropy, however the vanishing of the gap at T = 200 K, due to the cooperative effect of spin moment renormalisation and subtle magnetoelastic changes to the local crystalline environment, precludes any long range magnetic order above this temperature. The large Curie-Weiss temperature also explains the relatively modest renormalisation of the bandwidth, with an observed moment reduction of $\sim 10\%$ at T = 175 K, despite the proximity to the magnetic ordering temperature.

5.4 Conclusion

In this chapter it has been shown that the magnetic phase coexistence in $\mathrm{CaFe_2O_4}$ can be understood as originating from a parent B phase magnetic order with local A phase order arising due to the freezing of antiphase boundaries which become static below T $\approx$ 100 K. This is consistent with the lack of temperature dependence of the acoustic phonon linewidth, which is sensitive to instabilities in the crystal structure which would lead to changes in the magnetic structure. Neutron scattering data have been presented showing the temperature dependent opening of the anisotropy gap, which stabilises the low temperature A phase order. It was then shown that the magnon excitations are qualitatively consistent at high and low temperature, albeit broadened at high temperature by the dynamical antiphase boundaries. Using a Green's function formalism, it was shown that the spectrum can be modelled with the same exchange constants in both phases, save for a renormalisation factor at high temperature, but with two different anisotropy parameters owing to the anomalous temperature dependence of μ. The extracted exchange constants are consistent with the picture of antiphase boundary freezing, with a small value of J_2. By analysis of the spectrum, it was shown that stable spin waves cannot exist in the A phase and that this phase is metastable, frozen-in at low temperatures due to the growth of the single-ion anisotropy. The anisotropy acts to lock the antiphase boundaries in place, preventing relaxation of the magnetic structure back to the ground state B phase order.

Chapter 6

Anisotropy induced domain walls in the 2-d ferromagnet Fe_3GeTe_2

6.1 Introduction

Magnetism in two dimensions is rare owing to the restrictions of the Mermin-Wagner theorem [50] which precludes the spontaneous breaking of continuous symmetry in $d < 3$. Stable magnetism in low-dimensional materials at finite temperature is therefore usually contingent on magnetic interactions which explicitly break spin-rotational symmetry, or a weak inter-layer coupling. An instructive example is the case of $CaFe_2O_4$, discussed in Chapters 3 and 5, where the coupling along c is very weak. At temperatures exceeding the characteristic temperature of the c-axis coupling, where the correlations are essentially quasi-two-dimensional, magnetism is stabilised by the magnetic anisotropy. At temperatures greater than the energy scale of the magnetic anisotropy, the gap in the magnon spectrum is observed to close and magnetism is lost [5].

In the van der Waals magnet CrI_3, magnetism is stabilised by a second-nearest neighbour DM interaction which breaks spin-rotational symmetry and favours alignment of the spins out of the plane [269]. These interactions find their origin in the single-ion physics of the Cr^{3+} ions, specifically the spin-orbit interaction, as detailed in Chapter 1. Another trihalide compound will be discussed in Chapter 7 which owes its magnetic order to a single-ion anisotropy [4].

The understanding of magnetism in two dimensions is of great interest owing to the significant advances in heterostructure fabrication which promise to lead to a growing field yielding novel quantum devices that exploit magnetic interactions [270]. In this chapter, the nature of two-dimensional magnetic order in the itinerant ferromagnet Fe_3GeTe_2 is explored. Using neutron scattering the low energy spin wave excitations in the (H, H, L) plane are mapped out, demonstrating a significant broadening away from the magnetic zone centre. The nature of the bulk magnetism is then compared with the surface by modelling the magnetic domain walls classically. By comparing the expected domain wall profile with that extracted from the STM measurements of C. Trainer, O. Armitage, I. Benedičič and P. Wahl, the bulk-surface correspondence is examined showing little difference in exchange and anisotropy strength.

Fe_3GeTe_2 is a layered van der Waals magnet, comprising layers of two-dimensional sheets of Fe_3Ge, weakly bonded by van der Waals coupling to the intervening Te layers. The crystal structure is best understood as a hexagonal Fe^{3+} lattice but with one of the two sublattices duplicated along the c-axis (Fig. 6.1). The compound can be synthesised in a number of different ways, including flux growth [271, 272], molecular beam epitaxy [273], solid state solution [274] and chemical vapour transport [275, 276]. The crystals have a hexagonal morphology and differ in size depending on the growth method with the flux-grown samples typically bigger than those grown by chemical vapour transport [272], for example. The difference between flux-grown samples and those grown via vapour transport are not limited to the size, but also the composition, with an off-stoichiometry ($Fe_{3-y}GeTe_2$) that varies between samples. For flux-grown samples, a large Fe deficiency is typical with $y \approx 0.3$ [271, 272, 277]. In samples grown by vapour transport, the samples can in fact be almost stoichiometric [272, 275]. The known properties of Fe_3GeTe_2 are now discussed, with particular reference paid to the influence of synthesis technique and Fe concentration.

Magnetisation measurements show that Fe_3GeTe_2 orders ferromagnetically below room temperature, in the range T = 150-230 K. The ordering temperature varies between different samples, with flux-grown samples typically ordering at a lower temperature [271, 277] and those grown by molecular beam epitaxy [273], solid state solution [274] and chemical vapour transport [275, 276] ordering at higher temperature. The stoichiometric sample was found to order at T = 220 K [275]. Samples with increased Fe concentration, $Fe_{3.10}GeTe_2$, have a yet higher ordering temperature of T = 232 K [271]. The ferromagnetic transition appears to be somewhat sharper in the samples that order at a higher temperature [17, 275] than those which order at a lower temperature [271, 272]. Specific heat measurements

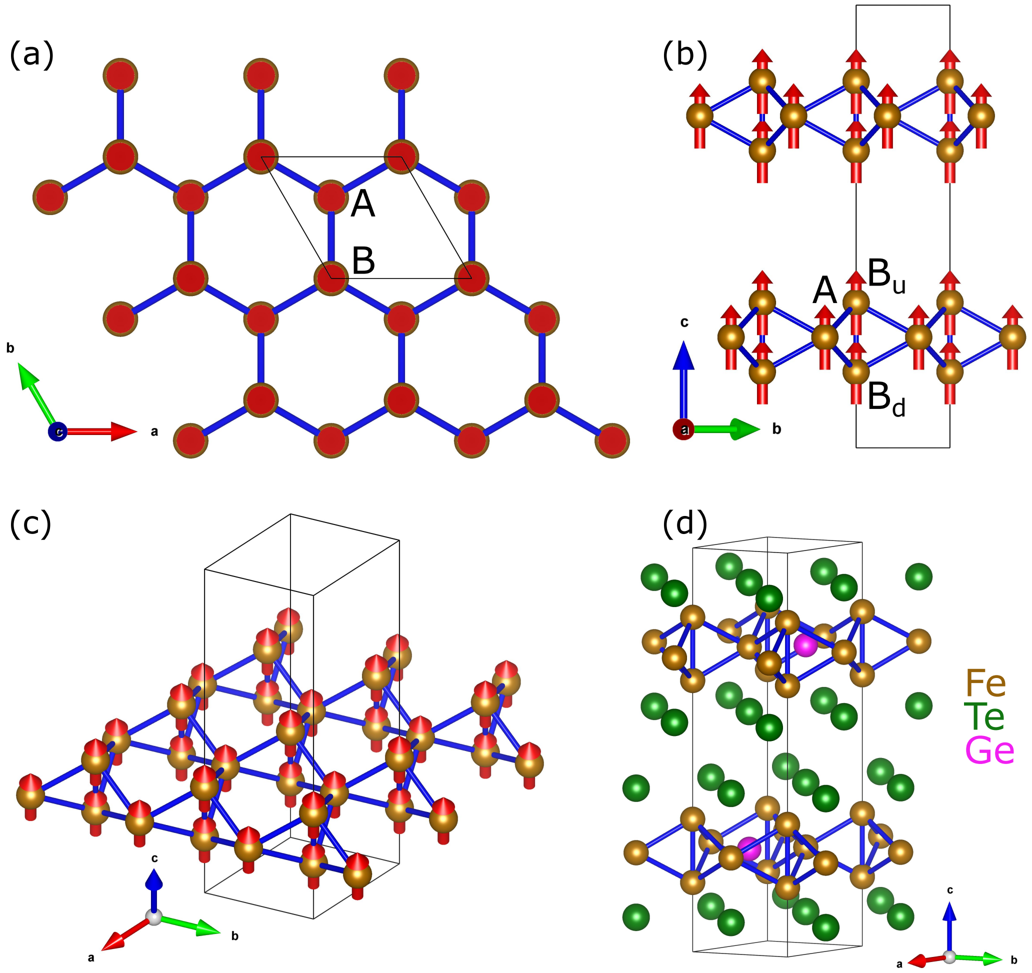

Figure 6.1 *(a) Schematic of the crystal structure of a single layer of* Fe_3GeTe_2 *as viewed from above, with only the* Fe^{3+} *ions plotted. Fe-Fe bonds are indicated in blue and show a hexagonal structure when viewed from above. Labelled are the two sublattices conventionally defined for the hexagonal lattice. (b) The crystal structure as viewed from the a-axis. A doubling of the B sublattice along c is seen and each of these sites are given a subscript* $B_{\mathrm{u/d}}$*. (c) A perspective view of the Fe bonds, demonstrating the quasi-hexagonal structure. (d) Crystal structure of* Fe_3GeTe_2 *with all atoms in the unit cell plotted. The structure takes the form of* Fe_3Ge *planes with Te between the layers.*

have been performed on both flux-grown [271] and chemical vapour transport grown samples [275]. In the vapour transport grown samples [275], a clear feature is observed at the ferromagnetic transition temperature. In contrast, measurements on flux-grown samples [271] show a much smaller anomaly at the ferromagnetic transition temperature, suggesting a broader transition to ferromagnetic order, in agreement with magnetisation measurements. The fitted Sommerfeld coefficient is broadly consistent across samples grown by both techniques [271, 275], $\gamma \approx 130$mJ/mol/K^2, and is significantly larger than that observed in Ni$_{3-x}$GeTe$_2$, $\gamma \approx 10$mJ/mol/K^2 [271], potentially indicating a large contribution from spin fluctuations.

Neutron diffraction measurements determined the magnetic structure of Fe$_3$GeTe$_2$ to be ferromagnetic, with spins oriented along c and a ferromagnetic inter-layer coupling [271]. In the study by May *et al* [271] no difference in the magnetic structure was found in samples of differing iron concentrations, save for an decreased intensity of the magnetic Bragg peaks in the iron deficient samples [271], consistent with a reduced magnetic moment on the Fe sites.

A key difference between iron rich and iron deficient sampled appears to be the magnetic moment, in that both magnetisation measurements [271, 272, 274, 275] and neutron diffraction [271, 272] indicate a decreased magnetic moment in the iron deficient samples. A further complication is suggested in the iron rich samples where magnetic refinements [271] and neutron scattering data [277] indicate the possibility of inequivalent Fe sites and a mixed valance structure [274, 276].

Inelastic neutron scattering experiments have been performed on flux-grown samples [272, 277] yet none have been carried out on those grown by vapour transport. This is likely due to the typical relative size of flux and vapour transport grown samples, with those grown by flux significantly larger in size than the vapour-grown crystals [272]. The excitations are shown to be broad in nature, reflecting the itinerant character of the magnetism in Fe$_3$GeTe$_2$. A parabolic dispersion is observed out of the magnetic zone centre, consistent with ferromagnetic interactions. A gap in the neutron scattering spectrum is seen, consistent with single-ion anisotropy. The magnitude of the gap was initially reported to be $\Delta \approx 3.7$ meV [277], but a later study on a compound of similar stoichiometry suggested that the excitations were almost gapless ($\Delta \sim 0.5$ meV) [272]. The apparent inconsistency was suggested to be the result of using a large integration range along c^*, given a finite out-of-plane dispersion [272]. There is some disagreement regarding the strength of correlations between layers, with Ref. [277] concluding that the excitations are essentially two-dimensional and Ref. [272] suggest a sizable inter-layer coupling. Away from the high symmetry point, extending above 100 meV, a columnar continuum of scattering is observed, indicative of particle-hole scattering between spin-up and spin-down bands [272] – a consequence of the the itinerant nature of the magnetism. The key influence of itinerance on the coherent spin-wave excitations is also seen in the weakening of Kondo screening at high temperatures [272]. This surprising effect leads to a sharpening of excitations as the temperature is increased and the electrons that screen local moments become less tightly bound. Evidence of Kondo lattice behaviour has also been observed in angle-resolved photoemission spectroscopy (ARPES) measurements, where the electron screening at low temperature is seen by the increase in the effective electron mass [278].

The properties of the sample used in this study are now summarised. Neutron diffraction measurements were carried out by E. Chan at the Institut Laue-Langevin on the hot neutron four-circle diffractometer D9 [279]. The nuclear and magnetic structure was refined with nuclear space group $P6_3/mmc$. An iron stoichiometry of $3 - y = 2.86(3)$ was found from the 60 K data set. The best refinement of the magnetic structure was achieved with the $P6_3/mm'c'$ magnetic space group, indicating a ferromagnetic alignment along the c-axis. In contrast to Refs. [274, 276, 277] the magnetic moments for both Fe sites were found to be equal with a magnetic moment $\mu = 1.6(2)\mu_B$ at T = 30 K. By tracking the intensity of the Bragg peak, the ordering temperature was extracted and determined to be T = 215(2) K, much larger than in the flux-grown samples studied in previous neutron scattering experiments [272, 277].

6.2 Experimental details

Neutron scattering measurements were performed on the MACS cold triple axis spectrometer (NIST, Gaithersburg) [280]. Single crystals of Fe_3GeTe_2 with varying size were edge-aligned on aluminium plates, using the hexagonal morphology as a guide[1]. A coating of hydrogen-free Fomblin oil was applied to the crystals to attach them to the mount and prevent degradation in air. The sample mount was positioned such that the (H, H, L) reflections lay in the horizontal scattering plane. The sample was then cooled to T = 5 K in a 100 mm bore Orange Cryostat. E_f was fixed to 3.7 meV by 20 PG(002) double bounce analyzers and E_i was varied between 4.3 meV and 13.7 meV by a vertically focused PG(002) monochromator, giving access to energy transfers between 0.5 meV and 10 meV. Cooled BeO filters were placed on the scattered side of the sample to remove contamination from higher order scattering. This

---

[1] The vectors along the hexagonal bonds in real space correspond to the a^* and b^* axes in reciprocal space.

experimental configuration allowed for an energy resolution of approximately 0.17 meV (FWHM) at the elastic line.

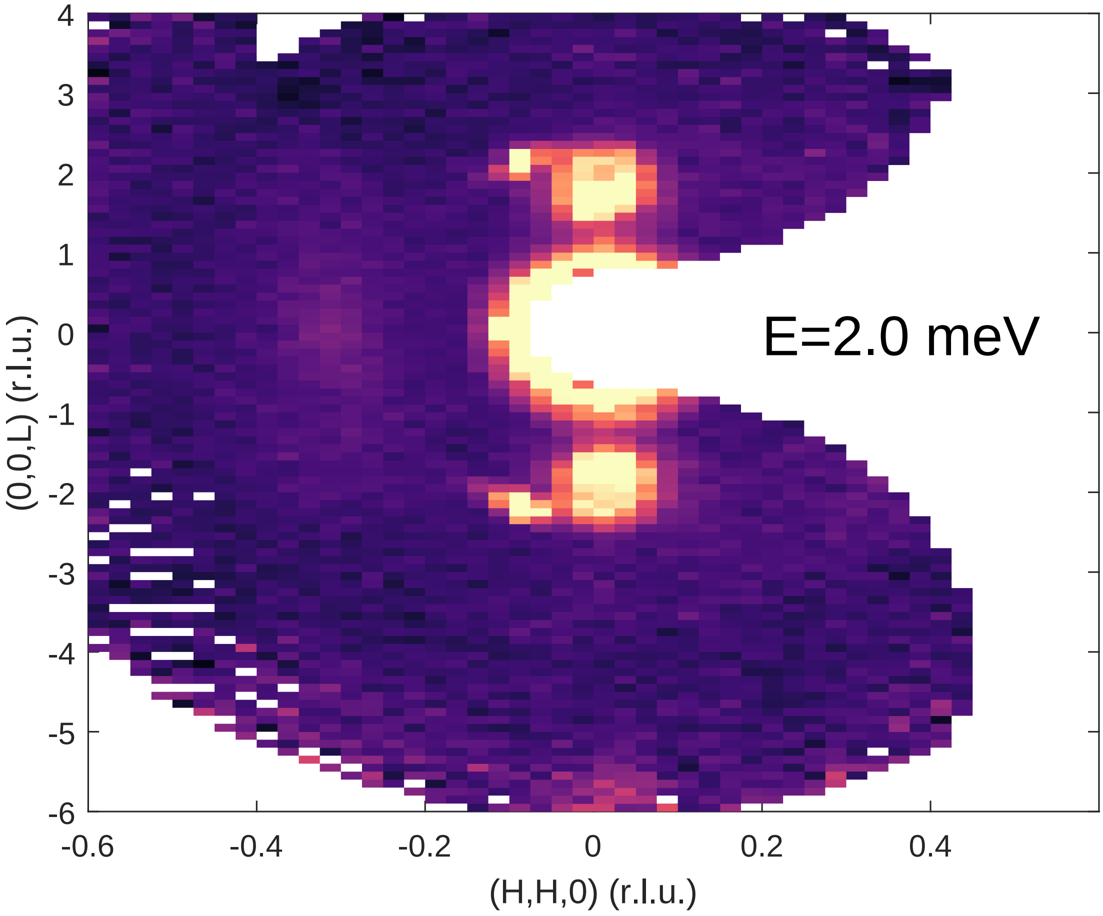

Figure 6.2 *Constant energy cut with $E = 2.0$ meV. The background has been subtracted as described in the text. Scattering is seen at the $(-2, -2, \pm 2)$ positions, with spurious signal visible proximate to this positions.*

6.3 Magnetic excitations

Background subtraction was performed by assuming the background intensity to be dependent only on the scattering angle (2θ) – conventionally referred to as A4 on TAS instruments. A region of scattering, far from any signal, was taken and the intensity was radially averaged in steps of constant $|Q|$ to produce a background for each E_f. This differs from the standard approach on TAS instruments where an empty can measurement is typically used but was necessitated due to the complex nature of the scattering caused by the Fomblin and sample mount geometry. Such an approach has been used with great success for other similar coaligned crystal mounts [18, 19]. Fig. 6.2 shows the scattering at a fixed energy transfer $\Delta E = 2.0$ meV. Scattering can be seen emanating from the $(-2, -2, \pm 2)$ positions, with evidence of a spurious signal on the $-H$ side. Given the proximity to the Bragg peak, it is likely that this is a Bragg tail [56] resulting from the resolution function overlapping with the Bragg peak.

A two-dimensional map of the scattering intensity for $(H, H, -2)$ was constructed by integrating over c^* in a 0.3r.l.u. window about $L = -2$ (Fig. 6.3). The scattering in the $[H, H]$ direction is shown to be ferromagnetic in nature, dispersing quadratically from $(0, 0, -2)$. The excitations are observed to be broad in nature, as expected for a magnet whose spins are not entirely localised and show a degree of itinerance. This itinerant nature is also manifested in a reduced spin moment, resolved by neutron diffraction to be $\mu = 1.6(2)\mu_B$ [17], consistent with an effective spin magnitude of $S = 0.8$. There is a small spectral gap ≈ 1 meV,

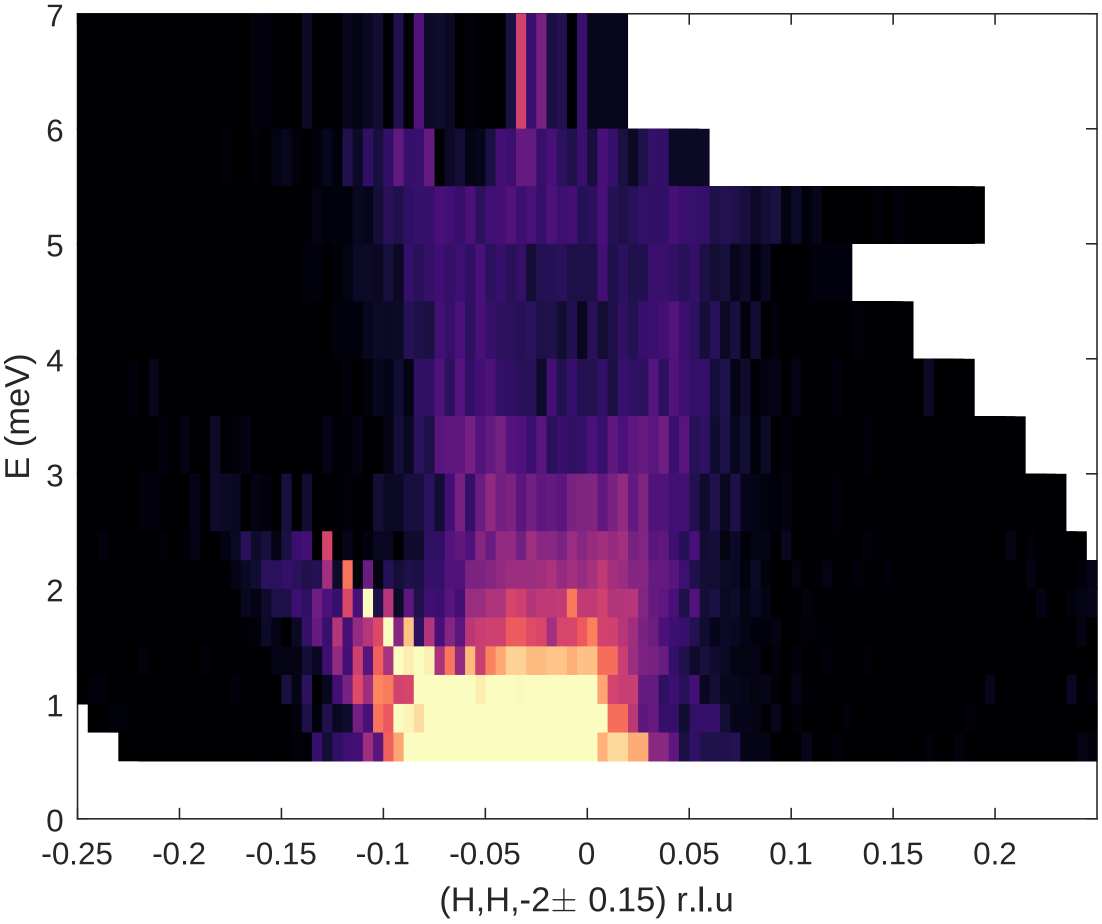

Figure 6.3 *Dispersion for $(HH-2)$ showing broad excitations emanating from the $(0, 0, -2)$ Bragg point. The data indicate an anisotropy gap ≤ 1 meV.*

indicative of a single-ion anisotropy. It should be noted that the anisotropy gap is slightly larger that measured in Ref. [272]. It should once again be noted that the anisotropy gap reported in Ref. [277] is even larger $\Delta = 3.7$ meV, though this may be an artifact from the integration range chosen, as discussed earlier. Fig. 6.4 shows the scattering for $(0, 0, L)$, which appears to be very broad in nature. It should also be noted that the slope of the dispersion is much shallower than in the $[H, H]$ direction. This is more clearly displayed in Fig. 6.5 in which $(H, H, -2)$ and $(0, 0, L)$ constant-$\mathbf{q}$ cuts are plotted on axes with scales adjusted for the reciprocal space periodicity. The shallower nature of the excitations for $(0, 0, L)$ indicates a much-reduced bandwidth compared with the scattering in the (H, H) plane. The excitations are also observed to be significantly broader (Fig. 6.5). This indicates the nature of magnetism in Fe_3GeTe_2 to be predominantly two-dimensional in nature, yet with a finite dispersion along L. The data presented here differ from the findings of Ref. [272] where the spin wave stiffness both in and out of the plane were found to be comparable. Such a dependence on

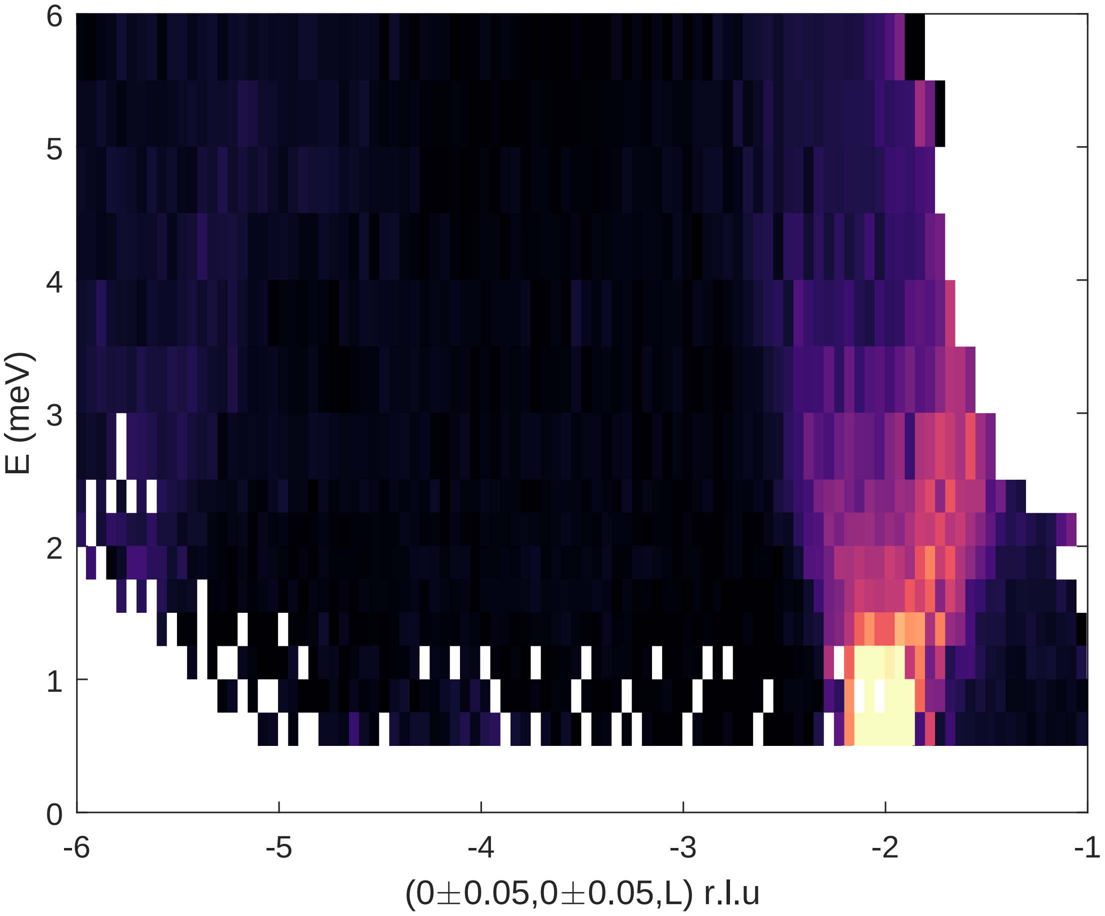

Figure 6.4 *Dispersion along* $(00L)$*, showing broad magnetic excitations emanating from* $(00-2)$*.*

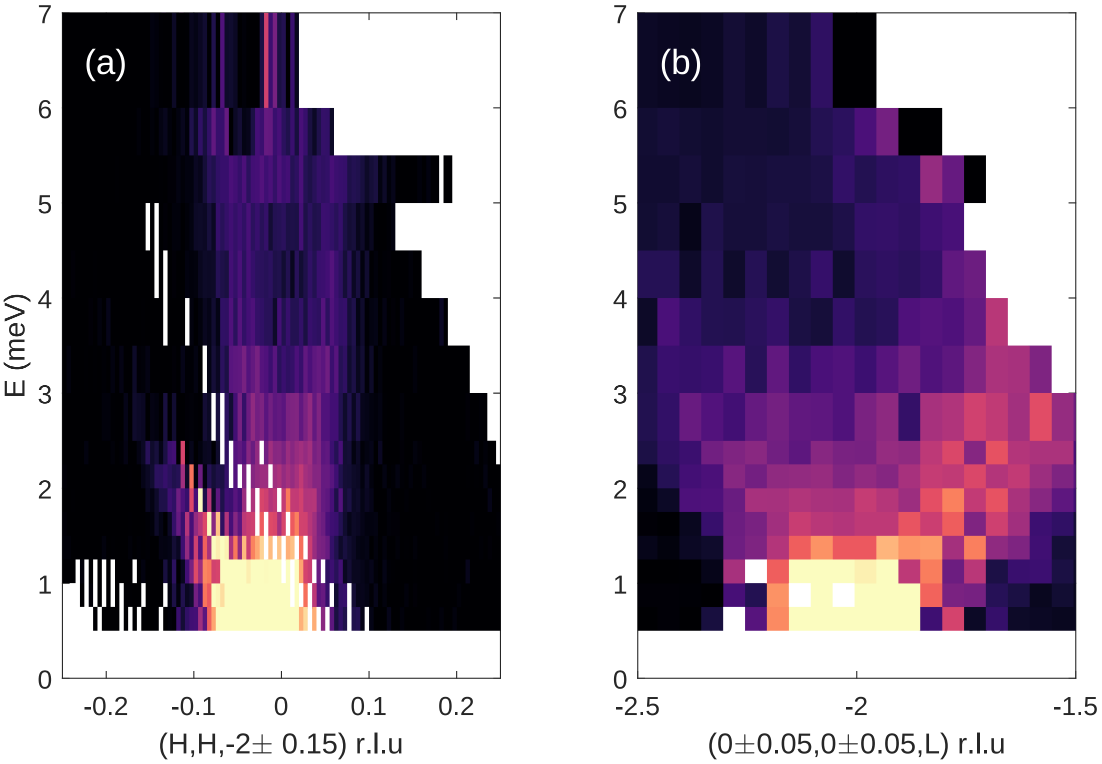

Figure 6.5 *Dispersion along (a) $(H, H, -2)$ and (b) $(0, 0, L)$. The x-axis range of (a) is half that of (b) to reflect the fact that each unit cell contains two Fe_3Ge sheets (Fig. 6.1 (d)).*

the iron concentration is to be expected, given the large distance between Fe_3Ge layers and intervening Te layers, which suggests that any interaction is likely to be be indirect, facilitated by the itinerant electrons. This may in turn explain why the excitations out of the plane are so broad in nature. In passing it is noted that Density Functional Theory calculations support this suggestion and show that the bands of minority character are three-dimensional in nature, whilst the majority character bands are two-dimensional. The minority spin bands carry a significant weight from the Te ions, particularly above the Fermi level [17].

Motivated by the predominantly two-dimensional nature of the excitations in Fe_3GeTe_2 a two-dimensional spin wave model is now introduced. Since STM measurements are only sensitive to the surface, the data will be modelled using a simple hexagonal lattice model. The validity of the mapping of Fe_3GeTe_2 onto a hexagonal model depends on the fact that the crystal structure has the $P6_3/mmc$ space group, the inter-layer coupling is weaker than the intra-layer coupling and the intinerant nature of the excitations, which dictates that only the small-$\mathbf{q}$ limit is modelled. In practice, any qualitative difference in the dispersion between a hexagonal model and the true lattice model (including the duplication along c)

is confined to the zone boundary, far out of the kinematic range of the cold triple-axis spectrometer. A full exposition of the validity of the mapping onto the hexagonal spin model is given in Appendix E.

The Hamiltonian for a hexagonal ferromagnet with a nearest-neighbour ferromagnetic Heisenberg coupling and easy-axis anisotropy is given by

$$\mathcal{H} = J \sum_{\mathbf{r}}^{j\in\{0,1,2\}} \mathbf{S}_A(\mathbf{r}) \cdot \mathbf{S}_B(\mathbf{r}+\mathbf{a}_j) + K[(\hat{S}^z_A(\mathbf{r}))^2 + (\hat{S}^z_B(\mathbf{r}))^2]. \tag{6.1}$$

Here, J is the nearest-neighbour interaction, $K > 0$ is an easy-axis magnetic anisotropy, $\mathbf{S}_{A,B}$ is the spin operator acting on sublattice A or B and the vectors $\mathbf{a}_0 = (0,0)$, $\mathbf{a}_1 = (0,1)$ and $\mathbf{a}_2 = (1,1)$ span between the unit cells containing nearest-neighbour spins (in the $P6_3/mmc$ space group). Further nearest neighbours are neglected since their effect in the limit of small $|\mathbf{q}|$ is a simple renormalisation of the spin-wave velocity and anisotropy gap. The eigenvalues obtained from the model are

$$E^{\pm}_{\mathbf{q}} = v_S \pm |\gamma_{\mathbf{q}}| \tag{6.2}$$

with $v_S = -(3JS + 2KS)$ and $\gamma_{\mathbf{q}} = JS\sum_j e^{i\mathbf{q}\cdot\mathbf{a}_j}$ where S is the spin [281, 282] (a full derivation is given in Appendix E). With a wavevector of $\mathbf{q} = (H, H)$, where H is here used to parametrise the reciprocal lattice vector, the dispersion is quadratic for small H,

$$E \approx v_S \pm 3JS \pm 4\pi^2 JSH^2. \tag{6.3}$$

For the purpose of extracting the exchange parameters and anisotropy, Gaussian peaks have been fitted to a series of constant energy cuts in the $(H, H, -2)$ plane through the MACS data to obtain the magnon dispersion (Fig. 6.6 (a)). The exchange coupling can be determined from the prefactor, $4\pi^2 JS$, of the quadratic term. Taking the reduced value of $S = 0.8(1)$, the fit yields $J \approx 43(10)$ meV and $|K| \approx 0.6(1)$ meV. The magnetic anisotropy is non-negligible, consistent with previous reports [276, 283]. This would indicate a small difference between vapour-grown and flux-grown samples, since the neutron experiments in Ref. [272] performed on the latter were unable to resolve a spin gap and surmised that the anisotropy gap must be $\Delta \approx 0.5$ meV [272]. The difference in implied single-ion anisotropy strength between the samples in this study with $y = 0.14$

and the more iron deficient samples studied in Ref. [272] (with $y = 0.28$) cannot be accounted for solely by the difference in spin magnitude since the spin moment in the flux-grown samples is reduced by approximately 10-20% [271] whereas the observed gaps differ by around a factor of two [272].

6.4 Domain walls

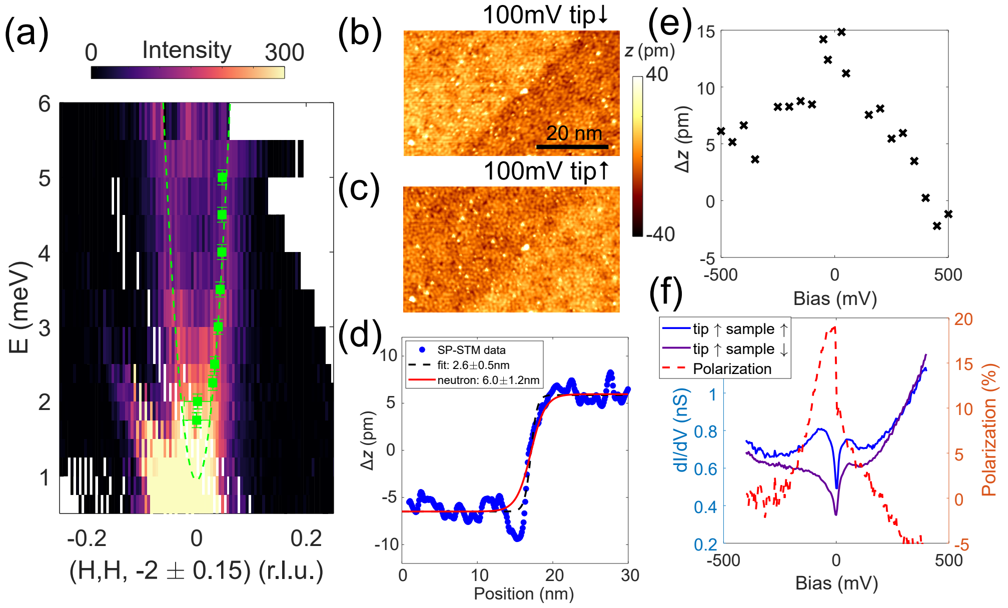

Figure 6.6 *(a) Neutron scattering measurements of the spin wave dispersion of* Fe_3GeTe_2 *around* $\mathbf{q} = (H, H, -2)$*. The green line represents a parabolic fit to the data. The fit results in* $J \approx 43(10)$ *meV and* $K \approx 0.6(1)$ *meV. (b) A ferromagnetic domain wall imaged using spin-polarised STM (*$V_s = 100$ *mV,* $I_s = 125$ *pA). The domain wall runs diagonally through the image. (c) The same region of the sample as in (b) imaged with a spin-polarised STM tip with the opposite spin polarisation from that used in (b) (*$V_s = 100$ *mV,* $I = 125$ *pA). (d) A line profile* $z(x)$ *taken through the difference of images (b) and (c) perpendicular to the domain wall. The red line shows the calculated domain wall profile (Appendix F) from the bulk exchange parameter. (e) The height difference* Δz *recorded between oppositely polarised areas as a function of applied bias voltage. (f)* dI/dV *spectra (blue curve) recorded on either side of the domain wall shown in (b) and (c) (*$V_s = 400$ *mV,* $I = 250$ *pA,* $V_{\text{mod}} = 3$ *mV). The spectroscopy set-point was chosen at a bias voltage where the domain wall was not visible. The resulting spin polarisation determined from the* dI/dV *spectra is shown by the red curve. Figure reproduced from Ref. [17].*

Attention is now turned to the domain wall dynamics of Fe_3GeTe_2. The formation of ferromagnetic domain walls is driven by the minimisation of the magnetic field energy. The termination of the magnetisation at a surface gives rise to a magnetic field, which can be minimised by the formation of domains which minimise the divergence of the magnetisation such that the resulting magnetic energy is similarly minimised [284]. The width of the induced domain walls is a function of the competition between the exchange stiffness, which promotes coalignment (and therefore a gradual rotation of spins such that $\mathbf{S}_i \cdot \mathbf{S}_j$ is maximised) and the anisotropy energy, which would favour a sharp domain wall with spins aligned closely to the easy-axis.

Given that the domain wall width is dictated by the exchange and anisotropy energy scales, it is therefore possible to infer the relative strengths of these two contributions by directly measuring the domain wall width on the surface of the crystal. However, it should be noted that one would expect the extracted exchange and anisotropy energies to be different on the surface in comparison to the bulk. Naïvely, one might expect the exchange stiffness to be different at the surface than in the bulk, as the indirect exchange paths are reduced owing to the termination of the crystal structure at the surface. Additionally, the anisotropy is likely to be stronger owing to the extreme asymmetry present at the surface. In this section, the parameters extracted from neutron scattering (reflective of the bulk exchange and anisotropy values) are compared to those implied by the measured surface domain wall widths extracted from STM measurements. By comparing the expected domain wall width based on the bulk exchange parameters with the STM measurement, one can compare the relative strengths of the anisotropy and exchange stiffness both in the bulk and at the surface.

STM measurements were performed by C. Trainer, O. Armitage and I. Benedičič at the University of St Andrews. The measurements were taken using instrumentation constructed at the University of St Andrews [285, 286] operating at temperatures down to 1.5 K. Further details can be found in Ref. [17]. STM measurements probe the local electronic density of states via $\frac{dI}{dV}$, the derivative of the tunnelling intensity with respect to the tip voltage. Spin-polarised STM was used to directly image the domain walls in Fe_3GeTe_2. By employing a feedback system to hold the current (and hence tunnelling intensity) and voltage constant by varying the tip height [287], the spin polarisation of the sample can be probed.

The height of the tip relative to the equilibrium position is plotted in Fig. 6.6 $(b - c)$ for both tip polarisations. As expected, the two figures appear inverted with respect to one another. A domain wall is clearly visible running diagonally across the image. Fig. 6.6 (*d*) shows a cut through the domain wall. Plotted is the difference between the two polarisations such that the zero polarisation position is normalised to $\Delta z = 0$. It was further found that the domain wall height exhibited a strong dependence on the bias voltage (Fig. 6.6). By measuring the electronic density of states either side of the domain wall, the polarisation of the sample can be calculated, revealing a sharp peak at the Fermi level. A detailed discussion of the insights gained into the electronic structure is beyond the scope of this Thesis but can be found in Ref. [17], along with additional measurements.

Having presented the STM measurements, a model of magnetic domain walls is now introduced. From the nearest-neighbour Heisenberg model on the hexagonal lattice (Eqn. 6.1), the continuum limit is taken, treating the spins as classical vectors on the surface of a sphere of unit length $\mathbf{S} = S\mathbf{n}(\mathbf{r})$. One finds the exchange energy and the anisotropy energy

$$\mathcal{H}_{exch} = \frac{\rho_S}{2}\int \mathrm{d}^2 r\left\{(\partial_x \mathbf{n})^2 + (\partial_y \mathbf{n})^2\right\} \tag{6.4a}$$

$$\mathcal{H}_{anis} = \kappa \int \mathrm{d}^2 r\left\{(n^z(\mathbf{r}))^2\right\} \tag{6.4b}$$

with the spin stiffness $\rho_S = \frac{3JS^2 d^2_{\mathrm{n.n}}}{2A_{\mathrm{site}}}$ and anisotropy constant $\kappa = \frac{KS^2}{A_{\mathrm{site}}}$. $d_{\mathrm{n.n}}$ refers to the distance between nearest neighbours on the hexagonal lattice and the area occupied by each site on the lattice (i.e. the area of the primitive unit cell) is A_{site}. By subtracting the energy of the fully polarised state, the energy of the domain wall can be calculated

$$E_{DW} = \int \mathrm{d}^2 r\left\{\frac{\rho_S}{2}(\partial_y \theta)^2 + \kappa\left(1 - \cos^2\theta\right)\right\}. \tag{6.5}$$

Note the similarity with the expression for the parallel component of the confinement energy in Chapter 3 (Eqn. 3.10). The saddle-point solutions may be found from Eqn. 6.5, yielding an expression for the z component of the unit vector field $\mathbf{n}$. The result is merely quoted here, but a full derivation is presented in Appendix F,

$$n^z(y) = \tanh\left[\sqrt{\frac{2\kappa}{\rho_S}}\,(y - y_0)\right] \tag{6.6}$$

where y is the direction perpendicular to the domain wall and y_0 is the position of the centre of the wall. The width of the domain wall is thus controlled by the ratio κ/ρ_S. As one might guess from the similarity between Eqns. 6.5 and 3.10, $\theta(y)$ has the form of a soliton solution (Appendix F).

Since the lineshape of the domain wall is a tanh function, the domain wall width is ill-defined. At large distances, the height of the function approaches ±1 asymptotically and hence some arbitrary cut-off must be chosen for the definition of a domain wall width. For ease of comparison with previous studies [287, 288], the domain wall width is defined according to

$$n^z(y) = \tanh\left(\frac{\pi y}{\delta}\right) \tag{6.7a}$$

$$\delta = \pi\sqrt{\frac{\rho_S}{2\kappa}}. \tag{6.7b}$$

It should be noted that this definition gives the same width as would be obtained if the domain wall were to be modelled using a cosine function, under the assumption that the angle of rotation of the spins varied continuously across the domain wall [289]. Such an assumption fails on the grounds that the spins rotate more rapidly close to the centre of the domain wall, where the anisotropy energy is large. Indeed, the shape of the domain wall (Fig. 6.6 (*d*)) is clearly better described by a tanh function than a cosine. Choosing to define the domain wall width in this manner amounts to placing the cutoff at $y_{\text{cutoff}} = \pm 0.92$.

Whilst the choice of a cutoff may seem somewhat arbitrary, the precise cutoff is unimportant so long as the definition used is consistent. The STM-measured domain wall width is now compared with the expected domain wall width based on Eq. 6.6 from the bulk values of the exchange coupling and anisotropy constant, extracted from neutron scattering. The calculated and measured domain wall profile is plotted in Fig. 6.6 (*d*). The fitted domain wall width $\delta_{\text{fit}} = 2.6\ (\pm 0.5)$nm is slightly smaller than the expected domain wall width $\delta_{\text{bulk}} = 6.0\ (\pm 1.2)$nm, yet is of the same order of magnitude. This in itself is somewhat surprising given the different physics expected at the surface, where a significantly smaller domain wall width might be expected do to an increased magnetocrystalline anisotropy [290]. However, it should be noted here that the domain wall analysis presented in this chapter is sensitive only to the ratio K/J.

6.5 Conclusion

In this chapter, neutron spectroscopic measurements of the two-dimensional itinerant ferromagnet, Fe_3GeTe_2 have been presented. The excitations have been shown to be predominantly two-dimensional in nature with a large exchange constant $J \approx 43(10)$ meV and a small single-ion anisotropy $|K| \approx 0.6(1)$meV. The excitations are shown to be broad in nature, with a parabolic dispersion out of the zone centre as is consistent with an itinerant ferromagnet. The neutron data were modelled with a localised hexagonal nearest-neighbour Heisenberg model in the limit of small wavevector, where the excitations are expected to be local in nature [59].

The correspondence between the physics of the bulk and of the surface was then explored by contrasting neutron scattering measurements with STM data. The extracted domain wall profile from spin-polarised STM measurements was compared with the expected domain wall profile, based on a classical field theoretical model of a hexagonal Heisenberg ferromagnet. The measured domain wall width at the surface (as measured by STM) was shown to be slightly reduced from the expected domain wall width, yet of the same order of magnitude. This is despite the expected increase in anisotropy at the surface due to reduced symmetry [290]. It is also not *a priori* evident that the surface exchange strength is consistent with that of the bulk and a relaxation of the exchange coupling may be justified [282, 291]. It was thus concluded that the ratio K/J is of the same magnitude at the surface of Fe_3GeTe_2 as in the bulk, with a slight reduction, consistent with an increased surface anisotropy or decreased edge coupling. This is of particular importance in the study of topological edge modes in Fe_3GeTe_2 [282, 291] where the relaxation of the magnetic exchange coupling at edges and surfaces can change the nature of topological surface excitations [282, 291]. Since the analysis presented here is sensitive only to the ratio K/J, further measurements of the surface physics, for example by magnon interference spectroscopy [292], would likely be required to unambiguously determine the relative contributions of exchange and anisotropy.

The neutron results further demonstrate a difference between chemical vapour transport grown and flux-grown samples, with a larger anisotropy gap measured in these chemical vapour transport grown samples than in Ref. [272]. The nature of the excitations in this Chapter also differ from previous studies on flux-grown samples, with a finite L dispersion measured, in contrast to Ref. [277], yet the inter-layer coupling was found to be weaker and less coherent than in Ref. [272]. This is taken as evidence of the crucial role played by the iron concentration in determining the magnetic properties of Fe_3GeTe_2, yet it hints that the nature of magnetic interactions may not smoothly vary as a function of iron concentration, although one cannot conclusively rule out other sample dependent characteristics such as defects. Further spectroscopic studies of chemical vapour transport grown Fe_3GeTe_2 are needed to map out excitations to higher energy and fully elucidate the role played by iron concentration on the properties of this material. It has also been demonstrated that the combination of bulk spectroscopic probes such as neutron scattering with surface measurements can offer insight into domain wall physics and layer-dependent magnetism. It is expected that these multi-probe studies will provide an important perspective as the family of van der Waals magnets is expanded.

Chapter 7

Two-dimensional ferromagnetic spin-orbital excitations in honeycomb VI$_3$

7.1 Introduction

Order in two dimensions is forbidden by the Mermin-Wagner theorem [50, 293–295] in isotropic ferromagnets. Although Ising magnetic anisotropy has been theoretically shown to stabilise long-range magnetic order in two dimensions [296, 297], achieving a strong enough single-ion anisotropy to overcome thermal fluctuations has been difficult to achieve in real materials. The discovery of stable, spatially long-range ferromagnetism in two-dimensional materials [298–300] such as CrI$_3$,[269, 301–305] Cr$_2$Ge$_2$Te$_6$,[306, 307] and Fe$_3$GeTe$_2$,[271, 275, 277, 278, 308] has opened up the possibility of designing materials useful to spintronic applications [309, 310] and for exotic two-dimensional physics to be explored such as topologically protected edge and surface modes [281, 282, 311]. In this chapter, two-dimensional ferromagnetism in a non-itinerant system is now discussed, illustrating the effects of an orbital degree of freedom on the magnetic Hamiltonian and it is shown that it can provide the necessary anisotropy to induce magnetic order.

VI$_3$ is unique amongst the two-dimensional van der Waals honeycomb ferromagnets as V^{3+} (S=1) has degeneracy in the lower energy t_{2g} orbitals [312, 313], resulting in an entanglement of spin-orbital degrees of freedom that are coupled to the local structural environment [314, 315]. The structure of VI_3 (Fig. 7.1 (a, b)) is built upon V^{3+} ions forming a layered honeycomb arrangement with an $R\overline{3}$ symmetry, stacked along c with an ABC arrangement. [312, 315] This stacking results in a rhombohedral superstructure [316], though other symmetries have been discussed. [317, 318] The c-axis stacking results in domains in large single crystals as evidenced by the scans of the $(1, 1, 0)$ structural Bragg peak (indexed on an $R\overline{3}$ unit cell in Fig. 7.1 (c)) showing a splitting. Given the interest in the two-dimensional properties of V^{3+}, an average $R\overline{3}$ structure is considered here. Below $T_s \approx 79$ K, a structural transition away from the $R\overline{3}$ is observed. [317]

Magnetisation and diffraction on VI_3 report a ferromagnetic transition ($T_c \approx 50$ K) [312, 314, 315, 317–320], in agreement with Density Functional Theory [321, 322]. Nuclear Magnetic Resonance (NMR) [314], which probes the local V^{3+} environment, has found the existence of two different ferromagnetic domains at low temperatures with differing local crystalline electric fields surrounding the V^{3+} sites. This has further been supported theoretically [323, 324] and also by diffraction [315]. To understand the magnetic coupling and spin-orbital ground state, neutron spectroscopy is now applied to probe the magnetic correlations at low temperatures.

7.2 Experiment

Over 1000 $\sim$ 1 mg single crystals of VI_3 were grown by C. Stock at the University of Edinburgh, using chemical vapour transport [325] and edge-aligned using the hexagonal morphology (Fig. 7.1 (d)). The crystals were coated in hydrogen-free Fomblin oil on aluminium plates given their hydroscopic nature [326].

Using the MAPS time-flight spectrometer (ISIS, Didcot, UK) [20], the low temperature magnetic fluctuations are first characterised in Fig. 7.2. E_i was set at 50 meV, with the Fermi chopper spinning at 200 Hz, giving an elastic energy resolution of 2.3 meV (FWHM). The data were combined with the Mantid/Horace packages [252, 327]. Figures 7.2 $(a-c)$ display constant energy cuts within the $a-b$ plane showing dispersive magnetic excitations. Figure 7.2 (d) shows a momentum-energy slice displaying the dispersive magnetic excitations up to the zone boundary at $\sim$ 20 meV.

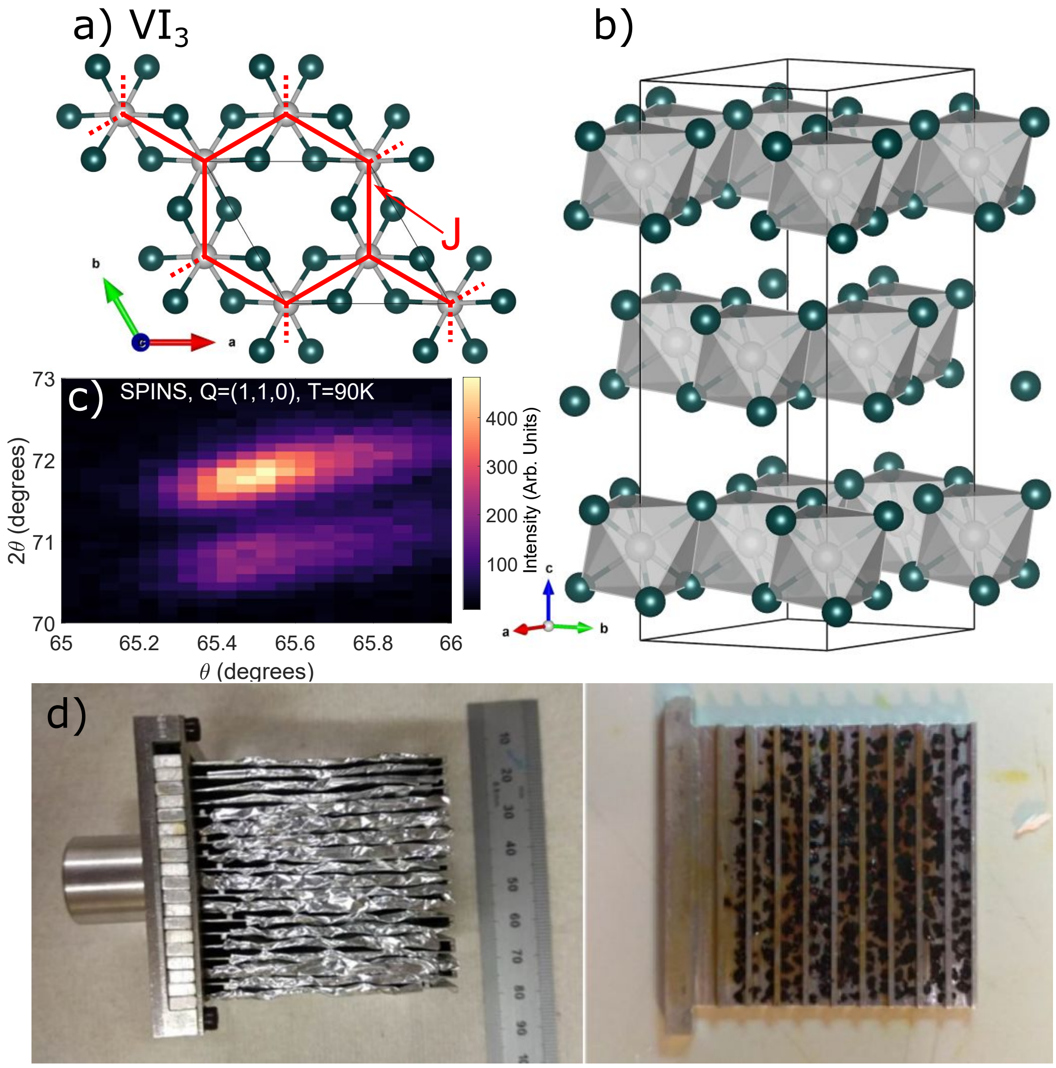

Figure 7.1 *(a) Structure of VI_3 in the a-b plane showing the honeycomb lattice of V^{3+} ions (gray) with an octahedral coordination of iodine ions (green). For this work, an $R\overline{3}$ unit cell is taken. (b) VI_3 structure showing the stacking of two-dimensional sheets. (c) (1,1,0) Bragg peak measured at SPINS, showing the existence of two domains at T=90 K. (d) Aluminium sample mount showing co-aligned VI_3 crystals covered in Fomblin grease and mounted to one of the nineteen panels.*

Low energy magnetic fluctuations were measured using the cold neutron spectrometer MACS (NIST, Gaithersburg, USA) [280]. The scattered neutron energy E_f was fixed at 3.5 meV while the incident energy E_i was varied, providing an elastic resolution of 0.25 meV (FWHM). Fig. 7.2 (*e*) displays the dispersion along c illustrating little dispersion along this direction and affirming the two-dimensional nature of the magnetic excitations and validating the consideration of a R$\overline{3}$ unit cell. This is confirmed in Fig. 7.3 (*a*) which plots a constant energy slice in the (H,H,L) plane illustrating a rod of scattering correlated in the $(H,H,0)$ (in-plane) direction but extended along $(0,0,L)$. The decay of intensity with increasing momentum transfer along $(0,0,L)$ follows the V^{3+} magnetic form factor [328], implying the scattering is magnetic. It should be noted that there is also a weak dispersion along L (Fig. 7.2 (*e*)) which also results in a decay of intensity for a fixed energy transfer. The magnetic in-plane coupling is illustrated in Figs. 7.3 (*b*) and (*c*) with cuts along (H,H) showing dispersive excitations at energies of 4.5 meV and 8 meV. Fig. 7.3 (*d*) displays a $(0,0,L)$ integrated momentum-energy slice that shows two magnetic excitations dispersing along (H,H) with gaps of $\Delta \sim 4$ and $\Delta \sim 7$ meV.

Figure 7.3 displays two gapped excitations indicative of local anisotropy which requires a finite energy to overcome. However, the intensity variation with momentum transfer of the two modes is different. The lower mode has a strong response near the zone centre, but the intensity decays quickly away from $Q = 0$ and is less dispersive. The upper mode is fully mapped out in Fig. 7.2 and extends to higher energy and has a much more uniform intensity distribution across the Brillouin zone.

The differing energy-momentum dependence of the two branches is suggestive of excitations from differing ground states. Corroborating this is a comparison to the excitations in $RbFe^{2+}Fe^{3+}F_6$ [23] where the Fe^{2+} (S=2, L=2) and Fe^{3+} (S=5/2, L=0) display spatially long-range charge and orbital order. In this case, two branches originating from the two different orbital iron ground states result in a weakly dispersive mode with intensity concentrated near the zone centre and another mode that disperses more strongly throughout the zone with an even intensity distribution. Motivated by this comparison and previous diffraction [315], NMR [314], and theoretical work [323] indicative of two orbital domains, the magnetic excitations of VI_3 are now investigated in the context of the spin-orbital properties of V^{3+}.

7.3 Single-ion physics

Given the near universality of the spatially-localised crystalline electric parameters for transition metal ions, the single ion V^{3+} Hamiltonian is first analysed with the goal of establishing the magnetic ground state of V^{3+} that needs to be coupled

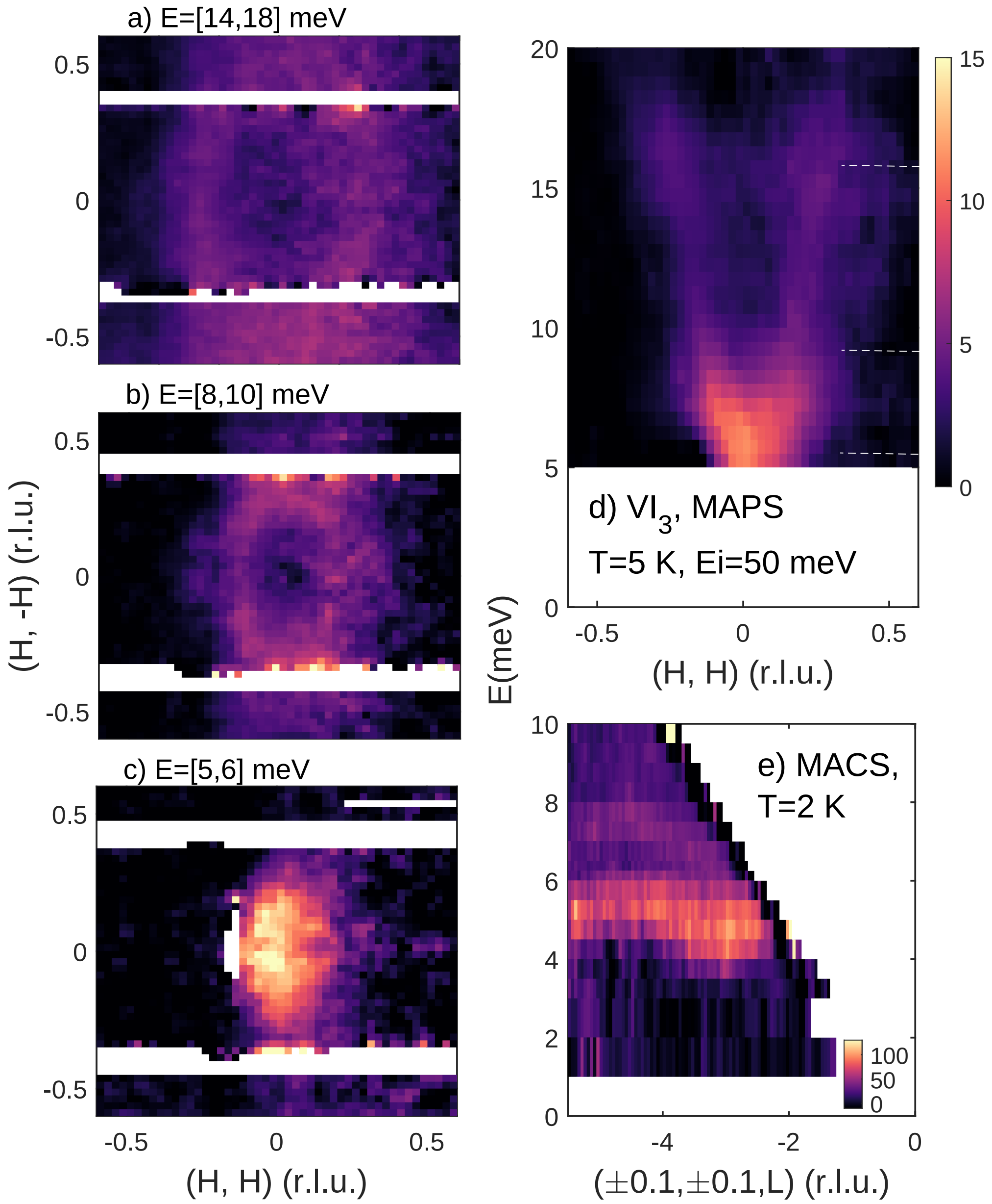

Figure 7.2 *(a−c) T=5 K constant energy slices from MAPS. Energy integration ranges for each of the cuts in panels (a − c) are given in square brackets. (d) Momentum-energy slice illustrating dispersive modes from $Q = 0$. The locations of the constant energy slices are given by the dashed white lines. (e) The excitations along the c-axis from MACS.*

in VI_3 and hence define the parameters to be extracted from experiment. With the presence of an orbital degree of freedom and the low-temperature crystalline

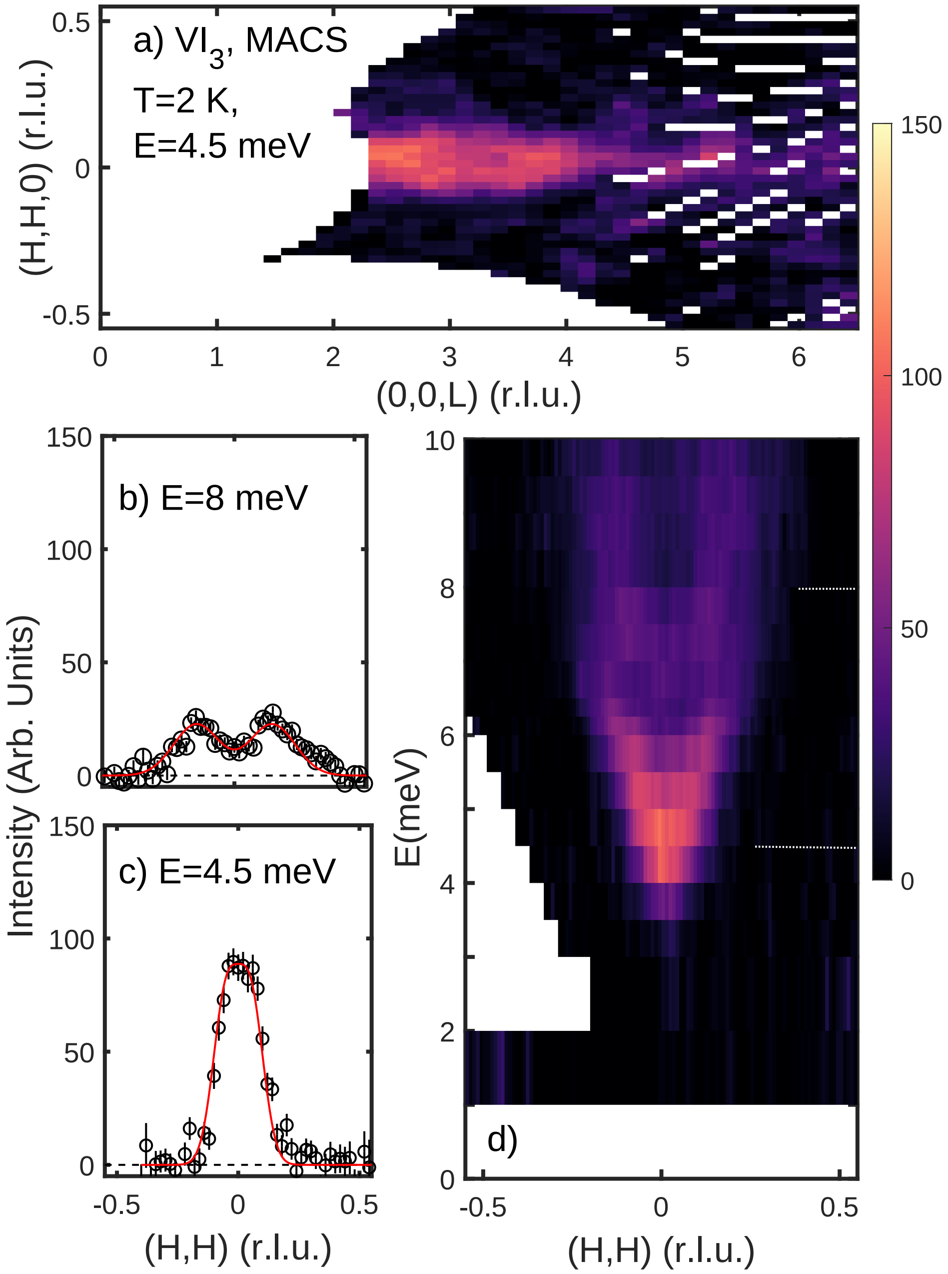

Figure 7.3 *(a) Constant E=4.5 meV slice at 2 K from MACS, with background subtracted using methodology in Refs. [18, 19]. (b − c) constant energy cuts and (d) momentum-energy slice integrating along* $(0, 0, L)$*. The location of the constant energy scans are indicated by the dashed white lines.*

distortion and ferromagnetism, there are four single-ion Hamiltonian terms,

$$\mathcal{H}_{SI} = \mathcal{H}_{CEF} + \mathcal{H}_{SO} + \mathcal{H}_{dis} + \mathcal{H}_{MF}. \tag{7.1}$$

This includes the octahedral crystalline electric field ($\mathcal{H}_{CEF}$), spin-orbit coupling ($\mathcal{H}_{SO}$), the structural distortion away from a perfect octahedron ($\mathcal{H}_{dis}$), and the local molecular field ($\mathcal{H}_{MF}$) imposed by ferromagnetic order. Each term in this Hamiltonian is discussed (Fig. 7.4 (a)) and its effect on the single-ion magnetic ground state.

7.3.1 $\mathcal{H}_{CEF}$-Octahedral field

In VI$_3$, the d^2 electrons forming a free ion ^3F are surrounded by six I$^-$ ions imposing a crystalline electric field on V^{3+}. In terms of Stevens operators [34, 329], this lattice potential is written as $\mathcal{H}_{CEF} = B_4(\mathcal{O}_4^0 + 5\mathcal{O}_4^4)$ [330] with the ^3F orbital ground state being energetically lowered by $360B_4$ (Fig. 7.4)a)), with an expected $B_4 \sim$ 3.8 meV [21, 22]. Refs. [323, 324] have alternatively discussed the single-ion properties of VI$_3$ using the strong crystal field approach [48, 331], whereby the crystalline electric field splits the five-fold d orbital degeneracy into a ground state triplet t_{2g}, and excited doublet, e_g. Either approach leads to a ground state projected ($L = \alpha l$) orbital triplet (l=1). Given that other inorganic $3d$ metal complexes are typically in a high-spin state, the intermediate crystalline electric field basis is chosen here, with a projection factor $\alpha = -\frac{3}{2}$ [332]. In practice, owing to a finite mixing of excited states, the projection factor lies in the range $-\frac{3}{2} \leq \alpha \leq -1$ [333, 334]. For V^{3+} it is expected that the magnitude of this projection factor is reduced from the maximal value [21]. The next excited state is $480B_4$ ~1.8 eV [206, 335–339] which fixes the magnetic ground state of V^{3+} to be $|l = 1, S = 1\rangle$.

7.3.2 $\mathcal{H}_{SO}$-Spin-orbit coupling

The effect of spin-orbit coupling on the $|l = 1, S = 1\rangle$ ground state, with $\mathcal{H} = \alpha\lambda \mathbf{l} \cdot \mathbf{S}$, is shown in Fig. 7.4 ($a$) and results in three levels with effective angular momentum values of $j_{eff} = 0, 1, 2$. These spin-orbit levels are spaced according to the Landé interval rule. The spin-orbit coupling is reported to be

λ=12.9 meV for a free V^{3+} ion [21], however significantly reduced spin-orbit coupling constants are measured in systems with covalent bonding. For example, in vanadium ammonium alum, λ = 7.9 meV is observed [21, 340]. Given that V^{3+} with d^2 electrons is less than half filled, it is expected that $\lambda > 0$, implying $\tilde{\lambda} = \alpha\lambda < 0$. The ground state is j_{eff}=2 separated from j_{eff}=1 by $2\alpha\lambda$ [21, 341].

7.3.3 $\mathcal{H}_{dis}$-Structural distortion

VI_3 is distorted from an ideal octahedron (Fig. 7.1 (*b*)). Given orbitally driven transitions are primarily tetragonal [306, 342–344], this is parameterised as a distortion along $\hat{z}$ of the octahedra with $\mathcal{H}_{dis} = \Gamma_{\text{I,II}} \left(\hat{l}_z^2 - \frac{2}{3} \right)$ where Γ is proportional to strain. This additional energy term results in two possible orbital ground states, with $\Gamma < 0$ (flattened octahedra), an orbital ground state doublet while $\Gamma > 0$ (elongation) is a ground state singlet. In the strong crystal field basis [323] one ground state is a doublet with the lower energy d_{xy} orbital and one of the degenerate d_{xz}, d_{yz} orbitals occupied, and for an elongated octahedron, a singlet ground state is found with a hole in the d_{xy} orbital. Given results in Refs. [207, 264, 345, 346], it is expected that $|\Gamma| \sim 10$ meV. Structural studies suggest that the octahedra are compressed in VI_3 [317], indicated that $\Gamma < 0$, as found in the vanadium spinels [333].

7.3.4 $\mathcal{H}_{MF}$-Molecular field

The final $\mathcal{H}_{SI}$ term is the molecular field present in the $T < T_c \sim 50$ K ferromagnetic phase from neighbouring ordered spins inducing a Zeeman field on a V^{3+} site. The $\mathcal{H}_{MF} = h_{MF}\hat{S}_z$ term splits the degenerate spin-orbit levels and is fixed by the spin exchange which induces a molecular field $h_{MF} = \sum_j \mathcal{J}_{ij} \langle \hat{S}_j^z \rangle = 3JS$ (Fig. 7.1 (*a*)). Ferromagnetic exchange is expected based on 90° bonds between nearest V^{3+} neighbours and validated by calculations [323]. Molecular orbital calculations [313] predict $J \sim$ -7 meV, implying $h_{MF} \sim$ -20 meV. This is of a similar magnitude to the spin-orbit coupling and induces many single-ion levels with a similar energy scale (Fig. 7.4).

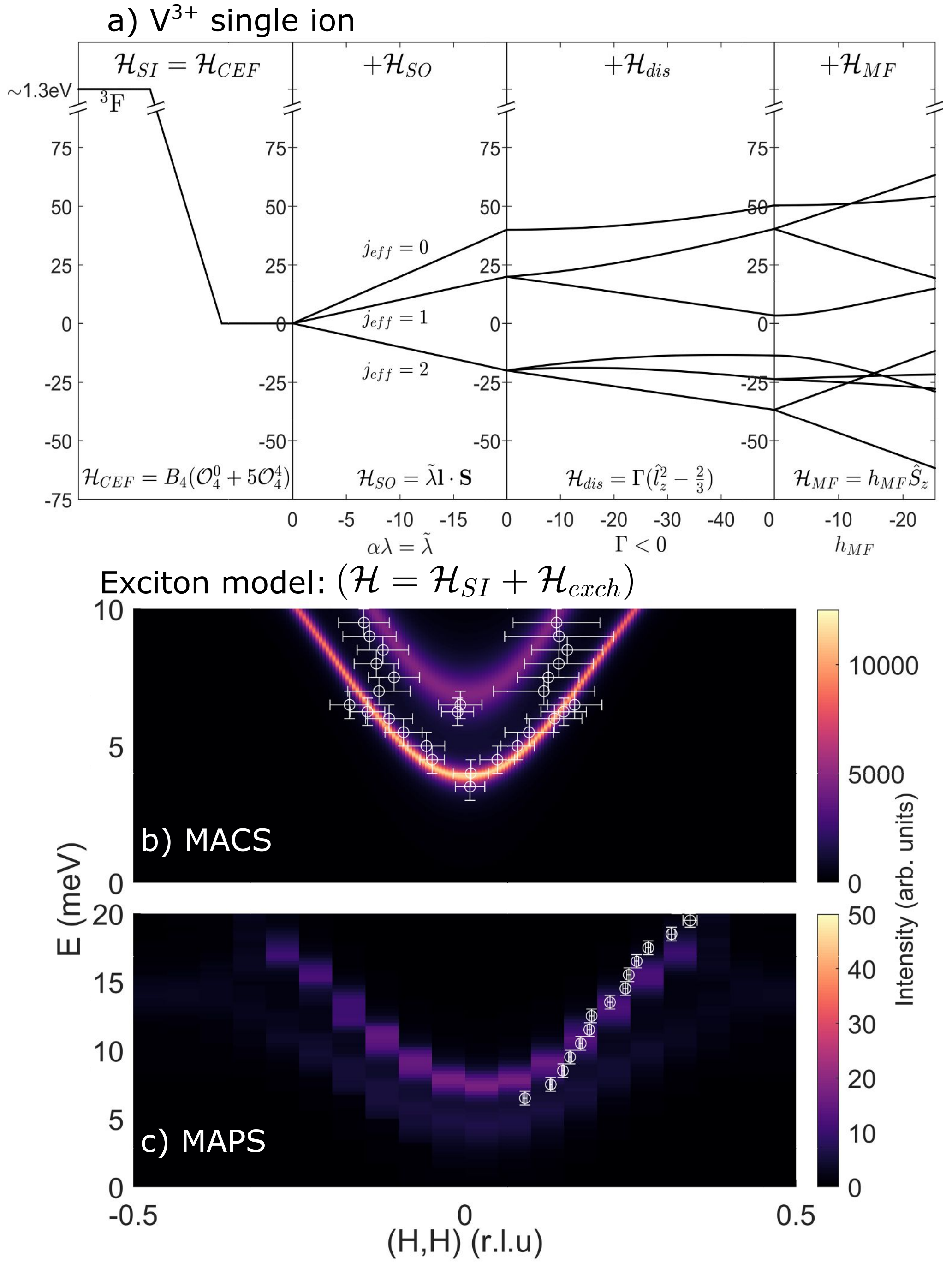

Figure 7.4 *(a) Energy of* V^{3+} *ion under a crystal field* $\mathcal{H}_{CEF}$*, spin-orbit coupling* $\mathcal{H}_{SO}$*, tetragonal distortion* $\mathcal{H}_{dis}$*, and molecular field* $\mathcal{H}_{MF}$*. (b)* $S(\mathbf{Q},\omega)$ *calculation of the MACS data (Fig. 7.3 (d)) using the fitted values of exchange parameters. (c) Model of the MAPS data (Fig. 7.2 (d)) using Horace [20] to account for the finite integration ranges and detector coverage. Overlaid points were extracted from fitting Gaussian peaks to constant energy cuts.*

7.4 Multi-level spin waves

The dispersive excitations shown in Figs. 7.2 and 7.3 are indicative of coupled V^{3+} ions with the Hamiltonian $\mathcal{H} = \mathcal{H}_{SI} + \mathcal{H}_{exchange}$, where $\mathcal{H}_{exchange} = \sum_j \mathcal{J}_{ij}\mathbf{S}_i \cdot \mathbf{S}_j$, describes an isotropic Heisenberg interaction between neighbouring V^{3+} ions. The usual method of parameterising such excitations is based on standard spin wave theory where transverse deviations of an angular momentum vector of fixed magnitude are considered. This is based on a ground state, energetically separated from other single-ion levels and is a valid approximation in many compounds with an orbital degeneracy [2, 14, 208, 347, 348] where spin-orbit coupling is a perturbation and is parameterised through anisotropic terms [27]. With the presence of spin-orbit coupling of a similar magnitude to the exchange coupling, as in VI_3, this approach is not valid due to the mixing (Fig. 7.4 (*a*)) of single-ion spin-orbit levels [349] and necessitates a multi-level approach to the excitations. Below, such a methodology is applied based on single-ion eigenstates where anisotropy terms are incorporated explicitly through the single-ion Hamiltonian described above.

Figs. 7.2 and 7.3 are fitted with four parameters - J, $\tilde{\lambda} = \alpha\lambda$ and $\Gamma_{I,II}$ (note h_{MF} is fixed by J). The Green's function equation of motion [207, 263, 264] is used, in terms of the eigenstates of $\mathcal{H}_{SI}$ to calculate the neutron response via the fluctuation-dissipation theorem $S(\mathbf{Q},\omega) \propto -f(\mathbf{Q})^2\mathfrak{Im}\left[G(\mathbf{Q},\omega)\right]$. This is consistent with other multi-level spin wave theories [350, 351]. Within the random phase approximation, the transverse Green's functions for nearest neighbour coupling is (Appendix G),

$$G^{+-}_{\mu\nu}(\mathbf{Q},\omega) = g^{+-}_{\mu}(\omega) + g^{+-}_{\mu}(\omega)\mathcal{J}_{\mu\nu}(\mathbf{Q})G^{+-}_{\mu\nu}(\mathbf{Q},\omega) \tag{7.2}$$

where $\mathcal{J}_{\mu\nu}(\mathbf{Q}) = \sum_{ij} J_{\mu\nu}e^{i\mathbf{Q}\cdot\delta_{ij}}$ is the Fourier transform of the exchange interaction between nearest sites ν and μ, and $g^{\alpha\beta}_{\mu}$ is the single-site susceptibility, defined as

$$g^{\alpha\beta}_{\mu}(\omega) = \sum_{mn} \frac{\langle m|\,\hat{S}^{\alpha}_{\mu}\,|n\rangle\,\langle n|\,\hat{S}^{\beta}_{\mu}\,|m\rangle}{\omega - (\omega_n - \omega_m)}. \tag{7.3}$$

The energies, ω_n, are the eigenvalues of $\mathcal{H}_{SI}$, with $|n\rangle$ the single ion eigenstates. VI_3 exhibits ABC stacking along c (Fig. 7.1 *b*) [317] requiring six sites $\mu, \nu = \{1, 2, ..., 6\}$.

Based on Refs. [314, 315, 323, 324], two domains are considered with differently distorted octahedra - $\Gamma_{\mathrm{I}} < 0$ and $\Gamma_{\mathrm{II}} < 0$. The sign of both distortions is chosen to be negative, consistent with a trigonal or tetragonal compression. For simplicity the volume ratio is fixed to Γ_I/Γ_{II}=1. Fig. 7.3 (*a*) and Fig. 7.2 (*e*) indicate $J/J_c \approx 17$, therefore coupling along c is neglected, considering the nearest-neighbour in-plane exchange J equal in both domains. In terms of the momentum-energy structure of the magnetic excitations, the parameter J tunes the dispersion of the magnetic modes and $\Gamma_{I,II}$ controls the size of the gap of the two excitations in Fig. 7.3. Including more complex structural deviations has the effect of changing this gap size. Akin to anisotropy terms incorporated into conventional spin wave theory, $\Gamma_{I,II}$ describe the effects of the local single-ion anisotropy from a distortion away from a perfect octahedral environment.

Fig. 7.4 displays a four parameter fit with $J = -4.37$ ($\pm$0.01) meV, $\tilde{\lambda} = -8.4$ ($\pm$0.26) meV, $\Gamma_{\mathrm{I}} = -45$ ($\pm$3.56) meV and $\Gamma_{\mathrm{II}} = -11.1$ ($\pm$0.50) meV. The upper mode is from the domain with a more distorted octahedron (domain I) and the lower from the less distorted domain (domain II). Despite the different energy bandwidths of the two modes, a common value of the nearest-neighbour J is sufficient to describe the dispersion in both domains, with the different dispersion bandwidths originating from the interplay of the orbital and spin degrees of freedom. A reduced strength of the spin-orbit coupling constant is found, as expected in the case of covalently bonded systems [340]. The presence of covalency effects in $\mathrm{VI_3}$ has been suggested by Density Functional Theory calculations [322]. The multi-level spin wave model captures the rapid intensity decay of the lower mode away from the zone centre, however, no intensity is observed near the zone boundary in experiment, in disagreement with model calculations. This can be understood by finite lifetime effects due to disorder which have been both theoretically and experimentally found to disproportionately affect shorter wavelength excitations away from the magnetic zone centre [267, 352–354]. This indicates stronger disorder for the less distorted domain $\mathrm{V^{3+}}$ (domain I). The stability of a flattening of the octahedron around the $\mathrm{V^{3+}}$ site is consistent with results found for other $\mathrm{V^{3+}}$ compounds [333, 355, 356]. Two distinct $\mathrm{V^{3+}}$ domains, with one disordered, is also consistent with NMR results [314].

The multi-level model coupling single-ion states determined by spin-orbit coupling, distorted octahedra, and a molecular field, results in gapped excitations consistent with the data with two distortion parameters - $\Gamma_{I,II}$ and a common exchange constant J and spin-orbit coupling constant λ for both domains. This is in contrast with traditional spin wave theory that would require two very different exchange parameters, for the differing domains, with the ratio scaling with the magnon bandwidths. Such a large difference in exchange constants is difficult to justify through the local bonding environments and small deviations away from an average $R\overline{3}$ unit cell.

The energy cost of excitations is determined by the energy gap at $Q = 0$. This is $\approx$ 5 meV = 58 K, similar to the Curie temperature in VI_3, which defines ferromagnetic order. This anisotropic gap, which facilitates magnetic order, originates from spin-orbit coupling. It is noted that other two-dimensional van der Waals magnets which lack spin-orbit coupling do not display spatially long-range order with $NiGa_2S_4$ an example. [357–360] The situation is different in CrI_3 [269] and $CrBr_3$ [361] where Cr^{3+} lacks an orbital degeneracy. It is interesting that CrI_3 has a large Curie temperature, but is comparatively three-dimensional in terms of the magnetic exchange coupling [269] and critical properties. [301, 319, 362] Spin-orbit coupling therefore can provide a route for creating a strong enough anisotropy that magnetic order is stable in two dimensions.

7.5 Conclusion

To summarise a neutron spectroscopy study of the effects of an orbital degree of freedom on the honeycomb van der Waals ferromagnet VI_3 has been presented in this chapter. Two modes are observed at low energy. The lower mode exhibits a gap ~ 4 meV and the upper mode has a gap ~ 7 meV. The upper mode is observed to have a greater bandwidth than the lower mode. The lower mode is observed to broaden significantly away from the zone centre. The two modes are thus observed to be qualitatively different. The two modes have been parameterised in terms of two differently distorted domains and multi spin-orbit level calculations have been presented to model the inelastic neutron scattering response with good agreement. It has been demonstrated that both magnetically ordered domains are stabilised, despite the two-dimensional nature of the magnetism, by the presence of anisotropy derived from the cooperative effect of crystallographic distortions and spin-orbit coupling.

The Green's function formalism, used in Chapter 5 to describe the spin-only antiferromagnet $CaFe_2O_4$, was extended to treat a system with an orbital degree of freedom. The formalism allows for the explicit treatment of spin-orbit coupling and crystal distortions. These on-site degrees of freedom are ultimately responsible for the single-ion anisotropy measured in coupled spin systems. This technique therefore provides a method for understanding the origin of anisotropy in terms of the parameter that describe the underlying single-ion physics.

Chapter 8

Excitonic transverse and amplitude fluctuations in the noncollinear and charge-ordered RbFe^{2+}Fe^{3+}F$_6$

8.1 Introduction

The concept of spin waves was first introduced by Bloch to describe the renormalisation of the spontaneous magnetisation of the simple ferromagnet [363]. Since this initial work, subsequent contributions by Dyson [364], and Holstein and Primakoff [365] have further expanded the understanding of the quasi-particle spectrum in magnetically ordered insulators. The importance of spin wave theory expanded significantly towards the latter part of the 20th century, following the advent of neutron scattering techniques by Shull and Brockhouse which offered a way of directly probing the fundamental spin wave excitations of magnetic systems through the spin-spin correlation function. To this day, linear spin wave theory (LSWT) remains one of the primary means of investigating long range magnetically ordered phases of matter as a means of understanding the underlying interactions. Its success in understanding spin interactions in insulators has resulted in several widely used computer routines for modelling neutron scattering data including SpinWave [366, 367], SpinWaveGenie [368], and SpinW [369]. Such programmes have opened up neutron scattering to a broader user based and have contributed significantly to the success of new neutron instrumentation and the expansion of the user community.

LSWT is fundamentally a semiclassical technique and results from the expansion in $1/S$ about a classical ground state. Physically, it can be interpreted as describing transverse fluctuations of an ordered magnetic moment around a fixed direction. It therefore enjoys greatest success in describing large-S systems, where corrections to the leading order theory are small and the ground state is not dominated by quantum fluctuations [370]. For small-S systems there exist many fundamental excitations which are not well-described by LSWT such as spinons, breathers, and solitons [130, 371, 372] as seen in Chapter 3. Nonetheless, LWST has been surprisingly successful in describing physics away from the large-S, long-range ordered limit [373–376].

The typical LSWT treatment of coupled magnetic ions directly treats the spin degree of freedom based on a Hamiltonian with dominant Heisenberg terms. The effect of single-ion terms, such as spin-orbit coupling, in the magnetic Hamiltonian can be included perturbatively via Dzyaloshinskii-Moriya interactions and anisotropy terms. [27] However, this treatment precludes the possibility of longitudinal amplitude fluctuations of the order parameter [377, 378] which give rise to new types of excitations given that the observable $\hat{S}_z$ does not commute with the magnetic Hamiltonian. Furthermore, the integrating out of the orbital degree of freedom can leave behind the incorrect single-ion ground state given the mixing of orbital and spin degrees of freedom.

Recently, effects of spin-orbit coupling on the magnetic excitations have been of intense interest in $4d$ or $5d$ transition metal ions [33, 379, 380]. However, given that the spin-orbit coupling scales as the atomic number squared ($\lambda \sim Z^2$) [381], the energy scale for spin-orbit coupling is reduced for $3d$ transition metal ions, introducing the possibility of mixing of spin and orbital degrees of freedom on a energy scale measurable with neutron scattering [382]. In such a situation, treatment of the magnetic excitations needs to incorporate the single-ion properties of the local crystalline electric field which define the eigenstates of the magnetic ions of interest.

In this chapter, the spin excitations previously reported in $\mathrm{RbFe^{2+}Fe^{3+}F_6}$ [23, 383] are revisited. $\mathrm{RbFe^{2+}Fe^{3+}F_6}$ has a structure related to the α pyrochlores $A_2B_2X_6X'$, but with a vacancy on one out of two A cations and another on the X' anion site that does not contribute to the BX_6 octahedra. Several compounds with similar structures have been reported in the literature [384, 385]. Charge order originates from the two different iron sites which have differing valences of $\mathrm{Fe^{2+}}$ and $\mathrm{Fe^{3+}}$. While the magnetic ground state of $\mathrm{Fe^{3+}}$ is $S = 5/2$ with each of the five d-orbitals half filled following Hund's rules and the Pauli principle, the situation for Fe^{2+} is slightly more complicated with an extra electron occupying one of the t_{2g} states with $S = 2$ and an effective $l = 1$ (which are discussed in more detail below). As a direct result of this orbital degeneracy [21, 386, 387], the $\mathrm{Fe}^{2+}\mathrm{F}_6$ octahedra are considerably more distorted than the $\mathrm{Fe}^{3+}\mathrm{F}_6$ octahedra.

The goal of this chapter is to investigate the spin fluctuations in $\mathrm{RbFe}^{2+}\mathrm{Fe}^{3+}\mathrm{F}_6$, specifically the role of orbital contributions, which are coupled to the spin response via spin-orbit coupling, in the neutron cross section. To understand the spin fluctuations and the role of the differing spin and orbital contributions from each of the iron sites, an extension to the Green's function formalism treating coupled multi-level sites is presented to account for noncollinear magnetic order. This formalism is applied to the noncollinear charge-ordered antiferromagnet $\mathrm{RbFe}^{2+}\mathrm{Fe}^{3+}\mathrm{F}_6$, calculating the excitation spectrum. The low energy excitations are discussed and the results compared to previous neutron experiments. The fluctuations in the amplitude of the order parameter resulting from the nonconservation of $\hat{S}_z$ are then examined.

This chapter is divided into five sections including this introduction. In Section 8.2 the structure factor is defined in terms of Green's functions and the Green's function formalism presented in previous chapters, and derived in Appendix G, is extended to treat noncollinear magnetic structures. This section illustrates the role of single-ion physics in modelling neutron spectra and magnetic fluctuations. In Section 8.3 this is applied to the situation in $\mathrm{RbFe}^{2+}\mathrm{Fe}^{3+}\mathrm{F}_6$ and the single-ion physics is discussed for Fe^{2+} and Fe^{3+} relevant in defining the ground state that is coupled via the Random Phase Approximation (RPA) in this Green's function approach. In Section 8.4 the neutron response is calculated and the chapter is ended with a discussion and concluding remarks in Section 8.5.

8.2 Green's function

In this section the calculation of the Green's function in a noncollinear magnet is discussed along with its relation to neutron spectroscopy. The Green's function formalism allows for the treatment of multi-level systems in a manner similar to SU(N) spin wave theory and the flavor wave expansion approach [351, 377, 388–391]. By formulating the calculation in terms of response functions, a direct connection can be made to the neutron scattering intensity.

8.2.1 Relation to neutron spectroscopy

The intensity measured with neutron scattering is directly proportional to the structure factor $S(\mathbf{Q},\omega)$,

$$S(\mathbf{Q},\omega) = g_L^2 f^2(\mathbf{Q}) \sum_{\alpha\beta} (\delta_{\alpha\beta} - \hat{Q}_\alpha \hat{Q}_\beta) S^{\alpha\beta}(\mathbf{Q},\omega), \tag{8.1}$$

corresponding to a product of the Landé-g factor g_L, the magnetic form factor $f(\mathbf{Q})$, a polarisation factor providing sensitivity to the component perpendicular to the momentum transfer $\mathbf{Q}$, and the dynamic spin structure factor $S^{\alpha\beta}(\mathbf{Q},\omega)$. This itself corresponds to the Fourier transform of the spin-spin correlations

$$S^{\alpha\beta}(\mathbf{Q},\omega) = \frac{1}{2\pi} \int \mathrm{d}t e^{i\omega t} \langle \hat{S}^\alpha(\mathbf{Q},t) \hat{S}^\beta(-\mathbf{Q},0) \rangle, \tag{8.2}$$

where $\alpha,\beta = x,y,z$. $S^{\alpha\beta}(\mathbf{Q},\omega)$ as written above considers only the spin contribution to the neutron scattering cross section. The contributions from orbital fluctuations are ignored given that the expectation value of the orbital angular momentum $\langle \mathbf{L} \rangle \equiv 0$ *via* quenching for d-orbitals [27]. The assumption to only consider the spin part of the neutron cross section depends on the experiment remaining in a single $|L, m_L\rangle$ multiplet and this is justified given the energy scales under consideration. Total moment sum rule analysis confirms that the spin contribution to the scattering cross section is dominant in $\mathrm{RbFe^{2+}Fe^{3+}F_6}$ [392]. As discussed in the following sections, orbital contributions to the structure enter via the spin-orbit ($\mathbf{L}\cdot\mathbf{S}$) coupling term in the magnetic Hamiltonian.

The relation of the structure factor $S^{\alpha\beta}(\mathbf{Q},\omega)$ to the response function is given by the fluctuation-dissipation theorem

$$S^{\alpha\beta}(\mathbf{Q},\omega) = -\frac{1}{\pi} \frac{1}{1-\exp(\omega/k_\mathrm{B}T)} \mathfrak{Im}\left[G^{\alpha\beta}(\mathbf{Q},\omega)\right], \tag{8.3}$$

and allows the magnetic neutron cross section to be defined in terms of a Green's response function $G^{\alpha\beta}(\mathbf{Q},\omega)$ [393]. Recognising that the neutron response function is proportional to the temperature dependent Bose factor multiplied by the Fourier transform of the retarded Green's function shows that calculating the Green's function response provides a means of modelling the neutron response.

Building on previous work [4, 5, 207, 263, 394], the Green's function formalism is now extended to treat noncollinear magnetic structures of arbitrary unit cell size. The derivation of the collinear Green's function formalism is given in Appendix G and is discussed in previous chapters. This serves as the starting point for the derivation of the rotating frame formalism.

8.2.2 Rotating frame formalism

The scheme presented in Appendix G cannot treat general noncollinear magnetic structures since, in the lab frame, (x, y, z), each unit cell has a different mean field Hamiltonian (and hence different $g_{\gamma\gamma}(\omega)$) up to the period of the magnetic supercell. This deficiency can be overcome by transforming to a reference frame that rotates with the magnetic structure [395], $(\tilde{x}, \tilde{y}, \tilde{z})$. In this rotating frame, the magnetic moment at each site is orientated along the $\tilde{z}$ axis. The spin vector in the lab frame can be related to the rotating frame by the rotation

$$\mathbf{S}_{i\gamma} = R_{i\gamma}\tilde{\mathbf{S}}_{i\gamma} \tag{8.4}$$

where $\tilde{\mathbf{S}}_{i\gamma}$ are the spin operators in the rotating frame. The rotation can be broken into two parts, the rotation of the spins within the unit cell onto a common coordinate system for the unit cell and a rotation of each unit cell onto a common rotating frame coordinate system, $R_{i\gamma} \to R_i R_\gamma$. In order to relate R_i to the magnetic ordering wavevector, $\mathbf{Q}$, and spin rotation plane, $\mathbf{n}$, one can make use of the Rodrigues formula

$$R_i = e^{i\mathbf{Q}\cdot\mathbf{r}_i} T + e^{-i\mathbf{Q}\cdot\mathbf{r}_i} T^* + \mathbf{n}\mathbf{n}^T \tag{8.5a}$$

$$T = \frac{1}{2}\left(\mathbf{1} - \mathbf{n}\mathbf{n}^T - i[\mathbf{n}]_\times\right). \tag{8.5b}$$

The matrix elements of the skew symmetric matrix can be conveniently written using the Levi-Civita symbol in Einstein notation, $[[\mathbf{n}]_\times]^i{}_j = \epsilon_i{}^{jk} n_k$.

In the rotating frame, the inter-site exchange Hamiltonian becomes

$$\begin{aligned}\mathcal{H}_{int} =& \frac{1}{2}\sum_{ij}^{\gamma\gamma'} \mathbf{S}_{i\gamma}^T \mathcal{J}_{ij}^{\gamma\gamma'} \mathbf{S}_{j\gamma'} \\ =& \frac{1}{2}\sum_{ij}^{\gamma\gamma'} \tilde{\mathbf{S}}_{i\gamma}^T R_\gamma^T R_i^T \mathcal{J}_{ij}^{\gamma\gamma'} R_j R_{\gamma'} \tilde{\mathbf{S}}_{j\gamma'}.\end{aligned} \tag{8.6}$$

To proceed with the calculation, $\mathbf{S}_{i\gamma}$ is written using the basis vectors of the space formed by the tensor product of the sublattice space and $\mathbb{R}_3$, $\mathbf{V}^{3N} = \mathbf{V}^N \otimes \mathbb{R}_3$, where N is the number of sites in the unit cell. Though competing Heisenberg exchange can give rise to noncollinear order, many noncollinear magnetic systems in nature arise due to more complicated exchange terms including Dzyaloshinskii-Moriya and other off-diagonal couplings. These terms can be motivated on symmetry grounds [51] and arise due to third order processes, involving exchange between excited spin-orbital levels [27, 52]. These can be readily incorporated into this model by defining the exchange matrix in the full $3N \times 3N$-dimensional space $\mathbf{V}^{3N}$ as

$$\underline{\underline{\mathcal{J}}}^{\gamma\gamma'} = \begin{pmatrix} J_{xx}^{11} & J_{xy}^{11} & J_{xz}^{11} & J_{xx}^{12} & & & \\ J_{yx}^{11} & J_{yy}^{11} & J_{yz}^{11} & J_{yx}^{12} & \cdots & & \\ J_{zx}^{11} & J_{zy}^{11} & J_{zz}^{11} & J_{zx}^{12} & & & \\ J_{xx}^{21} & J_{xy}^{21} & J_{xz}^{21} & \ddots & & & \\ & \vdots & & & & & \\ & & & & J_{xx}^{NN} & J_{xy}^{NN} & J_{xz}^{NN} \\ & & & & J_{yx}^{NN} & J_{yy}^{NN} & J_{yz}^{NN} \\ & & & & J_{zx}^{NN} & J_{zy}^{NN} & J_{zz}^{NN} \end{pmatrix} \tag{8.7}$$

forming a $3N \times 3N$ matrix. Note that for Heisenberg coupling, only the diagonal elements of each 3×3 block are nonzero. In order that the rotation $R_{i\gamma}$ acts only within $\mathbb{R}_3$, a projection into $\mathbf{V}^{3N}$ is performed, so that $T_{3N} = \mathbb{I}_3 \otimes T$. Since the rotation matrices are unitary, $R_i^T R_j = R_{ij}$, and the corresponding exponential factors from the Rodrigues formula (Eqn. 8.5a) can be absorbed into the definition of the Fourier transform of the exchange interaction. Expressed in the $3N \times 3N$ product space, the full inter-site Hamiltonian can then be written

$$\begin{aligned}\mathcal{H}_{int} = \frac{1}{2}\sum_{\mathbf{q}} \vec{\tilde{S}}^T_{\mathbf{q}} \Big\{ X' D_{\mathbf{q}} \Big[& \underline{\underline{\mathcal{J}}}(\mathbf{q}+\mathbf{Q}) T_{3N} \\ & + \underline{\underline{\mathcal{J}}}(\mathbf{q}-\mathbf{Q}) T^*_{3N} + \underline{\underline{\mathcal{J}}}(\mathbf{q})(\mathbb{I}_3 \otimes \mathbf{n}\mathbf{n}^T) \Big] D_{-\mathbf{q}} X \Big\} \vec{\tilde{S}}_{-\mathbf{q}} \end{aligned} \tag{8.8a}$$

$$\Big[\underline{\underline{\mathcal{J}}}(\mathbf{q})\Big]_{\gamma\gamma'} = \sum_{ij} \underline{\underline{\mathcal{J}}}^{\gamma\gamma'}_{ij} e^{-i\mathbf{q}\cdot(\mathbf{r}_i - \mathbf{r}_j)} \tag{8.8b}$$

$$X = \mathrm{diag}\left(R_1, R_2, ..., R_N\right) \tag{8.8c}$$

$$X' = \mathrm{diag}\left(R_1^T, R_2^T, ..., R_N^T\right) \tag{8.8d}$$

$$[D_{\mathbf{q}}]_{\gamma\gamma'} = e^{i\mathbf{q}\cdot\delta_\gamma}\delta_{\gamma\gamma'} \tag{8.8e}$$

where $\vec{\tilde{S}}^T_{\mathbf{q}} = (\tilde{S}^x_1(\mathbf{q}), \tilde{S}^y_1(\mathbf{q}), ..., \tilde{S}^z_N(\mathbf{q}))$. The contents of the braces, $\{\}$, can be identified as a rotated exchange parameter, $\underline{\underline{\tilde{\mathcal{J}}}}(\mathbf{q})$, defined such that, $\mathcal{H}_{int} = \frac{1}{2}\sum_{\mathbf{q}} \vec{\tilde{S}}^T_{\mathbf{q}} \underline{\underline{\tilde{\mathcal{J}}}}(\mathbf{q}) \vec{\tilde{S}}_{-\mathbf{q}}$. Even for Heisenberg coupling, this is no longer diagonal in $\mathbb{R}_3$ and contains terms that couple orthogonal modes. The matrix $D_{\mathbf{q}}$ originates from the expression of the spin operator at each site in terms of the Fourier transform $\mathbf{S}_{i\gamma} = \sum_{\mathbf{q}} e^{i\mathbf{q}\cdot\mathbf{r}_{i\gamma}} \mathbf{S}_\gamma(\mathbf{q})$. By separating the position vector into a unit cell vector and a vector describing the position within the unit cell, $\mathbf{r}_{i\gamma} = \mathbf{r}_i + \delta_\gamma$, one can define the matrix $[D_{\mathbf{q}}]_\gamma$ (Eqn. 8.8e) which acts as a form factor, resulting in interference between the ions in each unit cell.

In this rotated coordinate system, the calculation can be performed in a manner similar that outlined in previous chapters, except in the new coordinate frame the coupling is not in general a diagonal Heisenberg coupling. The Green's function can be written down by inspection of Eqn. G.8 by noting that, in this new rotating frame, $\underline{\underline{\tilde{\mathcal{J}}}}$ can couple orthogonal modes, hence

$$\begin{aligned}\tilde{G}^{\alpha\beta}_{\tilde{\gamma}\tilde{\gamma}'}(\mathbf{q},\omega) = {} & g^{\alpha\beta}_{\tilde{\gamma}\tilde{\gamma}'}(\omega)\delta_{\tilde{\gamma}\tilde{\gamma}'} \\ & + \sum_{\gamma\gamma'}^{\mu\nu} \tilde{\mathcal{J}}^{\mu\nu}_{\gamma\gamma'}(\mathbf{q}) g^{\alpha\mu}_{\tilde{\gamma}\gamma}(\omega) \tilde{G}^{\nu\beta}_{\gamma'\tilde{\gamma}'}(\mathbf{q},\omega)\end{aligned} \tag{8.9}$$

where $\tilde{G}(\mathbf{q},\omega)$ is the Green's function in the rotating frame. This can be solved as a matrix equation in a manner similar to that described in Chapters 5 and 7.

All that remains is to rotate back into the lab frame

$$\begin{aligned}\underline{\underline{G}}(\mathbf{q},\omega) = (\mathbb{I}_3 \otimes \mathbf{n}\mathbf{n}^T)X\tilde{\underline{\underline{G}}}(\mathbf{q},\omega)X'(\mathbb{I}_3 \otimes \mathbf{n}\mathbf{n}^T) \\ +T^*_{3N}X\tilde{\underline{\underline{G}}}(\mathbf{q}+\mathbf{Q},\omega)X'T'_{3N} \\ +T_{3N}X\tilde{\underline{\underline{G}}}(\mathbf{q}-\mathbf{Q},\omega)X'T^{*\prime}_{3N}\end{aligned}$$

where $T'_{3N} = (\mathbb{I}_3 \otimes T^T)$ and $T^{*\prime}_{3N} = (\mathbb{I}_3 \otimes T^\dagger)$ and the translational invariance of the correlation function has been used. If the ordering wavevector is $\mathbf{Q} = (0,0,0)$, then the Green's function in the lab frame is simply $\underline{\underline{G}}(\mathbf{q},\omega) = X\tilde{\underline{\underline{G}}}(\mathbf{q},\omega)X'$.

8.3 Application to rubidium iron fluoride

Attention is now turned to to the low energy magnetic fluctuations in the non-collinear antiferromagnet $\mathrm{RbFe^{2+}Fe^{3+}F_6}$. The crystal structure of $\mathrm{RbFe^{2+}Fe^{3+}F_6}$ is in the $Pnma$ space group (No. 62), with lattice parameters $a = 6.9663(4)$ Å , $b = 7.4390(5)$ Å and $c = 10.1216(6)$ Å at T = 4 K. The charge order originates from the differing valence on the two Fe sites, with one site occupied by an $\mathrm{Fe^{2+}}$ ion and the other by an $\mathrm{Fe^{3+}}$ ion, (henceforth referred to site A and B respectively). Consequently, the two ions have different single-ion ground states, the former having an orbital degree of freedom, with $(S = 2, L = 2)$ and the latter being an orbital singlet, $(S = 5/2, L = 0)$. As a result, whilst a projection onto a spin-only Hamiltonian is well-justified for the $\mathrm{Fe^{3+}}$ ions, the same is not necessarily true of the $\mathrm{Fe^{2+}}$ ions, where evidence of the influence of orbital physics in the correlated magnetic behaviour has already been reported [390].

The advantage of formulating the calculation in the manner described above is that one can explicitly treat the single-ion physics of the coupled magnetic ions, thus capturing the entangled nature of the spin and orbital degrees of freedom. Not only can inclusion of these single-ion terms change the energetics of the elementary excitations of the system, but terms such as spin-orbit coupling can lead to the non-conservation of $\hat{S}_z$ giving rise to correlated fluctuations of the spin amplitude in the form of longitudinal modes. Such modes are absent from conventional linear spin wave theory treatments. Attention is now paid to the single-ion physics of the Fe ions present in $\mathrm{RbFe^{2+}Fe^{3+}F_6}$.

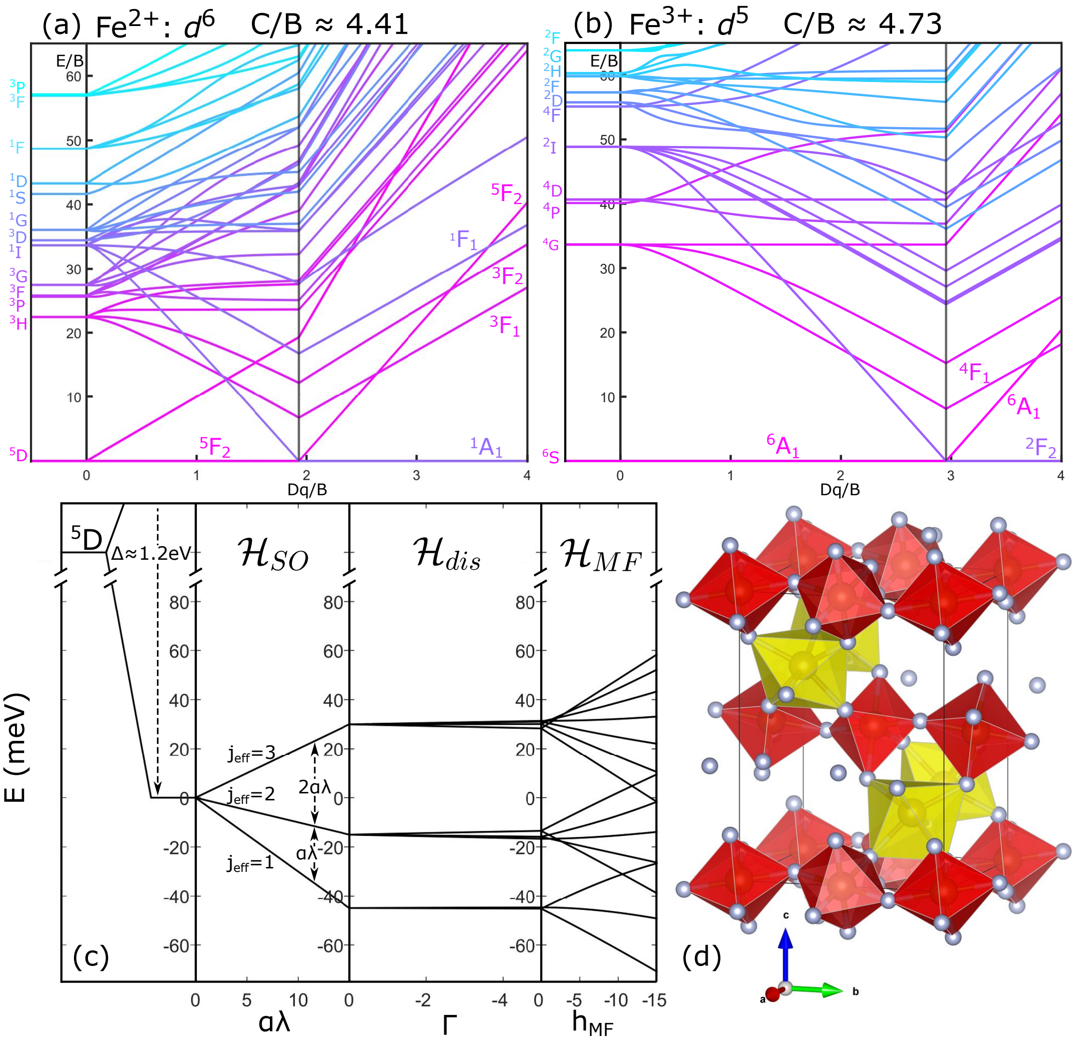

Figure 8.1 *(a) Tanabe-Sugano diagram for a* d^6 *ion.* $Dq/B \approx 1.1$ *[21, 22], hence one cannot neglect orbital angular momentum and instead one has a (S=2, L=2) ground state. The Racah parameter,* $C \approx 0.5$ *eV [22]. (b) Tanabe-Sugano diagram for a* d^5 *ion, showing the high spin to low spin transition at* $Dq/B \approx 3$*. For* Fe^{3+} *ions in an octahedral environment,* $Dq/B \approx 1.6$ *[21, 22] motivating a spin only* $(S = 5/2, L = 0)$ *ground state. The Racah parameter* $C \approx 0.6$ *eV. (c) single-ion energy levels for an* Fe^{2+} *ion under the influence of spin-orbit coupling, crystallographic distortions and a molecular mean field term, following the intermediate crystal field splitting which gives rise to the* $l = 1$ *ground state. (d) Crystal structure of* $RbFe^{2+}Fe^{3+}F_6$*, showing the octahedral* FeF_6 *coordination. Red octahedra surround* Fe^{3+} *ions and yellow octahedra surround* Fe^{2+} *ions.*

8.3.1 Single-ion physics

Whilst both Fe^{2+} and Fe^{3+} ions in the unit cell are surrounded by an octahedral environment of fluorine, the different sublattices are occupied by ions with a differing valence and local distorted environments. As a result, the ground state differs between sublattice A (Fe^{2+}) and sublattice B (Fe^{3+}). In this section (schematically outlined in Fig. 8.1) the single-ion physics on both these sites is discussed, which defines the eigenstates that are coupled up using the random phase approximation discussed above.

Sublattice A - Fe^{2+} single-ion physics

Sublattice A is occupied by Fe^{2+} ions which are in the $3d^6$ configuration. Since the $3d$ ions experience an intermediate ligand field [22], the single-ion ground state can be determined by the application of the Pauli exclusion principle and Hund's rules. Correspondingly, the ground state of the Fe^{2+} ions is ^5D (S=2, L=2, or $|L = 2, m_L; S = 2, m_S\rangle$) (Fig. 8.1 (a)).

Consideration is first paid to the strong crystalline electric field imposed on the Fe^{2+} by the locally coordinated fluorine atoms, denoted as $\mathcal{H}_{CEF}$, on the orbital component and then the effects of spin-orbit coupling are discussed below. Using Stevens operators [35, 329], for a d^6 ion in an octahedral crystal field this can be written as

$$\mathcal{H}_{CEF} = B_4(\mathcal{O}_4^0 + 5\mathcal{O}_4^4). \tag{8.10}$$

The five-fold degenerate $|L = 2, m_L\rangle$ states are split into a ground state orbital triplet and an excited doublet. The crystal field splitting for $3d$ ions is on the order of ~ 1 eV making this the largest single-ion energy scale. It should be noted that simplistic point charge calculations enjoy limited success in the treatment of the $3d$ ions owing, in part, to the significant role played by covalency effects [396]. Nonetheless, by measuring the crystal field splitting using optical spectra or RIXS, approximate values for the Steven's parameters can be extracted. The crystal field splitting in octahedrally-coordinated Fe^{2+} was determined to be $10Dq \approx 1.2$ eV [397], corresponding to $B_4 \approx 10$ meV. A similar energy scale has been reported [338, 339] in the oxides CoO [206] and NiO [337]. Writing the Stevens parameters in terms of the orbital angular momentum operators and using the notation for changing between $|L, m_L\rangle$ and the crystal field bases written in Refs.

[207, 264], one can diagonalise the crystal field Hamiltonian

$$E_{CEF} = \mathcal{C}^{-1}\mathcal{H}_{CEF}\mathcal{C} = B_4 \left(\begin{array}{ccc|cc} \mathbf{-48} & \mathbf{0} & \mathbf{0} & 0 & 0 \\ \mathbf{0} & \mathbf{-48} & \mathbf{0} & 0 & 0 \\ \mathbf{0} & \mathbf{0} & \mathbf{-48} & 0 & 0 \\ \hline 0 & 0 & 0 & \mathbf{72} & \mathbf{0} \\ 0 & 0 & 0 & \mathbf{0} & \mathbf{72} \end{array}\right) \tag{8.11}$$

and verify that the ground state orbital triplet is well separated from the excited orbital doublet. This is verified by the Tanabe-Sugano diagram for Fe^{2+} reproduced in Fig. 8.1 (*a*) with Dq/B ≈ 1.1 [21, 22] called the weak-intermediate crystal field limit. This orbital ground state is referred to as ^5D in Fig. 8.1 (*c*).

Given the ground state is an orbital triplet, one is justified in projecting the single-ion Hamiltonian into an effective $l = 1$ manifold. This transformation carries a projection factor $\mathbf{L} = \alpha\mathbf{l}$ [21] which can be read off the $l = 1$ block of the $\hat{L}_z$ operator projected into the space spanned by the eigenvectors of $\mathcal{H}_{CEF}$

$$\mathcal{C}^{-1}\hat{L}_z\mathcal{C} = \left(\begin{array}{ccc|c|c} \mathbf{-1} & \mathbf{0} & \mathbf{0} & 0 & 0 \\ \mathbf{0} & \mathbf{0} & \mathbf{0} & 0 & 2 \\ \mathbf{0} & \mathbf{0} & \mathbf{1} & 0 & 0 \\ \hline 0 & 0 & 0 & \mathbf{0} & 0 \\ \hline 0 & 2 & 0 & 0 & \mathbf{0} \end{array}\right) \tag{8.12}$$

thus $\alpha = -1$. Similar transformations for $\hat{L}_{x,y}$ show that this orbital triplet follows the correct commutator and Lie algebra for angular moment operators with $l = 1$. It should be noted that this is not guaranteed based on degeneracy alone as discussed in Ref. [18] for the case of Ce^{3+} in $CeRhSi_3$ in a comparatively anisotropic crystal field.

Having defined the orbital ground state, new basis states are defined to include spin as $|l = 1, m_l, S = 2, m_s\rangle$. The next term to be considered is the spin-orbit interaction, denoted as $\mathcal{H}_{SO}$ in Fig. 8.1 (*c*) acting on the projected orbital triplet with spin $S = 2$ ($|l = 1, m_l; S = 2, m_s\rangle$) (referred to as ^5D in Fig. 8.1 (*c*)). In terms of the projected orbital angular momentum, this can be written as

$$\mathcal{H}_{SO} = \lambda\mathbf{L}\cdot\mathbf{S} = \alpha\lambda\mathbf{l}\cdot\mathbf{S} \tag{8.13}$$

where λ is the spin-orbit coupling constant, which is negative for a greater-than-half-full outer shell [27]. For the free Fe^{2+} ion $\alpha\lambda \approx 12.4$ meV. [21, 22] This value is expected to be reduced due to the bonding with surrounding ligands, however this correction is expected to be small and is difficult to disentangle from the effects of Jahn-Teller distortions [21], so this correction will be neglected from the analysis. The spin-orbit coupling splits the triply degenerate $l = 1$ level into three j_{eff} levels

$$\mathcal{C}^{-1}\mathcal{H}_{SO}\mathcal{C} = \alpha\lambda \begin{pmatrix} -3\mathbb{I}_3 & \mathbf{0} & \mathbf{0} \\ \mathbf{0} & -\mathbb{I}_5 & \mathbf{0} \\ \mathbf{0} & \mathbf{0} & 2\mathbb{I}_7 \end{pmatrix} \tag{8.14}$$

that follow the Landé interval rule. For a $3d^6$ ion, the ground state is the triply degenerate $j_{eff} = 1$ level, with an excited quintet and septet.

Further to the octahedral crystal field described earlier, the effect of distortions away from the perfect octahedral coordination must be considered. The octahedron surrounding the Fe^{2+} is subtly compressed with four Fe-F bonds of length ≈ 2.1Å and two of length ≈ 2.0 Å. A tetrahedral distortion of this kind can be described in terms of the Stevens operator

$$\mathcal{H}_{dis} = B_2^0\mathcal{O}_2^0 = \Gamma\left(\hat{l}_z^2 - \frac{2}{3}\right). \tag{8.15}$$

The parameter Γ is negative for an octahedral compression. This term breaks the triplet orbital degeneracy, leading to a doublet ground state with an excited singlet. In addition to this distortion, the octahedra are twisted in a manner which destroys the fourfold axial symmetry. Since the point group of the octahedron surrounding the Fe^{2+} ion is the low symmetry $C_{1h} = C_s$ group, in principle, other terms of the form

$$\mathcal{H}_{CEF} = \sum_{kq} B_k^q\mathcal{O}_k^q \tag{8.16}$$

are possible. The number of terms that must be considered can be reduced by a number of symmetry and physical considerations. The first being that since the Stevens operators depend on the tesseral harmonics, only terms for which the tesseral harmonics respect the point symmetry of the local crystal environment ($\mathcal{C}_{1h}$) are nonzero [38]. The next consideration is that terms with $k > 4$ vanish in the $3d$ ions since the matrix elements of the crystal field Hamitonian depend on the product of two spherical harmonics $Y_2^{-m}(\mathbf{R})Y_2^m(\mathbf{R})$ (where $k=2$ since these are d electrons). From the Clebsch-Gordon expansion of this product, one finds that the terms with $k>4$ vanish [34]. The Stevens parameters are given by [34]

$$B_k^q = -|e|p_k^q\langle r^k\rangle\gamma_k^q\Theta_k \tag{8.17a}$$

$$\gamma_k^q = \frac{1}{2k+1}\int d^3\mathbf{R}\frac{\rho(\mathbf{R})Z_k^q(\mathbf{R})}{\epsilon_0 R^{k+1}} \tag{8.17b}$$

where Z_k^q are the tesseral harmonics, with related numerical coefficients p_k^q, ρ is the electrostatic charge density and Θ is a numerical factor originating from the conversion between polynomials and their operator equivalents [34]. For $k=2,4,6$, Θ_k are the well-known Stevens coefficients α_J, β_J, γ_J [35]. The evaluation of the integral (Eqn. 8.17b) is not a simple task. Practical calculations generally rely on vast simplifications such as a point-charge approximation which, as discussed previously, does not lead to quantitatively accurate predictions. It is therefore more appropriate to treat B_k^q as experimentally determined parameters. Since the magnitude of B_k^q scales as $\frac{1}{R^{k+1}}$, where R is the distance from the central ion to the charged ligand, the higher order terms can be excluded since their effect will be small, therefore terms with $k>2$ are excluded. Finally, the crystal field potential must satisfy time reversal symmetry [398], hence there is one further possible distortion term left

$$\mathcal{H}'_{dis} = \Gamma'\left(\hat{l}_+^2+\hat{l}_-^2\right) \tag{8.18}$$

where a conversion to operator equivalent terms has been performed and all factors have been collected into a single distortion parameter [399]. The effect of this term is to break the remaining degeneracy of the orbital doublet. Notice that the additional term has the same form as the perturbation in the widely-studied Lipkin model [400], which exhibits an exceptional point and a transition from a phase with an avoided crossing to one with a degeneracy [401]. In fact, this term gives rise to avoided crossings at $h_{MF}\approx 12.5$meV, $h_{MF}\approx 13.5$meV and $h_{MF}\approx 13.9$meV (Fig. 8.2), suggesting the presence of an exceptional point in the complex plane of (Γ', h_{MF}), close to the real axis [402]. These three identified instances of level repulsion also indicate that the single-ion eigenfunctions are strongly mixed between the $j_{eff} = 1$ and $j_{eff} = 2$ and the $j_{eff} = 2$ and $j_{eff} = 3$ manifolds.

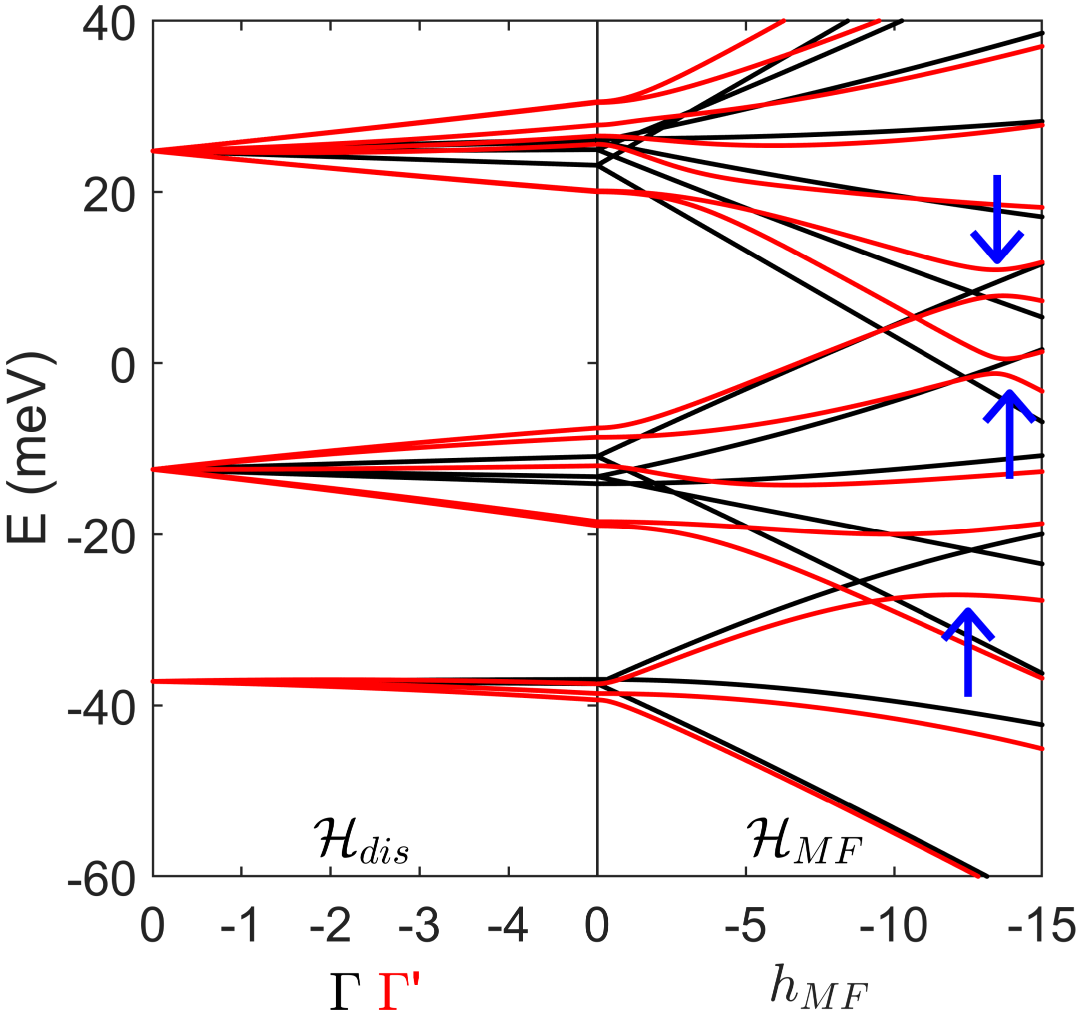

Figure 8.2 *Energy diagram for* Fe^{2+} *with spin-orbit coupling and crystallographic distortions. The black line represents a tetragonal distortion (Eqn. 8.15). The red lines indicate a distortion of the type described by Eqn. 8.18. A tetragonal distortion gives rise to an orbital doublet. The asymmetric distortion give rise to splitting of the orbital triplet. Other qualitative differences can be seen, for example there are avoided crossings at around 12.5 meV, 13.5 meV and 13.9 meV for the asymmetric distortion (indicated by the blue arrows). The level repulsion at 12.5 meV is between the* $j_{eff} = 1$ *and* $j_{eff} = 2$ *multiplets.*

The final term that must be considered in the single-ion Hamiltonian is the molecular mean field. The exchange interaction between magnetic ions results in an effective Zeeman term from the single-ion perspective. In order that the expansion is performed around the correct single-ion ground state, a mean field decoupling must be performed $\mathbf{S}_i \to \langle \mathbf{S}_i \rangle + \delta \mathbf{S}_i$ to quantify the strength of this effective Zeeman field. As outlined in the discussions above, in general a Heisenberg model can be written as

$$\mathcal{H} = \frac{1}{2} \sum_{ij}^{\gamma\gamma'} \mathcal{J}_{ij}^{\gamma\gamma'} \mathbf{S}_{i\gamma}^T \cdot \mathbf{S}_{j\gamma'}. \tag{8.19}$$

One can perform a mean field decoupling and discard terms $\sim \mathcal{O}(\delta \mathbf{S}_i)^2$. In the rotating frame, one has

$$\begin{aligned} \mathcal{H}_{MF} =& \frac{1}{2} \sum_{ij}^{\gamma\gamma'} \Big([\tilde{\mathbf{S}}_{i\gamma}^T - \frac{1}{2} \langle \tilde{\mathbf{S}}_{i\gamma}^T \rangle] \underline{\underline{\tilde{\mathcal{J}}}}_{ij}^{\gamma\gamma'} \langle \tilde{\mathbf{S}}_{j\gamma'} \rangle \\ & + \langle \tilde{\mathbf{S}}_{i\gamma}^T \rangle \underline{\underline{\tilde{\mathcal{J}}}}_{ij}^{\gamma\gamma'} [\tilde{\mathbf{S}}_{j\gamma'} - \frac{1}{2} \langle \tilde{\mathbf{S}}_{j\gamma'} \rangle] \Big), \end{aligned} \tag{8.20}$$

where $\underline{\underline{\tilde{\mathcal{J}}}}_{ij}^{\gamma\gamma'} = R_\gamma^T R_i^T \mathcal{J}_{ij}^{\gamma\gamma'} R_j R_{\gamma'}$. Neglecting constant terms, this expression can be simplified considerably, using the Rodrigues rotation formula

$$\begin{aligned} \mathcal{H}_{MF} =& \frac{1}{2} \sum_{ij}^{\gamma\gamma'} \tilde{\mathbf{S}}_{i\gamma}^T \Big(\underline{\underline{\tilde{\mathcal{J}}}}_{ij}^{\gamma\gamma'} + \underline{\underline{\tilde{\mathcal{J}}}}_{ji}^{\gamma'\gamma} \Big) \langle \tilde{\mathbf{S}}_{j\gamma'} \rangle \\ =& \sum_{i\gamma} \tilde{\mathbf{S}}_{i\gamma}^T \sum_{j\gamma'} \mathrm{Re} \left[\underline{\underline{\tilde{\mathcal{J}}}}^{\gamma\gamma'}(\mathbf{Q}) \right] \langle \tilde{\mathbf{S}}_{j\gamma'} \rangle. \end{aligned} \tag{8.21}$$

In the rotating frame, the expectation value of the spin operators only have nonzero z-components. For the $3d$ ions, the inter-ion coupling is predominantly described by a spin-spin Heisenberg model, owing to the breaking of the ground state orbital degeneracy due to crystallographic distortions or spin-orbit coupling [44]. This motivates a spin-only inter-ion interaction.

Collecting all of these single-ion terms together, one finds the single-ion Hamiltonian on sublattice A,

$$\mathcal{H}_1^A = \mathcal{H}_{SO} + \mathcal{H}_{dis} + \mathcal{H}'_{dis} + \mathcal{H}_{MF}. \tag{8.22}$$

The presence of $\mathcal{H}_{dis}$ and $\mathcal{H}_{SO}$ terms in the single-ion Hamiltonian results in the non-conservation of $\hat{S}_z$. Thus longitudinal transitions are allowed between different single-ion energy levels. Longitudinal modes are present in noncollinear magnets due to the loss of spin-rotational symmetry about $\hat{z}$ [354] and give rise to anharmonic scattering terms corresponding to coupling between transverse magnons and the two particle continuum. Systems with non-trivial single-ion physics offer an exciting opportunity for the observation of correlated amplitude fluctuations, since the fundamental excitonic spectrum includes a longitudinal component.

The effect of spin-orbital transitions between different j_{eff} levels has been observed in, for example, α,γ-CoV_2O_6 [14], α-$Co_3V_2O_8$ [208], $CoTiO_3$ [403], $Na_3Co_2SbO_6$ or $Na_2Co_2TeO_6$ [404, 405], and CoO [206, 208]. The spin-orbit splitting is typically on the order of ≈ 30 meV in $3d$ ions and hence these spin-orbit excitons may be expected to be short-lived due to a large kinematically-allowed decay region. The intensity of such modes depends strongly on the single-ion physics and whilst these spin-orbit transitions have been observed in Co^{2+} ions, they are not observed in some other $3d$ ions such as V^{3+} [4].

The propensity for longitudinal modes to decay can be overcome by moving these amplitude fluctuations out of the kinematically-allowed decay region. Therefore, the search for long-lived amplitude fluctuations at low energy may be fruitful. Amplitude fluctuations may be observed in other $3d$ ions where the excitonic modes originate not from the $j_{eff} \to j_{eff}$ transitions but from a smaller splitting due to $\mathcal{H}_{dis}$. The intensity of these transitions depends strongly on the nature of the distortion.

It is now demonstrated that crystallographic distortions offer a mechanism for longitudinal excitons in $3d$ ions, but that a large molecular Zeeman field reduces the longitudinal transition amplitude for many of the transitions in Fe^{2+} ions. The neutron scattering intensity is proportional to the transition amplitude $\mathcal{I}_{zz} = |\langle 1| \hat{S}_z |m\rangle|^2$. In Fig. 8.3, $\mathcal{I}_{zz}$ is plotted for the both the tetragonal and the asymmetric distortions introduced above. For both distortions, longitudinal transitions from the $j_{eff} = 1$ to $j_{eff} = 2$ have finite amplitude. For a tetragonal distortion, the transition A_1 is the sole longitudinal transition. In the case of the asymmetric distortion, the B_1 transition loses intensity with increasing h_{MF} and is overtaken by B_2. For the asymmetric distortion, an inter-multiplet mode is also observed, B_3. As the mean field is increased, the intensity of most longitudinal modes decreases, although an increase in the intensity of B_2 is observed, along with an increase in B_3 at large values of h_{MF}, as the single-ion energy landscape changes.

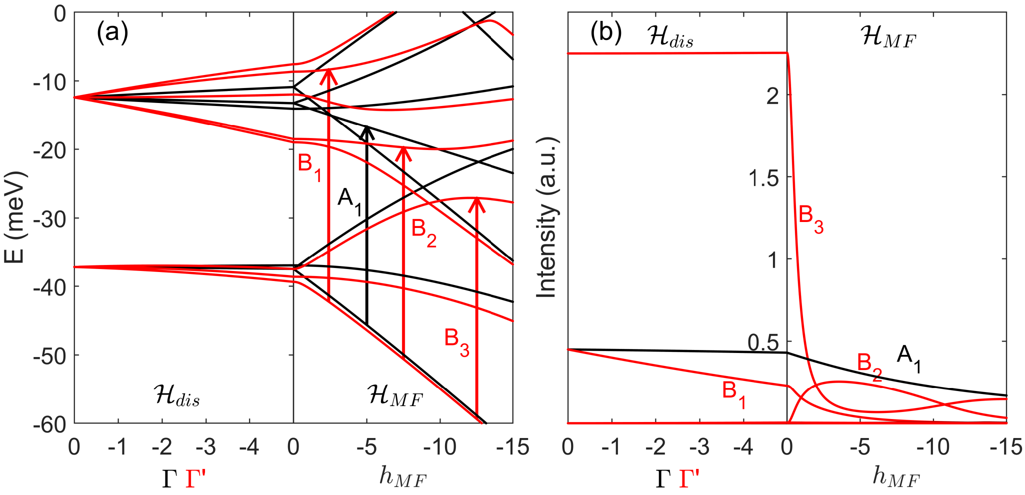

Figure 8.3 *(a) Single-ion energy levels for* Fe^{2+} *in a distorted octahedral environment. (b) Longitudinal (or amplitude) transition amplitudes,* $\mathcal{I}_{zz} = |\langle 1| \hat{S}_z |m\rangle|^2$*, for the excitations out of the ground state. As* h_{MF} *is increased the amplitude of the transitions* A_1*,* B_1 *and* B_3 *decreases. For a tetragonal/trigonal distortion (Γ), only the spin orbit transition has non-negligible intensity. For the low symmetry distortion (Γ′), the high intensity transition* B_3 *corresponds to a transition within the ground state* $j_{eff} = 1$ *multiplet. As the mean field increases, the inter-multiplet transition* B_2 *turns on and at large values of* h_{MF} *the intensity* B_3 *begins to increase again.*

The longitudinal excitations described in this chapter result from the non-conservation of $\hat{S}_z$. In other words, they correspond to amplitude fluctuations of the order parameter, in this case the spin operator. This motivates an analogy [406, 407] with the Higgs mechanism from particle physics, where amplitude fluctuations of the order parameter [378] in the presence of a gauge field give rise to the celebrated Higgs boson [408]. The case here is somewhat different, owing to the lack of a coupling of the order parameter to a gauge field as in the Higgs mechanism. Therefore these excitations will be referred to as "amplitude modes" to distinguish them both from the true gauge-field-coupled phenomena such as the Higgs boson [408], plasmons [409], the Meissner state in superconductors [410], and from other longitudinal excitations whose origins are fundamentally different, such as spinons and multi-magnon continua [411, 412].

Sublattice B - Fe^{3+} single-ion physics

In the case of a $3d^5$ ion in a perfectly octahedral environment, the ground state is an orbital singlet, $(S = 5/2, L = 0)$, hence one should only expect a mean molecular field contribution to the single-ion Hamiltonian. However, in many $3d^5$ systems, a spectral gap is measured, consistent with a single-ion anisotropy term [5, 277, 413]. This gap arises due to mixing of higher orbital energy levels into the ground state, facilitated by the cooperative effect of crystallographic distortions and spin orbit coupling [247–249]. This is phenomenologically accounted for in the model by adding a single-ion anisotropy term to the Fe^{3+} spin Hamiltonian,

$$\mathcal{H}_1^B = \mathcal{H}_{MF} + \mathcal{H}_{anis} \tag{8.23a}$$

$$\mathcal{H}_{anis} = \mu \tilde{S}_z^2. \tag{8.23b}$$

8.3.2 Spin Hamiltonian

Attention is now turned to the spin Hamiltonian that describes the interaction of ions on neighbouring sites. The Fe ions in RbFe^{2+}Fe^{3+}F$_6$ form two interpenetrating chain networks running perpendicular to one another (Fig. 8.4). The Fe^{2+} ions lie on a chain parallel to a with spins pointing along $\pm\hat{b}$, with Fe^{3+} ions on a chain parallel to a with spins along $\pm\hat{a}$. RbFe^{2+}Fe^{3+}F$_6$ can be described with a unit cell comprising eight spins (Table 8.1).

Table 8.1 *Definition of ions in the unit cell.*

Index	Sublattice	Valence	Position vector
1	B	3+	(0,0,0)
2	B	3+	(0,0.5,0)
3	B	3+	(0.5,0,0.5)
4	B	3+	(0.5,0.5,0.5)
5	A	2+	(0.1986,0.75,0.2698)
6	A	2+	(0.6986,0.75,0.2302)
7	A	2+	(0.3014,0.25,0.7698)
8	A	2+	(0.8014,0.25,0.7302)

A minimal model of nearest neighbour exchange for both inter- and intra-chain bonds is now considered. The exchange interactions are summarised below in Table 8.2. The intra-chain bonds are confined to the upper-left and lower-right

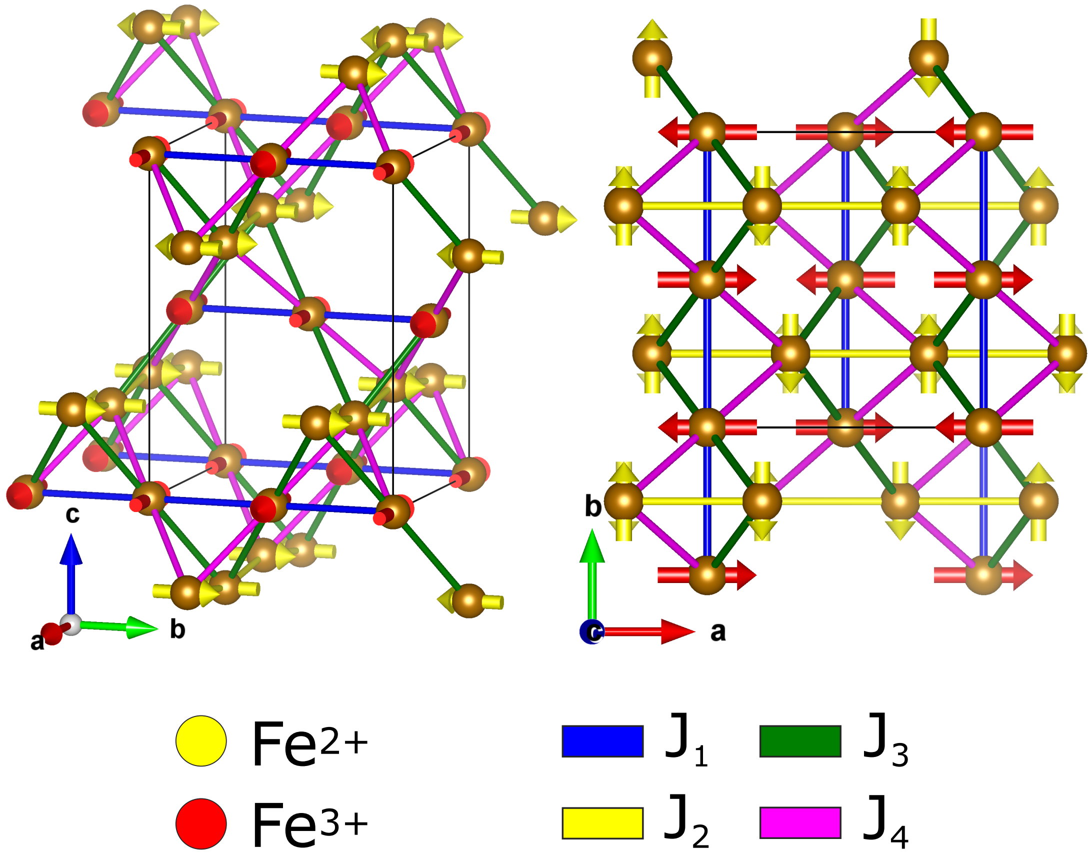

Figure 8.4 *(a, b) Crystallographic structure of $RbFe^{2+}Fe^{3+}F_6$, displaying the Fe ions and Fe-Fe bonds. Yellow arrows indicate Fe^{2+} spins and red arrows indicate Fe^{3+} spins. The Fe^{2+} ions form chains of spins along the a-axis and the Fe^{3+} ions lie in chains along the b-axis. J_1 and J_2 are intra-chain bonds whilst J_3 and J_4 couple spins lying on different chains.*

blocks, with inter-chain bonds coupling sites {1-4} with sites {5-8}. Following the approach outlined above, the Fourier transform of the exchange interaction is now taken. In the rotating frame one needs to calculate the matrix

$$\begin{aligned}\underline{\underline{\tilde{\mathcal{J}}}}(\mathbf{q}) =& X' D_{\mathbf{q}} \Big[\underline{\underline{\mathcal{J}}}(\mathbf{q}+\mathbf{Q}) T_{3N} + \underline{\underline{\mathcal{J}}}(\mathbf{q}-\mathbf{Q}) T^{*}_{3N} \\ &+ \underline{\underline{\mathcal{J}}}(\mathbf{q})(\mathbb{I}_3 \otimes \mathbf{n}\mathbf{n}^{T})\Big] D_{-\mathbf{q}} X.\end{aligned} \tag{8.24}$$

Since the propagation vector is $\mathbf{Q} = (0, 0, 0)$, the rotation of each unit cell need not be performed and instead one has $\underline{\underline{\tilde{\mathcal{J}}}}(\mathbf{q}) = X'\underline{\underline{\mathcal{J}}}(\mathbf{q})X$. The matrices, X and X' describe the matrices which rotate the spins in the unit cell onto a common axis. Since, in the lab frame, the spins lie in the a-b plane, one can define a

Table 8.2 *Inter-site bonds considered in the minimal model. J_1 and J_2 represent intra-chain bonds with J_3 and J_4 coupling sites on different chains.*

	1	**2**	**3**	**4**	**5**	**6**	**7**	**8**
1	0	J_1	0	0	J_3	J_4	J_4	J_3
2	J_1	0	0	0	J_3	J_4	J_4	J_3
3	0	0	0	J_1	J_4	J_3	J_3	J_4
4	0	0	J_1	0	J_4	J_3	J_3	J_4
5	J_3	J_3	J_4	J_4	0	J_2	0	0
6	J_3	J_3	J_4	J_4	J_2	0	0	0
7	J_4	J_4	J_3	J_3	0	0	0	J_2
8	J_3	J_3	J_4	J_4	0	0	J_2	0

rotation matrix

$$U(\theta) = \begin{pmatrix} 0 & \sin\theta & \cos\theta \\ 0 & -\cos\theta & \sin\theta \\ 1 & 0 & 0 \end{pmatrix} \tag{8.25}$$

that rotates spins by angle θ in the a-b plane. In terms of this rotation matrix, one has

$$X = \begin{pmatrix} U_{-a} & 0 & 0 & 0 & 0 & 0 & 0 & 0 \\ 0 & U_a & 0 & 0 & 0 & 0 & 0 & 0 \\ 0 & 0 & U_a & 0 & 0 & 0 & 0 & 0 \\ 0 & 0 & 0 & U_{-a} & 0 & 0 & 0 & 0 \\ 0 & 0 & 0 & 0 & U_b & 0 & 0 & 0 \\ 0 & 0 & 0 & 0 & 0 & U_{-b} & 0 & 0 \\ 0 & 0 & 0 & 0 & 0 & 0 & U_{-b} & 0 \\ 0 & 0 & 0 & 0 & 0 & 0 & 0 & U_b \end{pmatrix}, \tag{8.26}$$

where $U_a = U(0)$, $U_{-a} = U(\pi)$ and $U_{\pm b} = U(\pm\frac{\pi}{2})$, such that

$$U_a \begin{pmatrix} 0 \\ 0 \\ 1 \end{pmatrix} = \begin{pmatrix} 1 \\ 0 \\ 0 \end{pmatrix} \tag{8.27a}$$

$$U_{-a} \begin{pmatrix} 0 \\ 0 \\ 1 \end{pmatrix} = \begin{pmatrix} -1 \\ 0 \\ 0 \end{pmatrix} \tag{8.27b}$$

$$U_b \begin{pmatrix} 0 \\ 0 \\ 1 \end{pmatrix} = \begin{pmatrix} 0 \\ 1 \\ 0 \end{pmatrix} \tag{8.27c}$$

$$U_{-b}\begin{pmatrix}0\\0\\1\end{pmatrix}=\begin{pmatrix}0\\-1\\0\end{pmatrix}. \tag{8.27d}$$

Using these rotation matrices, one can write down the molecular mean field Hamiltonian for each site. In this minimal model the mean field, is the same for all spins on each sublattice,

$$\mathcal{H}_{MF} = \sum_{i\gamma} h_{MF}(i,\gamma)\tilde{S}^z_{i\gamma} \tag{8.28a}$$

$$h_{MF}(i,\gamma\in A) = -\,2J_2\langle S_A\rangle = -4J_2 \tag{8.28b}$$

$$h_{MF}(i,\gamma\in B) = -\,2J_1\langle S_B\rangle = -5J_1. \tag{8.28c}$$

The molecular mean field does not depend on the inter-chain bonds since the spins on sublattice A are perpendicular to sublattice B.

The matrix $D_{\mathbf{q}}\underline{\underline{\mathcal{J}}}(\mathbf{q})D_{-\mathbf{q}} = \sum_{ij}\underline{\underline{\mathcal{J}}}^{\gamma\gamma'}_{ij}e^{i\mathbf{q}\cdot(\mathbf{r}_{i\gamma}-\mathbf{r}_{j\gamma'})}$ can be constructed from Tables 8.1 and 8.2,

$$\begin{aligned}
\left[D_{\mathbf{q}}\underline{\underline{\mathcal{J}}}(\mathbf{q})D_{-\mathbf{q}}\right]_{12} &= J_1\left(e^{i\mathbf{q}\cdot(r_2-r_1)}+e^{i\mathbf{q}\cdot(r_2-r_1-[0,1,0])}\right)\\
\left[D_{\mathbf{q}}\underline{\underline{\mathcal{J}}}(\mathbf{q})D_{-\mathbf{q}}\right]_{25} &= J_3e^{i\mathbf{q}\cdot(r_5-r_2)}\\
\left[D_{\mathbf{q}}\underline{\underline{\mathcal{J}}}(\mathbf{q})D_{-\mathbf{q}}\right]_{26} &= J_4e^{i\mathbf{q}\cdot(r_6-r_2-[1,0,0])}\\
\left[D_{\mathbf{q}}\underline{\underline{\mathcal{J}}}(\mathbf{q})D_{-\mathbf{q}}\right]_{27} &= J_4e^{i\mathbf{q}\cdot(r_7-r_2-[1,0,0])}\\
\left[D_{\mathbf{q}}\underline{\underline{\mathcal{J}}}(\mathbf{q})D_{-\mathbf{q}}\right]_{28} &= J_3e^{i\mathbf{q}\cdot(r_8-r_2-[1,0,1])}\\
\left[D_{\mathbf{q}}\underline{\underline{\mathcal{J}}}(\mathbf{q})D_{-\mathbf{q}}\right]_{34} &= J_1\left(e^{i\mathbf{q}\cdot(r_4-r_3)}+e^{i\mathbf{q}\cdot(r_4-r_3-[0,1,0])}\right)\\
\left[D_{\mathbf{q}}\underline{\underline{\mathcal{J}}}(\mathbf{q})D_{-\mathbf{q}}\right]_{35} &= J_4e^{i\mathbf{q}\cdot(r_5-r_3-[0,1,0])}\\
\left[D_{\mathbf{q}}\underline{\underline{\mathcal{J}}}(\mathbf{q})D_{-\mathbf{q}}\right]_{36} &= J_3e^{i\mathbf{q}\cdot(r_6-r_3-[0,1,0])}\\
\left[D_{\mathbf{q}}\underline{\underline{\mathcal{J}}}(\mathbf{q})D_{-\mathbf{q}}\right]_{37} &= J_3e^{i\mathbf{q}\cdot(r_7-r_3)}\\
\left[D_{\mathbf{q}}\underline{\underline{\mathcal{J}}}(\mathbf{q})D_{-\mathbf{q}}\right]_{38} &= J_4e^{i\mathbf{q}\cdot(r_7-r_3)}\\
\left[D_{\mathbf{q}}\underline{\underline{\mathcal{J}}}(\mathbf{q})D_{-\mathbf{q}}\right]_{45} &= J_4e^{i\mathbf{q}\cdot(r_5-r_4)}\\
\left[D_{\mathbf{q}}\underline{\underline{\mathcal{J}}}(\mathbf{q})D_{-\mathbf{q}}\right]_{46} &= J_3e^{i\mathbf{q}\cdot(r_6-r_4)}\\
\left[D_{\mathbf{q}}\underline{\underline{\mathcal{J}}}(\mathbf{q})D_{-\mathbf{q}}\right]_{47} &= J_3e^{i\mathbf{q}\cdot(r_7-r_4)}\\
\left[D_{\mathbf{q}}\underline{\underline{\mathcal{J}}}(\mathbf{q})D_{-\mathbf{q}}\right]_{48} &= J_4e^{i\mathbf{q}\cdot(r_8-r_3)}
\end{aligned}$$

$$\begin{aligned}\left[D_{\mathbf{q}}\underline{\underline{\mathcal{J}}}(\mathbf{q})D_{-\mathbf{q}}\right]_{56} =& J_2\left(e^{i\mathbf{q}\cdot(r_6-r_5)}+e^{i\mathbf{q}\cdot(r_6-r_5-[1,0,0])}\right)\\ \left[D_{\mathbf{q}}\underline{\underline{\mathcal{J}}}(\mathbf{q})D_{-\mathbf{q}}\right]_{78} =& J_2\left(e^{i\mathbf{q}\cdot(r_8-r_7)}+e^{i\mathbf{q}\cdot(r_8-r_7-[1,0,0])}\right).\end{aligned}$$

The corresponding elements in the lower left triangle can be found by reversing position vector labels, hence the matrix is Hermitian. The exchange matrix in the lab frame contains only diagonal elements but on transforming to the rotating frame acquires components that couple y and z components of spins on different sublattices.

8.4 Dynamical structure factor calculations

8.4.1 Parameter choice

The rotating frame Green's function formalism is now used to calculate the dynamical structure factor of $\mathrm{RbFe^{2+}Fe^{3+}F_6}$. Samples of $\mathrm{RbFe^{2+}Fe^{3+}F_6}$ produced using hydrothermal growth techniques are typically small rod-like crystals, with the long-axis coinciding with the crystallographic b-axis [23, 383]. Neutron scattering experiments thus necessitate the coalignment of many single crystals and a broad integration of spectral weight along directions perpendicular to the scattering wavevector, offering sensitivity to fluctuations along all three directions. Consequently, the polarisation factor in the structure factor is dropped and a sum over all components of the partial dynamical structure factor is performed, $S^{\mathrm{tot}}(\mathbf{q},\omega) = \sum_{\alpha\beta} S^{\alpha\beta}(\mathbf{q},\omega)$. The parameters of the model are summarised in Table 8.3. Exchange parameters J_1-J_4 are taken from Ref. [23], along with the phenomenological anisotropy parameter μ. The value of λ was chosen in accordance with perturbative calculations and paramagnetic resonance of $\mathrm{Fe^{2+}}$ in MgO [414, 415]. The distortion parameter, Γ, is chosen to be small, on the order of meV ($\Gamma = -1.5$ meV), consistent in scale with the parameter extracted from fits to neutron data in $\mathrm{Co^{2+}}$ [207, 346] and $\mathrm{V^{3+}}$ [4] compounds.

In the case of a purely tetragonal or trigonal distortion, the sign of the distortion parameter can be inferred from the crystal structure, with $\Gamma < 0$ corresponding to a compression of the octahedron and an orbital doublet ground state [333, 416]. The term originating from the low symmetry nature of the local environment, appearing in $\mathcal{H}'_{dis}$, has no such intuitive interpretation. However, this term fully breaks the degeneracy of the $l = 1$ ground state and hence result in an orbital

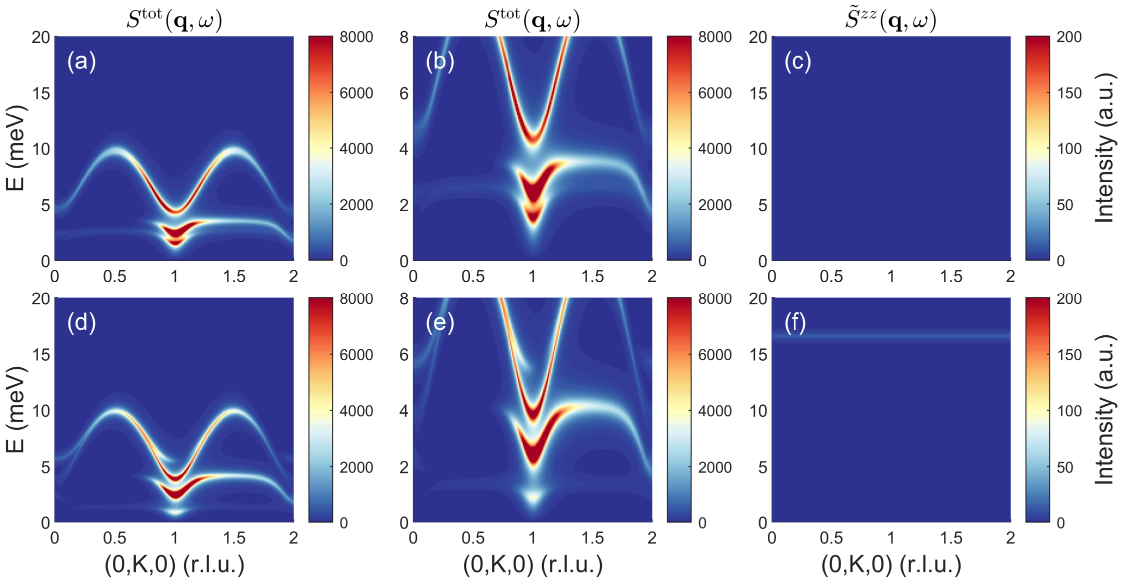

Figure 8.5 *Dynamical structure factor calculation for* $RbFe^{2+}Fe^{3+}F_6$*. In the right hand column is the longitudinal component in the rotating frame which contains the contribution from amplitude fluctuations. Panels (a-c) show the calculated response with exchange parameters taken from Ref. [23], along with a tetragonal compression,* $\Gamma = -1.5$ *meV. Panels (d-f) show the corresponding calculation with an asymmetric distortion* $\Gamma' = -1.5$ *meV.*

singlet ground state, regardless of the sign of this distortion. This distortion is therefore taken to be negative along with the tetragonal distortion.

Parameter	Value (meV)
J_1	1.9
J_2	1.4
J_3	1.4
J_4	0.75
$\alpha\lambda$	12.4
Γ	-1.5
μ	-0.075

Table 8.3 *Summary of the parameter values used in the Green's function calculation of the dynamical structure factor.*

8.4.2 Neutron scattering response

The neutron scattering response is plotted in Fig. 8.5 (a, b) for a tetragonal distortion (Eqn. 8.15) and Fig. 8.5 (d, e) for an asymmetric distortion (Eqn. 8.18). For both distortion types the spectra are qualitatively similar to the measured neutron response [23] with a gapped upper dispersive mode which reaches the zone boundary at around $E \approx 10$ meV. A further low energy mode is seen at around $E \approx 2.5$ meV. This mode has a smaller gap and bandwidth, with a spin wave velocity that approaches zero away from the zone centre. Both modes are observed to split for this set of parameters, in agreement with Ref. [23]. The splitting of both modes shows some difference between the two distortions, reflecting the quantitative difference between the Fe^{2+} single-ion energy levels for each distortion.

The presence of these dispersive modes in the linear spin wave calculation for $\mathrm{RbFe}^{2+}\mathrm{Fe}^{3+}\mathrm{F}_6$ [23] indicates a predominant transverse component, which is also captured by the Green's function formalism presented here.

8.4.3 Amplitude fluctuations

A particular aspect of this analysis is the prediction of amplitude fluctuations in the neutron scattering response to first order in the Dyson expansion where $\frac{\mathrm{d}\langle \hat{S}_z \rangle}{\mathrm{d}t} \neq 0$. Such excitations are not present in conventional spin wave theory based on the Landau equation. In this section, the key ingredients that allow such fluctuations to exist to first order in the neutron scattering response are analysed. It is important to note that these excitations appear in the zz component of the rotating frame, where the spins are coaligned and fluctuations in the magnitude of the order parameter appear along the common $\hat{z}$-axis. Upon rotating back to the laboratory frame, these fluctuations are no longer confined to the zz component of the structure factor. The structure factor will therefore be examined in the rotating frame so that the longitudinal, $\tilde{S}^{zz}(\mathbf{q}, \omega)$, and transverse components can be distinctly identified. The longitudinal component for both distortions is plotted in Fig. 8.5 (c, f). With $\Gamma' = -1.5$ meV, a weak longitudinal component can be observed (Fig. 8.5 (f)), manifested in a flat mode with $E \approx 17$ meV. The nature of these amplitude modes will now be further investigated.

Inter-multiplet spin-orbit excitons

Regardless of the nature of the distortion, longitudinal transitions between the $j_{eff} = 1$ and $j_{eff} = 2$ multiplet are permitted (Fig. 8.3). These modes generally occur at a higher energy scale than the dispersive magnon excitations, since the energy scale of these excitations are $\sim \lambda$ as per the Landé interval rule. These modes are particularly susceptible to decay since there is often a large kinematically allowed decay region. The longitudinal component in the rotating frame is plotted in Fig. 8.6 for both of the distortion terms, with $\Gamma = -1.5$ meV and $\Gamma' = -1.5$ meV respectively. For each of these distortions, a high energy spin-orbit exciton is seen at $E \approx 28$ meV.

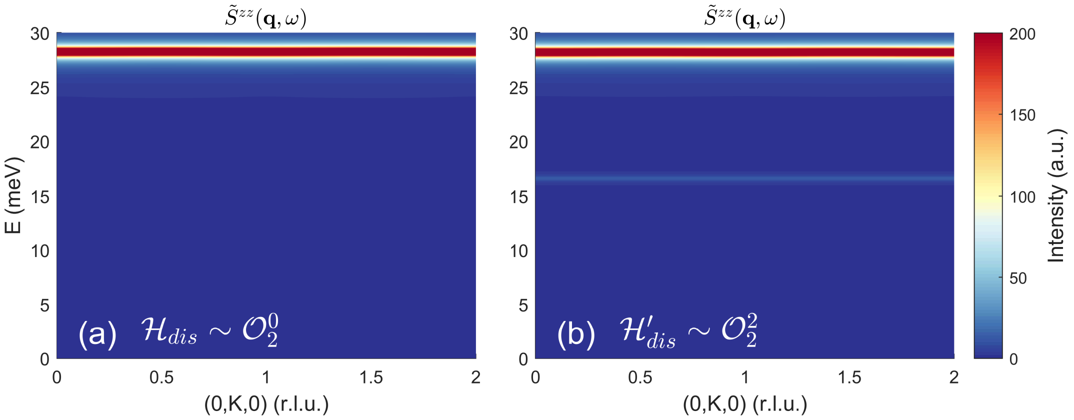

Figure 8.6 *Spin-orbital exciton at $E \approx 28$ meV for both types of distortion allowed by symmetry in RbFe^{2+}Fe^{3+}F$_6$. (a) In the case where $\mathcal{H}_{dis} = \mathcal{O}_2^0$, the spin-orbit exciton is the only amplitude fluctuation that carries any intensity. (b) The distortion $\sim \mathcal{O}_2^2$ exhibits a further flat mode at around 17 meV.*

Intra-multiplet distortion modes

In Fig. 8.6, (*b*) a second flat mode can be seen at $E \approx 17$ meV, originating from the intra-multiplet transition permitted by an asymmetrically distorted crystal field. This mode is weak, in agreement with Fig. 8.3, which suggests that the intensity of this amplitude mode is suppressed by the molecular field. It should also be noted that this mode is likely susceptible to decay owing to the fact that it lies at an energy that is less than two times the magnitude of the expected magnon bandwidth [23].

The nature of the asymmetric distortion is now further explored. Fig. 8.7 (*a*)

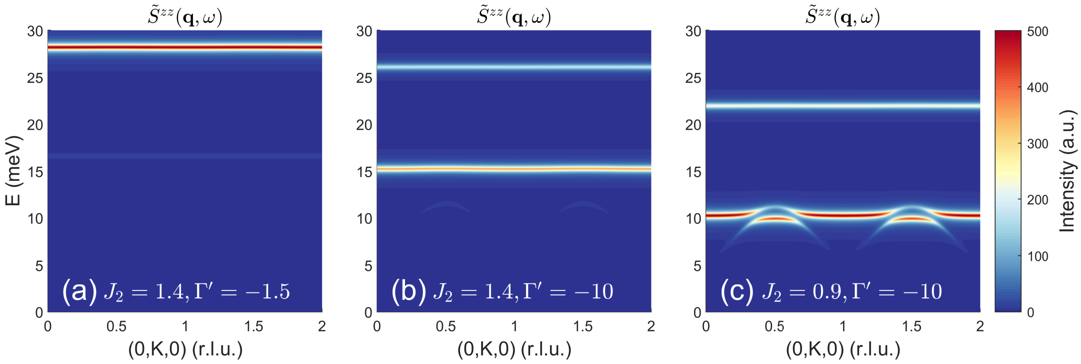

Figure 8.7 *(a) Longitudinal component of the structure factor in the rotating frame for $J_2 = 1.4$ meV and $\Gamma' = -1.5$ meV. Both the high energy spin-orbital exciton and a flat weak intra-multiplet mode are visible. (b) Amplitude fluctuations with $J_2 = 1.4$ meV and $\Gamma' = -10$ meV. Upon increasing the magnitude of the distortion, the flat intra-multiplet mode gains intensity. A very weak dispersive lower mode appears around $E \approx 12$ meV. (c) Upon decreasing the molecular mean field h_{MF} by decreasing J_2, the lower two modes hybridise and the intra-multiplet mode increases in intensity.*

shows the longitudinal component of the structure factor for the asymmetric distortion $\mathcal{H}'_{dis}$, with $\Gamma' = -1.5$ meV. A weak flat mode at $E \approx 17$ meV is visible. Upon increasing the magnitude of the distortion parameter to $\Gamma' = -10$ meV, the flat mode gains spectral weight and a very weak dispersive amplitude mode at lower energy appears (Fig. 8.7 (*b*)). Finally, after reducing the magnitude of J_2 and hence $|h_{MF}|$, the intensity of the intra-multiplet modes can be seen to increase in Fig. 8.7 (*c*) (in agreement with Fig. 8.3) and the flat intra-multiplet mode hybridises with the lower dispersive mode.

8.5 Conclusion

An excitonic description of the spin excitations in insulating $\mathrm{RbFe^{2+}Fe^{3+}F_6}$ has been presented, applying a multi-level formalism with Green's functions. This approach differs from semiclassical descriptions which focus on transverse perturbations of a spin of fixed magnitude. While such approaches incorporate local anisotropy through anisotropic and antisymmetric terms, the Green's function approach applied here explicitly incorporates single-ion physics and spin-orbit coupling. Bringing in spin-orbit coupling ($\propto \mathbf{l}\cdot\mathbf{S}$) is particularly important as the observable operator $\hat{S}_z$ no longer commutes with the Hamiltonian $[\mathcal{H}, \hat{S}_z] \neq 0$ and therefore the expectation value $\langle \hat{S}_z \rangle$ is no longer explicitly a conserved quantity (implying $\frac{\mathrm{d}\langle \hat{S}_z \rangle}{\mathrm{d}t} \neq 0$). This allows unusual types of excitations such as amplitude fluctuations to become allowed and observable with the dipolar selection rules of neutron scattering. As discussed above, such excitations are no longer forbidden in $\mathrm{RbFe^{2+}Fe^{3+}F_6}$ owing to the presence of an orbitally degenerate ground state of $\mathrm{Fe^{2+}}$ (as schematically illustrated in Fig. 8.1).

One of the issues with experimentally observing amplitude modes resulting from excitonic magnetic excitations is that they typically occur at higher energies than the lower energy transverse excitations. Typically, these modes then decay and appear experimentally as an energy and momentum broadened continuum of scattering, not a temporally sharp underdamped excitation like a harmonic spin wave. Such a situation has been analysed theoretically and experimentally in the fourth row transition metal ion compound $\mathrm{Ca_2RuO_4}$ [264, 406]. In this particular situation the amplitude mode was kinematically allowed to decay into lower transverse modes resulting in a continuum of scattering observable with the combination of polarised neutrons and the mapping capabilities afforded by modern neutron spectrometers. It should be noted that given the formalism presented here, and applied in Ref. [264], only corresponds to first order mean field theory, it does not capture such decay process which require higher order terms in the Dyson expansion. This is beyond the scope and the goal of this analysis presented here.

In this context, it is interesting, to apply this to the case of $\mathrm{RbFe^{2+}Fe^{3+}F_6}$. As experimentally reported in Ref. [23], the magnetic excitations consist of two components - a temporally well defined underdamped component and also a component that is broadened in both energy and momentum. Such a component may originate from quantum fluctuations owing to noncommuting observables reported in low-spin chains, however it is not expected to be strong in large spin components such as $S = 2$ of $\mathrm{Fe^{2+}}$ or $S = 5/2$ of $\mathrm{Fe^{3+}}$. This leads to the suggestion that it may originate from amplitude fluctuations allowed by the low local symmetry of the $\mathrm{Fe^{2+}}$ ion and the presence of spin-orbit coupling.

This work illustrates that there are two components required required for the presence of observable amplitude fluctuations at accessible low energies in intermediate field third-row transition metal ions. The first is spin-orbit coupling like found here in $\mathrm{Fe^{2+}}$ or present in $\mathrm{V^{3+}}$ or $\mathrm{Co^{2+}}$ which allows fluctuations in the order parameter amplitude $\langle \hat{S}_z \rangle$ to occur.

The second key component is the presence of low symmetry, permitting single-ion terms such as $\sim \mathcal{O}_2^2$ which are not present in tetragonal, trigonal or hexagonal symmetry [34]. A distortion of this form can permit amplitude fluctuations, both in the form of spin-orbit excitons ($\sim \lambda$) and lower energy intra-multiplet modes which can disperse. While tetragonal distortions can give rise to amplitude fluctuations, these are present at higher energies, close to the single-ion energy scale of the spin-orbit transitions ($\sim \lambda$), which is ~ 30 meV in $3d$ transition metal ions. Such fluctuations are less relevant as it is much more difficult to tune to such energy scales or stabilise them. Therefore, it is suggested that amplitude modes in $3d$ transition metal ions are best sought in compounds with low local symmetry and based on magnetic ions with an orbital degeneracy like Fe^{2+}, V^{3+}, or Co^{2+}.

Chapter 9

Conclusions

In this Thesis, the impact of local degrees of freedom on the correlated magnetic behaviour of $3d$ transition metal compounds has been examined, both in terms of order and excitations, through the use of neutron spectroscopy and complementary theoretical analysis. The local degrees of freedom, originating from the single-ion physics of the magnetic ions, give rise to magnetic anisotropy, influencing the dynamics and stabilising ordered phases of matter. The work contained within this Thesis demonstrates that anisotropy gives rise to unconventional magnetic excitations, not captured by linear spin wave theory and stabilises magnetic order in systems for which thermal fluctuations might be expected to preclude order due to low-dimensionality. Detailed in this Thesis is a framework for modelling the neutron scattering spectrum in systems where the local degrees of freedom cannot be neglected. This framework, based on the calculation of Green's functions, has been generalised, allowing for the treatment of noncollinear magnetically ordered systems of arbitrary unit cell size.

In Chapter 3, the low energy dynamics of large-spin anisotropic quasi-one-dimensional antiferromagnets were examined. It was shown that the presence of anisotropy gives rise to nonlinear excitations analogous to the spinons measured in spin-1/2 chain compounds. The equation of motion governing the dynamics in these systems was shown to admit kink-antikink soliton solutions, describing the movement of extended domain wall pairs. By considering the effect of a weak inter-chain coupling, a nonlinear confinement potential was developed, which captured the gradual annihilation of colliding domain walls owing to their spatially-extended nature. By treating the domain walls as point-like particles and the confinement potential as a potential well, the bound state spectrum was found numerically, showing the emergence of two regimes based on the ratio of anisotropy to inter-chain coupling strength. This theoretical model was then used to successfully model the bound state spectrum in $CaFe_2O_4$. This chapter demonstrated that the presence of anisotropy – a consequence of local single-ion physics – can give rise to exotic excitations usually only observed in spin-1/2 systems.

Chapter 4 concerned the antiferromagnetic compound, CoV_2O_6, where a series of magnetisation plateaux are observed in the absence of Bragg peaks which would indicate transitions between distinct long-range ordered phases of matter. Owing to the large spin-orbit coupling in this system, compared with a small inter-ion exchange coupling, this system was mapped onto a j_{eff} Ising model. By considering the restrictions placed on the allowed values of the magnetisation by translational symmetry, the Lieb-Schultz-Mattis theorem was applied to infer the ground state symmetries for each observed magnetisation plateau. The implied ground state periodicity from this analysis was then shown to be consistent with the appearance of momentum broadened peaks in diffraction data. The cascade of magnetisation plateaux was therefore shown to stem from metastable antiphase boundary order between domains with a three-site symmetry. The ultimate series of ground states achieved as the magnetic field is varied in CoV_2O_6 rely on the uniaxial symmetry afforded by the Ising anisotropy and the presence of a $j_{eff} = \frac{1}{2}$ ground state. The magnetisation plateaux can thus be taken as a strong example of how local degrees of freedom conspire to give different correlated states of matter than would be achieved in a purely isotropic system.

In Chapter 5, the magnon dynamics and magnetic order in the $S = 5/2$ antiferromagnet $CaFe_2O_4$ was investigated. This system exhibits two magnetic phases, characterised by the *c*-axis stacking. Using neutron spectroscopy, the low energy dynamics were measured at high temperature where a single phase is observed, and low temperature where the phases coexist. A Green's function analysis was performed to model the spectrum and extract exchange parameters for both phases. Both phases were modelled with a common set of exchange parameters, with a temperature renormalisation factor at high temperature. Through the Green's function analysis and a toy model of domain formation, the low temperature phase coexistence was shown to be the result of a freezing of thermally-activated dynamical antiphase domain boundaries, as the sample is cooled. The antiphase domain boundaries are stabilised by a single-ion anisotropy which prevents the relaxation into the ground state magnetic structure and thus the magnetic phase at low temperature is a metastable state that would not exist if not for single-ion anisotropy from local crystal distortions.

Chapter 6 detailed an investigation into the two-dimensional itinerant ferromagnet Fe_3GeTe_2. Neutron spectroscopy was performed to map out the low energy spin waves. The spin waves were shown to be broad, indicative of itinerance. The spin waves were modelled in the small-$\mathbf{q}$ limit, where the localised approximation is valid. The value of the spin stiffness was extracted, along with an anisotropy gap. By modelling domain walls in Fe_3GeTe_2, the expected domain wall width, based on the bulk exchange parameters, was extracted and compared with STM measurements on the surface. The expected width was observed to be close to the measured surface domain wall width, indicating that the surface exchange and anisotropy parameters may be close to those of the bulk.

In Chapter 7, using both a cold triple-axis and a thermal chopper spectrometer, the spin waves in the two-dimensional ferromagnet VI_3 were mapped out to the zone boundary. Two modes were observed with differing bandwidths, anisotropy gaps and intensities throughout the Brillouin zone. V^{3+} exhibits an orbitally degenerate crystal field ground state, with an effective orbital degree of freedom. The Green's function analysis used in Chapter 5 was extended to account for the orbital degree of freedom in VI_3. The neutron data were modelled with two different distorted domains and a single exchange parameter. The results of this work showed that crystal distortions are able to stabilise magnetism in two dimensions, overcoming the restrictions of the Mermin-Wagner theorem by explicitly breaking spin-rotational symmetry.

Chapter 8 discussed the extension of the Green's function analysis to treat noncollinear systems. By placing the calculation on the rotating frame, a general formalism is provided to treat any single-$\mathbf{Q}$ magnetic structure of arbitrary unit cell size and magnetic configuration. The magnetic excitations of the noncollinear charge-ordered antiferromagnet $RbFe^{2+}Fe^{3+}F_6$ were then revisited using the Green's function formalism. It was further shown that the asymmetric distortion present in $RbFe^{2+}Fe^{3+}F_6$ gives rise to the possibility of an asymmetric distortion term, not frequently considered in magnetic systems. It was then demonstrated that the presence of spin-orbit coupling gives rise to amplitude fluctuations of the order parameter which are not described by linear spin wave theory. The addition of an asymmetric distortion not only allows for longitudinal spin-orbital excitons but also dispersive low energy intra-multiplet excitations.

Chapter 8 thus demonstrates that by manipulating the local environment of the magnetic ions, unconventional collective magnetic excitations can be achieved.

Appendix A

List of tesseral harmonics

The tesseral harmonics, $Z_{n\alpha}$, are widely used to define the crystal field potential [34, 36, 417]. They are related to the spherical harmonics, Y_n^α by the relations

$$Z_{n0} = Y_n^0 \tag{A.1a}$$

$$Z_{n\alpha} = Z_{n\alpha}^c = \frac{1}{\sqrt{2}}\left(Y_n^{-\alpha} + (-1)^\alpha Y_n^\alpha\right) \;(\alpha > 0) \tag{A.1b}$$

$$Z_{n\alpha} = Z_{n\alpha}^s = \frac{i}{\sqrt{2}}\left(Y_n^{\alpha} - (-1)^\alpha Y_n^{-\alpha}\right) \;(\alpha < 0). \tag{A.1c}$$

The tesseral harmonics up to fourth order (as is relevant to the $3d$ ions) are tabulated below [417]

$$Z_{00} = \frac{1}{\sqrt{4\pi}}$$

$$Z_{11}^s = \sqrt{\frac{3}{4\pi}}\frac{y}{r}$$

$$Z_{10} = \sqrt{\frac{3}{4\pi}}\frac{z}{r}$$

$$Z_{11}^c = \sqrt{\frac{3}{4\pi}}\frac{x}{r}$$

$$Z_{22}^s = \frac{1}{4}\sqrt{\frac{15}{\pi}}\frac{2xy}{r^2}$$

$$Z_{21}^s = \frac{1}{2}\sqrt{\frac{15}{\pi}}\frac{yz}{r^2}$$

$$Z_{20} = \frac{1}{4}\sqrt{\frac{5}{\pi}}\frac{3z^2 - r^2}{r^2}$$

$$
\begin{aligned}
Z_{21}^{c} &= \frac{1}{2}\sqrt{\frac{15}{\pi}}\frac{xz}{r^{2}} \\
Z_{22}^{c} &= \frac{1}{4}\sqrt{\frac{15}{\pi}}\frac{x^{2}-y^{2}}{r^{2}} \\
Z_{33}^{s} &= \sqrt{\frac{35}{32\pi}}\frac{3x^{2}y-y^{3}}{r^{3}} \\
Z_{32}^{s} &= \sqrt{\frac{105}{16\pi}}\frac{2xyz}{r^{3}} \\
Z_{31}^{s} &= \sqrt{\frac{21}{32\pi}}\frac{y\left(5z^{2}-r^{2}\right)}{r^{3}} \\
Z_{30} &= \sqrt{\frac{7}{16\pi}}\frac{z\left(5z^{2}-3r^{2}\right)}{r^{3}} \\
Z_{31}^{c} &= \sqrt{\frac{21}{32\pi}}\frac{x\left(5z^{2}-r^{2}\right)}{r^{3}} \\
Z_{32}^{c} &= \sqrt{\frac{105}{16\pi}}\frac{\left(x^{2}-y^{2}\right)z}{r^{3}} \\
Z_{33}^{c} &= \sqrt{\frac{35}{32\pi}}\frac{x^{3}-3xy^{2}}{r^{3}} \\
Z_{44}^{s} &= \frac{3}{16}\sqrt{\frac{35}{\pi}}\frac{4\left(x^{3}y-xy^{3}\right)}{r^{4}} \\
Z_{43}^{s} &= \frac{3}{8}\sqrt{\frac{70}{\pi}}\frac{\left(3x^{2}y-y^{3}\right)z}{r^{4}} \\
Z_{42}^{s} &= \frac{3}{8}\sqrt{\frac{5}{\pi}}\frac{2xy\left(7z^{2}-r^{2}\right)}{r^{4}} \\
Z_{41}^{s} &= \frac{3}{4}\sqrt{\frac{5}{2\pi}}\frac{yz\left(7z^{2}-3r^{2}\right)}{r^{4}} \\
Z_{40} &= \frac{3}{16}\frac{1}{\sqrt{\pi}}\frac{35z^{4}-30z^{2}r^{2}+3r^{4}}{r^{4}} \\
Z_{41}^{c} &= \frac{3}{4}\sqrt{\frac{5}{2\pi}}\frac{xz\left(7z^{2}-3r^{2}\right)}{r^{4}} \\
Z_{42}^{c} &= \frac{3}{8}\sqrt{\frac{5}{\pi}}\frac{\left(x^{2}-y^{2}\right)\left(7z^{2}-r^{2}\right)}{r^{4}} \\
Z_{43}^{c} &= \frac{3}{8}\sqrt{\frac{70}{\pi}}\frac{\left(x^{3}-3xy^{2}\right)z}{r^{4}} \\
Z_{44}^{c} &= \frac{3}{16}\sqrt{35}\pi\frac{x^{4}-6x^{2}y^{2}+y^{4}}{r^{4}}.
\end{aligned}
$$

Appendix B

List of Stevens operators

In this Thesis, the crystalline electric field Hamiltonian is written in terms of the Stevens operators [21, 34, 35, 329]. These can be written in terms of angular momentum operators

$$\hat{X} = L(L+1)$$

$$\mathcal{O}_0^0 = 1$$

$$\mathcal{O}_1^{-1} = \frac{-i}{2}\left(\hat{L}_+ - \hat{L}_-\right)$$

$$\mathcal{O}_1^0 = \hat{L}_z$$

$$\mathcal{O}_1^1 = \frac{1}{2}\left(\hat{L}_+ + \hat{L}_-\right)$$

$$\mathcal{O}_2^{-2} = \frac{-i}{2}\left(\hat{L}_+^2 - \hat{L}_-^2\right)$$

$$\mathcal{O}_2^{-1} = \frac{1}{2}\left(\hat{L}_y\hat{L}_z + \hat{L}_z\hat{L}_y\right)$$

$$\mathcal{O}_2^0 = 3\hat{L}_z^2 - \hat{X}$$

$$\mathcal{O}_2^1 = \frac{1}{2}\left(\hat{L}_x\hat{L}_z + \hat{L}_z\hat{L}_x\right)$$

$$\mathcal{O}_2^2 = \frac{1}{2}\left(\hat{L}_+^2 + \hat{L}_-^2\right)$$

$$\mathcal{O}_3^{-3} = \frac{-i}{2}\left(\hat{L}_+^3 - \hat{L}_-^3\right)$$

$$\mathcal{O}_3^{-2} = \frac{-i}{4}\left[\left(\hat{L}_+^2 - \hat{L}_-^2\right)\hat{L}_z + \hat{L}_z\left(\hat{L}_+^2 - \hat{L}_-^2\right)\right]$$

$$\begin{aligned}\mathcal{O}_3^{-1} = \frac{-i}{4}\Bigg[&\left(\hat{L}_+ - \hat{L}_-\right)\left(5\hat{L}_z^2 - \hat{X} - \frac{1}{2}\right) \\ &+ \left(5\hat{L}_z^2 - \hat{X} - \frac{1}{2}\right)\left(\hat{L}_+ - \hat{L}_-\right)\Bigg]\end{aligned}$$

$$\mathcal{O}_3^{0} = 5\hat{L}_z^3 - \left(3\hat{X} - 1\right)\hat{L}_z$$

$$\mathcal{O}_3^{1} = \frac{1}{4}\left[\left(\hat{L}_+ + \hat{L}_-\right)\left(5\hat{L}_z^2 - \hat{X} - \frac{1}{2}\right) + \left(5\hat{L}_z^2 - \hat{X} - \frac{1}{2}\right)\left(\hat{L}_+ + \hat{L}_-\right)\right]$$

$$\mathcal{O}_3^{2} = \frac{1}{4}\left[\left(\hat{L}_+^2 + \hat{L}_-^2\right)\hat{L}_z + \hat{L}_z\left(\hat{L}_+^2 + \hat{L}_-^2\right)\right]$$

$$\mathcal{O}_3^{3} = \frac{1}{2}\left(\hat{L}_+^3 + \hat{L}_-^3\right)$$

$$\mathcal{O}_4^{-4} = \frac{-i}{2}\left(\hat{L}_+^4 - \hat{L}_-^4\right)$$

$$\mathcal{O}_4^{-3} = \frac{-i}{4}\left[\left(\hat{L}_+^3 - \hat{L}_-^3\right)\hat{L}_z + \hat{L}_z\left(\hat{L}_+^3 - \hat{L}_-^3\right)\right]$$

$$\mathcal{O}_4^{-2} = \frac{-i}{4}\left[\left(\hat{L}_+^2 - \hat{L}_-^2\right)\left(7\hat{L}_z^2 - \hat{X} - 5\right) + \left(7\hat{L}_z^2 - \hat{X} - 5\right)\left(\hat{L}_+^2 - \hat{L}_-^2\right)\right]$$

$$\begin{aligned}\mathcal{O}_4^{-1} = \frac{-i}{4}\Big[&\left(\hat{L}_+ - \hat{L}_-\right)\left(7\hat{L}_z^3 - \left(3\hat{X} + 1\right)\hat{L}_z\right) \\ &+ \left(7\hat{L}_z^3 - \left(3\hat{X} + 1\right)\hat{L}_z\right)\left(\hat{L}_+ - \hat{L}_-\right)\Big]\end{aligned}$$

$$\mathcal{O}_4^{0} = 35\hat{L}_z^4 - \left(30\hat{X} - 25\right)\hat{L}_z^2 + 3\hat{X}^2 - 6\hat{X}$$

$$\begin{aligned}\mathcal{O}_4^{1} = \frac{1}{4}\Big[&\left(\hat{L}_+ + \hat{L}_-\right)\left(7\hat{L}_z^3 - \left(3\hat{X} + 1\right)\hat{L}_z\right) \\ &+ \left(7\hat{L}_z^3 - \left(3\hat{X} + 1\right)\hat{L}_z\right)\left(\hat{L}_+ + \hat{L}_-\right)\Big]\end{aligned}$$

$$\mathcal{O}_4^{2} = \frac{1}{4}\left[\left(\hat{L}_+^2 + \hat{L}_-^2\right)\left(7\hat{L}_z^2 - \hat{X} - 5\right) + \left(7\hat{L}_z^2 - \hat{X} - 5\right)\left(\hat{L}_+^2 + \hat{L}_-^2\right)\right]$$

$$\mathcal{O}_4^{3} = \frac{1}{4}\left[\left(\hat{L}_+^3 + \hat{L}_-^3\right)\hat{L}_z + \hat{L}_z\left(\hat{L}_+^3 + \hat{L}_-^3\right)\right]$$

$$\mathcal{O}_4^{4} = \frac{1}{2}\left(\hat{L}_+^4 + \hat{L}_-^4\right)$$

Appendix C

Derivation of nonlinear σ model

In Chapter 3, the large-spin antiferromagnetic chain was mapped onto the nonlinear σ model. Here is presented a derivation of the action (Eqn. 3.2) starting from a Heisenberg spin Hamiltonian for a chain with nearest-neighbour interactions and easy-axis anisotropy

$$\mathcal{H} = J\sum_i \mathbf{S}_i \cdot \mathbf{S}_{i+1} - \alpha \sum_i \left(\hat{S}_i^z\right)^2 \tag{C.1}$$

with $\alpha > 0$ and $J > 0$. Assuming that the spin magnitude is large, the spin can be represented as a semiclassical vector moving on the surface of a sphere, $\mathbf{S} = S\mathbf{N}$, where $\mathbf{N}$ is a vector on a unit sphere. In order to perform a path integral over the system's phase space, it is convenient to define a coherent state representation of the system [137]. The Heisenberg model spin geometry allows such a state to be constructed very simply by defining a maximally polarised state $|\psi_0\rangle$ and performing unitary rotations about this reference state

$$|\mathbf{N}\rangle = e^{\Omega}\,|\psi_0\rangle \tag{C.2}$$

where $\Omega = z\hat{S}^+ - z^*\hat{S}^-$ and $z = \frac{\theta}{2}e^{-i\phi}$. The spin coherent state for the entire chain is then formed from a product state of each constituent spin whose position on the surface of the sphere is parameterised by some parameter, τ. In the continuum limit, the state of the chain becomes

$$|\mathbf{N}(x,\tau)\rangle = |S_1, m_1\rangle \otimes |S_2, m_2\rangle \otimes ... \otimes |S_N, m_N\rangle = |\mathbf{N}_1(\tau), \mathbf{N}_2(\tau), ..., \mathbf{N}_N\rangle\,. \tag{C.3}$$

The partition function is then

$$\mathcal{Z} = \int \mathrm{d}\mathbf{N}\delta\left(|\mathbf{N}|^2 - 1\right)\langle\mathbf{N}|\, e^{-\beta\mathcal{H}}\, |\mathbf{N}\rangle \tag{C.4}$$

where $\beta = \frac{1}{k_BT}$. The integral is performed over the unit sphere, $\int \mathrm{d}\mathbf{N}\delta\left(|\mathbf{N}|^2 - 1\right) = \int \mathrm{d}\mu(\mathbf{N})$, summing over all possible states. The Boltzmann distribution is then split into M small imaginary time steps, $\Delta\tau = \beta/M$, making use of the Suzuki-Trotter decomposition $e^{A+B} = \lim_{N\to\infty}(e^{A/N}e^{B/N})^N$ and inserting the resolution of the identity between each imaginary time-step evolution operator. One can therefore write down the partition function as a product of transitions, taking the chain from a state at imaginary time-step, $\mathbf{N}_n$, to a state at the next time-step $\mathbf{N}_{n+1}$,

$$\mathcal{Z} = \mathcal{N}\int \mathrm{d}\mu(\mathbf{N})\,\langle N_0|\, e^{-\Delta\tau\mathcal{H}}\,|\mathbf{N}_1\rangle\,\langle N_1|\, e^{-\Delta\tau\mathcal{H}}\,|\mathbf{N}_2\rangle \ldots \langle N_{M-1}|\, e^{-\Delta\tau\mathcal{H}}\,|\mathbf{N}_0\rangle \tag{C.5}$$

with the normalisation factor $\mathcal{N} = \frac{2S+1}{4\pi}$. The transition amplitudes can be calculated by expanding the state, $|\mathbf{N}(\tau + \Delta\tau)\rangle$ for a small time step

$$\langle\mathbf{N}_n|\, e^{-\Delta\tau\mathcal{H}}\,|\mathbf{N}_{n+1}\rangle = 1 + \langle\mathbf{N}(\tau)|\,\frac{\partial}{\partial\tau}\,|\mathbf{N}(\tau)\rangle\,\Delta\tau - \Delta\tau\mathcal{H}(S\mathbf{N}). \tag{C.6}$$

The expansion can be re-exponentiated and summed over τ to find the partition function

$$\mathcal{Z} = \int \mathrm{d}\mu(\mathbf{N})e^{-\int_0^\beta \mathrm{d}\tau\left\{-\langle\mathbf{N}(\tau)|\frac{\partial}{\partial\tau}|\mathbf{N}(\tau)\rangle + \mathcal{H}(S\mathbf{N})\right\}} = \int \mathrm{d}\mu(\mathbf{N})e^{-(S_H - S_B)} \tag{C.7}$$

which separates into a contribution from the Hamiltonian action S_H and the Berry action S_B. The quantity $\langle\mathbf{N}(\tau)|\,\frac{\partial}{\partial\tau}\,|\mathbf{N}(\tau)\rangle$ is a complex geometric phase, often termed the Berry phase [418], acquired when adiabatically transporting a system about a closed loop in parameter space. The Berry phase action can be computed using Eqn. C.2 and the definition of the derivative of an exponential operator [419, 420]

$$\frac{\mathrm{d}}{\mathrm{d}\tau}\left[e^{\hat{A}(\tau)}\right] = \int_0^1 e^{(1-u)\hat{A}}\frac{\mathrm{d}\hat{A}}{\mathrm{d}\tau}e^{u\hat{A}}\mathrm{d}u \tag{C.8}$$

which introduces a new variable, u, parameterising the path of $\mathbf{N}$. The integral yields the geometric interpretation that the Berry phase is the surface area of the cap swept out by the spin vector on the unit sphere

$$\int_0^\beta \mathrm{d}\tau \left\{ \langle \mathbf{N}(\tau)| \frac{\partial}{\partial \tau} |\mathbf{N}(\tau)\rangle \right\} = iS \int_0^\beta \mathrm{d}\tau \int_0^1 \mathrm{d}u \left(\frac{\partial \mathbf{N}}{\partial u} \times \frac{\partial \mathbf{N}}{\partial \tau} \right). \tag{C.9}$$

As described in Chapter 3, the staggered Néel order parameter is introduced through the transformation

$$\mathbf{N}_i(\tau) = (-1)^i \mathbf{n}_i(\tau) + a\mathbf{L}_i(\tau) \tag{C.10}$$

where the field, $\mathbf{L}_i(\tau)$ describes fluctuations perpendicular to $\mathbf{n}_i(\tau)$. Inserting Eqn. C.10 into Eqn. C.1 via $\mathbf{S}_i = S\mathbf{N}_i$ and integrating over u, one finds

$$\mathcal{Z} = e^{-(S_H - S_B)} \tag{C.11a}$$

$$S_H = \int_0^\beta \mathrm{d}\tau \int_{-\infty}^{\infty} \mathrm{d}x \left\{ \frac{J}{2} S^2 a \left(\partial_x \mathbf{n}\right)^2 - \frac{\alpha S^2}{a} n_z^2 + aJS^2\mathbf{L}^2 - \alpha a S^2 L_z^2 \right\} \tag{C.11b}$$

$$S_B = S_B' - iS \int_0^\beta \mathrm{d}\tau \int_{-\infty}^{\infty} \mathrm{d}x \left\{ \mathbf{L} \cdot \left(\mathbf{n} \times \frac{\partial \mathbf{n}}{\partial \tau} \right) \right\} \tag{C.11c}$$

where it has been used that τ is periodic, $\mathbf{L}$ is a small smoothly varying field, and $\mathbf{n} \perp \mathbf{L}$. S_B' is a rapidly oscillating term which alternates sign on neighbouring sites. Since the spin texture is smooth, this term is taken to interfere destructively and thus can be neglected. All that remains is to integrate out the fluctuating field $\mathbf{L}$ which can be performed by completing the square and performing a Gaussian integral, yielding

$$\mathcal{Z} = \exp\left(- \int_0^\beta \mathrm{d}\tau \int_{-\infty}^{\infty} \mathrm{d}x \left\{ \frac{J}{2} S^2 a \left(\partial_x \mathbf{n}\right)^2 - \frac{\alpha S^2}{a} n_z^2 + \frac{1}{4aJ} \left(\partial_\tau \mathbf{n}\right)^2 \right\} \right). \tag{C.12}$$

With the identification $c = \sqrt{2}JSa$, $\rho_S = JS^2a$ and $\kappa = 2\alpha/a^2J$, one finds the action of the nonlinear sigma model

$$S = \frac{\rho_S}{2} \int_0^\beta \mathrm{d}\tau \int_{-\infty}^{\infty} \mathrm{d}x \left\{ (\partial_x \mathbf{n})^2 + \frac{1}{c^2} (\partial_\tau \mathbf{n})^2 - \kappa n_z^2 \right\}. \tag{C.13}$$

Appendix D

Derivation of soliton solutions

In Chapter 3, the nonlinear σ model for the field $\mathbf{n}$ with the anisotropy term $-\kappa n_z^2$, under the saddle point approximation was shown yield a polar angle, θ, which obeys the sine-Gordon equation

$$\partial_x^2\theta - \frac{1}{c^2}\partial_t^2\theta = \frac{1}{2}\kappa\sin(2\theta) \tag{D.1}$$

admitting soliton solutions. In this appendix, those soliton solutions are obtained, starting with the single soliton solution.

D.1 Single soliton solution

Assuming a travelling wave solution of the form $\theta(x,t) = \frac{1}{2}f(x-vt) = f(\xi)$ the sine-Gordon equation (Eqn. D.1) becomes

$$\left(1 - \frac{v^2}{c^2}\right)\frac{\mathrm{d}^2 f}{\mathrm{d}\xi^2} = \kappa\sin f. \tag{D.2}$$

Multiplying both sides by $\frac{\mathrm{d}f}{\mathrm{d}\xi}$ and integrating one finds

$$\left(\frac{\mathrm{d}f}{\mathrm{d}\xi}\right)^2 = \left(1 - \frac{v^2}{c^2}\right)^{-1}(-2\kappa\cos f + 2\kappa K) \tag{D.3}$$

where K is a constant of integration. The constant of integration is chosen to be $K = 1$ such that $\frac{\mathrm{d}f}{\mathrm{d}\xi} \to 0$ as $f \to 0$. After rearranging and integrating, f can be found in terms of ξ

$$2\ln\left[\tan\left(\frac{f}{4}\right)\right] = \pm\frac{2\sqrt{\kappa}}{\sqrt{1-\frac{v^2}{c^2}}}\left(\xi-\xi_0\right) \tag{D.4}$$

and therefore the spatial and temporal dependence of the angle

$$\theta(x,t) = 2\arctan\left(\exp\left[\pm\frac{\sqrt{\kappa}}{\sqrt{1-\frac{v^2}{c^2}}}\left(x-vt-x_0\right)\right]\right). \tag{D.5}$$

D.2 Two soliton solution

The derivation of multi-soliton solutions is somewhat more involved. The typical approach is to exploit the properties of the sine-Gordon equation to generate N-soliton solutions from a known $N-1$ soliton solution [141, 142, 421]. Such a method can in fact be applied to generate the single-soliton solution from the vacuum solution. In this section, the two-soliton solution will be gained from the kink soliton solutions introduced in the previous section.

The sine-Gordon equation was first introduced in the study of pseudospherical surfaces [421, 422] as an equation which describes spaces of constant negative Gaussian curvature [423]. A great deal of mathematical interest has been focused on the properties of pseudospherical surfaces [141, 421], in particular, it has been shown that one can transform between different pseudospherical surfaces by employing a particular form of transformation known as a Bäcklund transform [421]. The full mathematical details are beyond the scope of this Thesis and can be found in more extensive texts [141, 421]. Instead, here is presented only the requisite details for the derivation.

As in the case of the single-soliton solution, one assumes a travelling wave solution, $f(\xi,\tau)$, depending on $\xi=\frac{1}{2}(x+ct)$ and $\tau=\frac{1}{2}(x-ct)$. The allows the sine-Gordon equation to be rewritten as [142]

$$\frac{\mathrm{d}^2 f}{\mathrm{d}\xi\mathrm{d}\tau} = \frac{1}{\eta^2}\sin f \tag{D.6}$$

where $\eta=\sqrt{(1-v^2/c^2)/\kappa}$. If one assumes two solutions to the sine-Gordon equation, ψ and ϕ, the Bäcklund transformation can be written as [141, 142, 421]

$$\partial_\xi \psi - \partial_\xi \phi = \frac{2a}{\eta} \sin\left(\frac{\psi + \phi}{2}\right) \tag{D.7a}$$

$$\partial_\tau \psi + \partial_\tau \phi = \frac{2}{a\eta} \sin\left(\frac{\psi - \phi}{2}\right) \tag{D.7b}$$

where a parameterises the transformation. The derivation now makes use of Bianchi's theory of permutability [142, 421], which dictates that the result of the Bäcklund transform with parameter a_1 followed by a second Bäcklund transform with parameter a_2 is the same function as generated with the two Bäcklund transformations swapped. This statement is summarised by a Bianchi diagram (Fig. D.1).

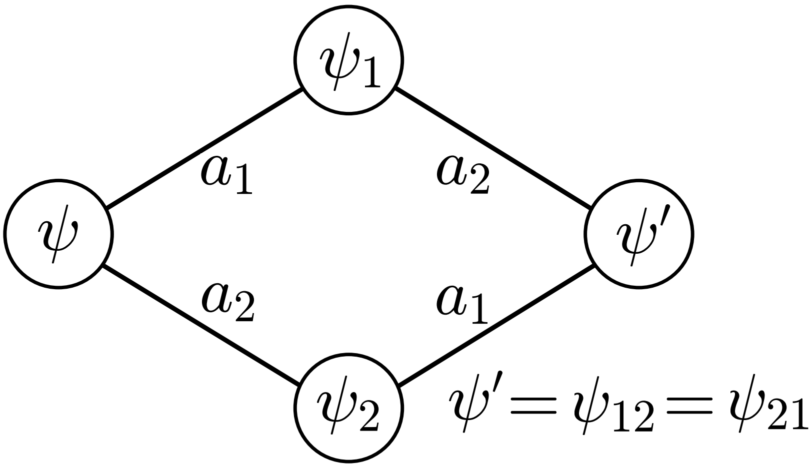

Figure D.1 *A Bianchi diagram, demonstrating the permutability of two subsequent Bäcklund transforms, parameterised by a_1 and a_2.*

Just considering the ξ-component at first, the Bäcklund transform associated with each leg can be written down

$$\partial_\xi \psi_1 = \partial_\xi \psi + \frac{2a_1}{\eta} \sin\left(\frac{\psi_1 + \psi}{2}\right) \tag{D.8a}$$

$$\partial_\xi \psi_2 = \partial_\xi \psi + \frac{2a_2}{\eta} \sin\left(\frac{\psi_2 + \psi}{2}\right) \tag{D.8b}$$

$$\partial_\xi \psi_{12} = \partial_\xi \psi_1 + \frac{2a_2}{\eta} \sin\left(\frac{\psi_{12} + \psi_1}{2}\right) \tag{D.8c}$$

$$\partial_\xi \psi_{21} = \partial_\xi \psi_2 + \frac{2a_1}{\eta} \sin\left(\frac{\psi_{21} + \psi_2}{2}\right). \tag{D.8d}$$

Since the operation is commutative, i.e. $\psi_{12} = \psi_{21} = \psi'$ one can eliminate the terms that contain derivatives with respect to ξ by equating $\partial_\xi \psi_{12}$ and $\partial_\xi \psi_{21}$

$$\begin{aligned} &\frac{2a_1}{\eta}\left[\sin\left(\frac{\psi+\psi_1}{2}\right)-\sin\left(\frac{\psi_2+\psi'}{2}\right)\right] \\ &\qquad \frac{2a_2}{\eta}\left[\sin\left(\frac{\psi_1+\psi'}{2}\right)-\sin\left(\frac{\psi+\psi_2}{2}\right)\right]=0. \end{aligned} \tag{D.9}$$

This can be rearranged using the law of addition of sine functions

$$a_1\sin\left[\frac{1}{4}\left\{(\psi'-\psi)-(\psi_1-\psi_2)\right\}\right]=a_2\sin\left[\frac{1}{4}\left\{(\psi'-\psi)+(\psi_1-\psi_2)\right\}\right] \tag{D.10}$$

such that the expressions takes the form of the law of sines. By constructing a geometrical representation of Eqn. D.10 (Fig. D.2), and if one chooses

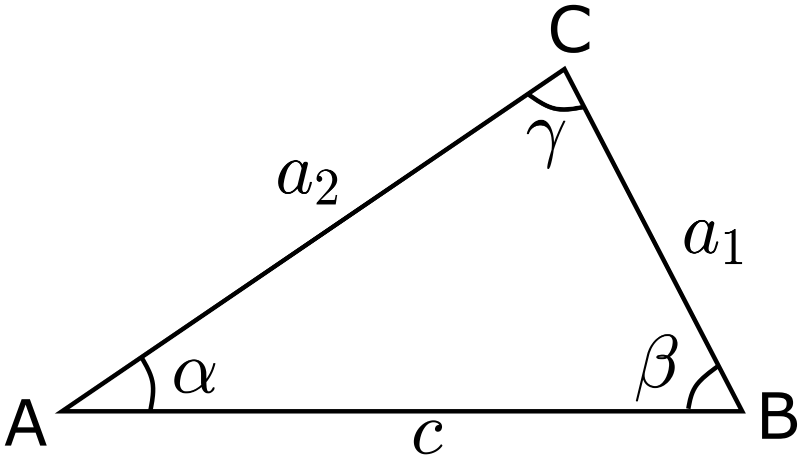

Figure D.2 *A geometric depiction of Eqn. D.10 with Bäcklund transformation parameters a_1 and a_2 identified, along with the angles α, β and γ.*

$$\alpha=\frac{1}{4}\left[(\psi'-\psi)-(\psi_1-\psi_2)\right] \tag{D.11a}$$

$$\beta=\frac{1}{4}\left[(\psi'-\psi)+(\psi_1-\psi_2)\right], \tag{D.11b}$$

Eqn. D.10 can be rearranged using the well-known law of tangents $\frac{a-b}{a+b}\tan\left(\frac{\alpha+\beta}{2}\right)=\tan\left(\frac{\alpha-\beta}{2}\right)$ to find

$$\tan\left(\frac{\psi'-\psi}{4}\right)=\frac{a_2+a_1}{a_2-a_1}\tan\left(\frac{\psi_2-\psi_1}{4}\right). \tag{D.12}$$

By choosing $\psi=0$ (the vacuum solution) and by choosing ψ_1 and ψ_2 to be the travelling wave single-soliton solutions (Eqn. D.5), one finds

$$\begin{aligned}\tan\left(\frac{\psi'}{4}\right) &= \frac{a_2+a_1}{a_2-a_1}\left(\frac{e^{(x+vt)/\eta}-e^{(x-vt)/\eta}}{1+e^{2x/\eta}}\right)\\ &= \frac{a_2+a_1}{a_2-a_1}\frac{\sinh\left(vt/\eta\right)}{\cosh\left(x/\eta\right)}\end{aligned} \tag{D.13}$$

where the transformation back to (x,t) has been performed. Attention now turns to the relationship between Bäcklund parameters a_1, a_2. The Bäcklund transformation can be employed to generate the single-soliton solution from the vacuum solution. By employing Eqn. D.7a and Eqn. D.7b one finds by integrating

$$\int\frac{\mathrm{d}\psi}{\sin\left(\frac{\psi}{2}\right)} = \int\frac{2a\mathrm{d}\xi}{\eta} \implies 2\ln\left[\tan\left(\frac{\psi}{4}\right)\right] = \frac{2a\xi}{\eta}+f_1(\tau) \tag{D.14a}$$

$$\int\frac{\mathrm{d}\psi}{\sin\left(\frac{\psi}{2}\right)} = \int\frac{2\mathrm{d}\tau}{a\eta} \implies 2\ln\left[\tan\left(\frac{\psi}{4}\right)\right] = \frac{2\tau}{a\eta}+f_2(\xi). \tag{D.14b}$$

By setting the two equations to be equal, one finds

$$f_1(\tau) = \frac{2\tau}{a\eta}+C \tag{D.15a}$$

$$f_2(\xi) = \frac{2a\xi}{\eta}+C \tag{D.15b}$$

where C is a constant. These can be substituted into the expression for ψ

$$\psi(x,t) = 4\arctan\left[\exp\left(\frac{a\xi}{\eta}+\frac{\tau}{a\eta}+\frac{C}{2}\right)\right] \tag{D.16}$$

and the single-soliton solution recovered. This expression can be compared to the single-soliton solution found previously (Eqn. D.5), to read off the relation between the Bäcklund parameter a and the physical parameters of the model. Doing so, reveals

$$\frac{v}{c} = \frac{1-a^2}{1+a^2}. \tag{D.17}$$

Since $v_1=-v_2=v$, it follows that $a_2=1/a_1=\sqrt{(c+v)/(c-v)}$. Performing the substitution, one can then find $\theta(x,t)=\frac{1}{2}f(x,t)$ in terms of the parameters of the model

$$\theta(x,t) = 2\arctan\left(\frac{c\sinh\frac{v\sqrt{\kappa}t}{\sqrt{1-\frac{v^2}{c^2}}}}{v\cosh\frac{\sqrt{\kappa}x}{\sqrt{1-\frac{v^2}{c^2}}}}\right) \tag{D.18}$$

where the substitution $\eta = \sqrt{(1 - v^2/c^2)/\kappa}$ has been performed.

Appendix E

Spin-wave calculations for Fe_3GeTe_2

In Chapter 6, neutron scattering measurements on the van der Waals itinerant ferromagnet Fe_3GeTe_2 were presented. The excitations were modelled using a hexagonal lattice Heisenberg model. In this appendix, linear spin wave calculations are presented to supplement the discussion given in Chapter 6. Firstly, the dispersion relation of the hexagonal lattice ferromagnet is derived using linear spin wave theory. Secondly, a model which provides a more realistic description of the Fe_3GeTe_2 crystal is presented. Finally, the correspondence between the two models in the long wavelength limit is found, motivating the use of the simpler model in Chapter 6 for comparison with STM measurements.

E.1 Linear spin wave theory on the hexagonal lattice

The starting point is the Heisenberg model on the hexagonal lattice. The hexagonal lattice can be described by two basis vectors, $\hat{\mathbf{e}}_1$ and $\hat{\mathbf{e}}_2$. These basis vectors are chosen to be non-orthogonal, separated by an angle of 120°. The hexagonal lattice has two sites per unit cell, which can be assigned a label, A or B

$$\mathcal{H} = J \sum_{\mathbf{r}}^{j\in\{0,1,2\}} \mathbf{S}_A(\mathbf{r}) \cdot \mathbf{S}_B(\mathbf{r} + \mathbf{a}_j) + K[(\hat{S}^z_A(\mathbf{r}))^2 + (\hat{S}^z_B(\mathbf{r}))^2] \tag{E.1}$$

where J is the nearest neighbour interaction, K is the magnetic anisotropy and $\mathbf{S}_{A,B}$ is the spin operator on site A or B. The vectors are defined as $\mathbf{a}_0 = (0, 0)$,

$\mathbf{a}_1 = (0,1)$ and $\mathbf{a}_0 = (1,1)$ in the $P6_3/mmc$ space group. In order to proceed, a Holstein-Primakoff transformation [365] can be performed

$$\hat{S}^{+}_{\alpha}(\mathbf{r}) = \sqrt{2S - \hat{b}^{\dagger}_{\mathbf{r}\alpha}\hat{b}_{\mathbf{r}\alpha}}\,\hat{b}_{\mathbf{r}\alpha} \tag{E.2a}$$

$$\hat{S}^{-}_{\alpha}(\mathbf{r}) = \hat{b}^{\dagger}_{\mathbf{r}\alpha}\sqrt{2S - \hat{b}^{\dagger}_{\mathbf{r}\alpha}\hat{b}_{\mathbf{r}\alpha}} \tag{E.2b}$$

$$\hat{S}^{z}_{\alpha}(\mathbf{r}) = S - \hat{b}^{\dagger}_{\mathbf{r}\alpha}\hat{b}_{\mathbf{r}\alpha} \tag{E.2c}$$

where the operators, $\hat{b}_{\mathbf{r}\alpha}$ obey the bosonic commutation relations, $[\hat{b}_{\mathbf{r}\alpha}, \hat{b}^{\dagger}_{\mathbf{r}'\beta}] = \delta_{\mathbf{r}\mathbf{r}'}\delta_{\alpha\beta}$. It can be verified that this transformation and the accompanying bosonic algebra reproduces the standard spin commutation relations, $[\hat{S}^{\mu}_{i\alpha}, \hat{S}^{\nu}_{j\beta}] = \delta_{ij}\delta_{\alpha\beta}\epsilon_{\mu\nu\eta}\hat{S}^{\eta}_{i\alpha}$. By performing the transformation and discarding terms of order three and higher (the harmonic approximation), the Hamiltonian can be written as

$$\begin{aligned}\mathcal{H} = JS\sum_{\mathbf{r}} \Big[&\hat{b}_A(\mathbf{r})\hat{b}^{\dagger}_B(\mathbf{r}+\mathbf{a}_j) + \hat{b}^{\dagger}_A(\mathbf{r})\hat{b}_B(\mathbf{r}+\mathbf{a}_j)\\ &- \hat{b}^{\dagger}_A(\mathbf{r})\hat{b}_A(\mathbf{r}) - \hat{b}^{\dagger}_B(\mathbf{r}+\mathbf{a}_j)\hat{b}_B(\mathbf{r}+\mathbf{a}_j)\Big]\\ &- 2KS\sum_{\mathbf{r}}\Big[\hat{b}^{\dagger}_A(\mathbf{r})\hat{b}_A(\mathbf{r}) + \hat{b}^{\dagger}_B(\mathbf{r})\hat{b}_B(\mathbf{r})\Big].\end{aligned} \tag{E.3}$$

Since the transformed Hamiltonian contains no anomalous terms, it can be diagonalised straightforwardly by a Fourier transform. In reciprocal space, the Hamiltonian (Eqn. E.3) can be written as

$$\mathcal{H} = \begin{pmatrix}\hat{b}^{\dagger}_A(\mathbf{q}) & \hat{b}^{\dagger}_B(\mathbf{q})\end{pmatrix}\begin{pmatrix} v_S & \gamma_{\mathbf{q}} \\ \gamma^{*}_{\mathbf{q}} & v_S\end{pmatrix}\begin{pmatrix}\hat{b}_A(\mathbf{q}) \\ \hat{b}_B(\mathbf{q})\end{pmatrix} \tag{E.4}$$

with $v_S = -(3JS + 2KS)$ and $\gamma_{\mathbf{q}} = JS\sum_j e^{i\mathbf{q}\cdot\mathbf{a}_j}$, yielding the dispersion relation

$$E^{\pm}_{\mathbf{q}} = v_S \pm |\gamma_{\mathbf{q}}|. \tag{E.5}$$

E.2 Linear spin wave theory for Fe_3GeTe_2

Having presented the derivation of the dispersion relation for the Heisenberg model on the hexagonal lattice, a more realistic model of Fe_3GeTe_2 is now introduced. As discussed in Chapter 6, the crystal structure is best understood in terms of a hexagonal lattice with one of the sublattices duplicated at $\pm\delta\mathbf{c}$.

These sublattices will be labelled $\mathrm{B_u}$ and $\mathrm{B_d}$ in the following. Consequently, the A and B sites now have a coordination of six and four respectively.

The spin wave Hamiltonian can now be written as

$$\begin{aligned}\mathcal{H} =& J \sum_{\mathbf{r}}^{\substack{\alpha\in\{\mathrm{u,d}\}\\ j\in\{0,1,2\}}} \mathbf{S}_A(\mathbf{r})\cdot\mathbf{S}_{B_\alpha}(\mathbf{r}+\mathbf{a}_j) + J\sum_{\mathbf{r}} \mathbf{S}_{B_\mathrm{u}}(\mathbf{r})\cdot\mathbf{S}_{B_\mathrm{d}}(\mathbf{r}) \\ &+ K \sum_{\mathbf{r}}^{\alpha\in\{\mathrm{u,d}\}} [(\hat{S}^z_A(\mathbf{r}))^2 + (\hat{S}^z_{B_\alpha}(\mathbf{r}))^2].\end{aligned} \tag{E.6}$$

A Holstein-Primakoff transformation can be performed and the Hamiltonian written in momentum space as

$$\begin{aligned}\mathcal{H} =& \sum_{\mathbf{q}} \Big\{ \Big(\gamma_{\mathbf{q}}\hat{b}^\dagger_A(\mathbf{q})\hat{b}_{B_\mathrm{u}}(\mathbf{q}) + \gamma_{\mathbf{q}}\hat{b}^\dagger_A(\mathbf{q})\hat{b}_{B_\mathrm{d}}(\mathbf{q}) + JS\hat{b}^\dagger_{B_\mathrm{u}}(\mathbf{q})\hat{b}_{B_\mathrm{d}}(\mathbf{q})\Big) + \text{h.c.} \\ &- 6JS\hat{b}^\dagger_A(\mathbf{q})\hat{b}_A(\mathbf{q}) - 4JS\left[\hat{b}^\dagger_{B_\mathrm{u}}(\mathbf{q})\hat{b}_{B_\mathrm{u}}(\mathbf{q}) + \hat{b}^\dagger_{B_\mathrm{d}}(\mathbf{q})\hat{b}_{B_\mathrm{d}}(\mathbf{q})\right] \Big\} \\ &- 2KS\sum_{\mathbf{q}}\left\{\hat{b}^\dagger_A(\mathbf{q})\hat{b}_A(\mathbf{q}) + \hat{b}^\dagger_{B_\mathrm{u}}(\mathbf{q})\hat{b}_{B_\mathrm{u}}(\mathbf{q}) + \hat{b}^\dagger_{B_\mathrm{d}}(\mathbf{q})\hat{b}_{B_\mathrm{d}}(\mathbf{q})\right\}.\end{aligned} \tag{E.7}$$

As above, $\gamma_{\mathbf{q}} = JS\sum_j e^{i\mathbf{q}\cdot\mathbf{a}_j}$. This Hamiltonian can be written in the compact form, $\mathcal{H} = \sum_{\mathbf{q}} \Psi^\dagger_{\mathbf{q}}\underline{\underline{M}}\Psi_{\mathbf{q}}$, where $\Psi^\dagger_{\mathbf{q}} = (\hat{b}^\dagger_A(\mathbf{q}), \hat{b}^\dagger_{B_\mathrm{u}}(\mathbf{q}), \hat{b}^\dagger_{B_\mathrm{d}}(\mathbf{q}))$ and

$$\underline{\underline{M}} = \begin{pmatrix} -6JS-2KS & \gamma_{\mathbf{q}} & \gamma_{\mathbf{q}} \\ \gamma^*_{\mathbf{q}} & -6JS-2KS & JS \\ \gamma^*_{\mathbf{q}} & JS & -4JS-2KS \end{pmatrix}. \tag{E.8}$$

This Hamiltonian can be diagonalised by a Bogoliubov transformation [424], or by diagonalising the matrix $\mathbf{g}\underline{\underline{M}}$, where $\mathbf{g} = [\Psi_{\mathbf{q}}, \Psi^\dagger_{\mathbf{q}}]$ is the metric that enforces the bosonic commutation relations [425], which in this case is just the identity matrix

$$\mathbf{g} = [\Psi_{\mathbf{q}}, \Psi^\dagger_{\mathbf{q}}] = \begin{pmatrix} 1 & 0 & 0 \\ 0 & 1 & 0 \\ 0 & 0 & 1 \end{pmatrix}. \tag{E.9}$$

After diagonalising $\mathbf{g}\underline{\underline{M}}$, the dispersion relation for the two dispersive modes along

(H, H) can be written as

$$\begin{aligned} E^{\pm}(H, H) = &-\left(\frac{9}{2}JS + 2KS\right) \\ &\pm \frac{1}{2}JS\sqrt{33 + 32\text{cos}(2\pi H) + 16\text{cos}(4\pi H)}. \end{aligned} \tag{E.10}$$

E.3 Correspondence between the two models

The motivation behind mapping Fe_3GeTe_2 onto a hexagonal spin model comes from the lack of sensitivity to magnetic correlations along the c-axis afforded by STM and the relatively broad c^* axis integration employed in neutron scattering. Since Fe_3GeTe_2 is itinerant, the localised spin model is only valid in the limit of small $\mathbf{q}$. The spin wave dispersion for each of these models is now compared in this limit by expanding about the high symmetry Γ-point.

Expanding the lower mode of the hexagonal model dispersion relation (Eqn. E.5) one finds for small $\mathbf{q} = (H, H)$, $E \approx -2KS - 4\pi^2 JSH^2$. Now for the more realistic model (Eqn. E.10), one finds $E \approx -2KS - \frac{16\pi^2}{3} JSH^2$. Therefore the extracted exchange parameters fitted from both models differ by a simple constant in the limit of small $\mathbf{q}$.

Appendix F

Domain wall calculations for Fe_3GeTe_2

A derivation of the domain wall profile of a hexagonal lattice Heisenberg model is now presented. It will then be shown that the more realistic model of Fe_3GeTe_2 presented in Section E.2 gives consistent results, justifying the use of the simple hexagonal model used in Chapter 6.

F.1 Continuum limit of spin model

The Heisenberg model on the hexagonal lattice, with nearest-neighbour coupling can be written as

$$\mathcal{H} = J \sum_{\mathbf{r}\ \text{(unit cells)}}^{j\in\{0,1,2\}} \mathbf{S}_A(\mathbf{r}) \cdot \mathbf{S}_B(\mathbf{r} + a\hat{\mathbf{e}}_j), \tag{F.1}$$

where the sum is over all unit cells. By representing the spins as classical vectors of length S, a continuum description of the magnetisation can be developed. The transformation $\mathbf{S}(\mathbf{r}) = S\mathbf{n}(\mathbf{r})$ can be introduced, dropping the site index in the spirit of a classical treatment of the spin degree of freedom. Neglecting constant terms, Eqn. F.1 can be written as

$$\mathcal{H} = -\frac{JS^2}{2} \sum_{\mathbf{r}\ \text{(unit cells)}}^{j\in\{0,1,2\}} \left[\mathbf{n}(\mathbf{r} + d_{\text{nn}}\hat{\mathbf{e}}_j) - \mathbf{n}(\mathbf{r})\right]^2. \tag{F.2}$$

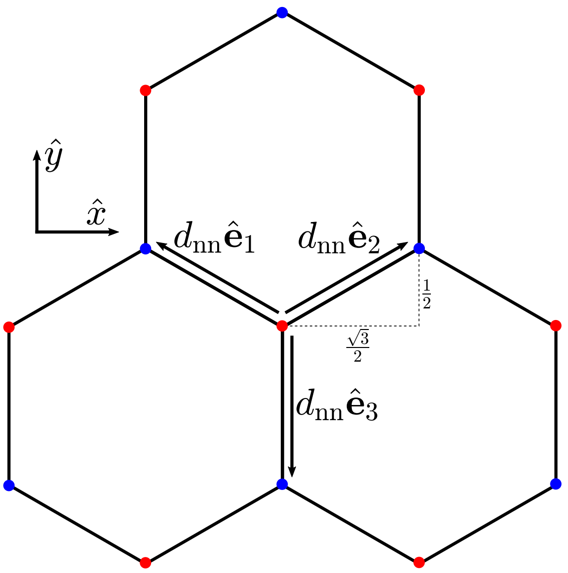

Figure F.1 *Definition of the basis vectors* $\hat{e}_i$ *(*$i = 1 \ldots 3$*) for a honeycomb lattice, as used in Chapter 6.*

The basis vectors $\hat{\mathbf{e}}_j$ can readily be converted from the non-orthogonal $P6_3/mmc$ rhombohedral coordinate system into Cartesian coordinates.

In Cartesian coordinates one has $\hat{\mathbf{e}}_1 = (-\frac{\sqrt{3}}{2}, \frac{1}{2})$, $\hat{\mathbf{e}}_2 = (\frac{\sqrt{3}}{2}, \frac{1}{2})$ and $\hat{\mathbf{e}}_3 = (0, -1)$ (Fig. F.1), and hence

$$[\mathbf{n}(\mathbf{r} + d_{\mathrm{nn}}\hat{\mathbf{e}}_1) - \mathbf{n}(\mathbf{r})] = -\frac{\sqrt{3}}{2} d_{\mathrm{nn}}\partial_x(\mathbf{n}) + \frac{1}{2} d_{\mathrm{nn}}\partial_y(\mathbf{n}) \tag{F.3a}$$

$$[\mathbf{n}(\mathbf{r} + d_{\mathrm{nn}}\hat{\mathbf{e}}_2) - \mathbf{n}(\mathbf{r})] = \frac{\sqrt{3}}{2} d_{\mathrm{nn}}\partial_x(\mathbf{n}) + \frac{1}{2} d_{\mathrm{nn}}\partial_y(\mathbf{n}) \tag{F.3b}$$

$$[\mathbf{n}(\mathbf{r} + d_{\mathrm{nn}}\hat{\mathbf{e}}_3) - \mathbf{n}(\mathbf{r})] = d_{\mathrm{nn}}\partial_y(\mathbf{n}) . \tag{F.3c}$$

Performing the sum over j one finds

$$\mathcal{H} = -\frac{3JS^2}{2} \sum_{\mathbf{r}\text{ (unit cells)}} d_{\mathrm{nn}} \left[(\partial_x \mathbf{n})^2 + (\partial_y \mathbf{n})^2\right] . \tag{F.4}$$

Finally the continuum limit $\sum_{\mathrm{r}} \to \frac{1}{A_{unit}} \int \mathrm{d}^2 r$, (where A_{unit} is the area of the unit cell) is taken to find a classical field theory of the Heisenberg model on the hexagonal lattice

$$\mathcal{H} = \frac{\rho_S}{2} \int \mathrm{d}^2 r \left\{(\partial_x \mathbf{n})^2 + (\partial_y \mathbf{n})^2\right\} \tag{F.5}$$

where the spin stiffness is $\rho_S = \frac{3JS^2 d_{\mathrm{nn}}^2}{A_{unit}} = \frac{3JS^2 d_{\mathrm{nn}}^2}{2A_{site}}$. A_{site} is the area occupied by one site and is hence half the value of A_{unit} for a hexagonal lattice. Performing the continuum limit of the single ion anisotropy term, one finds

$$\begin{aligned}\mathcal{H}_{anis} =& K \sum_{\mathbf{r}}^{\text{(unit cells)}} \left[\left(S^z_A(\mathrm{r})\right)^2 + \left(S^z_B(\mathrm{r})\right)^2 \right] = KS^2 \sum_{\mathbf{r}}^{\text{(sites)}} \left[n^z(\mathbf{r})\right]^2 \\ &= \kappa \int \mathrm{d}^2 r \left\{ \left(n^z(\mathbf{r})\right)^2 \right\}\end{aligned} \tag{F.6}$$

with the anisotropy parameter $\kappa = \frac{2KS^2}{A_{\text{unit}}} = \frac{KS^2}{A_{\text{site}}}$.

F.1.1 Domain wall solutions

The terms originating from exchange (Eqn. F.5) can be seen as representing the stiffness of the spin field, penalising the canting of spins away from ferromagnetic alignment. In a domain wall, these terms compete against the single-ion anisotropy terms (Eqn. F.6), the former favouring a spatially extended domain wall such that the spins remain closely aligned, and the latter favouring a rotation of spins over a short length scale when θ is far from 0 or π.

Following the general approach outlined in Ref. [284], an expression for the domain wall shape on the hexagonal lattice will be derived. For comparison with the STM data, a one-dimensional cut through the domain wall is required, which can be assumed to occur along $\hat{y}$ (Fig. F.2), assuming that the spins rotate in a common rotation plane (x, z) defined by the angle θ, $\mathbf{n}(\mathbf{r}) = (\sin\theta(\mathbf{r}), \cos\theta(\mathbf{r}))$. In terms of this rotation angle, the energy of a domain wall can be written as

$$E_{DW} = \int \mathrm{d}^2 r \left\{ \frac{\rho_S}{2} (\partial_y \theta)^2 + \kappa \left(1 - \cos^2\theta\right) \right\}. \tag{F.7}$$

Note here that it has been assumed that $\partial_x \theta = 0$, as required for a domain wall along $\hat{y}$. Using the domain wall Lagrangian $\mathcal{L} = \frac{\rho_S}{2}(\partial_y\theta)^2 + \kappa\sin^2\theta$, the static Euler-Lagrange equation, $\frac{\mathrm{d}}{\mathrm{d}y}\left(\frac{\partial\mathcal{L}}{\partial\dot{\theta}}\right) = \frac{d\mathcal{L}}{d\theta}$, (where $\dot{\theta} = \frac{\partial\theta}{\partial y}$) can be written down and solved for the domain wall profile. Using the boundary condition $\frac{\mathrm{d}\theta}{\mathrm{d}y} \to 0$ as $y \to \pm\infty$, one finds

$$\theta(y) = 2\arctan\left(e^{\sqrt{\frac{2\kappa}{\rho_S}}(y - y_0)}\right). \tag{F.8}$$

This is known as the kink soliton, and reflects the conflict between the exchange stiffness energy and the anisotropy energy in the domain wall. The spins rotate little between nearest neighbours at the edges of the domain wall, where the anisotropy energy is small, before rotating much more between adjacent sites

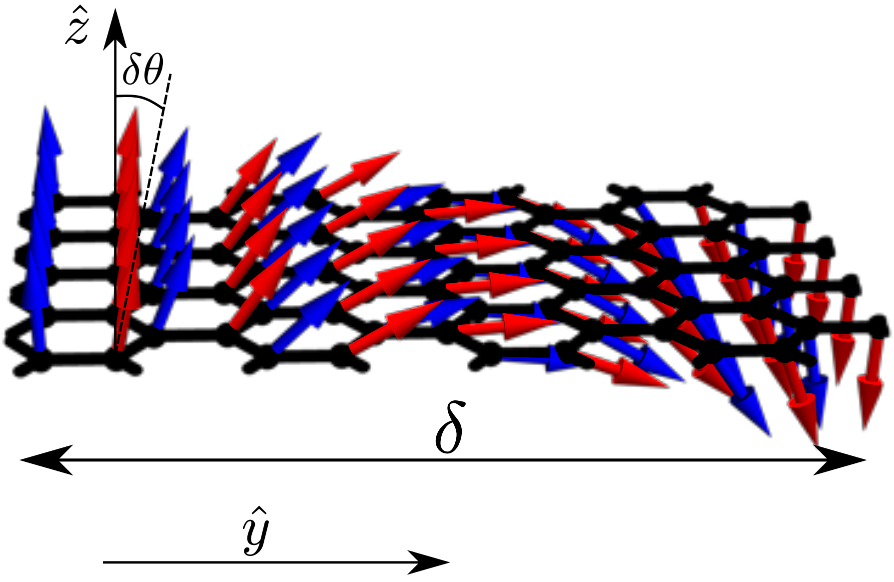

Figure F.2 *Visualisation of a Néel domain wall on the 2-d hexagonal lattice. The blue and red arrows indicate spins on the A and B sublattices respectively. The angle between the direction in which the spin is pointing locally and $\hat{z}$ is given by θ. The canting angle between neighbouring spins is $\delta\theta$, which is smaller close to the edges of the domain wall. Both θ and $\delta\theta$ are shown here for the second row of atoms parallel to the domain wall, where $\theta = \delta\theta$ (in the first row $\theta = 0$, and the spins are parallel to $\hat{z}$). Different colours represent spins on different sublattices.*

when this energy increases at the centre of the wall. Using Eqn. F.8, the z-component of the spin field can be written down

$$\begin{aligned} n^z(y) &= \tanh\left[\sqrt{\frac{2\kappa}{\rho_S}}(y - y_0)\right] \\ &= \tanh\left[\sqrt{\frac{4K}{3Jd_{\text{nn}}^2}}(y - y_0)\right] \end{aligned} \tag{F.9}$$

which takes the shape of a step function with a width that depends on $\sqrt{\frac{K}{J}}$.

Finally the equivalence of modelling the data using both the hexagonal model and the more realistic model presented in Section E.2, in the limit of small $\mathbf{q}$, will be demonstrated, so long as the choice of model is consistent for both the neutron and the STM data.

The spin model for the full crystallographic structure of Fe_3GeTe_2 is given by Eqn.

E.6. As in the previous section, the spins in the continuum limit are represented by a vector field $\mathbf{S}(\mathbf{r}) = S\mathbf{n}(\mathbf{r})$, where the site index is dropped and the spins on the u and d sublattices are assumed to be coaligned. Neglecting constant terms one has

$$\mathcal{H} = -JS^2 \sum_{\mathbf{r}\text{ (unit cells)}}^{j\in\{0,1,2\}} \left[\mathbf{n}(\mathbf{r} + d_{\text{nn}}\hat{\mathbf{e}}_j) - \mathbf{n}(\mathbf{r})\right]^2 \tag{F.10a}$$

$$\mathcal{H}_{anis} = \frac{3}{2}KS^2 \sum_{\mathbf{r}}^{\text{(sites)}}{}' \left[n^z(\mathbf{r})\right]^2 \tag{F.10b}$$

where $'$ indicates that the sum is performed over the sites of the hexagonal lattice since the sum over the u and d sublattices has already been explicitly performed. By comparing these expressions with the analogous expressions for the hexagonal model Eqns. F.2 and F.6, it is possible to map from one model to the other,

$$\rho_S^{hex} = \frac{1}{2}\rho_S^{FGT} \tag{F.11a}$$

$$\kappa^{hex} = \frac{2}{3}\kappa^{FGT} \tag{F.11b}$$

thus $\delta^{FGT} = \sqrt{\frac{4}{3}}\delta^{hex}$. Examination of the small-$\mathbf{q}$ expansion of the dispersion along (H,H) for the two models

$$\epsilon_+^{hex} \approx -2KS - 4\pi^2 J_{hex} S H^2 \tag{F.12a}$$

$$\epsilon_+^{FGT} \approx -2KS - \frac{16}{3}\pi^2 J_{FGT} S H^2 \tag{F.12b}$$

shows that $J_{hex} = \frac{4}{3}J_{FGT}$, therefore any consistent treatment of the STM and neutron data using either model in the small-$\mathbf{q}$ limit, as described above, yields consistent results.

Appendix G

Green's function formalism for a collinear system

The Green's function equation of motion in the laboratory frame is defined as

$$G^{\alpha\beta}_{\tilde{\gamma}\tilde{\gamma}'}(i'j',t) = -i\Theta(t)\langle[\hat{S}^{\alpha}_{i'\tilde{\gamma}}(t), \hat{S}^{\beta}_{j'\tilde{\gamma}'}]\rangle \tag{G.1}$$

The indices α and β label the spatial components in Cartesian coordinates, whilst $\tilde{\gamma}$ and $\tilde{\gamma}'$ label the atom site within the unit cell. Causality is enforced by the Heaviside step function $\Theta(t)$, which precludes negative values of t. Taking the derivative of both sides with respect to time and multiplying by a factor of i, one finds that

$$\begin{aligned} i\partial_t G^{\alpha\beta}_{\tilde{\gamma}\tilde{\gamma}'}(i'j',\omega) =& \delta(t)\langle[\hat{S}^{\alpha}_{i'\tilde{\gamma}}(t), \hat{S}^{\beta}_{j'\tilde{\gamma}'}]\rangle \\ & - i\Theta(t)\langle[i\partial_t\hat{S}^{\alpha}_{i'\tilde{\gamma}}(t), \hat{S}^{\beta}_{j'\tilde{\gamma}'}]\rangle. \end{aligned} \tag{G.2}$$

Taking advantage of the Heisenberg equation of motion, $i\partial_t\hat{S}^{\alpha}_{i\gamma}(t) = [\hat{S}^{\alpha}_{i\gamma}(t), \mathcal{H}]$, and performing a Fourier transform in time, Eqn. G.2 can be written as

$$\begin{aligned} \omega G^{\alpha\beta}_{\tilde{\gamma}\tilde{\gamma}'}(i'j',\omega) =& \langle[\hat{S}^{\alpha}_{i'\tilde{\gamma}}, \hat{S}^{\beta}_{j'\tilde{\gamma}'}]\rangle + \\ & G_{\tilde{\gamma}\tilde{\gamma}'}([\hat{S}^{\alpha}_{i'\tilde{\gamma}}, \mathcal{H}], \hat{S}^{\beta}_{j'\tilde{\gamma}'}, \omega). \end{aligned} \tag{G.3}$$

For a system which consists of coupled multi-level sites, one can separate the Hamiltonian into single-ion and inter-ion terms

$$\mathcal{H} = \sum_{i\gamma} \mathcal{H}'(i,\gamma) + \mathcal{H}_{int}, \tag{G.4}$$

where $\mathcal{H}'(i,\gamma)$ contains all of the manifestly single-ion terms such as spin-orbit coupling and the crystalline electric field whilst $\mathcal{H}_{int}$ describes the inter-ion terms such as the exchange interaction between sites and is therefore a sum over all bonds. In order that the correct single-ion ground state is expanded about, a mean field decoupling is now performed $\mathbf{S}_{i\gamma} \rightarrow \langle \mathbf{S}_{i\gamma} \rangle + \delta\mathbf{S}_{i\gamma}$, discarding terms $\sim \mathcal{O}(\delta\mathbf{S}_{i\gamma})^2$. Following this decoupling, the single-ion Hamiltonian gains a molecular mean field Zeeman term which breaks spin-rotational symmetry.

Assuming an interaction Hamiltonian of the form $\mathcal{H}_{int} = \frac{1}{2}\sum_{ij}^{\gamma\gamma'} \mathcal{J}_{i,j}^{\gamma\gamma'} \mathbf{S}_{i\gamma} \cdot \mathbf{S}_{j\gamma'}$, where $\mathcal{J}_{i,j}^{\gamma\gamma'}$ is a Heisenberg exchange parameter, the decoupled Hamiltonian becomes

$$\begin{aligned}
\mathcal{H} =& \mathcal{H}_1 + \mathcal{H}_2 \\
\mathcal{H}_1 =& \sum_{i\gamma} \{\mathcal{H}'(i\gamma) + \sum_{j\gamma'} \mathcal{J}_{ij}^{\gamma\gamma'} [\mathbf{S}_{i\gamma} - \frac{1}{2}\langle \mathbf{S}_{i\gamma} \rangle] \langle \mathbf{S}_{j\gamma'} \rangle\} \\
\mathcal{H}_2 =& \frac{1}{2}\sum_{ij}^{\gamma\gamma'} \mathcal{J}_{i,j}^{\gamma\gamma'} \mathbf{S}_{i\gamma} \cdot \mathbf{S}_{j\gamma'} \\
& - \sum_{ij}^{\gamma\gamma'} \mathcal{J}_{ij}^{\gamma\gamma'} [\mathbf{S}_{i\gamma} - \frac{1}{2}\langle \mathbf{S}_{i\gamma} \rangle] \langle \mathbf{S}_{j\gamma'} \rangle
\end{aligned}$$

The projection of the spin operators onto the space spanned by the eigenvectors of the single-ion Hamiltonian, $\mathcal{H}_1$ can be written as

$$\hat{S}_{i\gamma}^{\alpha} = \sum_{pq} S_{\alpha pq}^{\gamma} \hat{c}_p^{\dagger}(i) \hat{c}_q(i), \tag{G.5}$$

where the sum extends over all eigenstates, $|p\rangle$, of the Hamiltonian and $S_{\alpha pq}^{\gamma} = \langle p| \hat{S}_{\gamma}^{\alpha} |q\rangle$. The operators $\hat{c}_q^{\dagger}$ create the single-ion eigenstate q. Now one must calculate the commutator on the right hand side of Eqn. G.3 using the projected spin operator. The terms in the commutator are quartic in bosonic operators, however a random phase decoupling [426] can be performed,

$$\begin{aligned}\hat{c}_p^\dagger(i)\hat{c}_q(i)\hat{c}_m^\dagger(j)\hat{c}_n(j) =& f_p(i)\delta_{pq}\hat{c}_m^\dagger(j)\hat{c}_n(j) \\ &+ f_m(j)\delta_{mn}\hat{c}_p^\dagger(i)\hat{c}_q(i),\end{aligned} \tag{G.6}$$

where $f_p(i)$ is the Bose occupation factor of level p on site i. In Cartesian coordinates, the commutator can be written as $[\hat{S}^{\alpha}_{i'\tilde{\gamma}}, \mathcal{H}] = \sum_{s=1}^{4}\mathcal{C}_s$, with the individual terms given by,

$$\mathcal{C}_1 = \sum_{j\gamma\gamma'}^{lkpq} \phi_{qp}(i')\hat{c}_k^\dagger(j)\hat{c}_l(j)S^{\tilde{\gamma}}_{\alpha qp}S^{\gamma}_{xpq}S^{\gamma'}_{xkl}\mathcal{J}_{ij}^{\gamma\gamma'} \tag{G.7a}$$

$$\mathcal{C}_2 = \sum_{j\gamma\gamma'}^{lkpq} \phi_{qp}(i')\hat{c}_k^\dagger(j)\hat{c}_l(j)S^{\tilde{\gamma}}_{\alpha qp}S^{\gamma}_{ypq}S^{\gamma'}_{ykl}\mathcal{J}_{ij}^{\gamma\gamma'} \tag{G.7b}$$

$$\mathcal{C}_3 = \sum_{j\gamma\gamma'}^{lkpq} \phi_{qp}(i')\hat{c}_k^\dagger(j)\hat{c}_l(j)S^{\tilde{\gamma}}_{\alpha qp}S^{\gamma}_{zpq}S^{\gamma'}_{zkl}\mathcal{J}_{ij}^{\gamma\gamma'} \tag{G.7c}$$

$$\mathcal{C}_4 = \sum_{pq} \left(\omega_p - \omega_q\right)\hat{c}_q^\dagger(i')\hat{c}_p(i')S^{\tilde{\gamma}}_{\alpha qp}, \tag{G.7d}$$

where $\phi_{qp}(i') = (f_q(i') - f_p(i'))$. It should be noted that $\mathcal{J}_{ij}^{\gamma\gamma'}$ has been taken to be a Heisenberg coupling but off-diagonal terms can readily be considered and give rise to terms $\sim S^{\tilde{\gamma}}_{\alpha qp}S^{\gamma}_{\eta pq}S^{\gamma'}_{\nu kl}$, where $\eta \neq \nu$. By substituting Eqns. G.7a, G.7b and G.7c into Eqn. G.3 and performing a spatial Fourier transform one recovers an expression for the Green's function equation of motion

$$\begin{aligned}G^{\alpha\beta}_{\tilde{\gamma}\tilde{\gamma}'}(\mathbf{q},\omega) &= g^{\alpha\beta}_{\tilde{\gamma}\tilde{\gamma}'}(\omega)\delta_{\tilde{\gamma}\tilde{\gamma}'} \\ &\quad + \sum_{\gamma\gamma'}\mathcal{J}_{\gamma\gamma'}(\mathbf{q})g^{\alpha x}_{\tilde{\gamma}\gamma}(\omega)G^{x\beta}_{\gamma'\tilde{\gamma}'}(\mathbf{q},\omega) \\ &\quad + \sum_{\gamma\gamma'}\mathcal{J}_{\gamma\gamma'}(\mathbf{q})g^{\alpha y}_{\tilde{\gamma}\gamma}(\omega)G^{y\beta}_{\gamma'\tilde{\gamma}'}(\mathbf{q},\omega) \\ &\quad + \sum_{\gamma\gamma'}\mathcal{J}_{\gamma\gamma'}(\mathbf{q})g^{\alpha z}_{\tilde{\gamma}\gamma}(\omega)G^{z\beta}_{\gamma'\tilde{\gamma}'}(\mathbf{q},\omega),\end{aligned} \tag{G.8}$$

with the single ion Green's function given by

$$g^{\alpha\beta}_{\tilde{\gamma}\tilde{\gamma}'}(\omega) = \sum_{qp} \frac{S^{\tilde{\gamma}}_{\alpha qp} S^{\tilde{\gamma}'}_{\beta pq} \phi_{qp}}{\omega - (\omega_p - \omega_q)}, \tag{G.9}$$

where translational symmetry has been used to drop the site index on ϕ_{qp}.

The magnon propagator itself satisfies a Dyson equation and hence by performing this calculation in terms of Green's functions, one can go beyond the single magnon picture and calculate the effect of magnon-magnon scattering on the inelastic neutron response by using Feynman diagram rules. The effect of these higher order terms is, at one-loop level, to dress the magnon propagator with a self energy depending on the magnon density. At higher orders in perturbation theory one adds corrections this self energy. Two irreducible topologically distinct Feynman diagrams can be written down [427], with their interaction potentials calculable from the Dyson Maleev or Holstein Primakoff Hamiltonian [428, 429], since the single-ion physics has been treated in the bare magnon propagator, and the spin correlator can equally be written in terms of magnon creation operators. These higher order terms each carry a factor of $1/S$ per vertex [428] and are small for $S \to \infty$. The two-loop diagram (Fig. G.1 (b)) provides a real contribution to the self energy [427] and hence it renormalises the spectrum. The next diagram contains a real part and an imaginary part which represents a damping term. This gives an energy broadening to the magnon linewidth, which depends on momentum [427].

In some cases, there are further vertices that should be considered. In systems where $g^{zz}(\omega)$ is nonzero, that is to say, $\langle \hat{S}^z \rangle$ is not conserved, the extension beyond the harmonic approximation yields vertices where three lines meet. These terms are absent from spin-rotationally symmetric models, as is evident from the absence of cubic terms in the Holstein Primakoff Hamiltonian for collinear systems. Similar terms appear in noncollinear systems where SO(2) symmetry is broken [354]. These terms represent two magnon decays into a single magnon or vice versa. Using Wick's theorem [430], any n-point correlator can be decomposed into a sum of all possible contractions of the two-point correlators, thus one can calculate the effect of these decay vertices from the Green's functions evaluated by the approach outlined here (Eqn. G.8),

$$S(\mathbf{q},\omega) \propto -\mathrm{Im}\Bigg[\sum_{\theta\phi\tau\nu}\Big\{\int \mathrm{d}\mathbf{q}_1 \int \mathrm{d}\mathbf{q}_2 \int \mathrm{d}\omega_1 \int \mathrm{d}\omega_2 G^{\theta\phi}(\mathbf{q}_1,\omega_1)G^{\tau\nu}(\mathbf{q}_2,\omega_2) \\ \times\delta(\omega-\omega_1-\omega_2)\delta(\mathbf{q}-\mathbf{q}_1+\mathbf{q}_2)\Big\}\Bigg], \tag{G.10}$$

where conservation of momentum and energy has been ensured. The decay amplitudes are governed by kinematics. In particular, it has been argued that

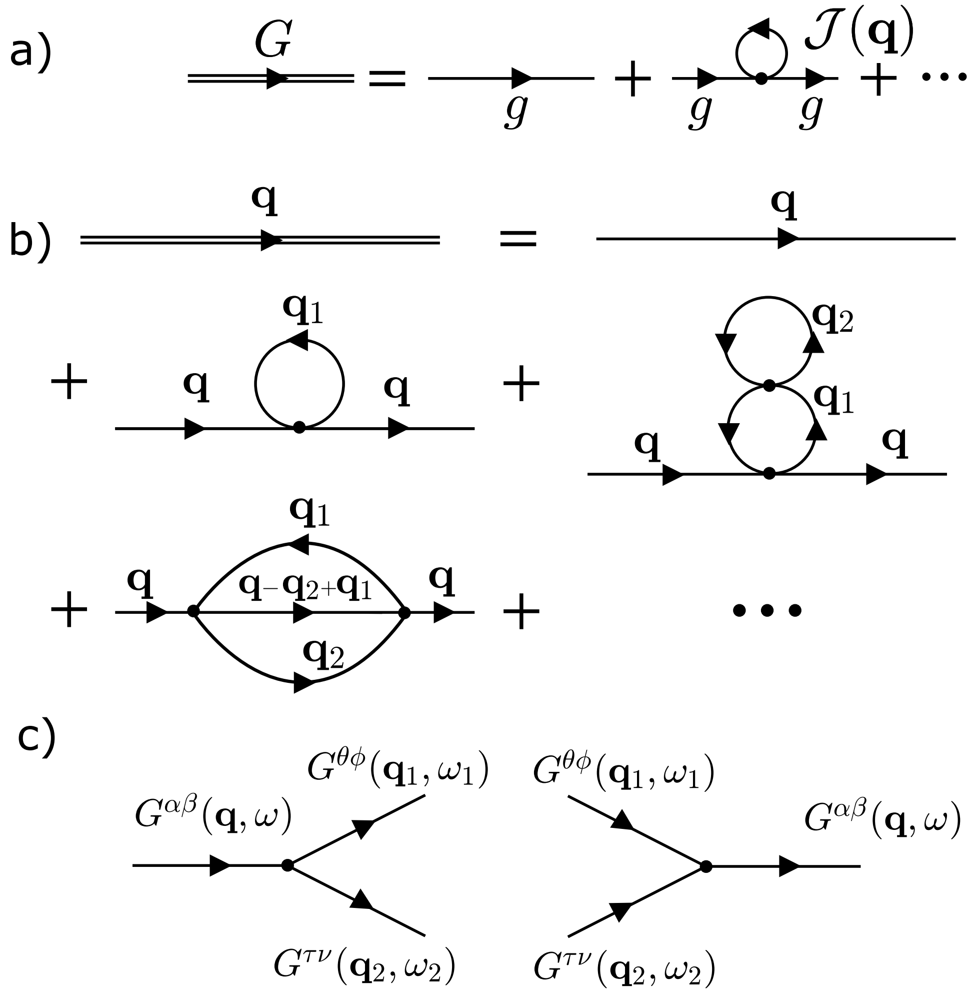

Figure G.1 *(a) Feynman diagrams showing the Dyson series structure of the expression for the Green's function obtained in Eqn. G.8. (b) Dyson series for the magnon Green's function showing the first and second order perturbative corrections to the magnon propagator for a collinear spin system. (c) Decay and source channels for three magnon interactions.*

the the longitudinal mode, G^{zz} is particularly susceptible to decay into two lower energy transverse spin waves [137]. Though the calculation of these terms has been simplified by formulating the spin wave calculation in terms of Green's functions, it still remains a formidable task to evaluate this integral in systems which disperse in more than one direction. This is especially true for the fitting of neutron scattering data measured on a time-of-flight spectrometer where one typically integrates over a finite window in momentum space to improve statistics.

Bibliography

[1] H. Lane, C. Stock, S.-W. Cheong, F. Demmel, R. A. Ewings, and F. Krüger, Phys. Rev. B **102**, 024437 (2020).

[2] L. Edwards, H. Lane, F. Wallington, A. M. Arevalo-Lopez, M. Songvilay, E. Pachoud, C. Niedermayer, G. Tucker, P. Manuel, C. Paulsen, E. Lhotel, J. P. Attfield, S. R. Giblin, and C. Stock, Phys. Rev. B **102**, 195136 (2020).

[3] Z. Liu, H. Lane, C. D. Frost, R. A. Ewings, J. P. Attfield, and C. Stock, J. Appl. Crystallogr. **54**, 957 (2021).

[4] H. Lane, E. Pachoud, J. A. Rodriguez-Rivera, M. Songvilay, G. Xu, P. M. Gehring, J. P. Attfield, R. A. Ewings, and C. Stock, Phys. Rev. B **104**, L020411 (2021a).

[5] H. Lane, E. E. Rodriguez, H. C. Walker, C. Niedermayer, U. Stuhr, R. I. Bewley, D. J. Voneshen, M. A. Green, J. A. Rodriguez-Rivera, P. Fouquet, S.-W. Cheong, J. P. Attfield, R. A. Ewings, and C. Stock, Phys. Rev. B **104**, 104404 (2021b).

[6] J. K. Cockcroft, "Nuclear reactors," `http://pd.chem.ucl.ac.uk/pdnn/inst3/reactors.htm`, [Accessed: 24-February-2022].

[7] J. Thomason, Nucl. Instrum. and Methods Phys. Res. A **917**, 61 (2019).

[8] J. A. Rodriguez, D. M. Adler, P. C. Brand, C. Broholm, J. C. Cook, C. Brocker, R. Hammond, Z. Huang, P. Hundertmark, J. W. Lynn, N. C. Maliszewskyj, J. Moyer, J. Orndorff, D. Pierce, T. D. Pike, G. Scharfstein, S. A. Smee, and R. Vilaseca, Meas. Sci. Technol. **19**, 034023 (2008a).

[9] ISIS Neutron and Muon Source, "MARI," `https://www.isis.stfc.ac.uk/Pages/mari.aspx` (a), [Accessed: 24-February-2022].

[10] K. Andersen, D. Martín y Marero, and M. Barlow, Appl. Phys. A **74**, s237 (2002).

[11] C. Stock, E. E. Rodriguez, N. Lee, M. A. Green, F. Demmel, R. A. Ewings, P. Fouquet, M. Laver, C. Niedermayer, Y. Su, K. Nemkovski, J. A. Rodriguez-Rivera, and S.-W. Cheong, Phys. Rev. Lett. **117**, 017201 (2016).

[12] P. M. Hill, H. S. Peiser, and J. R. Rait, Acta Crystallogr. **9**, 981 (1956).

[13] B. F. Decker and J. S. Kasper, Acta Crystallogr. **10**, 332 (1957).

[14] F. Wallington, A. M. Arevalo-Lopez, J. W. Taylor, J. R. Stewart, V. Garcia-Sakai, J. P. Attfield, and C. Stock, Phys. Rev. B **92**, 125116 (2015).

[15] C. Stock, E. E. Rodriguez, N. Lee, F. Demmel, P. Fouquet, M. Laver, C. Niedermayer, Y. Su, K. Nemkovski, M. A. Green, J. A. Rodriguez-Rivera, J. W. Kim, L. Zhang, and S.-W. Cheong, Phys. Rev. Lett. **119**, 257204 (2017).

[16] W. J. L. Buyers, "Spin dynamics, troisieme cycle de la physique, en suisse romande (lecture notes)," (1985).

[17] C. Trainer, O. R. Armitage, H. Lane, L. C. Rhodes, E. Chan, I. Benedičič, J. A. Rodriguez-Rivera, O. Fabelo, C. Stock, and P. Wahl, (2021), arXiv:2111.08013 [cond-mat.mtrl-sci] .

[18] J. Pásztorová, A. Howell, M. Songvilay, P. M. Sarte, J. A. Rodriguez-Rivera, A. M. Arévalo-López, K. Schmalzl, A. Schneidewind, S. R. Dunsiger, D. K. Singh, C. Petrovic, R. Hu, and C. Stock, Phys. Rev. B **99**, 125144 (2019).

[19] C. Stock, J. A. Rodriguez-Rivera, K. Schmalzl, F. Demmel, D. K. Singh, F. Ronning, J. D. Thompson, and E. D. Bauer, Phys. Rev. Lett. **121**, 037003 (2018).

[20] R. A. Ewings, J. R. Stewart, T. G. Perring, R. I. Bewley, M. D. Le, D. Raspino, D. E. Pooley, G. Škoro, S. P. Waller, D. Zacek, C. A. Smith, and R. C. Riehl-Shaw, Rev. Sci. Instrum. **90**, 035110 (2019).

[21] A. Abragam and B. Bleaney, *Electron paramagnetic resonance of transition ions* (Dover Publications, New York, 1986).

[22] D. S. McClure, "Electronic spectra of molecules and ions in crystals part ii. spectra of ions in crystals," (Academic Press, 1959) p. 399–525.

[23] M. Songvilay, E. E. Rodriguez, R. Lindsay, M. A. Green, H. C. Walker, J. A. Rodriguez-Rivera, and C. Stock, Phys. Rev. Lett. **121**, 087201 (2018).

[24] M. Songvilay, S. Petit, M. Koza, S. Rols, E. Suard, V. Skumryev, C. Martin, and F. Damay, Phys. Rev. B **101**, 014407 (2020a).

[25] S. Blundell, *Magnetism : a very short introduction* (Oxford University Press, 2012).

[26] S. Simon, *The Oxford Solid State Basics* (Oxford University Press, Oxford, 2013).

[27] K. Yosida, *Theory of Magnetism* (Springer, New York, 1996).

[28] L. Pauling and E. B. Wilson, *Introduction to quantum mechanics : with applications to chemistry* (McGraw-Hill, 1935).

[29] K. F. Riley, M. P. Hobson, and S. J. Bence, *Mathematical Methods for Physics and Engineering: A Comprehensive Guide*, 2nd ed. (Cambridge University Press, 2002).

[30] A. R. Edmonds, *Angular Momentum in Quantum Mechanics* (Princeton University Press, 2016).

[31] W. Gerlach and O. Stern, Z. Physik **9**, 349 (1922).

[32] R. Gurtler and D. Hestenes, J. Math. Phys. **16**, 573 (1975).

[33] J. G. Rau, E. K.-H. Lee, and H.-Y. Kee, Annu. Rev. Condens. Matter Phys. **7**, 195 (2016).

[34] E. Bauer and M. Rotter, "Magnetism of complex metallic alloys: Crystalline electric field effects," in *Properties and Applications of Complex Intermetallics*, pp. 183–248.

[35] K. W. H. Stevens, Proc. Phys. Soc. A **65**, 209 (1952).

[36] M. Hutchings (Academic Press, 1964) pp. 227–273.

[37] H. A. Jahn and E. Teller, Proc. R. Soc. Lond. A **161**, 220 (1937).

[38] C. Görller-Walrand and K. Binnemans, "Chapter 155 rationalization of crystal-field parametrization," (Elsevier, 1996) pp. 121–283.

[39] W. Heisenberg, Z. Physik **49**, 619 (1928).

[40] W. Heitler and F. London, Z. Physik **44**, 455 (1927).

[41] H. Iback and Lüth, *Solid State Physics* (Springer, Berlin, 2009).

[42] P. K. Misra, *Physics of Condensed Matter* (Academic Press, Boston, 2012).

[43] A. J. Freeman and R. E. Watson, Phys. Rev. **124**, 1439 (1961).

[44] K. I. Kugel' and D. I. Khomskiĭ, Sov. Phys. Usp. **25**, 231 (1982).

[45] C. G. Shull and J. S. Smart, Phys. Rev. **76**, 1256 (1949).

[46] P. W. Anderson, Phys. Rev. **115**, 2 (1959).

[47] J. Hubbard, Proc. R. Soc. London, Ser. A **276**, 238 (1963).

[48] D. I. Khomskii, *Transition Metal Compounds* (Cambridge University Press, 2014).

[49] D. I. Khomskii, *Basic Aspects of the Quantum Theory of Solids: Order and Elementary Excitations* (Cambridge University Press, 2010).

[50] N. D. Mermin and H. Wagner, Phys. Rev. Lett. **17**, 1133 (1966).

[51] I. Dzyaloshinsky, J. Phys. Chem. Solids **4**, 241 (1958).

[52] T. Moriya, Phys. Rev. **120**, 91 (1960).

[53] P. Coleman, *Introduction to Many-Body Physics* (Cambridge University Press, 2015).

[54] E. Fradkin, *Field Theories of Condensed Matter Physics*, 2nd ed. (Cambridge University Press, 2013).

[55] G. L. Squires, *Introduction to the Theory of Thermal Neutron Scattering*, 3rd ed. (Cambridge University Press, 2012).

[56] G. Shirane, S. M. Shapiro, and J. M. Tranquada, *Neutron Scattering with a Triple-Axis Spectrometer: Basic Techniques* (Cambridge University Press, 2002).

[57] A. T. Boothroyd, *Principles of neutron scattering from condensed matter* (Oxford University Press, 2002).

[58] J. M. Carpenter and C.-K. Loong, *Elements of Slow-Neutron Scattering: Basics, Techniques, and Applications* (Cambridge University Press, 2015).

[59] S. W. Lovesey, *Theory of Neutron Scattering from Condensed Matter, Volume II: Polarization Effects and Magnetic Scattering* (Claredon Press, 1986).

[60] ISIS Neutron and Source, "30 years of neutrons at ISIS!" https://www.isis.stfc.ac.uk/Pages/30-years-of-neutrons-at-ISIS.aspx (2014), [Accessed: 24-February-2022].

[61] Paul Scherrer Institut, "SINQ: The Swiss Spallation Neutron Source," https://www.psi.ch/en/sinq, [Accessed: 24-February-2022].

[62] Frank Laboratory of Neutron Physics, Joint Institute for Nuclear Research, "IBR-2," http://flnph.jinr.ru/en/facilities/ibr-2, [Accessed: 24-February-2022].

[63] W. H. Bragg and B. W. L., Proc. R. Soc. Lond. A **88**, 428–438 (1913).

[64] O. Steinsvoll, G. Shirane, R. Nathans, M. Blume, H. A. Alperin, and S. J. Pickart, Phys. Rev. **161**, 499 (1967).

[65] D. F. Johnston, Proc. Phys. Soc. **88**, 37 (1966).

[66] J. Zubáč, P. Javorský, and B. Fåk, J. Phys. Condens. Matter **30**, 255801 (2018).

[67] W. Henggeler, T. Chattopadhyay, B. Roessli, P. Vorderwisch, P. Thalmeier, D. I. Zhigunov, S. N. Barilo, and A. Furrer, Phys. Rev. B **55**, 1269 (1997).

[68] G. Amoretti, A. Blaise, R. Caciuffo, J. M. Fournier, M. T. Hutchings, R. Osborn, and A. D. Taylor, Phys. Rev. B **40**, 1856 (1989).

[69] G. Xu, Z. Xu, and J. M. Tranquada, Rev. Sci. Instrum. **84**, 083906 (2013).

[70] C. Carlile and M. Adams, Physica B **182**, 431 (1992).

[71] R. Bewley, R. Eccleston, K. McEwen, S. Hayden, M. Dove, S. Bennington, J. Treadgold, and R. Coleman, Physica B **385-386**, 1029 (2006).

[72] B. N. Brockhouse, Phys. Rev. **99**, 601 (1955).

[73] U. Stuhr, B. Roessli, S. Gvasaliya, H. Rønnow, U. Filges, D. Graf, A. Bollhalder, D. Hohl, R. Bürge, M. Schild, L. Holitzner, K. C., P. Keller, and T. Mühlebach, Nucl. Instrum. and Methods Phys. Res. A **853**, 16 (2017).

[74] T. Riste and K. Otnes, Nucl. Instrum. Methods **75**, 197 (1969).

[75] S. Shapiro and N. Chesser, Nucl. Instrum. Methods **101**, 183 (1972).

[76] I. E. Stamatelatos and S. Messoloras, Rev. Sci. Instrum. **71**, 70 (2000).

[77] T. W. Crane and M. P. Baker, in *Passive Nondestructive Assay of Nuclear Materials*.

[78] J. Ollivier, H. Casalta, H. Schober, J. C. Cook, P. Malbert, M. Locatelli, C. Gomez, S. Jenkins, I. J. Sutton, and M. Thomas, Appl. Phys. A **74**, s305 (2002).

[79] NIST Center for Neutron Research, "DCS Disk Chopper Spectrometer," `https://www.nist.gov/ncnr/dcs-disk-chopper-spectrometer` (a), [Accessed: 24-February-2022].

[80] R. I. Bewley, J. W. Taylor, and S. M. Bennington, Nucl. Instrum. and Methods Phys. Res. A **637**, 128 (2011).

[81] M. Russina and F. Mezei, J. Phys.: Conf. Ser. **251**, 012079 (2010).

[82] M. Nakamura, R. Kajimoto, Y. Inamura, F. Mizuno, M. Fujita, T. Yokoo, and M. Arai, J. Phys. Soc. Jpn. **78**, 093002 (2009).

[83] S. Itoh, K. Ueno, and T. Yokoo, Nucl. Instrum. and Methods Phys. Res. A **661**, 58 (2012).

[84] A. D. Taylor, M. Arai, and S. M. Bennington, *First results from the UK-Japanese spectrometer MARI*, Tech. Rep. (Japan, 1991) kEK–90-25(v2).

[85] N. Rhodes, E. Schooneveld, and R. Eccleston, Nucl. Instrum. and Methods Phys. Res. A **529**, 243 (2004).

[86] D. Colognesi, M. Celli, F. Cilloco, R. J. Newport, S. F. Parker, V. Rossi-Albertini, F. Sacchetti, J. Tomkinson, and M. Zoppi, Appl. Phys. A **74**, s64 (2002).

[87] G. Ehlers, F. Gallmeier, V. Graves, K. Herwig, G. Sala, L. Daemen, and A. Ramirez-Cuesta, Physica B **564**, 5 (2019).

[88] M. Arai, in *Neutron Scattering – Fundamentals*, Experimental Methods in the Physical Sciences, Vol. 44, edited by F. Fernandez-Alonso and D. L. Price (Academic Press, 2013) pp. 245–320.

[89] F. Groitl, D. Graf, J. O. Birk, M. Markó, M. Bartkowiak, U. Filges, C. Niedermayer, C. Rüegg, and H. M. Rønnow, Rev. Sci. Instrum. **87**, 035109 (2016).

[90] F. Groitl, R. Toft-Petersen, D. L. Quintero-Castro, S. Meng, Z. Lu, Z. Huesges, M. D. Le, S. Alimov, T. Wilpert, K. Kiefer, S. Gerischer, A. Bertin, and K. Habicht, Sci. Rep. **7**, 13637 (2017).

[91] Nucl. Instrum. and Methods Phys. Res. A **896**, 68 (2018).

[92] J. Kulda, J. Šaroun, P. Courtois, M. Enderle, M. Thomas, and P. Flores, Appl. Phys. A **74**, s246 (2002).

[93] NIST Center for Neutron Research, "SPINS," https://www.ncnr.nist.gov/instruments/spins/ (b), [Accessed: 24-February-2022].

[94] I. A. Zaliznyak, A. T. Savici, V. O. Garlea, B. Winn, U. Filges, J. Schneeloch, J. M. Tranquada, G. Gu, A. Wang, and C. Petrovic, J. Phys.: Conf. Ser. **862**, 012030 (2017).

[95] B. Dalla Piazza, M. Mourigal, N. B. Christensen, G. J. Nilsen, P. Tregenna-Piggott, T. G. Perring, M. Enderle, D. F. McMorrow, D. A. Ivanov, and H. M. Rønnow, Nat. Phys. **11**, 62 (2015).

[96] M. Loire, V. Simonet, S. Petit, K. Marty, P. Bordet, P. Lejay, J. Ollivier, M. Enderle, P. Steffens, E. Ressouche, A. Zorko, and R. Ballou, Phys. Rev. Lett. **106**, 207201 (2011).

[97] Z. Xu, J. A. Schneeloch, J. Wen, E. S. Božin, G. E. Granroth, B. L. Winn, M. Feygenson, R. J. Birgeneau, G. Gu, I. A. Zaliznyak, J. M. Tranquada, and G. Xu, Phys. Rev. B **93**, 104517 (2016).

[98] European Spallation Source, "European Spallation Source," `https://europeanspallationsource.se/` (a), [Accessed: 24-February-2022].

[99] European Spallation Source, "ESS revises project plan and budget," `https://europeanspallationsource.se/article/2021/12/10/ess-revises-project-plan-and-budget` (b), [Accessed: 24-February-2022].

[100] ISIS Neutron and Muon Source, "ALF," `https://www.isis.stfc.ac.uk/Pages/alf.aspx` (b), [Accessed: 24-February-2022].

[101] B. Ouladdiaf, J. Archer, G. McIntyre, A. Hewat, D. Brau, and S. York, Physica B **385-386**, 1052 (2006).

[102] C. Stock, "ALF analysis software," https://github.com/CSTOCK3/ALF-Analysis-Software, [Accessed: 24-February-2022].

[103] J. C. Collins and M. J. Perry, Phys. Rev. Lett. **34**, 1353 (1975).

[104] V. Berezinsky, Sov. Phys. JETP **32**, 493 (1971).

[105] J. M. Kosterlitz and D. J. Thouless, J. Phys. C **6**, 1181 (1973).

[106] S. Tomonaga, Prog. Theor. Phys. **5**, 544 (1950).

[107] J. M. Luttinger, J. Math. Phys. **4**, 1154 (1963).

[108] F. D. M. Haldane, J. Phys. C **14**, 2585 (1981).

[109] L. Faddeev and L. Takhtajan, Phys. Lett. A **85**, 375 (1981).

[110] A. H. Bougourzi, M. Couture, and M. Kacir, Phys. Rev. B **54**, R12669 (1996).

[111] M. Karbach, G. Müller, A. H. Bougourzi, A. Fledderjohann, and K.-H. Mütter, Phys. Rev. B **55**, 12510 (1997).

[112] J.-S. Caux, J. Mossel, and I. P. Castillo, J. Stat. Mech. **2008**, P08006 (2008).

[113] H. Bethe, Zeitschrift für Physik **71**, 205 (1931).

[114] Nat. Phys. **9**, 435 (2013).

[115] A. K. Bera, B. Lake, F. H. L. Essler, L. Vanderstraeten, C. Hubig, U. Schollwöck, A. T. M. N. Islam, A. Schneidewind, and D. L. Quintero-Castro, Phys. Rev. B **96**, 054423 (2017).

[116] W. J. Gannon, I. A. Zaliznyak, L. S. Wu, A. E. Feiguin, A. M. Tsvelik, F. Demmel, Y. Qiu, J. R. D. Copley, M. S. Kim, and M. C. Aronson, Nat. Commun. **10**, 1123 (2019).

[117] Nat. Commun. **10**, 698 (2019).

[118] M. Oshikawa and I. Affleck, Phys. Rev. Lett. **79**, 2883 (1997).

[119] I. Affleck and M. Oshikawa, Phys. Rev. B **60**, 1038 (1999).

[120] D. C. Dender, D. Davidović, D. H. Reich, C. Broholm, K. Lefmann, and G. Aeppli, Phys. Rev. B **53**, 2583 (1996).

[121] D. C. Dender, P. R. Hammar, D. H. Reich, C. Broholm, and G. Aeppli, Phys. Rev. Lett. **79**, 1750 (1997).

[122] E. Pytte, Phys. Rev. B **10**, 4637 (1974).

[123] N. Ishimura and H. Shiba, Prog. Theor. Phys. **57**, 1862 (1977).

[124] G. Müller, H. Thomas, H. Beck, and J. C. Bonner, Phys. Rev. B **24**, 1429 (1981).

[125] D. Sénéchal, "An introduction to bosonization," in *Theoretical Methods for Strongly Correlated Electrons*, edited by D. Sénéchal, A.-M. Tremblay, and C. Bourbonnais (Springer, New York, 2004) pp. 139–186.

[126] F. H. L. Essler, A. Furusaki, and T. Hikihara, Phys. Rev. B **68**, 064410 (2003).

[127] B. Lake, Nature Physics **1**, 143 (2005).

[128] H.-B. Braun, J. Kulda, B. Roessli, D. Visser, K. W. Krämer, H.-U. Güdel, and P. Böni, Nature Physics **1**, 159 (2005).

[129] M. Kenzelmann, Y. Chen, C. Broholm, D. H. Reich, and Y. Qiu, Phys. Rev. Lett. **93**, 017204 (2004).

[130] I. Umegaki, H. Tanaka, N. Kurita, T. Ono, M. Laver, C. Niedermayer, C. Rüegg, S. Ohira-Kawamura, K. Nakajima, and K. Kakurai, Phys. Rev. B **92**, 174412 (2015).

[131] S. A. Zvyagin, A. K. Kolezhuk, J. Krzystek, and R. Feyerherm, Phys. Rev. Lett. **93**, 027201 (2004).

[132] J. Liu, S. Kittaka, R. D. Johnson, T. Lancaster, J. Singleton, T. Sakakibara, Y. Kohama, J. van Tol, A. Ardavan, B. H. Williams, S. J. Blundell, Z. E. Manson, J. L. Manson, and P. A. Goddard, Phys. Rev. Lett. **122**, 057207 (2019a).

[133] B. Grenier, S. Petit, V. Simonet, E. Canévet, L.-P. Regnault, S. Raymond, B. Canals, C. Berthier, and P. Lejay, Phys. Rev. Lett. **114**, 017201 (2015).

[134] Z. Wang, M. Schmidt, A. K. Bera, A. T. M. N. Islam, B. Lake, A. Loidl, and J. Deisenhofer, Phys. Rev. B **91**, 140404 (2015).

[135] R. Coldea, D. A. Tennant, E. M. Wheeler, E. Wawrzynska, D. Prabhakaran, M. Telling, K. Habicht, P. Smeibidl, and K. Kiefer, Science **327**, 177 (2010).

[136] F. D. M. Haldane, Phys. Rev. Lett. **50**, 1153 (1983a).

[137] S. Sachdev, *Quantum Phase Transitions*, 2nd ed. (Cambridge University Press, 2011).

[138] J. Perring and T. Skyrme, Nucl. Phys. **31**, 550 (1962).

[139] R. Scharf, Y. S. Kivshar, A. Sánchez, and A. R. Bishop, Phys. Rev. A **45**, R5369 (1992).

[140] M. Crampin and D. Saunders, Rep. Math. Phys. **23**, 327 (1986).

[141] C. Rogers and W. K. Schief, *Bäcklund and Darboux Transformations: Geometry and Modern Applications in Soliton Theory*, Cambridge Texts in Applied Mathematics (Cambridge University Press, 2002).

[142] S. Cuenda, N. Quintero, and A. Sanchez, Discrete Contin. Dyn. Syst. - S **4**, 1047–1056 (2011).

[143] Physica D **19**, 165 (1986).

[144] V. A. Gani and A. E. Kudryavtsev, Phys. Rev. E **60**, 3305 (1999).

[145] "Wolfram research, inc., mathematica, version 12.1, champaign, il (2020)." https://www.wolfram.com/mathematica.

[146] L. M. Corliss, J. M. Hastings, and W. Kunnmann, Phys. Rev. **160**, 408 (1967).

[147] Y. Mizuno, T. Tohyama, S. Maekawa, T. Osafune, N. Motoyama, H. Eisaki, and S. Uchida, Phys. Rev. B **57**, 5326 (1998).

[148] T. Shimizu, T. Matsumoto, A. Goto, T. V. Chandrasekhar Rao, K. Yoshimura, and K. Kosuge, Phys. Rev. B **68**, 224433 (2003).

[149] P. L. Christiansen and O. H. Olsen, Phys. Scr. **20**, 531 (1979).

[150] J. D. Gibbon and G. Zambotti, Nuov. Cim. B **28**, 1 (2008).

[151] K. K. Kobayashi and M. Izutsu, J. Phys. Soc. Jpn **41**, 1091 (1976).

[152] A. G. Bratsos, J. Comput. Appl. Math. **206**, 251–277 (2007).

[153] N. Goldenfeld, *Lectures on Phase Transitions and the Renormalization Group* (CRC Press, Taylor & Francis Group, Boca Raton, 2019).

[154] A. V. Chubukov, S. Sachdev, and J. Ye, Phys. Rev. B **49**, 11919 (1994).

[155] S. Damerio, P. Nukala, J. Juraszek, P. Reith, H. Hilgenkamp, and B. Noheda, npj Quantum Mater. **5**, 33 (2020).

[156] A. V. Chubukov and D. I. Golosov, J. Phys.: Condens. Matter **3**, 69 (1991).

[157] M. E. Zhitomirsky and T. Nikuni, Phys. Rev. B **57**, 5013 (1998).

[158] K. Penc, N. Shannon, and H. Shiba, Phys. Rev. Lett. **93**, 197203 (2004).

[159] C. Lacroix, P. Mendels, and F. Mila, *Introduction to Frustrated Magnetism* (Springer, New York, 2010).

[160] J. S. White, C. Niedermayer, G. Gasparovic, C. Broholm, J. M. S. Park, A. Y. Shapiro, L. A. Demianets, and M. Kenzelmann, Phys. Rev. B **88**, 060409 (2013).

[161] Y. Kamiya, L. Ge, T. Hong, Y. Qiu, D. L. Quintero-Castro, Z. Lu, H. B. Cao, M. Matsuda, E. S. Choi, C. D. Batista, M. Mourigal, H. D. Zhou, and J. Ma, Nat. Commun. **9**, 2666 (2018).

[162] Y. Shirata, H. Tanaka, A. Matsuo, and K. Kindo, Phys. Rev. Lett. **108**, 057205 (2012).

[163] H. Tsujii, C. R. Rotundu, T. Ono, H. Tanaka, B. Andraka, K. Ingersent, and Y. Takano, Phys. Rev. B **76**, 060406 (2007).

[164] F. D. M. Haldane, Phys. Lett. **93A**, 464 (1983b).

[165] I. Affleck, T. Kennedy, E. H. Lieb, and H. Tasaki, Phys. Rev. Lett. **59**, 799 (1987).

[166] M. Oshikawa, Phys. Rev. Lett. **84**, 1535 (2000).

[167] A. Vasiliev, O. Volkova, E. Zvereva, and M. Markina, NPJ Quantum Mater. **3**, 18 (2018).

[168] D. A. Tennant, T. G. Perring, R. A. Cowley, and S. E. Nagler, Phys. Rev. Lett. **70**, 4003 (1993).

[169] J. Villain, Physica B **79**, 1 (1975).

[170] I. S. Jacobs, J. W. Bray, H. R. Hart, L. V. Interrante, J. S. Kasper, G. D. Watkins, D. E. Prober, and J. C. Bonner, Phys. Rev. B **14**, 3036 (1976).

[171] M. Hase, I. Terasaki, and K. Uchinokura, Phys. Rev. Lett. **70**, 3651 (1993).

[172] Y. H. Matsuda, N. Abe, S. Takeyama, H. Kageyama, P. Corboz, A. Honecker, S. R. Manmana, G. R. Foltin, K. P. Schmidt, and F. Mila, Phys. Rev. Lett. **111**, 137204 (2013).

[173] E. Lieb, T. Schultz, and D. Mattis, Ann. Phys. **16**, 407 (1961).

[174] M. Oshikawa, M. Yamanaka, and I. Affleck, Phys. Rev. Lett. **78**, 1984 (1997).

[175] K. Totsuka, Phys. Rev. B **57**, 3454 (1998).

[176] C. L. Henley, Phys. Rev. Lett. **62**, 2056 (1989).

[177] A. I. Smirnov, T. A. Soldatov, O. A. Petrenko, A. Takata, T. Kida, M. Hagiwara, A. Y. Shapiro, and M. E. Zhitomirsky, Phys. Rev. Lett. **119**, 047204 (2017).

[178] S. Agrestini, C. L. Fleck, L. C. Chapon, C. Mazzoli, A. Bombardi, M. R. Lees, and O. A. Petrenko, Phys. Rev. Lett. **106**, 197204 (2011).

[179] T. Takagi and M. Mekata, J. Phys. Soc. Jpn. **64**, 4609 (1995).

[180] H. Kikuchi, Y. Fujii, M. Chiba, S. Mitsudo, T. Idehara, T. Tonegawa, K. Okamoto, T. Sakai, T. Kuwai, and H. Ohta, Phys. Rev. Lett. **94**, 227201 (2005).

[181] H. Kageyama, K. Yoshimura, K. Kosuge, M. Azuma, M. Takano, H. Mitamura, and T. Goto, J. Phys. Soc. Jpn. **66**, 3996 (1997a).

[182] H. Kageyama, K. Yoshimura, K. Kosuge, H. Mitamura, and T. Goto, J. Phys. Soc. Jpn. **66**, 1607 (1997b).

[183] V. Hardy, M. R. Lees, A. Maignan, S. Hebert, D. Flahaut, C. Martin, and D. M. Paul, J. Phys. Condens. Matter **15**, 5737 (2003).

[184] Y. B. Kudasov, Phys. Rev. Lett. **96**, 027212 (2006).

[185] E. V. Sampathkumaran and A. Niazi, Phys. Rev. B **65**, 180401(R) (2002).

[186] S. Niitaka, K. Yoshimura, K. Kosuge, M. Nishi, and K. Kakurai, Phys. Rev. Lett. **87**, 177202 (2001).

[187] V. Hardy, C. Martin, G. Martinet, and G. André, Phys. Rev. B **74**, 064413 (2006).

[188] A. Maignan, V. Hardy, S. Hebert, M. Drillon, M. R. Lees, O. Petrenko, D. M. K. Paul, and D. Khomskii, J. Mater. Chem. **14**, 1231 (2004).

[189] K. Okamoto, T. Tonegawa, and M. Kaburagi, J. Phys. Condens. Matter **15**, 5979 (2003).

[190] K. C. Rule, A. U. B. Wolter, S. Süllow, D. A. Tennant, A. Brühl, S. Köhler, B. Wolf, M. Lang, and J. Schreuer, Phys. Rev. Lett. **100**, 117202 (2008).

[191] K. Katsumata, H. A. Katori, S. Kimura, Y. Narumi, M. Hagiwara, and K. Kindo, Phys. Rev. B **82**, 104402 (2010).

[192] R. Ishii, S. Tanaka, K. Onuma, Y. Nambu, M. Tokgunaga, T. Sakakibara, N. Kawashima, Y. Maeno, C. Broholm, D. P. Gatreaux, J. Y. Chan, and S. Nakatsuji, EPL **94**, 17001 (2011).

[193] H. Ueda, H. A. Katori, H. Mitamura, T. Goto, and H. Takagi, Phys. Rev. Lett. **94**, 047202 (2005).

[194] S. Mitsuda, M. Moase, K. Prokes, H. Kitazawa, and H. A. Katori, J. Phys. Soc. Jpn. **69**, 3513 (2000).

[195] N. Terada, S. Mitsuda, K. Prokes, O. Suzuki, H. Kitazawa, and H. Aruga Katori, Phys. Rev. B **70**, 174412 (2004).

[196] R. S. Fishman and S. Okamoto, Phys. Rev. B **81**, 020402(R) (2010).

[197] R. S. Fishman, Phys. Rev. Lett. **106**, 037206 (2011).

[198] M. Lenertz, A. Dinia, S. Colis, O. Mentre, G. Andre, F. Porcher, and E. Suard, J. Phys. Chem. C **118**, 13981 (2014).

[199] P. Fazekas and P. W. Anderson, Philos. Mag. **30**, 423 (1974).

[200] C. Stock, L. C. Chapon, O. Adamopoulos, A. Lappas, M. Giot, J. W. Taylor, M. A. Green, C. M. Brown, and P. G. Radaelli, Phys. Rev. Lett. **103**, 077202 (2009).

[201] M. Giot, L. C. Chapon, J. Androulakis, M. A. Green, P. G. Radaelli, and A. Lappas, Phys. Rev. Lett. **99**, 247211 (2007).

[202] R. L. Dally, R. Chisnell, L. Harriger, Y. Liu, J. W. Lynn, and S. D. Wilson, Phys. Rev. B **98**, 144444 (2018a).

[203] R. L. Dally, Y. Zhao, Z. Xu, R. Chisnell, M. B. Stone, J. W. Lynn, L. Balents, and S. D. Wilson, Nat. Commun. **9**, 2188 (2018b).

[204] M. Nandi, K. Nazir, B. Dilip, A. Midya, and M. Prabhat, J. Phys. Chem. C **118**, 1668 (2014).

[205] P. M. Sarte, A. M. Arévalo-López, M. Songvilay, D. Le, T. Guidi, V. García-Sakai, S. Mukhopadhyay, S. C. Capelli, W. D. Ratcliff, K. H. Hong, G. M. McNally, E. Pachoud, J. P. Attfield, and C. Stock, Phys. Rev. B **98**, 224410 (2018a).

[206] R. A. Cowley, W. J. L. Buyers, C. Stock, Z. Yamani, C. Frost, J. W. Taylor, and D. Prabhakaran, Phys. Rev. B **88**, 205117 (2013).

[207] P. M. Sarte, M. Songvilay, E. Pachoud, R. A. Ewings, C. D. Frost, D. Prabhakaran, K. H. Hong, A. J. Browne, Z. Yamani, J. P. Attfield, E. E. Rodriguez, S. D. Wilson, and C. Stock, Phys. Rev. B **100**, 075143 (2019).

[208] P. M. Sarte, R. A. Cowley, E. E. Rodriguez, E. Pachoud, D. Le, V. García-Sakai, J. W. Taylor, C. D. Frost, D. Prabhakaran, C. MacEwen, A. Kitada, A. J. Browne, M. Songvilay, Z. Yamani, W. J. L. Buyers, J. P. Attfield, and C. Stock, Phys. Rev. B **98**, 024415 (2018b).

[209] B. Kim, B. H. Kim, K. Kim, H. C. Choi, S.-Y. Park, Y. H. Jeong, and B. I. Min, Phys. Rev. B **85**, 220407(R) (2012a).

[210] N. Hollmann, S. Agrestini, Z. Hu, Z. He, M. Schmidt, C.-Y. Kuo, M. Rotter, A. A. Nugroho, V. Sessi, A. Tanaka, N. B. Brookes, and L. H. Tjeng, Phys. Rev. B **89**, 201101(R) (2014).

[211] Z. He, J. I. Yamaura, Y. Ueda, and W. Cheng, J. Am. Chem. Soc. **131**, 7554 (2009).

[212] M. Markkula, A. M. Arevalo-Lopez, and J. P. Attfield, J. Solid State Chem. **192**, 390 (2012a).

[213] L. C. Chapon, P. Manuel, P. G. Radaelli, C. Benson, L. Perrott, S. Ansell, N. J. Rhodes, D. Raspino, D. Duxbury, E. Spill, and J. Norris, Neutron News **22**, 22 (2011).

[214] K. Lefmann, C. Niedermayer, A. Abrahamsen, C. Bahl, N. Christensen, H. Jacobsen, T. Larsen, P. Häfliger, U. Filges, and H. Rønnow, Physica B **385-386**, 1083 (2006).

[215] M. Markkula, A. M. Arévalo-López, and J. P. Attfield, Phys. Rev. B **86**, 134401 (2012b).

[216] M. Lenertz, J. Alaria, D. Stoeffler, S. Colis, A. Dinia, O. Mentré, G. André, F. Porcher, and E. Suard, Phys. Rev. B **86**, 214428 (2012).

[217] M. F. Collins, *Magnetic Critical Scattering* (Oxford University Press, New York, 1989).

[218] S. T. Bramwell and P. C. W. Holdsworth, J. Appl. Phys. **73**, 6096 (1993).

[219] A. Guinier, *X-ray diffraction in crystals, imperfect crystals, and amorphous bodies* (W. H. Freeman, San Francisco, 1963).

[220] I. A. Zaliznyak and S. H. Lee, *Modern Techniques for Characterizing Magnetic Materials* (John Wiley & Sons, UK, 2007).

[221] M. E. Fisher and W. Selke, Phys. Rev. Lett. **44**, 1502 (1980).

[222] Y. Kudasov and R. Kozabaranov, EPJ Web Conf. **185**, 03002 (2018).

[223] J. Chen, W. Z. Zhuo, M. H. Qin, S. Dong, M. Zeng, X. B. Lu, X. S. Gao, and J. M. Liu, J. Phys.: Condens. Matter **28**, 346004 (2016).

[224] H. L. Stormer, D. C. Tsui, and A. C. Gossard, Rev. Mod. Phys. **71**, S298 (1999).

[225] R. B. Laughlin, Phys. Rev. B **23**, 5632 (1981).

[226] M. Oshikawa, Phys. Rev. Lett. **90**, 236401 (2003).

[227] J. Stephenson, J. Math Phys. **5**, 1009 (1964).

[228] H. Cho, J. B. Young, W. Kang, K. L. Campman, A. C. Gossard, M. Bichler, and W. Wegscheider, Phys. Rev. Lett. **81**, 2522 (1998).

[229] S. Ihnatsenka and I. V. Zozoulenko, Phys. Rev. B **75**, 035318 (2007).

[230] J. Alicea, A. V. Chubukov, and O. A. Starykh, Phys. Rev. Lett. **102**, 137201 (2009).

[231] T. Coletta, M. E. Zhitomirsky, and F. Mila, Phys. Rev. B **87**, 060407 (2013).

[232] T. Coletta, T. A. Tóth, K. Penc, and F. Mila, Phys. Rev. B **94**, 075136 (2016).

[233] D. A. Allwood, G. Xiong, M. D. Cooke, C. C. Faulkner, D. Atkinson, N. Vernier, and R. P. Cowburn, Science **296**, 2003 (2002).

[234] S. S. P. Parkin, M. Hayashi, and L. Thomas, Science **320**, 190–194 (2008).

[235] L. D. A. Ho, M.-T. Tran, X.-H. Cao, V.-A. Dao, D.-T. Ngo, and D.-Q. Hoang, RSC Adv. **8**, 14539 (2018).

[236] V. Baltz, A. Manchon, M. Tsoi, T. Moriyama, T. Ono, and Y. Tserkovnyak, Rev. Mod. Phys. **90**, 015005 (2018).

[237] S. K. Kim, O. Tchernyshyov, and Y. Tserkovnyak, Phys. Rev. B **92**, 020402(R) (2015).

[238] J. Železný, H. Gao, K. Výborný, J. Zemen, J. Mašek, A. Manchon, J. Wunderlich, J. Sinova, and T. Jungwirth, Phys. Rev. Lett. **113**, 157201 (2014).

[239] S. K. Kim, Y. Tserkovnyak, and O. Tchernyshyov, Phys. Rev. B **90**, 104406 (2014).

[240] R. Das, S. Debnath, G. N. Rao, S. Narasimhan, and F. C. Chou, Phys. Rev. B **98**, 144404 (2018).

[241] Y. Allain, B. Boucher, P. Imbert, and M. Perrin, C. R. Acad. Sc. Paris **9**, 263 (1966).

[242] E.-F. Bertaut, J. Chappert, A. Apostolov, and V. Semenov, Bull. Soc. franç. Minér. Crist. **89**, 206 (1966).

[243] NIST Center for Neutron Research, "High Resolution Powder Diffractometer - BT-1," https://www.nist.gov/ncnr/high-resolution-powder-diffractometer-bt-1 (c), [Accessed: 24-February-2022].

[244] M. Songvilay, S. Petit, F. Damay, G. Roux, N. Qureshi, H. C. Walker, J. A. Rodriguez-Rivera, B. Gao, S.-W. Cheong, and C. Stock, Phys. Rev. Lett. **126**, 017201 (2021a).

[245] F. Damay, C. Martin, V. Hardy, A. Maignan, G. André, K. Knight, S. R. Giblin, and L. C. Chapon, Phys. Rev. B **81**, 214405 (2010).

[246] F. Damay, C. Martin, V. Hardy, A. Maignan, C. Stock, and S. Petit, Phys. Rev. B **84**, 020402(R) (2011).

[247] M. H. L. Pryce, Phys. Rev. **80**, 1107 (1950).

[248] H. Watanabe, Prog. Theor. Phys. **18**, 405 (1957).

[249] B. Bleaney and R. S. Trenam, Proc. R. Soc. Lond. Ser. A **233**, 1 (1954).

[250] K. Lefmann, D. McMorrow, H. Rønnow, K. Nielsen, K. Clausen, B. Lake, and G. Aeppli, Physica B **283**, 343 (2000).

[251] A. L. Stancik and E. B. Brauns, Vib. Spectrosc. **47**, 66 (2008).

[252] R. Ewings, A. Buts, M. Le, J. van Duijn, I. Bustinduy, and T. Perring, Nucl. Instrum. Methods Phys. Res. **834**, 132–142 (2016).

[253] A. Pelissetto and E. Vicari, Phys. Rep. **368**, 549 (2002).

[254] H. Shenker, Phys. Rev. **107**, 1246 (1957).

[255] R. M. Bozorth, E. F. Tilden, and A. J. Williams, Phys. Rev. **99**, 1788 (1955).

[256] J. García, J. Carrizo, L. Elbaile, D. Lago-Cachón, M. Rivas, D. Castrillo, and A. Pierna, J. Magn. Magn. Mater. **372**, 27 (2014).

[257] G. Burns and F. H. Dacol, Solid State Commun. **48**, 853 (1983).

[258] T. Y. Koo, P. M. Gehring, G. Shirane, V. Kiryukhin, S.-G. Lee, and S.-W. Cheong, Phys. Rev. B **65**, 144113 (2002).

[259] C. Stock, R. J. Birgeneau, S. Wakimoto, J. S. Gardner, W. Chen, Z.-G. Ye, and G. Shirane, Phys. Rev. B **69**, 094104 (2004).

[260] C. Stock, H. Luo, D. Viehland, J. F. Li, I. P. Swainson, R. J. Birgeneau, and G. Shirane, J. Phys. Soc. Jpn. **74**, 3002 (2005a).

[261] C. Stock, P. M. Gehring, H. Hiraka, I. Swainson, G. Xu, Z.-G. Ye, H. Luo, J.-F. Li, and D. Viehland, Phys. Rev. B **86**, 104108 (2012).

[262] C. Stock, P. M. Gehring, G. Xu, D. Lamago, D. Reznik, M. Russina, J. Wen, and L. A. Boatner, Phys. Rev. B **90**, 224302 (2014).

[263] W. J. L. Buyers, T. M. Holden, and A. Perreault, Phys. Rev. B **11**, 266 (1975).

[264] P. M. Sarte, C. Stock, B. R. Ortiz, K. H. Hong, and S. D. Wilson, Phys. Rev. B **102**, 245119 (2020).

[265] H. Lane, E. Pachoud, J. A. Rodriguez-Rivera, M. Songvilay, G. Xu, P. M. Gehring, J. P. Attfield, R. A. Ewings, and C. Stock, Phys. Rev. B **104**, L020411 (2021c).

[266] C. Stock, W. J. L. Buyers, R. A. Cowley, P. S. Clegg, R. Coldea, C. D. Frost, R. Liang, D. Peets, D. Bonn, W. N. Hardy, and R. J. Birgeneau, Phys. Rev. B **71**, 024522 (2005b).

[267] H. Chou, J. M. Tranquada, G. Shirane, T. E. Mason, W. J. L. Buyers, S. Shamoto, and M. Sato, Phys. Rev. B **43**, 5554 (1991).

[268] E. Allroth and H. J. Mikeska, Z. Phys. B **43**, 209–219 (1981).

[269] L. Chen, J.-H. Chung, B. Gao, T. Chen, M. B. Stone, A. I. Kolesnikov, Q. Huang, and P. Dai, Phys. Rev. X **8**, 041028 (2018).

[270] A. K. Geim and I. V. Grigorieva, Nature **499**, 419 (2013).

[271] A. F. May, S. Calder, C. Cantoni, H. Cao, and M. A. McGuire, Phys. Rev. B **93**, 014411 (2016).

[272] S. Bao, W. Wang, Y. Shangguan, Z. Cai, Z.-Y. Dong, Z. Huang, W. Si, Z. Ma, R. Kajimoto, K. Ikeuchi, S.-i. Yano, S.-L. Yu, X. Wan, J.-X. Li, and J. Wen, Phys. Rev. X **12**, 011022 (2022).

[273] S. Liu, X. Yuan, Y. Zou, Y. Sheng, C. Huang, E. Zhang, J. Ling, Y. Liu, W. Wang, C. Zhang, J. Zou, K. Wang, and F. Xiu, npj 2D Mater. Appl. **1**, 30 (2017).

[274] H.-J. Deiseroth, K. Aleksandrov, C. Reiner, L. Kienle, and R. K. Kremer, Eur. J. Inorg. Chem. **2006**, 1561 (2006).

[275] B. Chen, J. Yang, H. Wang, M. Imai, H. Ohta, C. Michioka, K. Yoshimura, and M. Fang, J. Phys. Soc. Jpn. **82**, 124711 (2013).

[276] Y. Deng, Y. Yu, Y. Song, J. Zhang, N. Z. Wang, Z. Sun, Y. Yi, Y. Z. Wu, S. Wu, J. Zhu, J. Wang, X. H. Chen, and Y. Zhang, Nature **563**, 94 (2018).

[277] S. Calder, A. I. Kolesnikov, and A. F. May, Phys. Rev. B **99**, 094423 (2019).

[278] Y. Zhang, H. Lu, X. Zhu, S. Tan, W. Feng, Q. Liu, W. Zhang, Q. Chen, Y. Liu, X. Luo, D. Xie, L. Luo, Z. Zhang, and X. Lai, Sci. Adv. **4**, eaao6791 (2018).

[279] Institut Laue-Langevin, "D9," https://www.ill.eu/users/instruments/instruments-list/d9/description/instrument-layout.

[280] J. A. Rodriguez, D. M. Adler, P. C. Brand, C. Broholm, J. C. Cook, C. Brocker, R. Hammond, Z. Huang, P. Hundertmark, J. W. Lynn, and et al., Meas. Sci. Technol. **19**, 034023 (2008b).

[281] S. A. Owerre, J. Phys. Condens. Matter **28**, 386001 (2016).

[282] S. S. Pershoguba, S. Banerjee, J. C. Lashley, J. Park, H. Ågren, G. Aeppli, and A. V. Balatsky, Phys. Rev. X **8**, 011010 (2018).

[283] C. Tan, J. Lee, S.-G. Jung, T. Park, S. Albarakati, J. Partridge, M. R. Field, D. G. McCulloch, L. Wang, and C. Lee, Nat. Commun. **9**, 1554 (2018).

[284] A. Aharoni, *Introduction to the Theory of Ferromagnetism* (Oxford University Press, 2001).

[285] S. C. White, U. R. Singh, and P. Wahl, Rev. Sci. Instrum. **82**, 113708 (2011).

[286] C. Trainer, C. M. Yim, M. McLaren, and P. Wahl, Rev. Sci. Instrum. **88**, 093705 (2017).

[287] R. Wiesendanger, Rev. Mod. Phys. **81**, 1495 (2009).

[288] R. Moreno, R. F. L. Evans, S. Khmelevskyi, M. C. Muñoz, R. W. Chantrell, and O. Chubykalo-Fesenko, Phys. Rev. B **94**, 104433 (2016).

[289] S. Blundell, *Magnetism in Condensed Matter* (Oxford University Press, 2012).

[290] P. Gambardella, S. Rusponi, M. Veronese, S. S. Dhesi, C. Grazioli, A. Dallmeyer, I. Cabria, R. Zeller, P. H. Dederichs, K. Kern, C. Carbone, and H. Brune, Science **300**, 1130 (2003).

[291] A. Mook, J. Henk, and I. Mertig, Phys. Rev. B **90**, 024412 (2014).

[292] A. Mitra, A. Corticelli, P. Ribeiro, and P. A. McClarty, (2021), arXiv:2110.02662 [cond-mat.mes-hall] .

[293] P. C. Hohenberg, Phys. Rev. **158**, 383 (1967).

[294] N. D. Mermin, Phys. Rev. **176**, 250 (1968).

[295] J. Als-Nielsen, J. D. Litster, R. J. Birgeneau, M. Kaplan, C. R. Safinya, A. Lindegaard-Andersen, and S. Mathiesen, Phys. Rev. B **22**, 312 (1980).

[296] S. B. Khokhlachev, J. Exp. Theor. Phys. **43**, 137 (1976).

[297] M. Bander and D. L. Mills, Phys. Rev. B **38**, 12015 (1988).

[298] K. S. Burch, D. Mandrus, and J.-G. Park, Nature **563**, 47 (2018).

[299] A. Pulickel, P. Kim, and K. Banerjee, Physics Today **69**, 38 (2016).

[300] D. L. Duong, S. J. Yun, and Y. H. Lee, ACS Nano **11**, 11803 (2017).

[301] Y. Liu and C. Petrovic, Phys. Rev. B **97**, 014420 (2018).

[302] M. A. McGuire, H. Dixit, V. R. Cooper, and B. C. Sales, Chem. of Mater. **27**, 612–620 (2015).

[303] H. Wang, F. Fan, S. Zhu, and H. Wu, EPL **114**, 47001 (2016).

[304] H. Wang, V. Eyert, and U. Schwingenschlögl, J. Phys. Condens. Matter **23**, 116003 (2011).

[305] A. K. Kundu, Y. Liu, C. Petrovic, and T. Valla, Sci. Rep. **10**, 15602 (2020).

[306] C. Gong, L. Li, Z. Li, H. Ji, A. Stern, Y. Xia, T. Cao, W. Bao, C. Wang, Y. Wang, Z. Q. Qiu, R. J. Cava, S. G. Louie, J. Xia, and X. Zhang, Nature **546**, 265–269 (2017).

[307] V. Carteaux, D. Brunet, G. Ouvrard, and G. Andre, J. Phys. Condens. Matter **7**, 69–87 (1995).

[308] Ø. Johansen, V. Risinggård, A. Sudbø, J. Linder, and A. Brataas, Phys. Rev. Lett. **122**, 217203 (2019).

[309] E. C. Ahn, NPJ 2D Mater. Appl. **4**, 1–14 (2020).

[310] T. Dietl and H. Ohno, Rev. Mod. Phys. **86**, 187 (2014).

[311] G. Khaliullin, Phys. Rev. Lett. **111**, 197201 (2013).

[312] T. Kong, K. Stolze, E. I. Timmons, J. Tao, D. Ni, S. Guo, Z. Yang, R. Prozorov, and R. J. Cava, Adv Mater. **31**, 1808074 (2019).

[313] G.-D. Zhao, X. Liu, T. Hu, F. Jia, Y. Cui, W. Wu, M.-H. Whangbo, and W. Ren, Phys. Rev. B **103**, 014438 (2021).

[314] E. Gati, Y. Inagaki, T. Kong, R. J. Cava, Y. Furukawa, P. C. Canfield, and S. L. Bud'ko, Phys. Rev. B **100**, 094408 (2019).

[315] P. Doležal, M. Kratochvílová, V. Holý, P. Čermák, V. Sechovský, M. Dušek, M. Míšek, T. Chakraborty, Y. Noda, S. Son, and J.-G. Park, Phys. Rev. Materials **3**, 121401 (2019).

[316] T. Marchandier, N. Dubouis, F. m. c. Fauth, M. Avdeev, A. Grimaud, J.-M. Tarascon, and G. Rousse, Phys. Rev. B **104**, 014105 (2021).

[317] S. Tian, J.-F. Zhang, C. Li, T. Ying, S. Li, X. Zhang, K. Liu, and H. Lei, J. Am. Chem. Soc. **141**, 5326–5333 (2019).

[318] S. Son, M. J. Coak, N. Lee, J. Kim, T. Y. Kim, H. Hamidov, H. Cho, C. Liu, D. M. Jarvis, P. A. C. Brown, J. H. Kim, C.-H. Park, D. I. Khomskii, S. S. Saxena, and J.-G. Park, Phys. Rev. B **99**, 041402 (2019).

[319] Y. Liu, M. Abeykoon, and C. Petrovic, Phys. Rev. Res. **2**, 013013 (2020).

[320] B. Lyu, Y. Gao, Y. Zhang, L. Wang, X. Wu, Y. Chen, J. Zhang, G. Li, Q. Huang, N. Zhang, Y. Chen, J. Mei, H. Yan, Y. Zhao, L. Huang, and M. Huang, Nano Lett. **20**, 8 (2020).

[321] F. Subhan and J. Hong, J. Phys. Condens. Matter **32**, 245803 (2020).

[322] M. An, Y. Zhang, J. Chen, H.-M. Zhang, Y. Guo, and S. Dong, J. Phys. Chem. C **123**, 30545–30550 (2019).

[323] K. Yang, F. Fan, H. Wang, D. I. Khomskii, and H. Wu, Phys. Rev. B **101**, 100402 (2020).

[324] C. Huang, F. Wu, S. Yu, P. Jena, and E. Kan, Phys. Chem. Chem. Phys. **22**, 512–517 (2020).

[325] D. Juza, D. Giegling, and H. Schäfer, Z. Anorg. Allg. Chem. **366**, 121 (1969).

[326] M. Kratochvílová, K. Uhlířová, M. Míšek, V. Holý, J. Zázvorka, M. Veis, J. Pospíšil, S. Son, J.-G. Park, and V. Sechovský, Mater. Chem. Phys. **278**, 125590 (2022).

[327] O. Arnold, J. Bilheux, J. Borreguero, A. Buts, S. Campbell, L. Chapon, M. Doucet, N. Draper, R. Ferraz Leal, M. Gigg, V. Lynch, A. Markvardsen, D. Mikkelson, R. Mikkelson, R. Miller, K. Palmen, P. Parker, G. Passos, T. Perring, P. Peterson, S. Ren, M. Reuter, A. Savici, J. Taylor, R. Taylor, R. Tolchenov, W. Zhou, and J. Zikovsky, Nucl. Instrum. Methods Phys. Res. **764**, 156–166 (2014).

[328] P. J. Brown, International Tables for Crystallography, Volume C , 391 (1992).

[329] M. T. Hutchings, Solid State Phys. **16**, 227 (1964b).

[330] U. Walter, J. Phys. Chem. Solids **45**, 401 (1960).

[331] G. L. Stamokostas and G. A. Fiete, Phys. Rev. B **97**, 085150 (2018).

[332] W. Moffitt, G. L. Goodman, M. Fred, and B. Weinstock, Mol. Phys. **2**, 109 (1959).

[333] O. Tchernyshyov, Phys. Rev. Lett. **93**, 157206 (2004).

[334] A. Abragam and M. H. L. Pryce, Proc. Phys. Soc. London, Sec. A **205**, 135 (1951).

[335] Y. Tanabe and S. Sugano, J. Phys. Soc. Jpn. **9**, 753 (1954a).

[336] Y. Tanabe and S. Sugano, J. Phys. Soc. Jpn. **9**, 766 (1954b).

[337] Y.-J. Kim, A. P. Sorini, C. Stock, T. G. Perring, J. van den Brink, and T. P. Devereaux, Phys. Rev. B **84**, 085132 (2011).

[338] M. W. Haverkort, A. Tanaka, L. H. Tjeng, and G. A. Sawatzky, Phys. Rev. Lett. **99**, 257401 (2007).

[339] B. C. Larson, W. Ku, J. Z. Tischler, C.-C. Lee, O. D. Restrepo, A. G. Eguiluz, P. Zschack, and K. D. Finkelstein, Phys. Rev. Lett. **99**, 026401 (2007).

[340] A. S. Chakravarty, Proc. Phys. Soc. **74**, 711 (1959).

[341] J. S. Griffith, Trans. Faraday Soc. **56**, 193 (1960).

[342] J. H. V. Vleck, J. Chem. Phys. **7**, 72 (1939).

[343] A. Koriki, M. Misek, J. Pospisil, M. Kratochvilova, K. Carva, J. Prokleska, P. Dolezal, J. Kastil, S. Son, J. G. Park, and V. Sechovsky, (unpublished, arXiv:2101.03542).

[344] J. Valenta, M. Kratochvílová, M. Míšek, K. Carva, J. Kaštil, P. Doležal, P. Opletal, P. Čermák, P. Proschek, K. Uhlířová, J. Prchal, M. J. Coak, S. Son, J.-G. Park, and V. Sechovský, Phys. Rev. B **103**, 054424 (2021).

[345] W. J. L. Buyers, T. M. Holden, E. C. Svensson, R. A. Cowley, and M. T. Hutchings, J. Phys. C. **4**, 2139 (1971).

[346] R. Cowley, W. J. L. Buyers, P. Martel, and R. W. Stevenson, J. Phys. C **6**, 2997 (1973).

[347] B. J. Kim, H. Jin, S. J. Moon, J.-Y. Kim, B.-G. Park, C. S. Leem, J. Yu, T. W. Noh, C. Kim, S.-J. Oh, J.-H. Park, V. Durairaj, G. Cao, and E. Rotenberg, Phys. Rev. Lett. **101**, 076402 (2008).

[348] M. Moretti Sala, M. Rossi, S. Boseggia, J. Akimitsu, N. B. Brookes, M. Isobe, M. Minola, H. Okabe, H. M. Rønnow, L. Simonelli, D. F. McMorrow, and G. Monaco, Phys. Rev. B **89**, 121101 (2014).

[349] T. Feldmaier, P. Strobel, M. Schmid, P. Hansmann, and M. Daghofer, Phys. Rev. Research **2**, 033201 (2020).

[350] R. A. Muniz, Y. Kato, and C. D. Batista, Prog. Theor. Exp. Phys. **2014**, 083I01 (2014).

[351] Y. Hasegawa and M. Matsumoto, J. Phys. Soc. Jpn. **81**, 094712 (2012).

[352] J. S. Helton, S. K. Jones, D. Parshall, M. B. Stone, D. A. Shulyatev, and J. W. Lynn, Phys. Rev. B **96**, 104417 (2017).

[353] B. I. Halperin and P. C. Hohenberg, Phys. Rev. **188**, 898–918 (1969).

[354] M. E. Zhitomirsky and A. L. Chernyshev, Rev. Mod. Phys. **85**, 219 (2013).

[355] M. Onoda and J. Hasegawa, J. Phys. Condens. Matter **15**, L95 (2003).

[356] M. Reehuis, A. Krimmel, N. Büttgen, A. Loidl, and A. Prokofiev, Eur. Phys. J. **35** (2003), 10.1140/epjb/e2003-00282-4.

[357] S. Nakatsuji, Y. Nambu, H. Tonomura, O. Sakai, S. Jonas, C. Broholm, H. Tsunetsugu, Y. Qiu, and Y. Maeno, Science **309**, 1697 (2005).

[358] C. Stock, S. Jonas, C. Broholm, S. Nakatsuji, Y. Nambu, K. Onuma, Y. Maeno, and J.-H. Chung, Phys. Rev. Lett. **105**, 037402 (2010).

[359] S. Nakatsuji, Y. Nambu, and S. Onoda, J. Phys. Soc. Jpn. **79**, 011003 (2010).

[360] Y. Nambu, J. S. Gardner, D. E. MacLaughlin, C. Stock, H. Endo, S. Jonas, T. J. Sato, S. Nakatsuji, and C. Broholm, Phys. Rev. Lett. **115**, 127202 (2015).

[361] E. J. Samuelsen, R. Silberglitt, G. Shirane, and J. P. Remeika, Phys. Rev. B **3**, 157 (1971).

[362] Y. Liu, L. Qu, X. Tong, J. Li, J. Tao, Y. Zhu, and C. Petrovic, Sci. Rep. **9**, 13599 (2019b).

[363] F. Bloch, Z. Phys. **61**, 206 (1930).

[364] F. J. Dyson, Phys. Rev. **102**, 1217 (1956).

[365] T. Holstein and H. Primakoff, Phys. Rev. **58**, 1098 (1940).

[366] S. Petit, Collection SFN **10**, 449 (2010).

[367] M. Poienar, F. Damay, C. Martin, J. Robert, and S. Petit, Phys. Rev. B **81**, 104411 (2010).

[368] S. E. Hahn, R. S. Fishman, and G. Ehlers, (2019), spinWaveGenie.

[369] S. Toth and B. Lake, J. Phys. Condens. Matter **38**, 166002 (2015).

[370] M. Songvilay, S. Petit, F. Damay, G. Roux, N. Qureshi, H. C. Walker, J. A. Rodriguez-Rivera, B. Gao, S.-W. Cheong, and C. Stock, Phys. Rev. Lett. **126**, 017201 (2021b).

[371] B. Lake, D. A. Tennant, C. D. Frost, and S. E. Nagler, Nat. Mater. **4**, 329 EP (2005).

[372] M. Mourigal, M. Enderle, A. Klöpperpieper, J.-S. Caux, A. Stunault, and H. M. Rønnow, Nat. Phys. **9**, 435 (2013).

[373] S. Zhang, H. J. Changlani, K. W. Plumb, O. Tchernyshyov, and R. Moessner, Phys. Rev. Lett. **122**, 167203 (2019).

[374] D. Macdougal, A. S. Gibbs, T. Ying, S. Wessel, H. C. Walker, D. Voneshen, F. Mila, H. Takagi, and R. Coldea, Phys. Rev. B **98**, 174410 (2018).

[375] M. Pregelj, O. Zaharko, U. Stuhr, A. Zorko, H. Berger, A. Prokofiev, and D. Arčon, Phys. Rev. B **98**, 094405 (2018).

[376] D. Boldrin, B. Fåk, E. Canévet, J. Ollivier, H. C. Walker, P. Manuel, D. D. Khalyavin, and A. S. Wills, Phys. Rev. Lett. **121**, 107203 (2018).

[377] M. Zhu, M. Matsumoto, M. B. Stone, Z. L. Dun, H. D. Zhou, T. Hong, T. Zou, S. D. Mahanti, and X. Ke, Phys. Rev. Research **1**, 033111 (2019).

[378] Y. Su, A. Masaki-Kato, W. Zhu, J.-X. Zhu, Y. Kamiya, and S.-Z. Lin, Phys. Rev. B **102**, 125102 (2020).

[379] S. Hwan Chun, J.-W. Kim, J. Kim, H. Zheng, C. C. Stoumpos, C. D. Malliakas, J. F. Mitchell, K. Mehlawat, Y. Singh, Y. Choi, T. Gog, A. Al-Zein, M. M. Sala, M. Krisch, J. Chaloupka, and G. K. B. J. Jackeli, G.and Khaliullin, Nat. Phys. **11**, 462 (2015).

[380] A. Banerjee, J. Yan, J. Knolle, C. A. Bridges, M. B. Stone, M. D. Lumsden, D. G. Mandrus, D. A. Tennant, R. Moessner, and S. E. Nagler, Science **356**, 1055 (2017).

[381] L. D. Landau and E. M. Lifshitz, *Quantum Mechanics (Non-relativistic Theory)* (Elsevier Science, Oxford, 1977).

[382] P. M. Sarte, R. A. Cowley, E. E. Rodriguez, E. Pachoud, D. Le, V. García-Sakai, J. W. Taylor, C. D. Frost, D. Prabhakaran, C. MacEwen, A. Kitada, A. J. Browne, M. Songvilay, Z. Yamani, W. J. L. Buyers, J. P. Attfield, and C. Stock, Phys. Rev. B **98**, 024415 (2018c).

[383] S. W. Kim, S. H. Kim, P. S. Halasyamani, M. A. Green, K. P. Bhatti, C. Leighton, H. Das, and C. J. Fennie, Chem. Sci. **121**, 741 (2012b).

[384] C. C. Klepov, K. A. Pace, A. A. Berseneva, J. B. Felder, S. Calder, G. Morrison, Q. Zhang, M. J. Kirkham, D. S. Parker, and H.-C. Loye, J. Am. Chem. Soc. **143**, 11554 (2021).

[385] T. Fennell, M. J. Harris, S. Calder, M. Ruminy, M. Boehm, P. Steffens, M. H. Lemee-Cailleau, O. Zaharko, A. Cervellino, and S. T. Bramwell, Nat. Phys. **15**, 60 (2019).

[386] M. V. Gorev, I. N. Flerov, A. Tressaud, E. V. Bodganov, A. V. Kartashev, O. A. Bayukov, E. V. Eremin, and A. S. Krylov, J. Solid State Chem. **237**, 330 (2016).

[387] M. S. Molokeev, E. Bogdanov, S. Misyul, A. Tressaud, and I. Flerov, J. Solid State Chem. **200** (2013).

[388] Z.-Y. Dong, W. Wang, and J.-X. Li, Phys. Rev. B **97**, 205106 (2018).

[389] M. Elliot, P. A. McClarty, D. Prabhakaran, R. D. Johnson, H. C. Walker, P. Manuel, and R. Coldea, Nat. Commun. **12**, 3936 (2021).

[390] X. Bai, S.-S. Zhang, Z. Dun, H. Zhang, Q. Huang, H. Zhou, M. B. Stone, A. I. Kolesnikov, F. Ye, C. D. Batista, and M. Mourigal, Nat. Phys. **17**, 467 (2021).

[391] A. Legros, S.-S. Zhang, X. Bai, H. Zhang, Z. Dun, W. A. Phelan, C. D. Batista, M. Mourigal, and N. P. Armitage, Phys. Rev. Lett. **127**, 267201 (2021).

[392] M. Songvilay, A. Howell, I. Puente Orench, C. M. Brown, J. A. Rodriguez-Rivera, T. Guidi, E. E. Rodriguez, R. Lindsay, M. A. Green, and C. Stock, Unpublished.

[393] D. N. Zubarev, Phys.-Uspekhi **3**, 320 (1960).

[394] T. M. Holden and W. J. L. Buyers, Phys. Rev. B **9**, 3797 (1974).

[395] J. T. Haraldsen and R. S. Fishman, J. Phys. Condens. Matter **21**, 216001 (2009).

[396] N. M. Avram and M. G. Brik, *Optical Properties of 3d-Ions in Crystals: Spectroscopy and Crystal Field Analysis* (Springer, Berlin, 2013).

[397] R. G. Burns, *Mineralogical Applications of Crystal Field Theory*, 2nd ed., Cambridge Topics in Mineral Physics and Chemistry (Cambridge University Press, 1993).

[398] M. Tinkham, *Group Theory and Quantum Mechanics* (McGraw-Hill, 1964).

[399] O. Danielsen and P.-A. Lindgård, *Quantum mechanical operator equivalents used in the theory of magnetism*, Denmark. Forskningscenter Risoe. Risoe-R No. 259 (Risø National Laboratory, 1972).

[400] H. Lipkin, N. Meshkov, and A. Glick, Nucl. Phys. **62**, 188 (1965).

[401] W. D. Heiss, J. Phys. A Math. **45**, 444016 (2012).

[402] W. D. Heiss, F. G. Scholtz, and H. B. Geyer, J. Phys. A **38**, 1843 (2005).

[403] B. Yuan, M. B. Stone, G.-J. Shu, F. C. Chou, X. Rao, J. P. Clancy, and Y.-J. Kim, Phys. Rev. B **102**, 134404 (2020).

[404] M. Songvilay, J. Robert, S. Petit, J. A. Rodriguez-Rivera, W. D. Ratcliff, F. Damay, V. Balédent, M. Jiménez-Ruiz, P. Lejay, E. Pachoud, A. Hadj-Azzem, V. Simonet, and C. Stock, Phys. Rev. B **102**, 224429 (2020b).

[405] C. Kim, J. Jeong, G. Line, P. Park, T. Masuda, S. Asai, S. Itoh, H. S. Kim, H. Zhou, J. Ma, and J. G. Park, J. Phys.: Condens. Matter **34**, 045802 (2021).

[406] A. Jain, M. Krautloher, J. Porras, G. H. Ryu, D. P. Chen, D. L. Abernathy, J. T. Park, A. Ivanov, J. Chaloupka, G. Khaliullin, B. Keimer, and B. J. Kim, Nat. Phys. **13**, 633 (2017).

[407] S. M. Souliou, J. Chaloupka, G. Khaliullin, G. Ryu, A. Jain, B. J. Kim, M. Le Tacon, and B. Keimer, Phys. Rev. Lett. **119**, 067201 (2017).

[408] P. W. Higgs, Phys. Rev. Lett. **13**, 508 (1964).

[409] P. W. Anderson, Phys. Rev. **130**, 439 (1963).

[410] R. Shimano and N. Tsuji, Annu. Rev. of Condens. Matter Phys. **11**, 103 (2020).

[411] R. Coldea, D. A. Tennant, and Z. Tylczynski, Phys. Rev. B **68**, 134424 (2003).

[412] B. Lake, D. A. Tennant, and S. E. Nagler, Phys. Rev. Lett. **85**, 832 (2000).

[413] M. A. de Vries, T. K. Johal, A. Mirone, J. S. Claydon, G. J. Nilsen, H. M. Rønnow, G. van der Laan, and A. Harrison, Phys. Rev. B **79**, 045102 (2009).

[414] W. Low and M. Weger, Phys. Rev. **118**, 1119 (1960a).

[415] W. Low and M. Weger, Phys. Rev. **118**, 1130 (1960b).

[416] U. Öpic and M. H. L. Pryce, Proc. R. Soc. Lond. A **238**, 425 (1957).

[417] McPhase, "Tesseral harmonics," http://www.mcphase.de/manual/node123.html, [Accessed: 24-February-2022].

[418] M. V. Berry, Proc. Roy. Soc. Lond. A **392**, 45 (1984).

[419] R. M. Wilcox, J. Math. Phys. **8**, 962 (1967).

[420] D. Lehmann, *Mathematical Methods of Many-Body Quantum Field Theory* (CRC Press, 2004).

[421] L. Debnath, *Nonlinear Partial Differential Equations for Scientists and Engineers* (Birkhäuser, 2012).

[422] E. Bour, Journal de l'École Impériale Polytechnique **19**, 1 (1862).

[423] R. Sasaki, Nuclear Physics B **154**, 343 (1979).

[424] N. N. Bogoliubov, Il Nuovo Cimento (1955-1965) **7**, 794 (1958).

[425] R. M. White, M. Sparks, and I. Ortenburger, Phys. Rev. **139**, A450 (1965).

[426] J. F. Cooke, Phys. Rev. B **7**, 1108 (1973).

[427] E. Rastelli, *Statistical Mechanics of Magnetic Excitations* (World Scientific, 2013).

[428] A. B. Harris, D. Kumar, B. I. Halperin, and P. C. Hohenberg, Phys. Rev. B **3**, 961 (1971).

[429] S. P. Bayrakci, D. A. Tennant, P. Leininger, T. Keller, M. C. R. Gibson, S. D. Wilson, R. J. Birgeneau, and B. Keimer, Phys. Rev. Lett. **111**, 017204 (2013).

[430] E. Peskin, Michael and V. Schroeder, Daniel, *An Introduction To Quantum Field Theory* (CRC Press, 1995).